Dynamic Instabilities of Thin Sheets in Fluid Media

Thesis submitted in partial fulfillment
of the requirements for the degree of

"DOCTOR OF PHILOSOPHY"

by

Kirill Goncharuk

Submitted to the Senate of Ben-Gurion University
of the Negev

October 2025

Beer-Sheva

Dynamic Instabilities of Thin Sheets in Fluid Media

Thesis submitted in partial fulfillment
of the requirements for the degree of

"DOCTOR OF PHILOSOPHY"

by

Kirill Goncharuk

Submitted to the Senate of Ben-Gurion University
of the Negev

Approved by the advisors _____

October 2025

Beer-Sheva

This work was carried out under the supervision of

Prof. Yuri Feldman
Dr. Oz Oshri

In the Department of Mechanical Engineering
Faculty of Engineering

Acknowledgements

I am deeply grateful to my advisors, Prof. Yuri Feldman and Dr. Oz Oshri, for their guidance, patience, and persistent encouragement throughout this work. Their scientific insight and constructive criticism shaped the questions asked and the methods developed, while their high standards set the tone for the research programme. I also thank my colleagues and collaborators in the Department of Mechanical Engineering, whose comments and discussions improved both the analytical and numerical components of this thesis. Finally, I am indebted to my family for their unwavering support.

Abstract

The interaction of thin elastic sheets with surrounding fluids is ubiquitous in nature and technology, from insect wings in air to compliant valves in microfluidic devices. Motivated by such systems, this thesis advances the understanding of sheet and fluid coupling by analysing the fundamental balance between inertia, elasticity, and fluid resistance, and by developing numerical methods capable of capturing rapid two way fluid–structure interactions.

The thesis is based on three papers. The first, published in the *Journal of Fluid Mechanics*, establishes an analytical framework for flutter-induced flow in a novel setup. In this study, we investigate the onset of fluid motion within a closed chamber induced by dynamic deformations of an elastic sheet. The sheet is compressed between the chamber's sidewalls and divides it into two compartments, each initially containing an inviscid fluid at rest. When fluid exchange between the two compartments is allowed, the sheet becomes unstable and triggers a flow. An analytical framework is developed to describe the coupled, two-way interaction between the sheet and the surrounding fluid. We analyze the dynamics at both early and intermediate stages of evolution. The growth rates and oscillation frequencies associated with the second and first buckling modes are obtained analytically within the small-amplitude limit. At later times, we examine the transition of the sheet from the unstable second mode to the stable first mode. For a given chamber geometry, we find that the initial elastic energy of the sheet is primarily converted into the fluid's hydrodynamic energy when the sheet is relatively lighter than the fluid, and into the sheet's kinetic energy when it is relatively heavier.

The second paper, published in the *Journal of Computational Physics*, introduces a semi-implicit direct-forcing immersed-boundary method embedded in a SIMPLE scheme. We retain the core SIMPLE algorithm: a velocity predictor advances the flow using the pressure from the previous step, and a pressure-correction equation enforces continuity, recognising the Lagrange-multiplier role of pressure in the incompressible Navier–Stokes equations. The novelty is to embed the immersed-boundary constraint into this correction: we treat the boundary force as a Lagrange-multiplier

enforcing the immersed-body velocity and solve it together with the pressure in a single, coupled correction step. In this way, incompressibility and no-slip are enforced simultaneously at correction while the predictor remains unchanged. The result is a very fast solver with only tiny residual interface decoupling, well suited to broad parameter studies and large-scale FSI computations.

The third paper, published in *Theoretical and Computational Fluid Dynamics*, develops a fully implicit direct-forcing immersed-boundary solver built around a big-box Vanka smoother. It solves the Navier–Stokes equations together with the immersed-boundary constraint in a single coupled system at each time step, eliminating interface decoupling to machine accuracy. While slower than the semi-implicit scheme, it remains affordable with order N memory and order $O(N^{4/3})$ computational cost on Cartesian grids. The method is robust under strong fluid–structure coupling, rapid motion, tight clearances and large global displacements, making it the tool of choice for strongly coupled instabilities.

Contents

Chapter 1

Introduction

Thin elastic bodies are ubiquitous in nature. Consequently, a significant body of recent work has focused on the mechanics of thin sheets: flying insects [1], microfluidic devices [2], viruses [3], human skin [4], flapping flags [5], band-pass microfilters [6], and even tectonic plates in geophysics are successfully described by elastic theories of slender bodies [7–9]. Examples across scales are shown in Fig. 1.1.

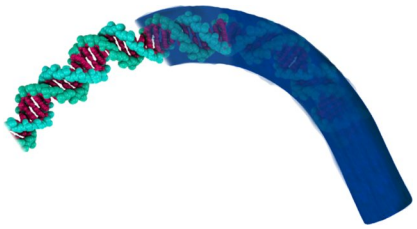

(a) DNA—elastic rod approximation. Radius is about 2 nm, whereas the length is metres. [10]

(b) Dragonfly wings are 3.6–15 μm in thickness; the other two dimensions are approximately 40×10 mm. [11]

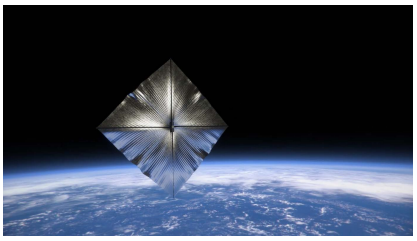

(c) Solar-sail concepts require sails of $\sim$5 μm thickness and up to 40×40 m in length. [12]

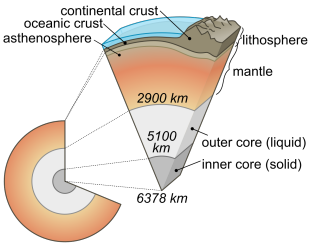

(d) Continental crust is typically $\sim$40 km thick, whereas oceanic crust averages $\sim$6 km; the lateral dimensions of plates are at least $\mathcal{O}(10^3)$ km. [7]

Figure 1.1: Thin sheets across scales in nature.

This ubiquity is no coincidence. Many elastic bodies are, by design, required

to undergo relatively large but reversible deformations. This reversibility is readily achieved when one dimension of the body is much smaller than the other two. Indeed, from everyday experience it is intuitive that thin bodies can sustain large deflections without undergoing plastic deformation. For example, a sheet of paper that bends gently under a small load, or the branch of a leaf that flexes in response to the wind. In general, elastic bodies may exhibit softness either through a low elastic modulus, which is known as material softness (e.g., elastomers), or through slenderness, which is known as geometric softness (e.g., thin sheets) [13].

To define a thin elastic body we address both parts of the term. We consider a three-dimensional continuous solid that undergoes reversible (elastic) deformations, and we assume it is thin, namely that one of its dimensions is significantly smaller than the other two. Two canonical classes of thin sheets are distinguished: thin shells, which possess a stress-free non-planar reference configuration, and thin plates (sheets), which are planar in the absence of load.

We quantify slenderness by the aspect ratio $\xi = L/h$, where h is the small dimension of the sheet (thickness) and L is a characteristic in-plane dimension; for thin bodies, ξ typically lies between $(0.1\text{–}10) \times 10^3$. A closely related measure, frequently used in the literature [3], is the Föppl–von Kármán (FvK) number $\lambda_{VfK} = \frac{YL^2}{B}$, where Y and B are the stretching and bending moduli of the sheet, respectively.

Thin sheets are pliable materials: they deform appreciably under relatively small boundary confinements. In static systems, this can be understood from energetic considerations: as the body becomes thinner, the energetic cost of out-of-plane deformation (bending) becomes significantly smaller than that of in-plane deformation (stretching). In dynamic systems, the picture is even more involved: beyond the bending and stretching competition, inertial effects of the sheet and, where applicable, the surrounding fluid also govern the evolution and thresholds.

Therefore, elastic instabilities of thin bodies may be broadly divided into static and dynamic classes, according to whether the evolution proceeds through quasi-equilibria or is inherently time dependent. We begin an overview of current research in the field of elastic instabilities with the static (time independent) case, and subsequently discuss dynamic phenomena and, finally, fluid–structure interactions.

1.1 Instabilities of slender elastic bodies

1.1.1 Static instabilities

The first broad class of time-independent (“static”) instabilities is characterized by the loss of stability of an equilibrium state when time can be neglected at onset. In

this case, the system evolves through a sequence of quasi-equilibrium configurations as the control parameters are slowly varied. Here, it is important to clarify the meaning of this slowness. The external forcing may vary in time, but its rate of change is sufficiently slow for the system to relax to a new equilibrium configuration after each small increment. In other words, the characteristic timescale of the external loading is much longer than the intrinsic relaxation time of the system, and allows the evolution to be treated as a sequence of quasi-static equilibria.

Guided by this framework, we now survey exemplar phenomena whose onsets are captured by quasi-static equilibrium arguments. We group selected classical and state-of-the-art studies according to the instabilities they describe, to briefly indicate where a static approach is effective.

Classical Euler buckling. Under slowly increasing compressive load, a straight rod loses stability via a pitchfork bifurcation whose critical force and wavenumber are dictated by geometry, i.e., the total length of the rod, boundary conditions, and elasticity [14–16]. For example, the critical load and wavenumber of a hinged-hinged rod scale as $F_{\mathrm{cr}} = \pi^2 B/L^2$ and $k = \pi/L$, where B is the bending modulus, L is the total length. The numerical coefficient arises from the boundary conditions. Post-buckling may be supercritical (smooth amplitude growth) or subcritical (discontinuous change in amplitude with force drop and snap) when imperfection sensitivity is added to the theory [17, 18].

Wrinkling and folds on compliant foundations. When a thin sheet lies on (or is bonded to) a soft substrate and is laterally compressed, the emerging pattern results from the competition between two energetic contributions: the bending energy of the sheet, proportional to the bending modulus B, and the elastic energy of the foundation, proportional to the substrate stiffness K. These two energies define a characteristic length scale, $\lambda \propto (B/K)^{\alpha}$, where the exponent α depends on the nature of the substrate, in addition to the total sheet length. At the onset of instability, the sheet typically buckles into a wavy pattern with wavelength proportional to λ. At small confinement one observes near-sinusoidal wrinkles [19].

Far from the onset of the wrinkle instability, a secondary bifurcation occurs, whose characteristics are determined by the stiffness of the substrate. For a fluid substrate, the sheet tends to form a localized pattern called a fold [20–22], whereas on an elastic foundation period doubling of the wrinkles occurs, in a manner analogous to the mechanism responsible for parametric-resonance-type instabilities [23].

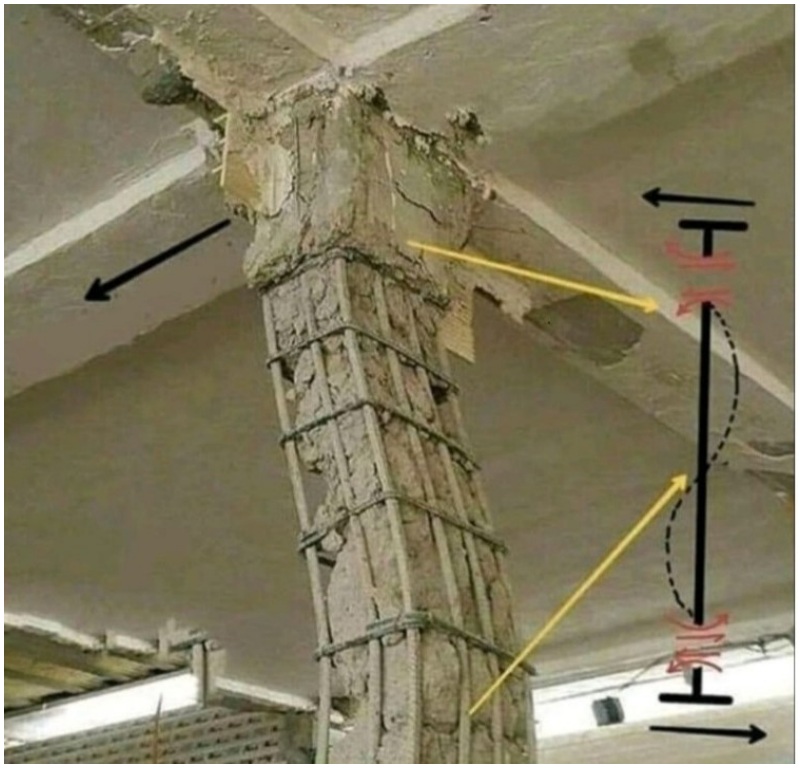

Figure 1.2: Buckling failure in reinforced concrete column

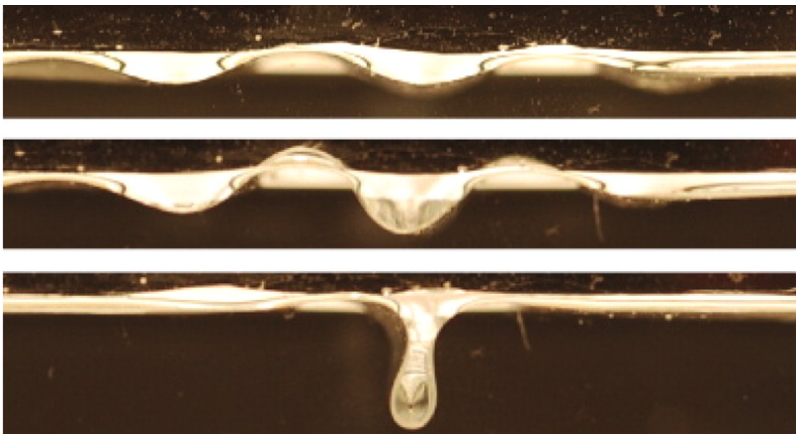

Figure 1.3: Wrinkles-to-fold transition under increasing confinement: top—unidirectional wrinkles; middle—intermediate, weakly localised state; bottom—a fully localised fold [19].

Crumpling and stress focusing. In the uniaxial settings discussed above, the sheet deforms nearly isometrically: the surface remains approximately developable, i.e., the Gaussian curvature is close to zero. However, when deformation occurs simultaneously in two directions, the response is qualitatively different and more localised. A typical example is crumpling, where the sheet organises into a network of narrow ridges with high curvature that separate relatively flat facets; these ridges

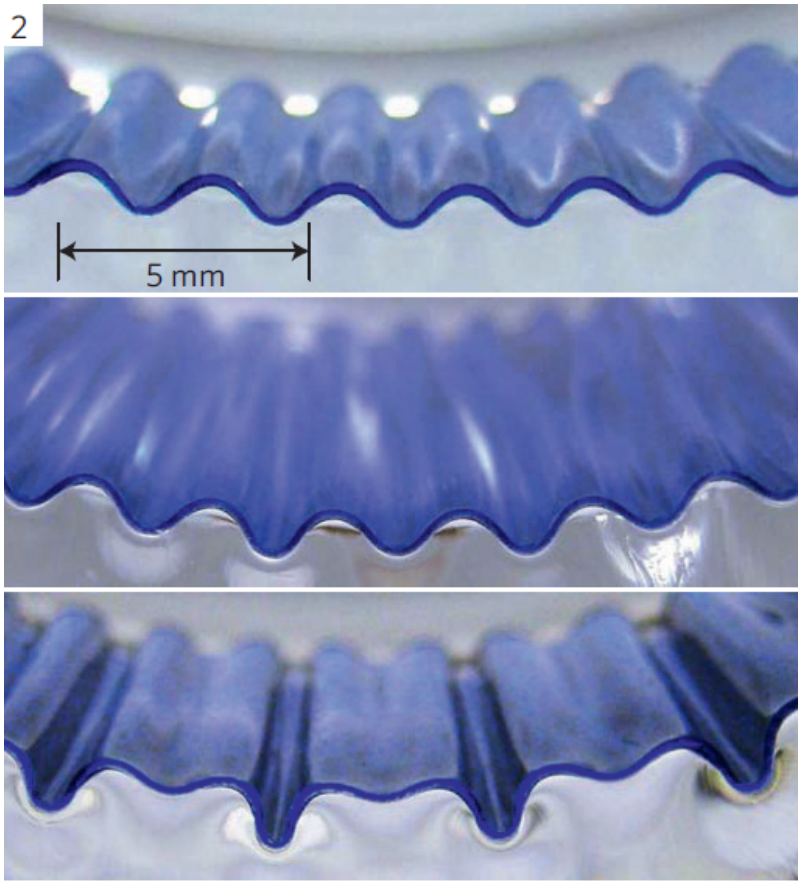

Figure 1.4: A period-doubling bifurcation [23]

.

terminate and intersect at vertices that carry large Gaussian curvature and strong stress focusing. Confinement therefore concentrates curvature and strain into a ridge and vertex network, so crumpled sheets exhibit a surprisingly large resistance to further compression and indentation, and show clear loading and unloading hysteresis [24]. As explained by Amar, in the large deformation limit the energy minimiser is developable almost everywhere except near d cone tips where curvature and stresses concentrate, which rationalises both the high apparent stiffness and the formation of permanent scars when yield is reached [25]. The broader framework of stress focusing and the singular structures that emerge in the zero thickness limit is reviewed in [26].

Ultra-thin, thickness-controlled regimes. Ultra thin sheets exhibit wrinkling patterns that classical small amplitude theories fail to capture. In annular geometries, for example the Lamé configuration, an azimuthal band of compression near the inner boundary produces a forest of radial wrinkles. Related capillary setups, such as a floating sheet indented by a droplet or a sheet draped over a drop, show

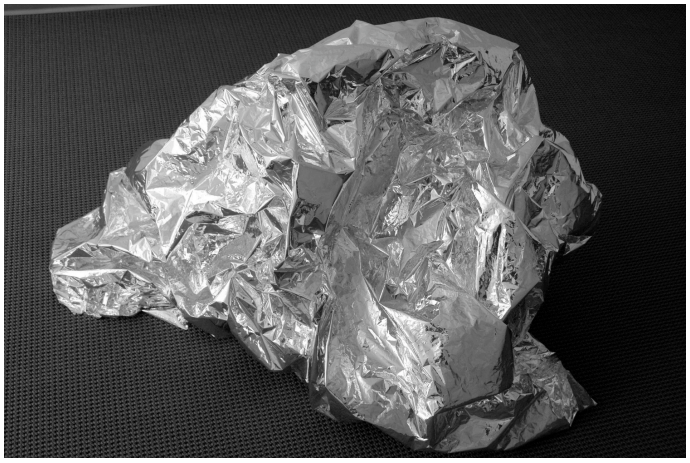

Figure 1.5: A loosely crumpled sheet of aluminised Mylar, 2 metres in width and 10 microns in thickness [26].

similarly robust wrinkle fields with measurable wavelengths and amplitudes [27, 28]. Previous studies attempted to predict the relation between the number of wrinkles and the sheet thickness. They showed that a regular perturbation expansion, which assumes the wrinkle amplitude to be the small parameter, fails to reproduce the experimental observations even slightly above the onset of the instability.

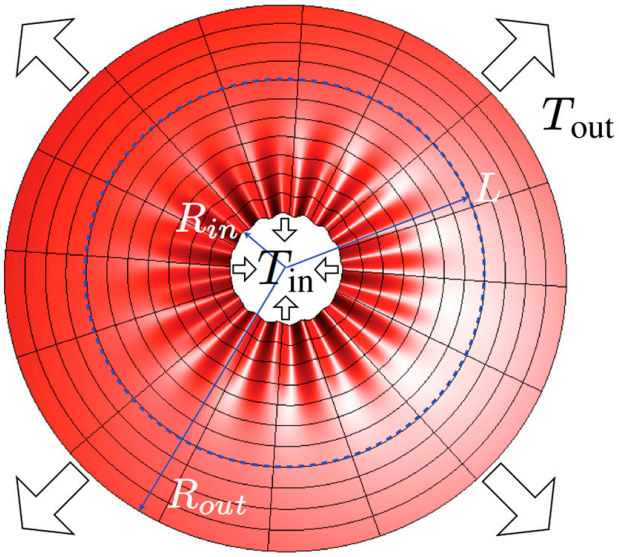

Figure 1.6: Radial wrinkles in the Lamé configuration [29].

This discrepancy motivated an alternative asymptotic approach in which the sheet thickness, rather than the deformation amplitude, serves as the small parameter. In this framework, a key assumption is that when the sheet is very thin, it cannot sustain compressive hoop stresses; hence, to leading order, these stresses vanish altogether. This formulation yields quantitative scalings consistent with experimental observations in the Lamé annulus and related capillary-wrinkling problems

[29]. Accordingly, this approach is most suitable for ultra-thin sheets, for which the far-from-threshold regime is reached rapidly.

Elastocapillary encapsulation. In addition to wrinkling instabilities on elastic foundations such as in the Lamé problem, a thin sheet can also deform under the action of surface tension from a liquid droplet. The competition between bending energy, scaling with the modulus B, and capillary energy, scaling with the surface tension γ, defines a characteristic elastocapillary length, $\ell_B \sim \sqrt{B/\gamma}$, that sets the minimal droplet size required to bend the sheet. Above this threshold, the sheet spontaneously folds and encapsulates the droplet, a process known as "capillary origami" [30]. Elastocapillary encapsulation thus provides a fundamental example of how a two-dimensional sheet can be reshaped into a three-dimensional structure under interfacial forces [30–32].

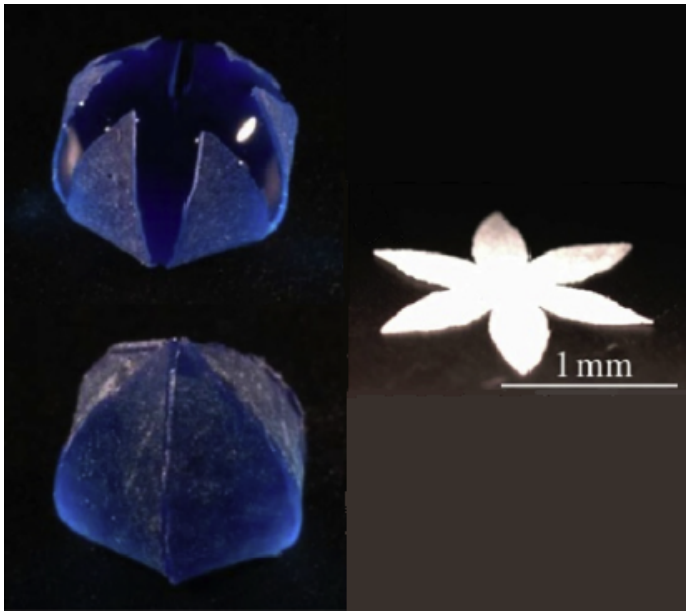

Figure 1.7: Elastocapillary encapsulation ("capillary origami"): a flat elastic sheet spontaneously wraps a drop when the surface-energy gain exceeds the bending cost. After [30].

Static snap-through exemplars. Snap through is often observed as a dynamic phenomenon in which bistable structures transition between two stable configurations once a critical load is exceeded; however, the onset can be analysed with static theory. Under slow loading the structure traces an equilibrium path that, in many bistable systems, exhibits a nonmonotonic force–displacement relation with a limit point. At the turning point the tangent stiffness vanishes, the equilibrium loses stability, and any infinitesimal disturbance drives a jump to the remote configuration.

An equivalent energy view is that a local minimum of the potential energy merges with a saddle so that the barrier height goes to zero, providing a quasi static threshold independent of the subsequent fast motion. A well known biological example is the Venus flytrap, which closes in $\mathcal{O}(10^2)$ ms through a snap buckling instability of a doubly curved leaf, with a mechanical threshold that the plant can actively modulate [33].

A closely related example shows how a quasi static bifurcation analysis can predict passive flow control: snap through of immersed arches or plates produces sharp, discontinuous changes in hydraulic resistance, enabling regulation of flow rate and confirmed experimentally [34].

As a further example, consider fluid induced snap of a spherical elastic cap mounted coaxially inside a circular channel and driven by a viscous throughflow. The Poiseuille pressure drop across the cap acts as a load; when it exceeds the elastic barrier the cap undergoes a limit point transition and snaps. A reduced model, desktop scale experiments, and fluid–structure simulations yield a compact onset criterion in terms of a Cauchy number

$$C_Y = \frac{\mu\, U_{\max} R^2}{\bar{B}}, \qquad \bar{B} = \frac{2Eh^3}{\sqrt{3}\,(1-\nu^2)},$$

which compares viscous stresses $\sim \mu U_{\max}/R$ with elastic stresses $\sim Eh^3/R^3$. By analogy with classical pressure buckling one expects $C_Y^{\mathrm{cr}} \sim R/h$, while geometry refines this through a function $C_Y^{\mathrm{cr}} = F(\theta, \delta, h/R)$, where θ is the shell opening angle and $\delta = (R\sin\theta)/R_c$ measures hydrodynamic confinement by the tube of radius R_c. The same mechanism realises a passive snapping valve with a sharp, hysteretic change in hydraulic resistance. At the time of writing this study is available as a preprint [35].

1.1.2 Dynamic instabilities

Dynamic instabilities require a time-dependent treatment in which inertia and, where relevant, dissipation are essential to both the onset of the instability and its evolution. In many cases, the temporal evolution can be divided into three main regimes. First, early times analysis, where linear stability about a base state captures the critical thresholds and the fastest-growing mode. Second, moderate times analysis, where weakly nonlinear reductions and normal forms with inertia and damping organize transient amplification, modal competition, and secondary bifurcations. Third, full evolution, where strongly nonlinear dynamics and rate effects, necessitate reduced-order models calibrated to experiments or high-fidelity

simulations.

In practice, these three regimes yield different analytical approximations, each valid on its own domain. Linear stability is local to the vicinity of the bifurcation and cannot describe the subsequent large-amplitude evolution. Weakly nonlinear reductions extend validity to small but finite amplitudes, capturing saturation, modal competition, and secondary onsets. Full-evolution descriptions (time-dependent PDEs or reduced-order models) are required for strongly nonlinear dynamics, but they often trade physical transparency for accuracy, so extracting simple laws can be challenging if possible.

Even when static analyses accurately predict the onset of instability, subsequent dynamics-such as amplitude growth, coarsening, mode switching, or sustained oscillations—remain history- and rate-dependent. The phenomena underlying dynamic instabilities of thin bodies are numerous, and the associated literature is vast. Rather than attempting an exhaustive survey, we highlight selected state-of-the-art studies, organised by the degree and role of fluid involvement. This taxonomy clarifies how structural dynamics evolve from dry to fully fluid-coupled settings.

No fluid influence (dry dynamics). A substantial body of recent work treats the dynamics of thin elastic bodies in the absence of surrounding fluid, providing clear baselines for later fluid coupled analysis. Nonlinear dynamic buckling of shallow arches under sudden central loading reveals trajectories that graze unstable equilibria and rebound, with thresholds shaped by imperfections and damping [36]. Reduced normal form models for boundary actuated strips near shape transitions capture transient amplification, dwell times, and mode selection [37]. Material effects have also been examined: structural viscoelasticity induces critical slowing and pseudo bistability, with divergent snap times near threshold and memory dependent basin reshaping [38]. Time modulated magnetic fields can drive snapping in hard magnetic bistable beams, enabling programmable post snap trajectories [39]. Rapidly forced elastic rings under effective external pressure provide a controlled paradigm for dynamic buckling: theory and post bifurcation analysis show that inertia drives selection of higher modes that are inaccessible in static buckling [40]. These examples show that even without fluid, state of the art methods continue to uncover the intricate mechanics of elastic instabilities.

Fluid on one side (confinement, loading, confined flows). In the examples below the fluid occupies one side of the structure. In some setups it provides confinement by restricting motion via a liquid bath, a meniscus, adhesive contact, or a viscous foundation; in others it provides loading through pressure, shear, or

capillary moments. The coupling to the solid may be weak or strong, and whether the fluid stress serves as a control parameter depends on the specific geometry and actuation. We distinguish two geometric subcases.

Open interfaces and substrates. The fluid is unconfined on the fluid side (bath or free surface) and acts mainly as a boundary load or dissipative substrate; feedback is present but does not set the dominant inertial scale. Impact on a floating elastic sheet shows how redistribution of inertia in the bath governs early wrinkle formation and coarsening, with transient matched linear theory predicting the evolving wavelength [41]. When the substrate is viscous, the compression rate becomes a bifurcation parameter: experiments and models distinguish uniform wrinkles from localised ridges and trace relaxation sequences shaped by viscous drainage [42, 43]. Surface tension can also provide a static like load, where meniscus induced moments drive snap through in beams and plates, supplying a threshold crossing mechanism [44].

Confined elastohydrodynamics. The fluid is geometrically confined in a conduit, gap, or membrane backed cavity, so pressure and deformation are mutually constrained by conservation laws; the load cannot be prescribed independently but emerges from the coupled problem. Pressure driven viscous flows in soft conduits apply both pressure and shear at the interface, deform the cross section, and thereby alter the relation between flow rate and pressure drop [45]. Multistable membranes driven by viscous flow exhibit rate dependent trajectories and pressure driven snaps between elastic walls without direct actuation of the solid [46].

Immersed structures (fluid-driven and flow–structure-controlled dynamics). In fully immersed settings, the fluid and the structure can each drive or sustain the other's motion. We first highlight cases where an instability may be triggered by either the flow or the structure, but once perturbed the subsequent dynamics are sustained primarily by the structure's inertia. At steady throughflow, periodic snapping can emerge as a limit cycle, with energy accumulation and release governed by flow strength and geometry [47]. In a closed channel, snap induced flow has been analysed by coupling a pre buckled sheet to the surrounding fluid, showing how structural instability can actively generate transient pressure gradients and throughflow [48]. Related work demonstrates that bistable arches embedded along the channel wall can be tuned to snap at prescribed flow rates via boundary stiffness, effectively turning them into programmable valves [49].

By contrast, in fluid driven flutter the mean flow supplies the energy that sustains oscillations: the external flow destabilises an initially quiescent body and maintains

motion through unsteady pressure and added mass. The canonical example is the flapping flag, in which a flexible plate or filament aligned with the flow undergoes a Hopf type bifurcation as the speed increases; onset and nonlinear dynamics have been mapped in theory and experiment [5, 50]. Variants including inverted flags and confined geometries reveal rich post critical regimes with frequency lock in, modal transitions, and sensitivity to confinement [51]. Arrays and plates in axial flow further exhibit hydrodynamic coupling that produces collective flutter modes and synchronisation; recent reviews summarise these interactions and their parameter dependence [52, 53]. A broader survey of biological and microfluidic contexts documents how flexible elements in surrounding flow display flutter, frequency selection, and flow controlled transport [2].

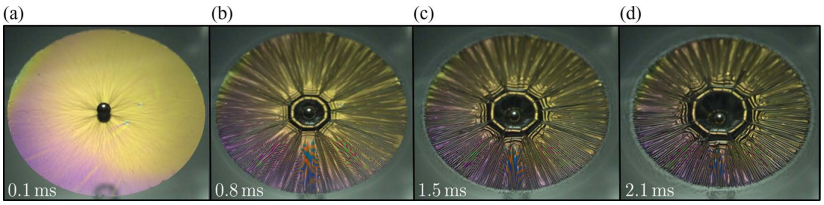

(a) Snapshots of impact-driven wrinkling by a steel sphere of radius $R_s = 1.25\,\text{mm}$ [41].

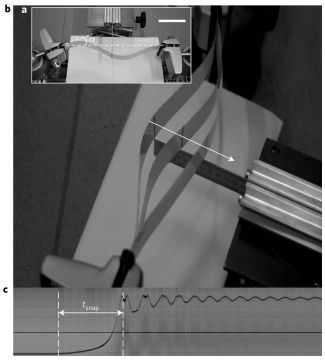

(b) A thin strip beyond the snapping threshold under end-shortening [54].

(c) Flutter of a flag [5].

Figure 1.8: Examples of dynamic instabilities in thin sheets.

1.1.3 FSI regimes for thin bodies

The dynamic instabilities surveyed above span cases with very different roles for the fluid: from dry, purely structural responses, through one sided situations where a fluid supplies confinement or loading, to fully immersed problems with strong coupling. To set the stage for what follows, we now restrict attention to the immersed

case, where the fluid's inertia and unsteady pressure must be coupled explicitly to the motion of the structure. The dry and one sided examples serve as context; the remainder of this section organises only the immersed settings.

To organise these responses more precisely, we compare the characteristic time scales of the fluid and the solid, along with their inertial coupling. For slender bodies, the most relevant dimensionless parameter is the solid-to-fluid mass ratio:

$$\lambda = \frac{\rho_s\, h}{\rho\, L},$$

where ρ_s and ρ are the densities of the solid and the fluid, respectively, h is the structure's thickness, and L is a representative in-plane length. When $\lambda \gg 1$ or when the solid and fluid time scales are well separated, the instability remains essentially structural. The fluid may add weak damping or loading but does not substantially alter the onset or dynamics. In such regimes, classically fluid-driven instabilities are suppressed.

For $\lambda \sim \mathcal{O}(1)$ the interaction is mixed: structural and fluid inertia are comparable, and coupling must be resolved to predict onset and evolution. For $\lambda \ll 1$ the fluid dominates; depending on geometry and rates, a simplified description with the fluid prescribed and the structure responding can be acceptable, but added mass and unsteady pressure still organise the dynamics and should be retained when they are of the same order as structural effects. Typical behaviours are then fluid driven, e.g. flapping flags and filaments, in which the external flow destabilises the body and sustains oscillations. Even here the structural response can feed back on the flow not via mass, but via boundary conditions, so a coupled analysis remains required. In some configurations one can adopt a massless structure approximation, treating the body as an inextensible constraint embedded in the flow, which captures essential features of flapping and vortex shedding [55]. This approximation is problem dependent and loses validity once structural inertia, stiffness contrasts, or geometric nonlinearities become comparable to fluid effects.

Within regimes that are not structurally dominated ($\lambda = \mathcal{O}(1)$ or $\lambda \ll 1$), we will distinguish two recurrent types of FSI categorized by the source of energy input. The first we call flow induced flutter, where the external flow destabilises an initially quiescent structure and sustains oscillations; classic cases are flags and plates in axial flow [5, 50]. In structure induced flutter, that we will call flutter induced flow, a structural instability first injects energy into the fluid and organises an oscillatory response; a representative instance is snap induced flow, where a snapping element generates a transient pressure difference and transport in confinement [48]. The

present thesis focuses on this flutter-induced flow: self-excited, time-dependent sheet motion that generates a pressure difference and net transport.

Flutter-induced flow

Structure driven transport generated by moving slender bodies is well documented experimentally. In open domains, flapping insect wings produce unsteady vortical flows and thrust [1]. In microfluidic settings, flutter of compliant membranes can be harnessed for pumping and filtering: membrane flutter has been used to realise on chip filtering [6], and single active chamber piezoelectric membrane pumps with passive check valves show frequency dependent flow rate and backpressure suitable for precise dosing and anti backflow operation [56]. Some flutter-induced flow phenomena have been treated analytically using static approaches, e.g. static analysis—volume-constrained deformation of a thin sheet as a route to harvest elastic energy—was presented in Oshri [57]. These studies demonstrate that elastic instabilities can modulate transport, but they do not address the fully time-dependent feedback present in self-excited flutter.

Analytical gap. Despite extensive experimental work and informative static analyses, the dynamics of flutter-induced flow—self-excited, time-dependent sheet motion that drives a pressure drop and net transport—remains incompletely described. This thesis addresses that gap by formulating and analysing a canonical problem: a confined thin sheet, immersed in an inviscid fluid, released from its second buckling mode and allowed to evolve freely. Our objective is to establish a quantitative relation between the sheet dynamics, the induced pressure difference, and the resulting transport in confinement.

1.2 Numerical simulations of slender bodies

We will use numerical simulations to corroborate and extend the analytical results. Numerical solvers allow us to capture the full two-way coupling and geometric nonlinearity of slender-body FSI beyond the simplifying assumptions of reduced models, and thus to investigate regimes and transient behaviours that are analytically inaccessible. For fixed geometries and linear (or weakly nonlinear, early-time) stability about a known base state, conforming FE/FV formulations are the natural choice: exact boundary representation and strong boundary enforcement reduce stability to a well-posed eigenproblem, while high-order discretisations accurately resolve boundary layers and eigenmodes with minimal dispersion and dissipation [58, 59].

There are monolithic finite-element body-fitted hydroelastic formulations for thin

members that achieve tight, energy-consistent coupling while retaining high geometric accuracy [60]. Yet beyond the linear regime, once a slender body undergoes large deflections the body-fitted mesh becomes the bottleneck: mesh motion, quality control, and remeshing dominate cost and can deteriorate accuracy over long evolutions. Even with advanced high-order/curvilinear meshing, generating and maintaining high-quality *hp* meshes around evolving thin features is algorithmically involved and computationally expensive [61].

For moving bodies, the Arbitrary Lagrangian–Eulerian (ALE) approach updates the computational mesh by solving a mesh-motion problem (e.g. elastic or Laplacian smoothing) so that grid nodes follow the structure while still allowing fluid to convect through the grid; this reduces the frequency of full remeshing and helps maintain cell quality [62]. Hybrid partitioned–monolithic ALE/FE treatments extend this approach to multiphysics and demonstrate, with careful linear–algebra design, that ALE can be robust across many coupled problems [63]. Unfortunately, when the structure is slender and undergoes large curvature changes, mesh skewness accumulates, and topological transformations (self-contact, snap-through, rapid shape change) still force mesh regeneration in ALE, reintroducing the very grid logistics the method seeks to avoid [62].

Immersed-boundary methods (IBM) offer a non-conforming alternative by separating interface representation (Lagrangian) from the fluid grid (Eulerian). The foundational contributions of Peskin introduced regularised delta function distributions that map forces and velocities between the two grids, enabling moving deformable interfaces without remeshing [64, 65]. Over time, many variants appeared, and they can be broadly grouped into two classes: (i) *diffuse-interface* IBM, in which boundary forces are regularised and spread to nearby Eulerian points via discrete delta kernels (yielding an $\mathcal{O}(\Delta x)$-thick numerical interface), and (ii) *sharp-interface* methods, which reconstruct the interface geometry in the background grid and enforce boundary conditions directly or via modified stencils.

Sharp–interface methods—ghost-cell [66], cut-cell/embedded-boundary [67], shifted-boundary [68, 69], and related CutFEM ideas [70]—typically enforce no-slip/no-penetration geometrically without adding explicit body–force terms to the Navier–Stokes equations, yielding exact boundary velocities and excellent near-wall resolution. However, these approaches fundamentally target *codimension-1* interfaces that partition the fluid into subdomains. For *vanishing-thickness slender bodies* (e.g. filaments in 3D, or plates treated as measure-zero sets), the interface does not bound a finite fluid region at grid scale, so the geometric machinery of cell cutting and stencil modification has nothing well-posed to operate on; in practice one must inflate the

body to a finite surrogate thickness. This requirement conflicts with our goal of modelling bodies best approximated as lines/surfaces of zero thickness. Moreover, the sharp jump enforcement can induce local discrete mass conservation errors unless special compatible reconstructions are used. For these reasons, sharp-interface IBM is poorly matched to truly vanishing-thickness structures, motivating our focus on diffuse-interface IBM for the present work.

Diffuse–interface immersed–boundary formulations augment the incompressible Navier–Stokes equations with a distributed body force that represents the action of the (Lagrangian) structure on the (Eulerian) fluid. Let $\Omega \subset \mathbb{R}^d$ be the Eulerian fluid domain with velocity $\boldsymbol{u}(\boldsymbol{x}, t)$ and pressure $p(\boldsymbol{x}, t)$, and let $\Gamma(t)$ be the immersed boundary (a material curve for $d = 2$ or surface for $d = 3$) parameterised by a Lagrangian coordinate $s \in \mathcal{S}$ with configuration $\boldsymbol{X}(s, t) \in \Omega$. In diffuse IBM, the action of the structure on the fluid enters the incompressible Navier–Stokes equations as a *distributed* body force

$$\boldsymbol{f}(\boldsymbol{x}, t) = \int_{\mathcal{S}} \boldsymbol{F}(s, t)\, \delta_\varepsilon\big(\boldsymbol{x} - \boldsymbol{X}(s, t)\big)\, \mathrm{d}s,$$

where $\boldsymbol{F}(s, t)$ is the Lagrangian force density per unit s along $\Gamma(t)$ and δ_ε is a compactly supported, regularised Dirac delta function[65, 71]. Interpolation of the Eulerian velocity to the immersed boundary,

$$\boldsymbol{U}(s, t) := \boldsymbol{u}\big(\boldsymbol{X}(s, t), t\big) = \int_{\Omega} \boldsymbol{u}(\boldsymbol{x}, t)\, \delta_\varepsilon\big(\boldsymbol{x} - \boldsymbol{X}(s, t)\big)\, \mathrm{d}\boldsymbol{x}.$$

Discretely, the integrals are replaced by sums using tensor–product kernels.

In the classical (Peskin) immersed–boundary formulation, the structure is represented on the Lagrangian set $\Gamma(t)$ and acts on the fluid through a prescribed *continuum* force density $\boldsymbol{F}(s, t)$ defined along $\Gamma(t)$ and expressed in terms of local geometric fields such as the unit tangent $\boldsymbol{\tau}(s, t) = \partial_s \boldsymbol{X} / \|\partial_s \boldsymbol{X}\|$ and curvature. The distributed body force in the Eulerian momentum equation is obtained by *spreading* $\boldsymbol{F}$ with a regularised delta, while the boundary points are *advected* by the interpolated fluid velocity, $\partial_t \boldsymbol{X}(s, t) = \boldsymbol{U}(s, t)$ [64, 65, 71].

For tension–dominated membranes and filaments, typical constitutive choices recover familiar geometric models. For example, for an inextensible string with constant tension T_0, Roma [71] writes the Lagrangian force density as

$$\boldsymbol{F}(s, t) = T_0\, \partial_{ss} \boldsymbol{X}(s, t),$$

which corresponds to the continuum limit of a taut filament. More generally, one

may take stretching/tension[72] or Euler–Bernoulli bending possibly augmented by inextensibility constraints enforced through a Lagrange multiplier tension $T(s,t)$ [65, 72]. These forces are then mapped to the Eulerian grid by regularised kernels, while kinematic coupling is enforced by interpolation, as detailed above. This continuum, geometry–based forcing is natural and effective for strings and membranes. For bending-dominated *plates/shells* of vanishing thickness, however, casting Kirchhoff–Love or related plate equations directly into this advection–plus–spreading framework becomes delicate: (i) the high-order derivatives in the bending operator increase stiffness and tighten time–step constraints, (ii) enforcing inextensibility or near-inextensibility via Lagrange multipliers is numerically sensitive when combined with fractional-step fluid updates, and (iii) the diffuse transfer operators limit the near-wall order of accuracy, which is critical for thin structures. These issues motivate our turn to direct-forcing approach and tighter coupling strategies developed later.

In the direct–forcing (DF) approach, the Lagrangian force is *chosen algebraically* so that, after a fluid update over a time step, the interpolated Eulerian velocity at the immersed boundary equals the prescribed boundary velocity. Let I denote interpolation from the Eulerian grid to the Lagrangian points (built from δ_ε) and R the adjoint regularization operator. Consider a fractional-step Navier–Stokes update that advances the velocity from t^n to an intermediate field $\tilde{\boldsymbol{u}}^{n+1}$ without the IBM force. The DF idea is to add a *localized impulse* $R(\boldsymbol{F}^{n+1})$ over Δt so that the post–IBM velocity $\boldsymbol{u}^{n+1}$ satisfies the kinematic condition of no-slip

$$I\left(\boldsymbol{u}^{n+1}\right) = \boldsymbol{U}_b^{n+1},$$

with $\boldsymbol{U}_b^{n+1}$ the desired boundary velocity (e.g. rigid motion or the structural velocity). Writing the fluid update in linearized form as

$$\boldsymbol{u}^{n+1} = \tilde{\boldsymbol{u}}^{n+1} + \mathcal{A}^{-1} R\left(\boldsymbol{F}^{n+1}\right),$$

where $\mathcal{A}^{-1}$ is the (time–discrete) fluid response over Δt (e.g. $\mathcal{A} = \rho\mathbf{I}/\Delta t - \nu\nabla^2$ for a viscous implicit step), the constraint yields the small Lagrangian system

$$\underbrace{I\left(\mathcal{A}^{-1} R\right)}_{\text{mobility}}\left(\boldsymbol{F}^{n+1}\right) = \boldsymbol{U}_b^{n+1} - I\left(\tilde{\boldsymbol{u}}^{n+1}\right),$$

from which $\boldsymbol{F}^{n+1}$ is computed and then spread to the grid. In the simplest explicit

variant, $\mathcal{A}^{-1} \approx (\Delta t/\rho)\mathbf{I}$, giving the familiar algebraic impulse

$$\boldsymbol{F}^{n+1} \;\approx\; \frac{\rho}{\Delta t}\Big(\boldsymbol{U}_b^{n+1} - I\,(\tilde{\boldsymbol{u}}^{\,n+1})\Big),$$

which is then regularized and applied as $R(\boldsymbol{F}^{n+1})$ [73, 74]. DF–IBM thereby *enforces no–slip kinematically* without invoking fictitious springs: the interpolation–regularization pair (I, R) ties Lagrangian and Eulerian descriptions, and the Lagrangian force plays the role of a distributed Lagrange multiplier enforcing $I(\boldsymbol{u}) = \boldsymbol{U}_b$. Subsequent developments refined accuracy and robustness of I/R and their coupling to the fluid solver for moving bodies and dense suspensions [75–77].

Further development of DF–IBM comes in Taira and Colonius [78], where the immersed–boundary force is treated as a *distributed Lagrange multiplier* (DLM), so that the no–slip constraint on the Lagrangian set is enforced simultaneously with incompressibility on the Eulerian grid. This viewpoint enables implicit and semi–implicit DF–IBM schemes. Let G and D be the discrete gradient and divergence (with $D = G^{\top}$ under the standard inner product), I the Eulerian→Lagrangian interpolation assembled from δ_ε, R its adjoint regularization ($R = I^{\top}$), and let $\mathcal{H}$ denote the Helmholtz–like operator arising from the chosen time/viscous update (e.g. $\mathcal{H} = \rho\,\mathbf{I}/\Delta t - \nu\nabla^2$ for an implicit–viscous step). A compact coupled form is

$$\begin{bmatrix} \mathcal{H} & G & -R \\ D & 0 & 0 \\ I & 0 & 0 \end{bmatrix} \begin{bmatrix} \boldsymbol{u}^{n+1} \\ p^{n+1} \\ \boldsymbol{F}^{n+1} \end{bmatrix} = \begin{bmatrix} \boldsymbol{r}_u \\ 0 \\ \boldsymbol{U}_b^{n+1} \end{bmatrix}, \qquad D = G^{\top},\; R = I^{\top},$$

where $\boldsymbol{F}^{n+1}$ plays the role of the DLM/IBM force. In practice, this framework has proven effective for moving rigid bodies and is typically realized in semi–implicit form via a projection step that retains the coupling of the Lagrange multipliers (pressure and boundary force) in the correction solve [78–80]. Related semi–implicit extensions [81–83].

However, these projection/DLM formulations share an important drawback: some degree of *temporal decoupling* between the force update and the velocity correction remains. The result is a decoupling error that produces a small but finite difference between fluid and boundary velocities ("leakage") and spurious pressure/force artifacts. These errors are often mitigated under periodic or highly regular settings, but they remain non-negligible in many realistic slender-body applications. When one must also evolve structural dynamics, the situation worsens: if the structural equations are treated in a loosely coupled outer loop, they are effectively decoupled from the inner incompressible solution. For bending-dominated, vanishing-thickness

plates governed by Kirchhoff–Love–type dynamics, such loose coupling is typically too weak, and standard IBM approaches become inapplicable [84, 85].

A natural remedy is to tighten the coupling further. Fully implicit, *strongly coupled* approaches—solving velocity, pressure, and structural unknowns together—can robustly handle challenging mass ratios and large motions [86, 87]. The trade-off is cost and complexity: each time step generally requires Newton iterations on the coupled system together with sophisticated preconditioners, which makes extensive parameter sweeps and long-time integrations expensive.

Numerical gap. The state of the art offers (i) efficient semi-implicit projection/DLM schemes with residual decoupling and potential leakage [78–83], and (ii) fully coupled Newton–Krylov formulations with exemplary robustness but high per-step cost and reduced flexibility for extensive parameter sweeps [86, 87]. What remains comparatively underserved is a *practical, implicit/semi-implicit, direct-forcing IBM for slender-body two-way-coupled FSI* that (a) enforces near-impenetrability at the interface with decoupling errors reduced to the level of spatial discretisation, and (b) remains computationally lean enough to execute large enough ensembles for validation and exploration.

1.3 Roadmap of the thesis

The thesis is organised as follows.

- **Chapter 1 (Introduction).** Motivates thin elastic sheets in fluids, defines core notions (geometric vs material softness; static vs dynamic instabilities; one-way vs two-way FSI), and clarifies *flutter-induced flow* versus *flow-induced flutter*; identifies the analytical and numerical gaps.

- **Chapter 2 (Fluttering-induced flow in a closed chamber).** Formulates the inviscid confined-sheet problem (release from the second buckling mode), derives early-time growth/frequency and moderate-time energy-exchange scalings with dimensional predictions, and cross-checks key results numerically. *Based on* JFM 976 A15 (2023).

- **Chapter 3 (Semi-implicit IBM within SIMPLE).** Develops a semi-implicit direct-forcing immersed-boundary formulation integrated into a SIMPLE scheme with a Schur update for tighter pressure–boundary coupling; validates via convergence, leakage, and cost benchmarks on moving slender-body cases. *Based on* JCP 487:112148 (2023).

- **Chapter 4 (Implicit IBM with Vanka 'big-box' smoother).** Constructs an implicit direct-forcing IBM embedded in a Vanka "big-box" smoother with multigrid acceleration; benchmarks accuracy, stability, and efficiency against strongly coupled references on representative problems. *Based on* TCFD 39:36 (2025).
- **Chapter 5 (Summary and outlook).** Synthesises the analytical and numerical findings, delineates limitations (e.g. viscous effects, Reynolds-number range, three-dimensionality), and outlines extensions and applications to broader FSI scenarios.

Chapter 2

Fluttering-induced flow in a closed chamber

This chapter is based on: Goncharuk, K., Feldman, Y., & Oshri, O. (2023). *Fluttering-induced flow in a closed chamber. Journal of Fluid Mechanics*, **976**, A15.

Time-dependent deformations of a thin elastic sheet confined within a closed chamber are analysed. While the chamber is sealed from the external environment, the compartments remain interconnected through a valve, which is idealized as a periodic boundary condition between the two compartments. The sheet is modeled as an undamped, inextensible elastica with bending rigidity, while the surrounding fluid is taken inviscid and, to leading order, irrotational. The regime considered is release from the second buckling mode. Small-amplitude modal descriptions are developed for the early evolution and the subsequent nonlinear energy exchange is tracked up to the first peak at moderate times. In subsequent work [48], a pipe partitioned by a thin sheet into two isolated subdomains was considered. By imposing a pressure drop Δp across the sheet, it was shown that once a critical threshold Δp_c is exceeded, the pre-snap configuration approaches the sheet's second buckling eigenmode, after which a snap-through occurs. This scenario shares key features with the release-from-second-mode studied here—such as the dominance of the same modal content in the initial response and similar scaling motifs for the pressure–flow relation—yet the snap dynamics are more involved and include additional nonlinear effects. Additional manuscript currently under review further extends the analysis of fluttering-induced flow [88] to unconfined domains, showing analogous scalings and dynamical behaviour. All this research is based on the results presented in this chapter.

Structure of the article.

1. **Introduction.** Context and motivation for fluttering-induced flow in confinement; summary of parameters and assumptions.
2. **Formulation.** Governing equations and boundary conditions for the fluid and the confined sheet; small-amplitude approximation and modal expansions about the second buckling mode.
3. **Early-time evolution.** Recap of the quasi-static baseline; linear stability analysis yielding growth rates and vibration frequency.
4. **Moderate-time evolution.** Nonlinear energy-exchange scalings and dimensional predictions up to the first peak.
5. **Experimental consequences.** Implications for measurement, controllable parameters, and results discussion.

Note on wording in the reproduced article. The remainder of this chapter reproduces the published article verbatim. There are three phrases in the following text that may be read ambiguously when taken out of context, and we therefore clarify the intended meaning here.

- **Sidewalls and contact.** Any wording suggesting that the sheet is "compressed between the sidewalls" refers only to end constraints and end-shortening (the sheet is attached at its ends to the sidewalls). The model assumes no contact between the sheet and the sidewalls along its span, and no self-contact, throughout the motion.
- **"Rotational" flow in a potential-flow model.** Although the surrounding flow is modelled as inviscid and (to leading order) irrotational, the sheet motion can produce recirculating streamline patterns. The term "rotational" should be interpreted in this kinematic sense (recirculation), not as vorticity generation.
- **Pressure jump at valve opening.** The instantaneous change in the pressure difference at $t = 0$ relies on a separation of time scales: the valve-opening time and acoustic adjustment are assumed negligible compared with the sheet inertial time scale. If these time scales are comparable, the jump would be smoothed over a short transient.

J. Fluid Mech. (2023), *vol*. 976, A15, doi:10.1017/jfm.2023.901

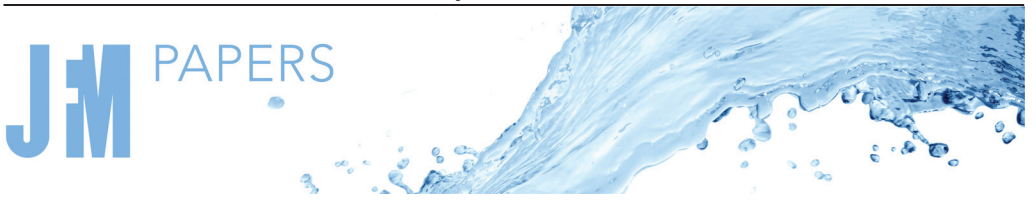

Fluttering-induced flow in a closed chamber

Kirill Goncharuk[1], **Yuri Feldman**[1] **and Oz Oshri**[1],†

[1]Department of Mechanical Engineering, Ben-Gurion University of the Negev, Beer-Sheva 84105, Israel

(Received 16 June 2022; revised 17 July 2023; accepted 22 October 2023)

We study the emergence of fluid flow in a closed chamber that is driven by dynamical deformations of an elastic sheet. The sheet is compressed between the sidewalls of the chamber and partitions it into two separate parts, each of which is initially filled with an inviscid fluid. When fluid exchange is allowed between the two compartments of the chamber, the sheet becomes unstable, and its motion displaces the fluid from rest. We derive an analytical model that accounts for the coupled, two-way, fluid–sheet interaction. We show that the system depends on four dimensionless parameters: the normalized excess length of the sheet compared with the lateral dimension of the chamber, Δ; the normalized vertical dimension of the chamber; the normalized initial volume difference between the two parts of the chamber, $v_{du}(0)$; and the structure-to-fluid mass ratio, λ. We investigate the dynamics at the early times of the system's evolution and then at moderate times. We obtain the growth rates and the frequency of vibrations around the second and the first buckling modes, respectively. Analytical solutions are derived for these linear stability characteristics within the limit of the small-amplitude approximation. At moderate times, we investigate how the sheet escapes from the second mode. Given the chamber's dimensions, we show that the initial energy of the sheet is mostly converted into hydrodynamic energy of the fluid if $\lambda \ll 1$ and into kinetic energy of the sheet if $\lambda \gg 1$. In both cases, most of the initial potential energy is released at time $t_p \simeq \ln[c\Delta^{1/2}/v_{du}(0)]/\sigma$, where σ is the growth rate and c is a constant.

Key words: flow-structure interactions, bifurcation

1. Introduction

Many natural processes and technological applications rest on fluid–structure interactions to maintain their regular functionality. Of particular interest are the mutual interactions between slender elastic objects and a fluid medium that trigger elastohydrodynamic instabilities. Such instabilities are vital for the control, for example, of the passage of air through the lungs (Ishizaka & Flanagan 1972; Grotberg & Jensen 2004), the directionality

† Email address for correspondence: oshrioz@bgu.ac.il

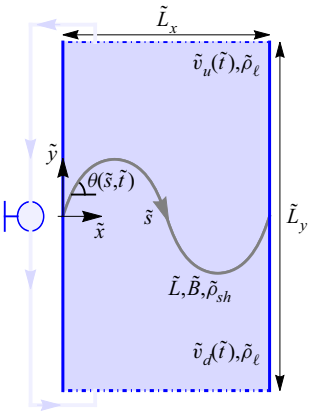

Figure 1. Schematic overview of the system. A thin sheet of total length $\tilde{L}$, bending modulus $\tilde{B}$, density $\tilde{\rho}_{sh}$ and thickness $\tilde{h}$ divides a closed rectangular chamber of dimensions $\tilde{L}_x \times \tilde{L}_y$ into two parts. The excess length of the sheet compared with the lateral dimension of the chamber is given by $\tilde{\Delta} = \tilde{L} - \tilde{L}_x$ (not shown in the figure). The volumes of the chamber above and below the sheet, $\tilde{v}_i(t)$ $(i = u, d)$, are filled with an inviscid and irrotational fluid of density $\tilde{\rho}_\ell$. At $\tilde{t} \geq 0$, fluid is allowed to exchange freely between the two compartments of the chamber. In our formulation, the fluid exchange occurs through the upper and lower walls of the chamber (represented by dashed-dotted blue lines). To model this exchange, we apply periodic boundary conditions along these walls. One possible experimental set-up that corresponds to the above model involves a valve-controlled channel that connects the two compartments of the chamber.

of blood flow (Pedley, Brook & Seymour 1996) and the blood pressure of tall animals (Pedley *et al.* 1996). Moreover, bending deformations of slender objects in viscous or inertial fluids have been manipulated for applications in soft robotics (Kim, Laschi & Trimmer 2013; Matia & Gat 2015; Rothemund *et al.* 2018), the fabrication of microfluidic soft actuators (Thorsen, Maerkl & Quake 2002; Hosoi & Mahadevan 2004; Holmes *et al.* 2013; Fargette, Neukirch & Antkowiak 2014; Gomez, Moulton & Vella 2017; Christov *et al.* 2018; Boyko *et al.* 2019; Jiao & Liu 2021), the manufacture of semiconductors (King 1989) and the design of soft and active matter through catalytic reactions (Laskar *et al.* 2022; Manna *et al.* 2022) and dynamical wrinkles (Chopin, Dasgupta & Kudrolli 2017; Kodio, Griffiths & Vella 2017; Box *et al.* 2019; Pocivavsek *et al.* 2019; O'Kiely *et al.* 2020; Diamant 2021; Guan *et al.* 2022, 2023).

Despite recent achievements, novel designs of small-scale devices still call for a deeper understanding of elastohydrodynamic couplings. One such design was recently introduced by Oshri (2021). In that set-up, a thin sheet is compressed between the two sides of a closed chamber and divides it into two separate parts that are connected by a valve (figure 1). At time $t < 0$, the valve is closed, and each part of the chamber is filled with an incompressible fluid. In the absence of fluids, the sheet would have accommodated its minimum energetic state, i.e. the lowest mode of buckling, but in the presence of fluids, the sheet is forced to accommodate a higher energetic state. The additional energy can be exploited to displace the fluid from rest, if, for example, the valve is opened to allow the transfer of fluids between the two compartments of the chamber.

In the above mentioned study, Oshri (2021) analysed the quasi-static evolution of the system, wherein the volume of fluid exchanged between the two parts of the chamber is the control parameter. In contrast, the present work focuses on the dynamical evolution of the system, wherein the fluid is driven by the spontaneous relaxation of the sheet from higher to lower energetic states. We believe that the dynamic analysis of this set-up will

open new avenues for designing advanced technological devices, such as micromechanical switches (Krylov *et al.* 2008; Zhang *et al.* 2014; Preston *et al.* 2019) and microfluidic mixing devices (Stroock *et al.* 2002; Liu, Kim & Sung 2004; Lee *et al.* 2011). Indeed, the additional coupling between the sheet and the surrounding fluid confers increased flexibility in the design of such switches. Different fluids with different viscosities can be used to manipulate the time that is required for the sheet to release its stored energy, thereby increasing, for example, the time scales over which the switches operate. In addition, when the two parts of the chamber are filled with different fluids, the elastic energy released from the sheet can be exploited for mixing: the pressure field induced in the chamber can be utilized to inject the fluid from one side of the chamber into the fluid on the other side, thereby inducing mixing of the two fluids. Typically, such devices function in conditions of low Reynolds numbers, where the effects of viscosity are significant. However, our system can also be applied in the design of pneumatic time-delay switches and soft pneumatic actuators (Rothemund *et al.* 2018; Preston *et al.* 2019; Drotman *et al.* 2021), which typically operate in the opposing limit of high Reynolds numbers.

While successful implementation of these applications is in itself a challenging task (which we plan to pursue in future research), in this work, we aim to answer more fundamental questions related to the underlying physical behaviour of the system. For example, how much of the initial elastic energy is subsequently transferred from the sheet to the fluid? How is the velocity of the fluid that is induced in the chamber related to the elastic properties of the sheet? What is the maximum pressure difference that the sheet induces in the chamber?

As a first step to answering these questions, we derive an analytical model that encompasses the elasticity of thin sheets and the hydrodynamics of inviscid fluids. Our model reveals that the system depends on four dimensionless parameters: the normalized excess length of the sheet compared with the lateral dimension of the chamber, Δ, where the total length of the sheet is used to normalize all lengths; the normalized vertical dimension of the chamber, L_y; the normalized initial volume difference in the chamber, $v_{du}(0)$; and the structure-to-fluid mass ratio, λ. We show that for fixed dimensions of the chamber, L_y and Δ, the system exhibits two asymptotic solutions as a function of λ. The sheet's inertia dominates the dynamics when $\lambda \gg 1$, and is therefore referred to below as the 'solid-dominated' region, while the dynamics is governed by the fluid's inertia when $\lambda \ll 1$, and is therefore referred to as the 'fluid-dominated' region.

We investigate the system's behaviour both in the early stages of its evolution and at moderate times during which nonlinear effects control the dynamics. For the early stages, we employ linear stability analysis around the (unstable) second buckling mode and the (stable) first buckling mode. We obtain the highest growth rate, σ, and the lowest frequency of vibration, ω, around these initial states. The two solutions exhibit similar behaviour as a function of λ, namely they converge to a constant in the solid-dominated region, while they exhibit the scaling $\lambda^{1/2}$ in the fluid-dominated region. Furthermore, we show that in the solid-dominated region only one mode of the sheet is essentially excited at the instability, while an infinite number of modes are excited in the fluid-dominated region. Analytical approximations are derived for each of these cases under the assumption that the amplitude of the sheet remains small, i.e. $\Delta \ll 1$ (Landau & Lifshitz 1986).

At moderate times, a weakly nonlinear analysis is performed around the second buckling mode. Given a small initial volume difference between the upper and lower parts of the chamber, we analyse the dynamic evolution of the system up to the peak time t_p, at which the sheet releases most of its initial potential energy. We show that, after some initial delay, the sheet rapidly escapes from the unstable state. We derive the approximation $\sigma t_p \simeq$

$\ln[c\Delta^{1/2}/v_{du}(0)]$, where σ is the growth rate of the linear instability and c is a constant, and show that it agrees well with the numerical results. At t_p, most of the initial potential energy is converted into kinetic energy of the sheet if $\lambda \gg 1$ and into hydrodynamic energy if $\lambda \ll 1$. We show that at $t = t_p$ a relatively large spike of pressure drop is applied on the sheet.

The paper is organized as follows. In § 2, we first formulate the problem for finite excess lengths. Then, we reduce this formulation to the small-amplitude approximation and introduce the modal expansion of the solution. In § 3, we investigate the early stages of the evolution. After recalling the static solution, we employ a linear stability analysis around the second and the first modes of buckling. In § 4, we investigate the system's evolution at moderate times. In particular, we examine the energetic interplay between the sheet and the fluid, derive the scaling for the peak time, t_p, and explore the relation between the volume difference and the pressure drop on the sheet. Finally, in § 5, we discuss a possible experimental realization of the system and, in § 6, we draw conclusions, and propose a direction for future study.

2. Formulation of the problem

We consider an inextensible thin sheet of total length $\tilde{L}$, bending modulus $\tilde{B}$, thickness $\tilde{h}$ and density $\tilde{\rho}_{sh}$. The sheet divides a rectangular closed chamber into two parts, which are connected by a valve (figure 1). The lateral, the vertical and the width dimensions of the chamber are denoted by $\tilde{L}_x$, $\tilde{L}_y$ and $\tilde{W}$, respectively. A Cartesian coordinate system is located on the left edge of the sheet. A cross-section of the chamber on the $\tilde{x}\tilde{y}$ plane is placed at $0 \le \tilde{x} \le \tilde{L}_x$ and $-\tilde{L}_y/2 \le \tilde{y} \le \tilde{L}_y/2$. When $\tilde{t} < 0$, the valve connecting the two parts of the chamber is closed, and the volumes above and below the sheet, $\tilde{v}_u(\tilde{t})$ and $\tilde{v}_d(\tilde{t})$, are filled with an incompressible, inviscid fluid of density $\tilde{\rho}_\ell$. Hereafter, we denote quantities related to the upper and lower parts of the chamber by the subscripts 'u' and 'd', respectively. At $\tilde{t} \ge 0$, the valve is opened, and free exchange of fluid is allowed in the chamber.

In the analysis that follows, we normalize all lengths by the total length of the sheet, $\tilde{L}$, and we normalize time by the inertial time scale of the sheet $\tilde{t}_\star = \tilde{L}^2(\tilde{\rho}_{sh}\tilde{h}/\tilde{B})^{1/2}$, i.e.

$$t = \tilde{t}/\tilde{t}_\star, \quad x = \tilde{x}/\tilde{L}, \quad L_x = \tilde{L}_x/\tilde{L}, \quad v_d(t) = \tilde{v}_d(\tilde{t})/\tilde{L}^3, \quad \text{etc.} \qquad (2.1a\text{–}d)$$

We choose this normalization because we anticipate that the wavelengths on the sheet will scale with the sheet's total length. In addition, since the dynamics in the system is driven by the sheet's motion, we chose the sheet's inertial time scale for the normalization. Note that our normalization with respect to lengths and time implies the normalization of the hydrodynamic fields and of the elastic fields, as will be emphasized further during the formulation. Hereafter, we denote all dimensional quantities with tildes over the symbols, and the corresponding non-dimensional quantities without a tilde.

Our model is based on the following six assumptions. Firstly, we assume that the system remains uniform along the width dimension of the chamber. Therefore, we set $W = 1$ and consider a two-dimensional system. Secondly, we assume that the volume occupied by the elastic sheet is negligible compared with the total volume of the chamber, i.e. $\tilde{h}\tilde{L}/(\tilde{L}_x\tilde{L}_y) \ll 1$, and as a result $v_u(t) + v_d(t) = L_xL_y$. Thirdly, we assume that the fluid exchange between the two parts of the chamber occurs through the upper and lower walls, i.e. the walls located at $y = \pm L_y/2$. Fourthly, we assume that the vertical dimension of the chamber, L_y, is larger than the typical length scale, ℓ, over which the disturbances in the flow caused by

the sheet's motion decay to zero. In addition, we assume that there is no contact between the sheet and the sidewalls of the chamber, or of the sheet with itself, at any time during the system's evolution. Lastly, we assume that at $t = 0$ the system is at rest and that the sheet accommodates a configuration that is dictated by the volume difference $v_{du}(0) = v_d(0) - v_u(0)$.

For an inviscid and irrotational fluid, the state of the flow is determined by four fields. Two of these are the fluid's potential functions $\phi_i(x, y, t)$, where $i = u, d$, from which we can determine the velocity profile of the fluid as $\boldsymbol{v}_i = \boldsymbol{\nabla}\phi_i$, where $\boldsymbol{\nabla}$ is the two-dimensional gradient operator. The other two fields that characterize the flow are the pressures $p_i(x, y, t)$ in each side of the chamber. Using our normalization convention, we find that the potential functions are normalized by $\phi_i = \tilde{\phi}_i(\tilde{\rho}_{sh}\tilde{h}/\tilde{B})^{1/2}$ and the pressures by $p_i = \tilde{p}_i\tilde{L}^3/\tilde{B}$. The evolution of these hydrodynamic fields, in space and over time, is determined by the continuity equation and Bernoulli's equation:

$$\nabla^2\phi_i = 0, \tag{2.2a}$$

$$\lambda p_i + \frac{\partial\phi_i}{\partial t} + \frac{1}{2}|\boldsymbol{\nabla}\phi_i|^2 = c_i(t), \tag{2.2b}$$

where $c_i(t)$ are arbitrary functions that depend on time. Throughout the system's development, these functions are employed to maintain a constant pressure at a point within each part of the chamber (Lamb 1945). In addition, in (2.2*b*) and (2.5), we define the dimensionless parameters:

$$\lambda = \frac{\tilde{\rho}_{sh}\tilde{h}}{\tilde{\rho}_\ell\tilde{L}}, \quad \Delta = 1 - L_x. \tag{2.3a,b}$$

The structure-to-fluid mass ratio, λ, accounts for the ratio between the densities of the sheet and the fluid and the slenderness of the sheet. This dimensionless parameter plays a role, for example, in the problem of a flag flapping under a uniform axial flow (Argentina & Mahadevan 2005; Connel & Yue 2007; Alben 2008; Alben & Shelley 2008). The parameter Δ accounts for the difference between the total length of the sheet and the lateral dimension of the chamber. In dimensional form, it may be expressed as $\tilde{\Delta} = \tilde{L} - \tilde{L}_x$. For a given system, the parameters λ and Δ remain constant throughout the dynamic evolution.

To solve the continuity equation (2.2*a*), we must first specify the boundary conditions on the chamber's walls and the fluid–sheet interfaces. Since the fluid that exits the upper wall of the chamber enters through the lower wall, we set periodic boundary conditions through $y = \pm L_y/2$. Thereafter, we ensure that there is no penetration of fluid through the sidewalls of the chamber. These restrictions give the boundary conditions:

$$\phi_u\left(x, \frac{L_y}{2}, t\right) = \phi_d\left(x, -\frac{L_y}{2}, t\right) \quad \text{and} \quad \frac{\partial\phi_u}{\partial y}\left(x, \frac{L_y}{2}, t\right) = \frac{\partial\phi_d}{\partial y}\left(x, -\frac{L_y}{2}, t\right), \tag{2.4a}$$

$$\frac{\partial\phi_i}{\partial x}(0, y, t) = \frac{\partial\phi_i}{\partial x}(1 - \Delta, y, t) = 0. \tag{2.4b}$$

In addition to the periodic boundary conditions at $y = \pm L_y/2$, it is necessary to ensure that $p_u(x, L_y/2, t) = p_d(x, -L_y/2, t)$ along these walls. By utilizing Bernoulli's equation (2.2*a*), and the periodic boundary conditions, it becomes apparent that this requirement is satisfied when $c_d(t) = c_u(t) \equiv c(t)$. Consequently, we can determine the function $c(t)$ by fixing the pressure at a specific point in the lower part of the chamber. In the following

analysis we choose

$$p_d\left(\frac{1-\Delta}{2}, -\frac{L_y}{2}, t\right) = 0. \tag{2.5}$$

Two sets of equations model the contact between the sheet and the fluid. The first set corresponds to the kinematic boundary conditions that ensure continuous contact between the sheet and the fluid. The second set corresponds to the force balance equations on the sheet that ensure proper transfer of the momentum between the solid and the fluid. To obtain these two sets of equations, we first define the elastic fields that describe the position of the sheet on the xy plane. It is important to note that, as we assumed the sheet to be inextensible, the elastic model accounts only for bending deformations and does not include stretching deformations. In contrast to the Eulerian description of the fluid, it is convenient to adopt a Lagrangian description for the sheet and to define the elastic fields as functions of the normalized arclength parameter on the sheet, $s \in [0, 1]$. With this change of reference frame, we define the position vector to a point on the sheet as $\boldsymbol{x}_{sh}(s, t) = (x_{sh}(s, t), y_{sh}(s, t))$ and the angle between the tangent to the sheet and the x axis as $\theta(s, t)$ (see figure 1). These three elastic fields, i.e. $x_{sh}(s, t)$, $y_{sh}(s, t)$ and $\theta(s, t)$, are not independent, since they are related by the geometric constraints

$$\frac{\partial x_{sh}}{\partial s} = \cos\theta, \tag{2.6a}$$

$$\frac{\partial y_{sh}}{\partial s} = \sin\theta. \tag{2.6b}$$

By using these definitions, the kinematic boundary conditions on the sheet–fluid interfaces are given by

$$y = y_{sh}(x(s), t), \quad \frac{\mathrm{D}y_{sh}}{\mathrm{D}t} = \frac{\partial \phi_i}{\partial y}, \tag{2.7a,b}$$

where $\mathrm{D}/\mathrm{D}t = \partial/\partial t + \boldsymbol{v}_i \cdot \boldsymbol{\nabla}$ is the two-dimensional convective derivative. The balance of moments and forces on the sheet is given by

$$\frac{\partial^2 \theta}{\partial s^2} = -F_x \sin\theta + F_y \cos\theta, \tag{2.8a}$$

$$\frac{\partial^2 \boldsymbol{x}_{sh}}{\partial t^2} = -\frac{\partial \boldsymbol{F}}{\partial s} + \left[p_d(x_{sh}, y_{sh}, t) - p_u(x_{sh}, y_{sh}, t)\right]\hat{\boldsymbol{n}}_d, \tag{2.8b}$$

where $\boldsymbol{F} = (F_x(s, t), F_y(s, t))$ is the vector of reaction forces per unit length at a cross-section of the sheet and our normalization implies that $\boldsymbol{F} = \tilde{\boldsymbol{F}}\tilde{L}^2/\tilde{B}$. In addition, $\hat{\boldsymbol{n}}_d = (-\sin\theta, \cos\theta)$ is a unit normal vector on the sheet that points outwards from the lower part of the chamber, and the hydrodynamic pressures in (2.8b) are calculated on their respective sides of the sheet–fluid interfaces. Note that in (2.8a) we neglect the rotational inertia term. This is justified in the limit of a thin and inextensible sheet, as assumed in this analysis (Neukirch *et al.* 2012; Goriely 2017; Kodio, Goriely & Vella 2020). Equations (2.8) are supplemented by the following boundary conditions on the sheet's edges:

$$x_{sh}(0, t) = 0, \quad x_{sh}(1, t) = 1 - \Delta, \tag{2.9a}$$

$$y_{sh}(0, t) = 0, \quad y_{sh}(1, t) = 0, \tag{2.9b}$$

$$\frac{\partial \theta}{\partial s}(0, t) = 0, \quad \frac{\partial \theta}{\partial s}(1, t) = 0, \tag{2.9c}$$

where we assume hinged boundary conditions in (2.9c).

This completes the formulation of the problem. In summary, given the excess length Δ, the vertical dimension of the chamber L_y, the parameter λ and the initial volume difference in the chamber $v_{du}(0)$, the dynamic evolution of the system is determined from the solution of the coupled equations (2.2)–(2.9). In the analysis that follows, we always assume that the sheet and the fluid are initially at rest, i.e. $(\partial \boldsymbol{x}_{sh}/\partial t)(s, 0) = 0$ and $\phi_i(x, y, 0) = 0$.

While solutions to our set of nonlinear equations can, in practice, be sought only numerically, some analytical progress that sheds light on the underlying physics of the system can be achieved under the assumption that the excess length remains small, i.e. $\Delta \ll 1$. For this reason, in the next section, we reduce our model to this so-called small-amplitude approximation (Landau & Lifshitz 1986) and exploit this formulation to study the time-dependent behaviour of the system.

However, before we proceed to the next section, we should add a comment regarding the system's energy. Since we assumed an ideal fluid, i.e. one without viscous dissipation, and since we consider an elastic model, our equations have a conserved first integral that corresponds to the system's total energy. In accordance with Appendix A, it can be shown that the total energy of the system is given by the sum of the energies of the sheet and the fluid, $E = E_{sh}(t) + E_f(t)$, where $E_{sh}(t)$ accounts for the sum of the kinetic and the potential energies of the sheet, which are designated $E^p_{sh}(t)$ and $E^k_{sh}(t)$, respectively, and $E_f(t)$ accounts for the kinetic energy of the fluid. Therefore, the total energy is given by

$$E = \frac{1}{2}\int_0^1 \left[\left|\frac{\partial \boldsymbol{x}_{sh}}{\partial t}\right|^2 + \left(\frac{\partial \theta}{\partial s}\right)^2\right] \mathrm{d}s + \sum_{i=u,d} \frac{1}{2\lambda} \iint_{v_i(t)} |\nabla \phi_i|^2 \,\mathrm{d}x\,\mathrm{d}y, \tag{2.10}$$

where $|\cdot|$ corresponds to the norm of the enclosed vector and our normalization implies that $E = \tilde{E}\tilde{L}/\tilde{B}$. Since our system starts from rest, the total energy of the system equals the initial potential energy of the sheet, $E = E^p_{sh}(0)$, and this energy is conserved throughout the system's evolution.

2.1. *The small-amplitude approximation*

The assumption that the amplitude of the sheet remains small, or equivalently that $\Delta \ll 1$, implies that the geometric relations (2.6) reduce to $\partial y_{sh}/\partial s \simeq \theta$ and $\partial x_{sh}/\partial s \simeq 1 - \frac{1}{2}(\partial y_{sh}/\partial s)^2$. The nonlinearity in the derivative of $x_{sh}(s, t)$ is retained in the leading order of the theory so as to satisfy the constraint on the excess length (2.9*a*). Indeed, in the small-amplitude approximation, this constraint is given by

$$\Delta = \frac{1}{2}\int_0^1 \left(\frac{\partial y_{sh}}{\partial x}\right)^2 \mathrm{d}x. \tag{2.11}$$

Here, we replace the arclength coordinate of the sheet with the Eulerian coordinate of the fluid, $s \simeq x$, according to our level of approximation. Correspondingly, the balance of forces and moments on the sheet (2.8) reduces to

$$\frac{\partial^2 y_{sh}}{\partial t^2} + \frac{\partial^4 y_{sh}}{\partial x^4} + F_x(t)\frac{\partial^2 y_{sh}}{\partial x^2} + \big[p_u(x, 0, t) - p_d(x, 0, t)\big] = 0, \tag{2.12}$$

where the lateral compression, $F_x(t)$, is a function that depends solely of time. In addition, the pressure difference that the fluid exerts on the sheet, i.e. the last term in (2.12), is calculated at the sheet–fluid interface, $y = 0$.

Thus far, we have approximated only the elastic part of the model. To further simplify the hydrodynamic part, we need to estimate the order of its corresponding fields. Given that the initial energy of the sheet scales linearly with the excess length, $E_{sh}(0) \propto \Delta$, and that the total energy of the system is conserved, the energy of the fluid is, at most, proportional to $E_f \sim \Delta$. Therefore, if we approximate the energy of the fluid by $E_f \sim |\boldsymbol{v}|^2 \ell$, where $|\boldsymbol{v}|$ is the typical velocity in the chamber and ℓ is the decay length of the disturbances in the flow, we obtain $|\boldsymbol{v}| \sim \sqrt{\Delta/\ell}$. Furthermore, if we assume that the order of approximation of a derivative over the potential function, with respect to either a spatial dimension or time, does not change, then we can approximate Bernoulli's equation (2.2*b*), and the kinematic boundary conditions by

$$\lambda p_i + \frac{\partial \phi_i}{\partial t} = c(t), \tag{2.13a}$$

$$\frac{\partial y_{sh}}{\partial t} = \left(\frac{\partial \phi_i}{\partial y}\right)_{y=0}. \tag{2.13b}$$

These approximations will further be verified *a posteriori* in § 4, where we analyse the nonlinear dynamics of the system. In particular, we compare the results of this approximation with the numerical solution of the nonlinear model (2.2)–(2.9). Note that since the continuity equations (2.2*a*) are already linear in the potential functions, they remain unchanged in our approximated model.

This completes the reduction of our model to the small-amplitude limit. In summary, (2.2*a*) and (2.11)–(2.13), supplemented by the linearized form of the boundary conditions (2.5), (2.4), (2.9*b*) and (2.9*c*), form a closure and describe the coupled dynamics of the sheet and the fluid in the small-amplitude approximation. A comment is necessary regarding this simplified formulation. In accordance with the derivation in Appendix B, it can be shown that the reduced model emanates from the minimization of the action $\mathcal{S} = \int_0^{\mathrm{T}} \mathcal{L}\,\mathrm{d}t$, where

$$\begin{aligned}\mathcal{L} = \int_0^1 \Bigg[&\frac{1}{2}\left(\frac{\partial y_{sh}}{\partial t}\right)^2 - \frac{1}{2}\left(\frac{\partial^2 y_{sh}}{\partial x^2}\right)^2 + F_x(t)\left(\frac{1}{2}\left(\frac{\partial y_{sh}}{\partial x}\right)^2 - \Delta\right) \\ &+ \frac{1}{\lambda}\left[\phi_d(x,0,t) - \phi_u(x,0,t)\right]\frac{\partial y_{sh}}{\partial t}\Bigg]\mathrm{d}x \\ &- \frac{1}{2\lambda}\int_0^{L_y/2}\int_0^1 |\nabla\phi_u|^2\,\mathrm{d}x\,\mathrm{d}y - \frac{1}{2\lambda}\int_{-L_y/2}^0\int_0^1 |\nabla\phi_d|^2\,\mathrm{d}x\,\mathrm{d}y,\end{aligned} \tag{2.14}$$

with respect to the elastic fields $y_{sh}(x, t)$ and $F_x(t)$ and the hydrodynamic fields $\phi_i(x, y, t)$. In the next section, we employ a modal expansion of these fields and combine it with the Lagrangian formulation to derive a simplified set of equations that are dependent solely on time.

2.1.1. *Modal expansion*

The continuity equations (2.2*a*), and their corresponding boundary conditions on the fluid–chamber interfaces (2.4), are satisfied when the potential functions are

given by

$$\phi_i(x, y, t) = a_0(t)\left(y \pm \frac{L_y}{2}\right) + \sum_{m=1}^{\infty} \cos(\pi m x)\left[a_m(t)\exp\left(\pi m\left(y \pm \frac{L_y}{2}\right)\right)\right.$$
$$\left. + c_m(t)\exp\left(-\pi m\left(y \pm \frac{L_y}{2}\right)\right)\right], \tag{2.15}$$

where $a_m(t)$ $(m = 0, 1, 2, \ldots)$ and $c_m(t)$ $(m = 1, 2, 3, \ldots)$ are unknown time-dependent coefficients and the $\pm$ signs correspond to the solutions of the potential functions in the lower and the upper parts of the chamber, respectively. Similarly, we expand the solution of the sheet's height function in the following normal modes:

$$y_{sh}(x, t) = \sum_{n=1}^{\infty} A_n(t)\sin(\pi n x), \tag{2.16}$$

where the functions $\sin(\pi n x)$ automatically satisfy the boundary conditions on the sheet edges (2.9*b*) and (2.9*c*), and $A_n(t)$ are as-yet unknown coefficients.

With these expansions, the solution to our problem reduces to finding the unknown coefficients, $a_m(t)$, $c_m(t)$ and $A_n(t)$, and the compression force $F_x(t)$, from the solution of the force balance equation (2.12), Bernoulli's equation (2.13*a*), the kinematic boundary conditions (2.13*b*) and the geometric constraint (2.11). Equation (2.16) involves infinite summation over the modes of the height function, but, in practice, we will truncate this series at $n = N$. A closed system of equations is then obtained when the coefficients of $a_m(t)$ and $c_m(t)$ are truncated at $N - 1$.

However, instead of directly using these equations, we take a different – yet equivalent – approach, by utilizing the Lagrangian formulation (2.14). To this end, we follow the analysis in Appendix C and substitute the potential functions (2.15), and the height function (2.16), into the Lagrangian (2.14). We then integrate over the spatial coordinates. Thereafter, we minimize the Lagrangian with respect to $a_m(t)$ and $c_m(t)$ and express these coefficients in terms of $A_n(t)$. Substituting $a_m(t)$ and $c_m(t)$ back into the Lagrangian gives

$$\mathcal{L}[A_1, \ldots, A_N, F_x] = T_{nk}\frac{\mathrm{d}A_k}{\mathrm{d}t}\frac{\mathrm{d}A_n}{\mathrm{d}t} - V_{nk}A_kA_n + F_x(t)C_{nk}A_kA_n - \Delta F_x(t), \tag{2.17}$$

where Einstein's summation rule is implied for repeated indices, and we define the following symmetric matrices:

$$T_{nk} = \frac{1}{4}\delta_{nk} + \frac{L_y}{2\lambda}W(n, 0)W(k, 0) + \sum_{m=1}^{N-1}\frac{2}{\pi m\lambda}\tanh\left(\frac{\pi m L_y}{2}\right)W(k, m)W(n, m), \tag{2.18a}$$

$$V_{nk} = \frac{\pi^4}{4}n^2k^2\delta_{nk}, \quad C_{kn} = \frac{\pi^2}{4}nk\delta_{nk}, \tag{2.18b}$$

where δ_{nk} is the Kronecker delta, and $W(n, m) = (n/\pi)((1 - (-1)^{n+m})/(n^2 - m^2))$ for $n \neq m$ and zero otherwise.

Two comments are in order regarding this Lagrangian. First, since the matrix T_{nk} is coupled to the kinetic terms in the Lagrangian, it takes on the role of a mass matrix in this formulation. This mass matrix has contributions from both the inertia of the sheet, i.e. the first term in T_{nk}, and the hydrodynamics of the fluid, i.e. the terms proportional to $1/\lambda$.

The latter hydrodynamic terms are frequently referred to as added mass or virtual mass, since they describe an additional mass that the sheet appears to acquire when it accelerates in the fluid (Munk 1924; Lighthill 1960; Coene 1992).

The second comment is related to the potential functions $\phi_i(x, y, t)$ that result from the minimization. Using (C2*b*), we substitute $c_m(t) = -a_m(t)$ in the potential functions (2.15) to obtain

$$\phi_i(x, y, t) = a_0(t)\left(y \pm \frac{L_y}{2}\right) + 2\sum_{m=1}^{N-1} a_m(t)\cos(\pi m x)\sinh\left[\pi m\left(y \pm \frac{L_y}{2}\right)\right]. \tag{2.19}$$

This solution implies that at $y = \pm L_y/2$ the velocity of the fluid is oriented only in the y direction, i.e. $\partial\phi_i/\partial x(x, \pm L_y/2, t) = 0$. It also implies that $\phi_i(x, \pm L_y/2, t) = 0$, which, given (2.5) and (2.13*a*), yields a constant zero pressure along the inlet and the outlet walls of the chamber, $p_i(x, \pm L_y/2, t) = 0$. We anticipate that these conditions will occur only when the disturbances that the sheet induces in the flow decay to zero. Therefore, the small-amplitude model holds strictly when $L_y \gg \ell$, where $\ell \simeq 1/(\pi m)$, for the smallest non-zero mode, is now explicitly identified as the decay length of the hydrodynamic disturbances.

Keeping in mind these limitations of the small-amplitude model, we go back to derive the equations for the coefficients $A_n(t)$. Given an initial volume difference, which, in turn, corresponds to an initial configuration of the sheet, i.e. a set of initial conditions for the coefficients $A_n(0)$, and keeping in mind that the system starts from rest, i.e. $(\mathrm{d}A_n/\mathrm{d}t)(0) = 0$, we can determine the dynamic evolution of the system from the minimization of (2.17) with respect to $A_n(t)$ and $F_x(t)$. This minimization yields $N + 1$ algebraic differential equations that, in our matrix notation, read

$$T_{nk}\frac{\mathrm{d}^2 A_k}{\mathrm{d}t^2} + (V_{nk} - F_x(t)C_{nk})A_k = 0, \tag{2.20a}$$

$$C_{nk}A_k A_n = \Delta. \tag{2.20b}$$

Once $A_n(t)$ are determined from the solution of (2.20), the position of the sheet in time and in space is given by (2.16), and the hydrodynamic potentials and the pressure fields are determined from (2.15), (C2) and (2.13*a*). In the next section, we utilize this formulation to investigate the early time evolution. Then, in § 4 we use it to analyse the dynamics at later times.

3. The early time evolution

In this section, we investigate the system's stability close to an initial equilibrium state. The section is divided into two parts. In the first, we recall the static solutions of the system in the small-amplitude approximation. In the second, we employ a linear stability analysis around the first two buckling modes to extract the growth rates and the flow fields of the perturbation around these modes.

3.1. *Recap of the quasi-static solution*

Following the analysis in the study of Oshri (2021), the quasi-static evolution of the system is governed by two different branches of solutions, which we call 'asymmetric' and 'symmetric'. Here, we recall the height functions in these branches.

On the one hand, when the initial volume difference is set as $0 \le v_{du}(0) \le v_{du}^{cr}$, where $v_{du}^{cr} = (2(3+\pi^2)/\pi\sqrt{3(15+2\pi^2)})\Delta^{1/2}$, the system is governed by the asymmetric branch. In this branch, the lateral compression is constant, $F_x(0) = 4\pi^2$, and the height functions are given by

$$y_{sh}(x,0) = \frac{p_{ud}(x,y,0)}{16\pi^4}\left[2\pi^2(1-x)x + 1 - \cos(2\pi x)\right] + \frac{1}{\pi}\sqrt{\Delta - \frac{15+2\pi^2}{768\pi^6}p_{ud}(x,y,0)^2}\sin(2\pi x), \tag{3.1a}$$

$$p_{du}(x,y,0) = \frac{24\pi^4}{3+\pi^2}v_{du}(0), \tag{3.1b}$$

where $p_{ud}(x,y,0) = p_u(x,y,0) - p_d(x,y,0)$ is the pressure difference between the upper and lower parts of the chamber. The potential energy of the sheet in this branch is given by

$$E_{as} = 4\pi^2\Delta - \frac{6\pi^4}{3+\pi^2}v_{du}(0)^2. \tag{3.2}$$

Note that when $v_{du}(0) \to 0$ we know from (3.1*b*) that the pressure difference vanishes, $p_{ud}(x,y,0) \to 0$, and the elastic configuration converges to the second, asymmetric, mode of buckling, $y_{sh}(x,0) \to \sqrt{\Delta/\pi^2}\sin(2\pi x)$. The total energy of the system in this configuration is given by $E_{as} = 4\pi^2\Delta$. Note also that we considered solutions with an initial volume difference that is greater than zero. This is because the static solution has mirror symmetry around the x axis. Solutions with $v_{du}(0) < 0$ (and $p_{ud}(x,y,t) < 0$) are obtained by a reflection of the height functions (3.1) around the horizontal axis.

On the other hand, when the volume difference is set as $v_{du}^{cr} \le v_{du}(0) < \sqrt{2\Delta/3}$, the system is governed by the symmetric branch. In this case, the inextensibility of the sheet implies an upper limit on the volume difference. In the case of a hinged sheet, this limit is given by $\sqrt{2\Delta/3}$. The height functions in this branch are given by the parametric solution:

$$y_{sh}(x,0) = \frac{p_{ud}(x,y,0)}{8u^2}(1-x)x + \frac{p_{ud}(x,y,0)}{16u^4}\left[1 - \frac{\cos\left[2u(x-1/2)\right]}{\cos u}\right], \tag{3.3a}$$

$$p_{ud}(x,y,0) = -\frac{16\sqrt{6}u^{7/2}\cos u}{\sqrt{6u + 4u(6+u^2)\cos^2 u - 15\sin(2u)}}\Delta^{1/2}, \tag{3.3b}$$

$$v_{du}(0) = -\frac{2\sqrt{2}\left[u(3+u^2) - 3\tan u\right]\cos u}{\sqrt{3}u^{3/2}\sqrt{6u + 4u(6+u^2)\cos^2 u - 15\sin(2u)}}\Delta^{1/2}, \tag{3.3c}$$

where $u = \sqrt{F_x(0)}/2$ is a function of the lateral compression. Given the initial volume difference, $v_{du}(0)$, and the excess length, Δ, we can determine the lateral compression, $F_x(0)$, from (3.3*c*), and then substitute this solution into (3.3*a*) and (3.3*b*) to obtain the height profile. When $p_{ud}(x,y,0) \to 0$, the height function converges to the first, symmetric, mode of buckling, which is given by $y_{sh}(x,0) \to \sqrt{4\Delta/\pi^2}\sin(\pi x)$ and $v_{du}(0) = 8\Delta^{1/2}/\pi^2$. The total elastic energy of this shape is given by $E_s = \pi^2\Delta$. An example of the evolution of the sheet and the $p_{ud}(x,y,0)$–$v_{du}(0)$ relation in this static solution, where $0 \le v_{du}(0) < \sqrt{2\Delta/3}$, is plotted in figure 2. In the following sections,

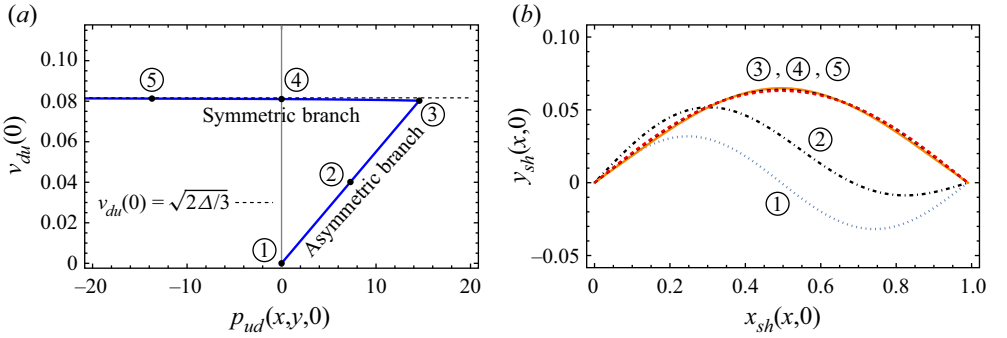

Figure 2. Evolution of the static solution in the small-amplitude approximation, where $\Delta = 0.01$. (*a*) The volume difference, $v_{du}(0)$, as a function of the pressure difference, $p_{ud}(x, y, 0)$. In the asymmetric branch the $p_{ud}(x, y, 0)$–$v_{du}(0)$ relation is given by (3.1*b*), while in the symmetric branch it is given by (3.3*b*) and (3.3*c*). The volume difference at the asymmetric-to-symmetric transition, $v_{du}(0) = v_{du}^{cr}$, is labelled by ③. The pressure difference in the chamber vanishes when the sheet accommodates either the second or the first mode of buckling, labels ① and ④. As the volume difference approaches its limiting value $v_{du}(0) \to (2\Delta/3)^{1/2}$, the pressure difference diverges. (*b*) Evolution of the sheet's profile as the volume difference increases; see the corresponding labelled numbers in (*a*). Note, that despite the relatively large change in the pressure difference in the symmetric branch, the elastic configurations remain almost unchanged.

we use these height functions (3.1*a*) and (3.3*a*) as the base solutions for our perturbative time-dependent expansion.

Before we proceed, we emphasize that while the sheet's configuration evolves continuously from the moment that we open the valve, the static pressure difference, given in (3.1*b*) and (3.3*b*), changes instantaneously at $t = 0$. This is because we assumed an incompressible fluid, in which the speed of sound is infinite. Nonetheless, the asymmetric and the symmetric modes of buckling, obtained respectively from (3.1*a*) and (3.3*a*) in the limit $p_{ud}(x, y, 0) \to 0$, are exceptions. These configurations remain in static equilibrium, which can nevertheless be unstable, when the valve is opened. For this reason, in the next section, we investigate the linear stability of the system around these two limiting initial states.

3.2. *Linear stability*

To derive the linear stability around the two limiting scenarios, i.e. the second and first buckling modes, we assume that the sheet's height function is given by the static solution, up to a small perturbation that grows exponentially with time. Correspondingly, we first perturb the amplitudes of the normal modes and the lateral compression around the base solutions, i.e. $A_n(t) = A_n(0) + \epsilon \bar{A}_n \, \mathrm{e}^{\sigma t}$ and $F_x(t) = F_x(0) + \epsilon \bar{F}_x \, \mathrm{e}^{\sigma t}$, where $\bar{A}_n$ and $\bar{F}_x$ are unknown constants, σ is the growth rate and $\epsilon \ll 1$ is an arbitrarily small parameter. Then, we substitute these perturbed functions into the equations of motion (2.20), and expand them up to linear order in ϵ. The leading order of this expansion, order ϵ^0, is given by

$$V_{nk}A_k(0) - F_x(0)C_{nk}A_k(0) = 0, \tag{3.4a}$$

$$C_{nk}A_k(0)A_n(0) = \Delta, \tag{3.4b}$$

and the subleading order, order ϵ, is given by

$$\left[\sigma^2 T_{nk} + V_{nk} - F_x(0)C_{nk}\right]\bar{A}_k - C_{nk}A_k(0)\bar{F}_x = 0, \tag{3.5a}$$

$$C_{nk}A_k(0)\bar{A}_n = 0. \tag{3.5b}$$

The above equations in the subleading order always have the trivial solution $\bar{A}_n = 0$ and $\bar{F}_x = 0$, unless their corresponding determinant vanishes. This condition gives the growth rate, σ. Once σ is determined, its corresponding eigenfunction is obtained from the solution of (3.5). The hydrodynamic fields related to this eigenfunction are determined from (2.15) and (C2).

3.2.1. *Linear stability around the second mode of buckling*

When the initial configuration of the sheet is given by the second mode of buckling, the base solution is derived from (3.1*a*) in the limit $p_{ud}(x, y, 0) \to 0$. This solution reads $y_{sh}(x, 0) = \sqrt{\Delta/\pi^2}\sin(2\pi x)$ and $F_x(0) = 4\pi^2$. A projection of this configuration on the normal mode expansion (2.16) gives $A_n(0) = \sqrt{\Delta/\pi^2}\delta_{2n}$. As expected, this initial state exactly satisfies the equilibrium equations at order ϵ^0 (3.4). At the next order, i.e. order ϵ, we find that $\bar{F}_x = 0$ and $\bar{A}_n = 0$ for all the even perturbations, i.e. $n = 2, 4, 6, \ldots$. Consequently, (3.5) yields linear and homogeneous equations that involve only the odd perturbations. These equations always have the trivial solution $\bar{A}_n = 0$, except when the corresponding determinant vanishes. A tractable solution to this condition, which also gives a good approximation to the highest growth rate, is obtained at the lowest order when $N = 2$. This solution reads

$$\sigma = \frac{\sqrt{3}\pi^2}{\sqrt{1 + \dfrac{8L_y}{\pi^2\lambda}}}. \tag{3.6}$$

In figure 3, we plot this analytical approximation for the growth rate as a function of λ, and compare it with the numerical solution of (3.5) for the case where $N = 8$. In addition, we compare this analytical solution with the growth rate obtained from the linearization of (2.2)–(2.9), i.e. where Δ is assumed to be finite. See Appendix D for the details of this solution.

Equation (3.6) is one of the central results in this paper. Several comments are in order regarding this solution. Firstly, note that the highest growth rate is always real and positive, i.e. the second mode of buckling is always an unstable state of the system.

Secondly, while (3.6) depends on the parameter $\lambda/L_y = \tilde{\rho}_{sh}\tilde{h}/(\tilde{\rho}_\ell\tilde{L}_y)$, this result is not general but depends on the order of approximation. Had we solved (3.5) with $N \geq 3$, the two parameters λ and L_y would have appeared independently in the solution. Nonetheless, comparing the lowest order solution, i.e. the solution with $N = 2$, with that of, say, $N = 8$, we find that the growth rate remains almost unchanged (compare the solid and dashed lines in figure 3). For this reason, we conclude that (3.6) well describes the growth rate in the limit $\Delta \ll 1$.

Thirdly, while the solution of the small-amplitude approximation is independent of the excess length, Δ, the more general solution for finite values of Δ does depend on this parameter. See figure 3 for a comparison. In particular, for a fixed value of λ, the growth rate increases with an increase in Δ.

Fourthly, the analytical solution of the growth rate (3.6), exhibits two different regions as a function of λ. When $\lambda/L_y \gg 1$, the growth rate is a constant, $\sigma \simeq \sqrt{3}\pi^2$, that coincides with the growth rate of a sheet that is uncoupled from an external fluid. However, when $\lambda/L_y \ll 1$, the growth rate exhibits the scaling $\sigma \simeq \sqrt{3\pi^6/8}(\lambda/L_y)^{1/2}$. These asymptotic solutions define two limiting behaviours of the system. The former scenario represents

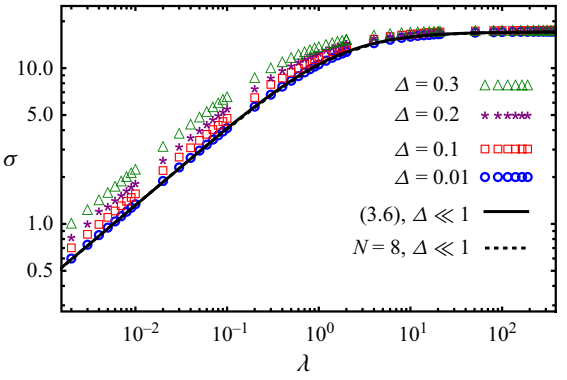

Figure 3. Log–log plot of the highest growth rate as a function of λ where $L_y = 2$. Symbols correspond to the linear stability analysis of (2.2)–(2.9), and solid and dashed lines correspond to the growth rates obtained from the small-amplitude approximation. When $\lambda \gg 1$, the growth rate converges to the constant $\sigma \simeq \sqrt{3}\pi^2$, whereas when $\lambda \ll 1$ the growth rate is given by $\sigma \simeq \sqrt{3\pi^6/8}(\lambda/L_y)^{1/2}$. Note that the differences between the solid ($N = 2$) and dashed ($N = 8$) lines are almost not visible in the figure. While the growth rate is independent of the excess length in the small-amplitude approximation, the more general solution (symbols) shows that the growth rate increases with Δ.

a 'solid-dominated' region, in which the pressure difference exerted by the fluid on the sheet is negligible compared with the inertia of the sheet. The latter scenario, where $\sigma \propto (\lambda/L_y)^{1/2}$, represents the opposite limit of a 'fluid-dominated' region, in which the inertia of the sheet is negligible compared with the pressure difference exerted by the fluid on the sheet. Similarly, these two regions are also reflected in the added mass term, $8L_y/(\pi^2\lambda)$, in the denominator of the growth rate. When λ is large, the added mass approaches zero and the sheet's inertia is not affected by the fluid's motion. In contrast, when λ is small, the effective mass of the sheet increases, resulting in slower dynamics. It is worth noting that since the dynamics of the system becomes very slow in the fluid-dominated region, we would expect some aspects of this solution to align with our earlier, quasi-static solution in the asymmetric branch, as shown in (3.1). This is because the quasi-static solution describes a slow spontaneous relaxation of the system, where the inertia of the sheet is negligible. This convergence to the quasi-static solution is further demonstrated in the following analysis.

Fifthly, note that if we fix L_y, the matrices in (3.5) and (2.18) become diagonal in the solid-dominated region. Therefore, up to small corrections of the order $1/\lambda$, $\bar{A}_1$ alone is excited at the instability. Indeed, in figure 4(*a*), in which we plot the eigenfunction for the case where $\lambda = 100$ for both $N = 2$ and $N = 8$, we find that the two solutions are almost identical. In contrast, in the fluid-dominated region, $\lambda \ll 1$ and the matrices in (3.5) have non-zero off-diagonal terms. Therefore, all the odd modes become coupled and are excited at the instability. Nonetheless, our numerical investigation indicates that $\bar{A}_n/\bar{A}_1 \ll 1$ for all $n \geq 3$. Therefore, while we would expect the leading-order solution, i.e. $N = 2$, to approximate the eigenfunction well, it will not coincide with the higher-order solution. Indeed, in figure 4(*b*), we compare the eigenfunctions obtained from the lowest order and the high orders of approximations and find finite differences between them. We note that the eigenfunction in the fluid-dominated region emerges from the quasi-static configuration (3.1*a*), when we expand (3.1*a*) in powers of $p_{ud}(x, y, 0)$, extract the linear order of this expansion and normalize it in accordance with our convention. The agreement

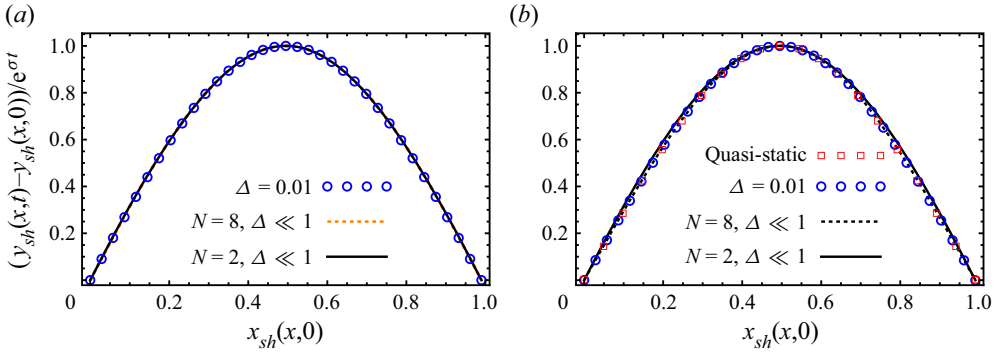

Figure 4. Eigenfunctions of the sheet's height function in both the solid- and fluid-dominated regions. In both panels, $L_y = 2$ and open blue circles correspond to the linear stability analysis at finite Δ, i.e. derived from (2.2)–(2.9). The eigenfunctions are normalized such that $[y_{sh}(1/2, t) - y_{sh}(1/2, 0)]/e^{\sigma t} = 1$ (numerically we choose $\hat{y}_{sh}(1/2) = 1$; see Appendix D). (*a*) In the solid-dominated region ($\lambda = 100$), only one mode is excited, i.e. the low ($N = 2$) and the high ($N = 8$) mode approximations coincide. (*b*) In the fluid-dominated region ($\lambda = 0.1$), all odd modes are excited. Therefore, the lowest approximation, $N = 2$, does not coincide with that obtained with higher modes, $N = 8$. Nonetheless, since $\bar{A}_n/\bar{A}_1 \ll 1$, the differences between the low and the high orders of the approximations are still small. Open squares represent the quasi-static approximation obtained from (3.1).

between this quasi-static profile and the eigenfunction obtained from the linear stability analysis is shown in figure 4(*b*) (open squares).

Sixthly, in figure 5(*a*), we plot the flow field obtained from the linear stability analysis at finite Δ. Note that the maximum velocity of the fluid is obtained at the sheet's centre, where the eigenfunction of the sheet's height is maximized (see figure 4). Unlike the growth rate, for which the small-amplitude approximation provided us with a good estimation already at $N = 2$, the flow field converges at a slower pace. Convergence to the spatially dependent solution, presented in figure 5(*b*), is obtained only when higher modes, say $N \geq 3$, are included. This is because each coefficient $a_m^i(t)$ in the fluid's potential functions (2.15) depends on all the excited modes; see (C2). In addition, in figure 5(*b*), we plot the eigenfunctions of the pressure fields. Note that the sheet moves upwards towards the higher-pressure field. This is because the sheet's motion drives the flow, and the pressure drop in the fluid acts to slow down the onset of the elastic instability. We note that there are no qualitative differences in the flow fields and the pressure distributions between the solid- and fluid-dominated regions. For this reason, the plots in figure 5 refer only to the fluid-dominated region.

Lastly, in addition to the growth rate, the flow field and the hydrodynamic pressures, another experimentally measurable quantity is the system's 'compressibility', i.e. the change in the volume difference relative to the change in the pressure difference. Since the pressure difference varies in space, we define the compressibility as $\beta \equiv \mathrm{d}v_{du}/\mathrm{d}\bar{p}_{ud}$, where $\bar{p}_{ud}(t)$ is the average pressure drop on the sheet. In the small-amplitude approximation the average pressure drop on the sheet is given by $\bar{p}_{ud}(t) = \int_0^1 [p_u(x, 0, t) - p_d(x, 0, t)]\,\mathrm{d}x$ and the volume difference in the chamber is given by $v_{du}(t) = 2\int_0^1 y_{sh}(x, t)\,\mathrm{d}x$ (Oshri 2021). Keeping in mind that the base solution is asymmetric, and therefore does not contribute to the above integral, we find that the leading order ($N = 2$) is $v_{du}(t)/\bar{A}_1 = (4/\pi)\,\mathrm{e}^{\sigma t}$. In addition, the average pressure difference at this order is given by $\bar{p}_{ud}(t)/\bar{A}_1 = 2L_y\sigma^2\,\mathrm{e}^{\sigma t}/(\pi\lambda)$. Consequently, at the onset of the instability, the compressibility is a

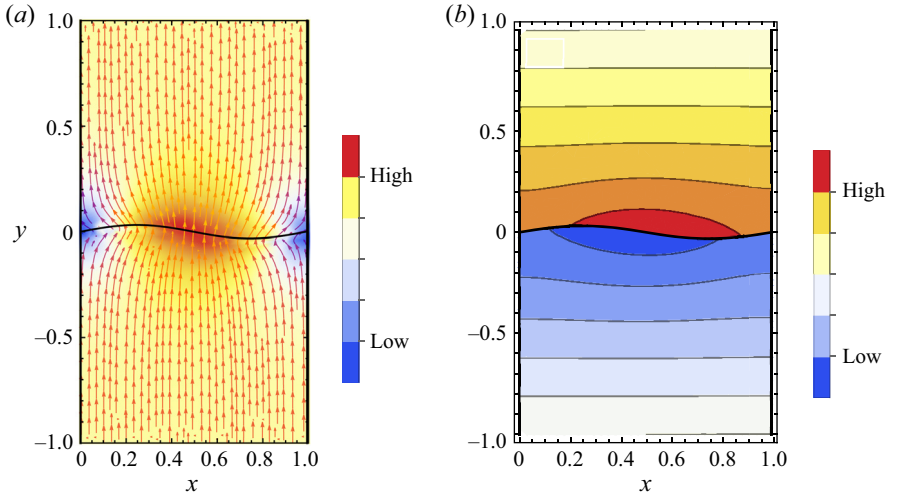

Figure 5. (*a*) The flow field and (*b*) the hydrodynamic pressures obtained from the linear stability analysis of (2.2)–(2.9) at the highest growth rate. In both panels, $\Delta = 0.01$, $\lambda = 0.1$ and $L_y = 2$. The eigenfunctions are normalized as indicated in figure 4. This gives [Low, High] = [0.98, 2.94] in the colour bar of the flow field and [Low, High] = [−78, 78] in the colour bar of the hydrodynamic pressures. The solid black line corresponds to the initial configuration of the sheet, i.e. the asymmetric second mode of buckling. In (*a*), arrows represent the streamlines and colours represent the relative magnitudes of the velocity.

constant, which is given by

$$\beta = \frac{2\lambda}{\sigma^2 L_y}. \tag{3.7}$$

In figure 6, we plot this result as a function of λ and compare the lowest-order approximation with the solution at finite values of Δ. On the one hand, since the growth rate is constant in the solid-dominated region, we find that the compressibility scales linearly with λ, i.e. $\beta \to 2\lambda/(3\pi^4 L_y)$. On the other hand, since in the fluid-dominated region the growth rate scales as $(\lambda/L_y)^{1/2}$, the compressibility converges to the constant $\beta \to 16/(3\pi^6) \simeq 5.54 \times 10^{-3}$. As expected, this result for the fluid-dominated region is very close to the compressibility obtained in the quasi-static solution (3.1*b*), which gives $\beta = (3 + \pi^2)/(24\pi^4) \simeq 5.50 \times 10^{-3}$.

3.2.2. *Linear stability around the first mode of buckling*

This section analyses the system's stability around the first mode of buckling. In contrast to the second mode, which is always unstable, the first mode represents the minimum of the elastic potential energy. Therefore, the first mode is expected to remain stable and to yield oscillatory motion under a small dynamical perturbation. Since a purely imaginary growth rate represents this oscillatory motion, we set $\sigma \equiv i\omega$, where $i = \sqrt{-1}$, and look for the lowest frequency of oscillation at the onset of the instability.

When the initial state of the sheet is given by the first mode of buckling, we have from (3.3) that the base solution is given by $y(x, 0) = (2\sqrt{\Delta}/\pi)\sin(\pi x)$ and $F_x(0) = \pi^2$. A projection of this configuration on the normal mode expansion (2.16) gives $A_n(0) = (2\sqrt{\Delta}/\pi)\delta_{1n}$. This initial state, as expected, satisfies the leading order of our perturbative expansion (3.4). Substituting this leading order in (3.5) and solving for the unknown constants, we find that $\bar{F}_x = 0$ and $\bar{A}_n = 0$ for all the odd modes ($n = 1, 3, 5, \ldots$).

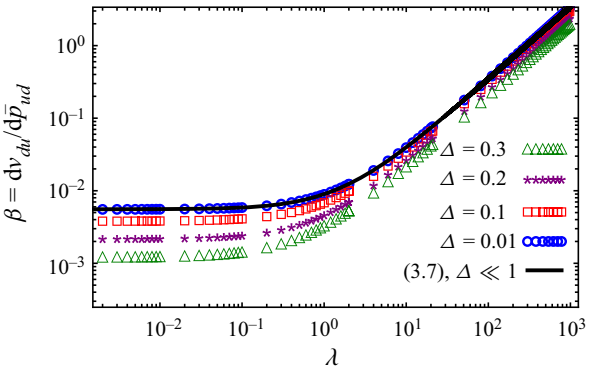

Figure 6. Log–log plot of the compressibility as a function of λ close to the onset of the instability. Symbols correspond to the compressibility at finite values of Δ and the solid black line corresponds to the analytical solution obtained from the small-slope approximation. While in the solid-dominated region $\beta \propto \lambda$, in the fluid-dominated region β converges to a constant.

Consequently, (3.5) yields linear and homogeneous equations that involve only the even modes of the height function. As in the previous case that we considered, a tractable solution to the vanishing determinant condition is obtained when we cut the normal mode expansion at the smallest value, $N = 2$. (We note that when $L_y \gg 1$, the solution obtained from the two-mode approximation ($N = 2$) is pre-empted by a different branch of solutions. The new branch emanates from a higher-order correction in the modal expansion, and its details are beyond the scope of the present study.) This gives

$$\omega = \frac{2\sqrt{3}\pi^2}{\sqrt{1 + \dfrac{128}{9\pi^3}\dfrac{\tanh(\pi L_y/2)}{\lambda}}}. \tag{3.8}$$

In figure 7(*a*), we plot this solution and compare it with the solution of (3.5) for the case of $N = 8$. Note that our solution, (3.8) with $N = 2$, approximates well the small-amplitude limit, $\Delta \ll 1$. Higher-order corrections, e.g. with $N = 8$, almost do not alter this solution; compare the solid and dashed lines in figure 7(*a*). In addition, we compare (3.8) with the eigenvalues obtained from the linearization of (2.2)–(2.9), where the small-amplitude approximation is relaxed. We observe that as Δ increases, the oscillation frequency decreases with increasing excess length. However, the overall trend of the dependence of ω on λ remains consistent with the small-amplitude solution. We also note that the relatively large decrease in ω when $\lambda \gg 1$ is a result of our chosen hinged boundary conditions. In contrast, systems with clamped boundary conditions display a much milder dependence on Δ, as reported in previous studies (Neukirch *et al.* 2012; Pandey *et al.* 2014).

The frequency ω exemplifies the two limiting scenarios that we encountered for the growth rate in (3.6). On the one hand, in the solid-dominated region, where $\lambda \gg 1$, the frequency converges to the constant $\omega \simeq 2\sqrt{3}\pi^2$ that coincides with the frequency of oscillation of a sheet that is uncoupled from a fluid flow. On the other hand, in the fluid-dominated region, where $\lambda \ll 1$, we find the scaling $\omega \simeq \sqrt{27\pi^7/32}[\lambda/\tanh(L_y\pi/2)]^{1/2}$, i.e. $\omega \propto \lambda^{1/2}$. Alternatively, since the added mass is given by $(128/9\pi^3)(\tanh(\pi L_y/2)/\lambda)$, when $\lambda \gg 1$ the sheet's inertia is almost unaffected by the fluid motion, but when $\lambda \ll 1$, the added mass increases and slows down the dynamics.

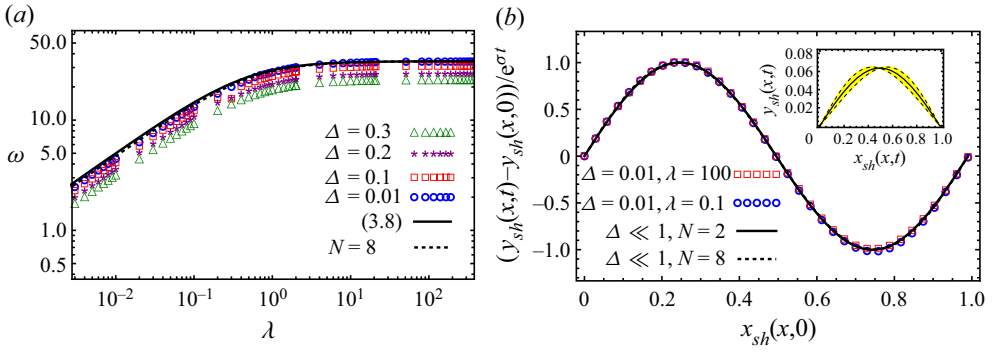

Figure 7. The lowest oscillation frequency and the sheet's eigenfunction obtained from the linear stability analysis around the first buckling mode. In both panels $L_y = 2$. (*a*) Log–log plot of the oscillation frequency as a function of the parameter λ. Solid and dashed lines correspond to the solution of (3.8) when $N = 2$ and $N = 8$, respectively. All symbols correspond to the linear stability analysis of (2.2)–(2.9) at finite Δ. (*b*) The sheet's eigenfunctions in the solid- and fluid-dominated regions. All eigenfunctions are normalized such that their height at $x = 1/4$ is equal to one (numerically we choose $\hat{y}_{sh}(1/4) = 1$; see Appendix D). Although only one mode is excited when $\lambda \gg 1$ and infinite modes are excited when $\lambda \ll 1$, the eigenfunctions of the two regions are almost identical. Inset: an example of the sheet's oscillations around the base solution. Dashed lines correspond to an illustration of the dynamic oscillations, and the solid line to the base solution.

These two scenarios are also manifested in the eigenfunction of the sheet's height function. In the solid-dominated region, (3.5) becomes diagonal, up to corrections of the order of $1/\lambda$, and essentially only the second mode, i.e. $\bar{A}_2$, is excited at the instability, while in the fluid-dominated region (3.5) has non-zero off-diagonal terms, and all the even modes are excited. Nonetheless, our numerical investigation of the solution of (3.5) in the fluid-dominated region indicates that the ratio $\bar{A}_n/\bar{A}_2$ remains small for all n. Therefore, in both regions, deviations of the eigenfunction from the second mode are almost not visible in figure 7(*b*).

The oscillations of the sheet induce rotational flow in the chamber, whose magnitude decreases monotonically as y approaches the far distant walls; see figure 8(*a*). Indeed, the solution for ω (3.8) becomes independent of L_y as the vertical dimension of the chamber increases. Furthermore, the fluid's maximum velocity is obtained close to the centre point, $x = 1/2$, where the sheet's velocity equals zero. This is because the sheet moves up and down around this centre line and drives a net flux across it. The velocity of this flux is maximized at the centre of the sheet. It is important to note that there is a slight asymmetry in the flow patterns observed in the upper and lower regions of the chamber, which may be attributed to the initial non-zero volume difference in the base solution.

The pressure fields induced by the elastic oscillations are plotted in figure 8(*b*) and show an asymmetric profile in correlation with the eigenfunction of the sheet (figure 7*b*). Since only even modes are excited at the instability, the average pressure difference on the sheet, $\bar{p}_{ud}(t)$, vanishes. Therefore, in this case, there is no analogue to the compressibility calculated in § 3.2.1.

4. The evolution at moderate times

In this section, we relax the assumption that $t \ll 1$ and extend the analysis up to moderate times. The limits of this analysis are discussed at the end of this section. In particular, we require that the initial configuration of the sheet be close in shape to the second mode of buckling, i.e. $v_{du}(0) \ll v_{du}^{cr}$, where $v_{du}^{cr} = (2(3+\pi^2)/\pi\sqrt{3(15+2\pi^2)})\Delta^{1/2}$ (see

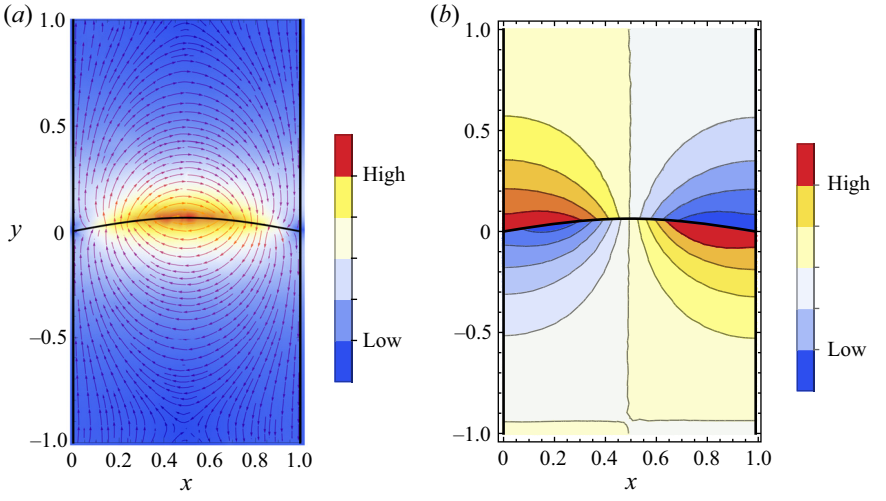

Figure 8. (*a*) The flow fields and (*b*) the hydrodynamic pressure fields obtained from the linear stability analysis of (2.2)–(2.9) when $\Delta = 0.01$, $\lambda = 0.1$ and $L_y = 2$. The normalization of the eigenfunctions is as in figure 7(*b*). This normalization implies [High, Low] = [5.3, 26.5] in the flow fields and [High, Low] = [−560, 560] in the pressure fields. In (*a*), arrows represent the streamlines and colours represent the relative magnitudes of the velocity.

§ 3.1), and we investigate the following questions: (i) What is the maximum amount of energy that is transferred from the sheet to the fluid? (ii) How long does it take the system to convert this maximum elastic energy into a fluid flow? (iii) What is the time-dependent behaviour of the $\bar{p}_{ud}(t)$–$v_{du}(t)$ relation. To address these questions, we assume that the amplitude of the sheet remains small during the dynamic evolution of the system and utilize the approximated formulation derived in § 2.1. This formulation yields the simplified set of nonlinear equations (2.20) that describe the coupling between the elastic and the hydrodynamic equations. As may be seen, this set of equations has a conserved first integral, $E = T_{nk}(\mathrm{d}A_k/\mathrm{d}t)(\mathrm{d}A_n/\mathrm{d}t) + V_{nk}A_kA_n$, that corresponds to the total energy of the system (2.10). This conserved energy constitutes the starting point for the discussion that follows.

When the initial configuration of the sheet is close in shape to the second mode of buckling, we expect the system's dynamics at moderate times to depend strongly on the first two modes, $A_1(t)$ and $A_2(t)$. This is because the initial shape of the sheet and its corresponding eigenfunction at the highest growth rate are described approximately by these two modes (see figure 4). Therefore, we reduce the expression for the total energy to the case in which $N = 2$ and obtain the following equation:

$$E = \frac{1}{4}\left(1 + \frac{8L_y}{\pi^2\lambda}\right)\left(\frac{\mathrm{d}A_1}{\mathrm{d}t}\right)^2 + \frac{1}{4}\left(1 + \frac{128\tanh(\pi L_y/2)}{9\pi^3\lambda}\right)\left(\frac{\mathrm{d}A_2}{\mathrm{d}t}\right)^2 + \frac{\pi^4}{4}A_1^2 + 4\pi^4A_2^2. \tag{4.1}$$

We keep in mind that $A_1(t)$ and $A_2(t)$ are related through the constraint of the excess length (2.20*b*).

To obtain some insight regarding the validity of this two-mode approximation, we solve (2.20) numerically with $N = 2$ and compare the results with the solution of the nonlinear model, i.e. the numerical solution of (2.2)–(2.9). In our investigation, we set $\Delta = 0.01$ and $L_y = 2$, and consider two different values for the parameter λ. The initial configuration is given by (3.1), where $v_{du}(0) = 0.01\,v_{du}^{cr}$. (The initial

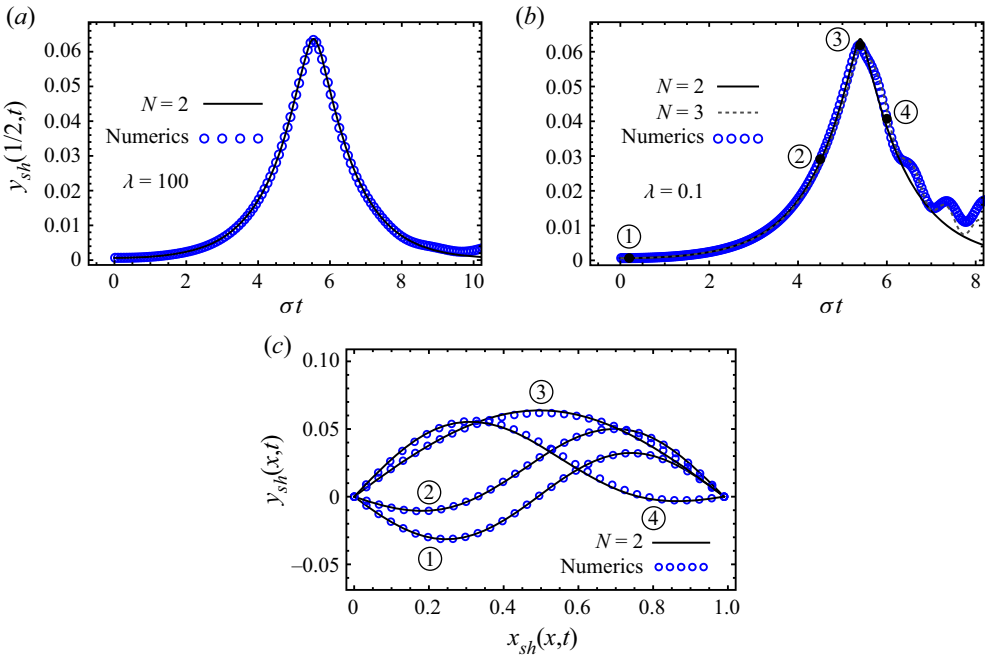

Figure 9. The sheet's midpoint as a function of time in (*a*) the solid-dominated ($\lambda = 100$) and (*b*) the fluid-dominated ($\lambda = 0.1$) regions. In both panels, $\Delta = 0.01$, $L_y = 2$ and the growth rate, σ, is approximated by (3.6). The solid black line denotes the two-mode approximation, i.e. (2.20) with $N = 2$, and the open blue circles denote the solution of the nonlinear model (2.2)–(2.9). In (*b*), the dashed grey line denotes the solution of (2.20) with $N = 3$. The initial configuration of the sheet is given by (3.1) with $v_{du}(0) = 0.01 v_{du}^{cr}$. In both cases, the approximated solution breaks down after $y_{sh}(1/2, t)$ reaches its first maximum. In the solid-dominated region, the two-mode approximation holds for longer times compared with the fluid-dominated region. (*c*) The configurations of the sheet along the trajectory depicted in (*b*); see the corresponding markers in (*b*). Between ① and ③ the sheet releases potential energy as it transforms from the second mode of buckling to the first mode of buckling. After ③, the height of the sheet's midpoint decreases and the sheet gains back potential energy, as seen in ④.

conditions are given by $A_1(0) = 2\int_0^1 y_{sh}(x, 0)\sin(\pi x)\,\mathrm{d}x = 32 v_{du}(0)/(3\pi + \pi^3)$ and $A_2(0) = \sqrt{\Delta/\pi^2 - 256 v_{du}(0)^2/(3\pi + \pi^3)^2}$, such that (2.20*b*) is satisfied. In addition, we keep in mind that the system starts from rest, $(\mathrm{d}A_1/\mathrm{d}t)(0) = (\mathrm{d}A_2/\mathrm{d}t)(0) = 0$.) The results of these numerical solutions are presented in figures 9(*a*) and 9(*b*), where we follow the time-dependent behaviour of the midpoint on the sheet, $y_{sh}(1/2, t)$. The configurations of the sheet along the trajectory depicted in figure 9(*b*) are presented in figure 9(*c*). In both cases, we find that the approximated solution breaks down slightly after $y_{sh}(1/2, t)$ reaches its first maximum. In the solid-dominated region ($\lambda = 100$), the two-mode approximation holds over one period of motion, while in the fluid-dominated region ($\lambda = 0.1$), the approximation breaks down a little earlier. This difference is probably due to the different number of excited modes at the instability in each region of the system (see discussion in § 3.2.1). We conjecture that higher modes become active beyond moderate times in the fluid-dominated region and perturb the system's trajectory from the two-mode approximation. Indeed, by solving (2.20) with $N = 3$ instead of $N = 2$, we observe a convergence towards the numerical data for longer times (see the dashed grey line in figure 9*b*).

Nonetheless, in both cases, i.e. the solid- and fluid-dominated regions, the agreement between the numerical solution of (2.2)–(2.9) and the analytical approximation, (2.20)

with $N = 2$, holds up to the first maximum. Similar results are also obtained when we perturb the system's parameters, Δ and L_y, and the initial configuration. Therefore, in the following analysis, we utilize this approximation to examine the system's behaviour up to the point where the midpoint of the sheet reaches its first maximum. We refer to this stage of the system as moderate times.

4.1. *The elastohydrodynamic energetic interplay*

Since the initial configuration of the sheet is close in shape to the second mode of buckling and the total energy of the system is conserved, the total energy at any $t > 0$ is given by (3.2). In the limit $v_{du}(0) \ll v_{du}^{cr}$, this energy is approximated as $E_{as} \simeq 4\pi^2\Delta$, i.e. the energy of the second mode of buckling. In addition, since the first mode of buckling is the global minimizer of the elastic sheet's potential energy, the potential energy of the sheet cannot fall below $E_s = \pi^2\Delta$. Therefore, at most, our system can convert $\delta E = E_{as} - E_s \simeq 3\pi^2\Delta$ of the initial potential energy either into kinetic energy of the sheet or into hydrodynamic energy of the fluid. We remind the reader that the kinetic and potential energies of the sheet, $E_{sh}^k(t)$ and $E_{sh}^p(t)$, and the energy of the fluid, $E_f(t)$, are given by the first, second and third terms, respectively, on the right-hand side of (2.10). In the small-amplitude approximation, these energies reduce to $E_{sh}^k(t) = (\lim_{\lambda\to\infty} T_{kn})(\mathrm{d}A_k/\mathrm{d}t)(\mathrm{d}A_n/\mathrm{d}t)$, $E_{sh}^p(t) = V_{kn}A_kA_n$ and $E_f(t) = T_{kn}(\mathrm{d}A_k/\mathrm{d}t)(\mathrm{d}A_n/\mathrm{d}t) - E_{sh}^k$.

The typical evolution of the three components of the energy, i.e. the kinetic energy of the sheet, the potential energy of the sheet and the energy of the fluid, is plotted in figures 10(*a*) and 10(*b*). These plots are obtained from the solution of (2.20) with $N = 2$ in the solid- and the fluid-dominated regions, $\lambda = 10$ and $\lambda = 0.1$ respectively, where the initial configuration is given by (3.1) with $v_{du}(0) = 0.01\,v_{du}^{cr}$. In both cases, we find that, after some initial delay, the potential energy of the sheet drops from $E \simeq 4\pi^2\Delta$, i.e. the energy of the second mode of buckling (3.2), to $E \simeq \pi^2\Delta$, i.e. the energy of the first mode of buckling. The energy released in this process, $\delta E \simeq 3\pi^2\Delta$, is converted to the kinetic energy of the sheet and the energy of the fluid, while the total energy remains fixed. In the solid-dominated region (figure 10*a*) the kinetic energy of the sheet becomes much larger than the energy of the fluid, while as λ decreases, the opposite picture emerges, i.e. the energy of the fluid becomes much larger than the kinetic energy of the sheet (figure 10*b*). In both scenarios, shortly after the initial peak, a portion of the kinetic energy is converted back into potential energy of the sheet. As a result, the sheet tends to return to its configuration of the second buckling mode, thereby decreasing the height of the sheet's midpoint, as shown in figure 9(*c*).

Our two-mode approximation allows us to quantify these findings and to further estimate the maximum values of $E_{sh}^k(t_p)$ and $E_f(t_p)$ as a function of λ, where t_p denotes the time at which the potential energy of the sheet reaches its minimum value. Indeed, at $E_{sh}^p(t_p) = \pi^2\Delta$, the sheet is close in shape to the first mode of buckling, i.e. $A_1(t_p) \simeq 2\sqrt{\Delta}/\pi$. The constraint on the excess length (2.20*b*) then implies that $A_2(t_p) \simeq 0$ and that $(\mathrm{d}A_1/\mathrm{d}t)(t_p) \simeq 0$. In addition, the derivative of the second mode at that moment, $(\mathrm{d}A_2/\mathrm{d}t)(t_p)$, is obtained from (4.1) when we substitute $E = 4\pi^2\Delta$ for the total energy. Taken together, these approximations yield the following maximum energies at $t = t_p$:

$$\frac{E_{sh}^k(t_p)}{3\pi^2\Delta} = \frac{1}{1 + \dfrac{128\tanh(\pi L_y/2)}{9\pi^3\lambda}}, \tag{4.2a}$$

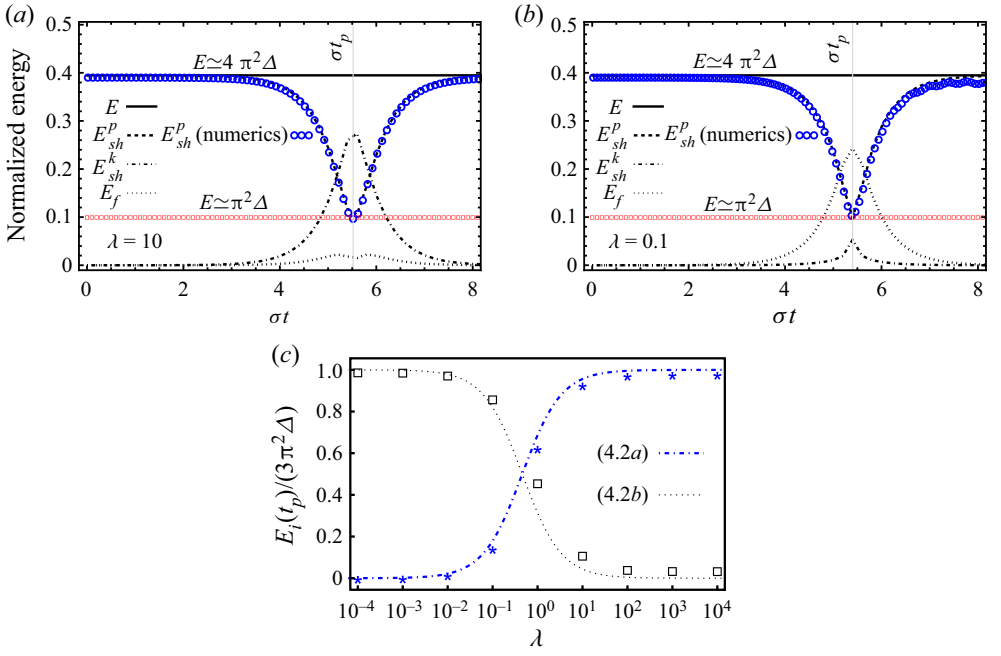

Figure 10. The energetic interplay between the three components of the total energy in (*a*) the solid-dominated ($\lambda = 10$) and (*b*) the fluid-dominated ($\lambda = 0.1$) regions of the system. In these two panels, we solve (2.20) for the case where $N = 2$, $\Delta = 0.01$, $L_y = 2$, and σ is given by (3.6). The initial configuration of the sheet is given by (3.1), where $v_{du}(0) = 0.01 v_{du}^{cr}$. After some initial delay, the potential energy of the sheet drops from $E^p_{sh}(t \ll 1) \simeq 4\pi^2\Delta$ to $E^p_{sh}(t_p) \simeq \pi^2\Delta$. Open blue circles represent the potential energy obtained from the solution of the nonlinear equations (2.2)–(2.9). The energy released from the sheet is divided between the kinetic energy of the sheet, $E^k_{sh}(t)$, and the hydrodynamic energy of the fluid, $E_f(t)$, such that the total energy, E, remains constant. In the solid-dominated region, $E^k_{sh}(t_p) \gg E_f(t_p)$, while in the fluid-dominated region we find the opposite relation, $E^k_{sh}(t_p) \ll E_f(t_p)$. (*c*) The kinetic energy of the sheet and the fluid at $t = t_p$ as a function of λ, i.e. $E_i(t_p) = E^k_{sh}(t_p), E_f(t_p)$. A logarithmic scale is used on the x axis. The dotted and the dashed-dotted lines correspond to our analytical solution from the two-mode approximation, and the colour symbols correspond to the numerical solution of (2.2)–(2.9), where the initial conditions are similar to those used in (*a*,*b*).

$$\frac{E_f(t_p)}{3\pi^2\Delta} = \frac{1}{1 + \dfrac{9\pi^3\lambda}{128\tanh(\pi L_y/2)}}. \tag{4.2b}$$

In figure 10(*c*), we compare these maximum energies with the numerical solution of (2.2)–(2.9). Overall, we find a good fit between the analytical approximation and the numerical solution over the entire range of λ.

Using (4.2), we find that in the solid-dominated region, $\lambda \gg 1$, most of the initial energy is converted into the kinetic energy of the sheet, i.e. $E^k_{sh}(t_p) \simeq 3\pi^2\Delta - \delta_1$ and $E_f(t_p) \simeq \delta_1$, where $\delta_1 = 128\Delta\tanh(\pi L_y/2)/(3\pi\lambda)$, while in the fluid-dominated region, $\lambda \ll 1$, most of the energy is converted into the energy of the fluid, i.e. $E^k_{sh}(t_p) \simeq \delta_2$ and $E_f(t_p) \simeq 3\pi^2\Delta - \delta_2$, where $\delta_2 = 27\pi^5\Delta\lambda/[128\tanh(\pi L_y/2)]$. Furthermore, if we estimate the average instantaneous velocity of the fluid, $\bar{v}(t_p)$, by using $E_f(t_p) \propto \bar{v}(t_p)^2\ell/\lambda$, we find that in the solid-dominated region the average velocity is proportional to $\bar{v}(t_p) \propto (\Delta/\ell)^{1/2}$, while in the fluid-dominated region it is proportional to $\bar{v}(t_p) \propto (\lambda\Delta/\ell)^{1/2}$; namely, while $E_f(t_p, \lambda \ll 1) \gg E_f(t_p, \lambda \gg 1)$, their corresponding velocities present the

opposite relationship, i.e. $\bar{v}(t_p, \lambda \ll 1) \ll \bar{v}(t_p, \lambda \gg 1)$. This is because the momentum of the fluid $p_f \propto \bar{v}(t_p)/\lambda$ – but not its velocity – increases in the fluid-dominated region.

4.2. *The peak time*

In the previous section, we demonstrated through energetic considerations that the sheet tends to release most of its stored potential energy. In this section, we investigate the time it takes for the system to release this energy. Given an initial configuration of the sheet that is close in shape to the second mode of buckling, i.e. (3.1) with $v_{du}(0) \ll v_{du}^{cr}$, we aim to find the time $t = t_p$ at which the potential energy of the sheet first drops to the minimum value, $E_{sh}^{p}(t_p) \simeq \pi^2 \Delta$. To do so, we first use (2.20*b*) and (3.6) to eliminate $A_2(t)$ and λ in favour of $A_1(t)$ and σ, respectively, in (4.1). Then, we substitute the energy of the initial configuration (3.2) into (4.1) and integrate it between $t \in [0, t_p]$. This gives

$$\sigma t_p = \int_{A_1(0)}^{A_1(t_p)} \frac{\sqrt{432\pi^3\Delta + \left[9\pi\left(-12\pi^4 + \sigma^2\right) + \dfrac{16\left(3\pi^4 - \sigma^2\right)}{L_y \coth(\pi L_y/2)}\right] A_1^2}}{6\sqrt{3}\pi^{3/2}\sqrt{\left(A_1^2 - \dfrac{8 v_{du}(0)^2}{3+\pi^2}\right)\left(4\Delta - \pi^2 A_1^2\right)}} \mathrm{d}A_1, \tag{4.3}$$

where $A_1(t_p) \simeq 2\Delta^{1/2}/\pi$ is approximately the amplitude of the sheet at time t_p and $A_1(0) = 2\int_0^1 y_{sh}(x, 0)\sin(\pi x)\,\mathrm{d}x = 32 v_{du}(0)/(3\pi + \pi^3)$ is the projection of the initial configuration (3.1) on the first mode of the sheet.

In figure 11(*a*), we fix the excess length and the vertical dimension of the chamber at $\Delta = 0.01$ and $L_y = 2$, respectively, and plot σt_p for $\lambda \in [10^{-3}, 10^3]$ ($\sigma \in [0.4, \sqrt{3}\pi^2]$). We find that at a given initial volume difference, $v_{du}(0)$, the peak time, σt_p, changes by less than 5 % over more than six orders of magnitude in λ. While σt_p is almost independent of λ, it does depend strongly on the initial configuration of the sheet, $v_{du}(0)$, and the excess length, Δ. An analytical approximation of this dependence can be extracted from (4.3), if we assume that the system is in the solid-dominated region, where $\sigma \simeq \sqrt{3}\pi^2$. Under this assumption, we can integrate the right-hand side of this equation and take the limit $v_{du}(0) \ll 1$ of the resulting expression. (We use *Mathematica* (Wolfram Research 2018) for the symbolic integration.) This gives

$$\sigma t_p \simeq \ln\left(c\frac{\Delta^{1/2}}{v_{du}(0)}\right), \tag{4.4}$$

where $c \simeq 2.9$. While the scaling in (4.4) agrees well with our numerical solution of the nonlinear model, there is a small deviation in the numerical prefactor. The best fit to the nonlinear model gives $c \simeq 2.0$ (see figure 11*b*). We note that the independence of L_y on the right-hand side of (4.4) is a result of our assumption that $\lambda \gg 1$. Had we derived this scaling using the fluid-dominated region, we would have found that the integral in (4.3) does depend on the vertical dimension of the chamber. However, this dependence diminishes to zero when $L_y \gtrsim 1$, as is required by our fourth assumption in § 2.

We also note that the logarithmic divergence of σt_p in the limit $v_{du}(0) \to 0$ is similar to the divergence of the period of a pendulum near the separatrix (Butikov 1999). Within this analogy between the two problems, the small initial deviation of the pendulum from the unstable vertical position is analogous to the small initial volume difference $v_{du}(0)$. The separatrix of the pendulum is analogous to the trajectory $v_{du}(0) = 0$ in the phase space of our system.

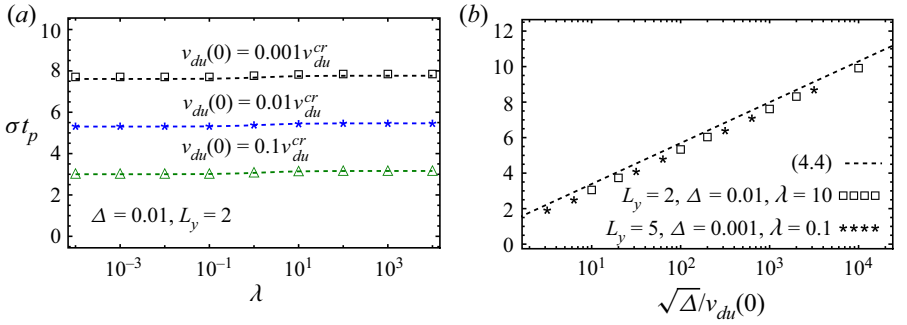

Figure 11. The peak time, σt_p, as a function of the system's parameters. (*a*) The peak time as a function of λ, where $\Delta = 0.01$ and $L_y = 2$, for two different values of the initial volume difference. Dashed lines correspond to the numerical integration of (4.3) and symbols with corresponding colours represent the numerical solution of (2.2)–(2.9). For a given $v_{du}(0)$, the time σt_p changes by less than 5 % over six orders of magnitude of the parameter λ. (*b*) Comparison between the analytical scaling (4.4) and the solution obtained from the nonlinear model. A logarithmic scale is used on the x axis. Symbols correspond to the numerical solution of the nonlinear model. While the scaling of the analytical solution agrees well with the numerical data, the prefactor $c \simeq 2.9$ slightly overestimates the numerical prediction.

4.3. *The $\bar{p}_{ud}$–v_{du} relation*

In this section, we investigate the behaviour of the $\bar{p}_{ud}$–v_{du} relation at moderate times. To this end, we first use the two-mode approximation to calculate the pressure difference in the chamber. From Bernoulli's equation (2.13*a*), and the normal mode expansion (2.15) and (C2), we have that the average pressure difference on the sheet is given by $\bar{p}_{ud}(t) = (2L_y/\pi\lambda)(\mathrm{d}^2 A_1/\mathrm{d}t^2)$. In addition, using (2.16), we find the volume difference as a function of time, $v_{du}(t) = 2\int_0^1 y_{sh}(x, t)\,\mathrm{d}x = 4A_1(t)/\pi$. Thereafter, we solve (2.20) numerically with $N = 2$ and plot the parametric solution $(\bar{p}_{ud}(t),\ v_{du}(t))$ in the range $t \in [0, t_p]$.

The results of these solutions are plotted in figures 12(*a*) and 12(*b*) for the solid-dominated ($\lambda = 100$) and fluid-dominated ($\lambda = 0.01$) regions, respectively. Qualitatively, the two regions exhibit similar behaviour. The pressure difference in the chamber increases from almost zero up to a maximum positive value, from which it rapidly decreases and becomes negative. The backward pressure is maximized at the peak time t_p; see the time-dependent behaviour of $\bar{p}_{ud}(t)$ in the insets of these figures. Quantitatively, however, the two profiles are considerably different, because the maximum backward pressure is much larger in the fluid-dominated region (figure 12*b*) than in the solid-dominated region (figure 12*a*).

The transition from positive to negative pressure differences can be explained as follows. Initially, the system exhibits a 'negative feedback' between the sheet and the fluid, meaning that the sheet's motion drives the fluid's dynamics, which, in turn applies a positive pressure difference and resists the sheet's motion. As the system evolves, the fluid continuously gains kinetic energy and reduces its resistance to the sheet's motion. Then, at some instant, the pressure difference vanishes, $\bar{p}_{ud} = 0$, and the resistance of the fluid is almost eliminated. Beyond this moment, the pressure difference becomes negative, and the system exhibits a 'positive feedback', meaning that the sheet transfers energy to the fluid, which, in turn, enhances the sheet's motion. This positive feedback accelerates the system's dynamics and creates a spike of pressure drop in the chamber. The process terminates when the system meets the constraint on the maximum volume difference.

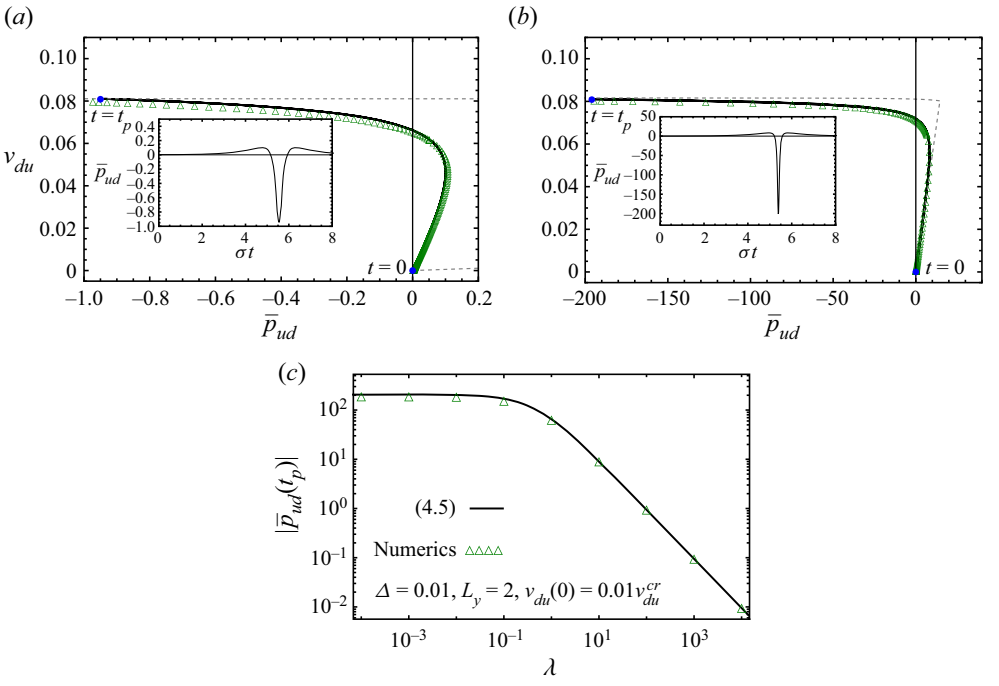

Figure 12. The $\bar{p}_{ud}$–v_{du} relation and the maximum backward pressure. In all three panels, open green triangles correspond to the numerical solution of (2.2)–(2.9) and solid lines correspond to the solution of the two-mode approximation. The volume difference as a function of the average pressure difference on the sheet is plotted in (*a*) the solid-dominated ($\lambda = 100$) and (*b*) the fluid-dominated ($\lambda = 0.01$) regions. In both panels, the solid black line corresponds to the solution of (2.20) with $N = 2$, $\Delta = 0.01$, $L_y = 2$ and $v_{du}(0) = 0.01 v_{du}^{cr}$. The blue points correspond to times $t = 0$ and $t = t_p$. The dashed grey lines correspond to the static solution (3.1*b*) and (3.3*b*). The insets show $\bar{p}_{ud}(t)$ as a function of time, where σ is given by (3.6). In the fluid-dominated region, the maximum backward pressure ($\bar{p}_{ud}(t_p) \simeq -200$) is much larger than that in the solid-dominated region ($\bar{p}_{ud}(t_p) \simeq -1$). In addition, the evolution of the $\bar{p}_{ud}$–v_{du} relation in the fluid-dominated region follows the static solution, except for some deviations close to the asymmetric-to-symmetric transition. (*c*) The absolute value of the maximum average pressure difference on the sheet.

To estimate the magnitude of the pressure spike, $\bar{p}_{ud}(t_p)$, we use the two-mode approximation. Recalling that near the peak time when the sheet is close in shape to the first mode of buckling, i.e. $A_1(t_p) \simeq 2\Delta^{1/2}/\pi$ and $A_2(t_p) \simeq 0$, and that $E \simeq 4\pi^2\Delta$, we find from (2.20*b*) and (4.1) an expression for $(\mathrm{d}^2A_1/\mathrm{d}t^2)(t_p)$ as a function of the system's parameters. This gives the maximum backward pressure:

$$\bar{p}_{ud}(t_p) \simeq -\frac{432\pi^5 L_y \Delta^{1/2}}{9\pi^3\lambda + 128\tanh(\pi L_y/2)}. \tag{4.5}$$

This analytical approximation compares well with the numerical solution of (2.2)–(2.9) (see figure 12*c*). Therefore, in the solid-dominated region, the maximum backward pressure decays to zero as $\bar{p}_{ud}(t_p, \lambda \gg 1) \simeq -48\pi^2 L_y \Delta^{1/2}/\lambda$, whereas in the fluid-dominated region it is independent of λ, i.e. $\bar{p}_{ud}(t_p, \lambda \ll 1) \simeq -(27\pi^5/8) L_y \Delta^{1/2}/\tanh(\pi L_y/2)$.

Note also that the $\bar{p}_{ud}$–v_{du} relation approximately follows the static solution (3.1*b*) and (3.3*b*) in the fluid-dominated region (see the dashed lines in figure 12*b*). This is because the dynamics of the fluid in this region is much slower than that in the solid-dominated region.

Nonetheless, deviations between the two solutions, static and dynamic, are observed close to the asymmetric-to-symmetric transition. These deviations may be attributed to inertial effects in the dynamics solution.

5. Discussion on experimental consequences

To fully define the system, eight physical parameters are needed: four parameters specify the properties of the sheet $\{\tilde{L}, \tilde{\rho}_{sh}, \tilde{B}, \tilde{h}\}$, three parameters define the dimensions of the chamber $\{\tilde{L}_x, \tilde{L}_y, \tilde{W}\}$ and an additional parameter characterizes the fluid $\tilde{\rho}_\ell$. The control parameter is the initial volume difference in the chamber $\tilde{v}_{du}(0) = \tilde{v}_d(0) - \tilde{v}_u(0)$.

To facilitate comparisons between our theory and experimental observations, we present two of our central predictions in dimensional form. The first prediction relates to the scenario where the initial configuration of the sheet is close in shape to the second buckling mode. In this case, the experimentally measurable quantities are the growth rate σ, which is defined in (3.6) and characterizes the early stage of the evolution, and the time t_p, which is given in (4.4) and characterizes the behaviour at moderate times. In dimensional form, these quantities are given by

$$\tilde{\Delta}/\tilde{L} \ll 1 \quad \text{and} \quad \tilde{v}_{du}(0)/\tilde{v}_{du}^{cr} \ll 1 : \tilde{\sigma} = \frac{\sqrt{3}\pi^2}{\sqrt{1 + \dfrac{8}{\pi^2}\dfrac{\tilde{\rho}_\ell \tilde{L}_y}{\tilde{\rho}_{sh}\tilde{h}}}} \left(\frac{\tilde{B}}{\tilde{\rho}_{sh}\tilde{h}\tilde{L}^4}\right)^{1/2}, \tag{5.1a}$$

$$\tilde{\sigma}\tilde{t}_p \simeq \ln\left(\frac{\pi\sqrt{3(15+2\pi^2)}}{(3+\pi^2)}\frac{\tilde{v}_{du}^{cr}}{\tilde{v}_{du}(0)}\right), \tag{5.1b}$$

where $\tilde{v}_{du}^{cr} = (2(3+\pi^2)/\pi\sqrt{3(15+2\pi^2)})\tilde{\Delta}^{1/2}\tilde{L}^{3/2}\tilde{W}$ is the volume difference at the asymmetric-to-symmetric transition in the quasi-static solution (§ 3.1), and we keep in mind that the normalized excess length is assumed small in our analysis, i.e. $\tilde{\Delta}/\tilde{L} = (\tilde{L} - \tilde{L}_x)/\tilde{L} \ll 1$.

The second prediction of our theory corresponds to the frequency of oscillations ω around the first buckling mode (3.8). In dimensional form the frequency is given by

$$\tilde{\omega} = \frac{2\sqrt{3}\pi^2}{\sqrt{1 + \dfrac{128}{9\pi^3}\tanh\left(\dfrac{\pi\tilde{L}_y}{2\tilde{L}}\right)\dfrac{\tilde{\rho}_\ell \tilde{L}}{\tilde{\rho}_{sh}\tilde{h}}}} \left(\frac{\tilde{B}}{\tilde{\rho}_{sh}\tilde{h}\tilde{L}^4}\right)^{1/2}, \tag{5.2}$$

where in the small-amplitude approximation the first buckling mode is obtained when $\tilde{v}_{du}(0) = (8/\pi^2)\tilde{\Delta}^{1/2}\tilde{L}^{3/2}\tilde{W}$. It is important to note that this analytical prediction is valid only for very small excess lengths $\tilde{\Delta}/\tilde{L} \lesssim 0.01$. Larger excess lengths will probably result in significant quantitative deviations from this solution.

To obtain a sense of the physical time and pressure scales that can potentially be induced in the system, let us consider a chamber, with dimensions $\tilde{L}_x = \tilde{L}_y = \tilde{W} = 5$ mm, that is filled with water ($\tilde{\rho}_\ell \simeq 10^3\,\mathrm{kg\,m^{-3}}$). In addition, let us assume that the sheet is made of polyethylene terephthalate with Young's modulus $\tilde{E} \simeq 1$ GPa, Poisson's ratio $\nu \simeq 0.3$ and thickness $\tilde{h} \simeq 0.1$ mm, such that the bending modulus is $\tilde{B} = \tilde{E}\tilde{h}^3/[12(1-\nu^2)] \simeq 9 \times 10^{-5}$ J (Gomez *et al.* 2017). The density of the sheet is approximately $\tilde{\rho}_{sh} \simeq 1500\,\mathrm{kg\,m^{-3}}$,

and its total length is $\tilde{L} = 5.5$ mm ($\tilde{\Delta}/\tilde{L} = 0.09$). Under these conditions, the inertial time scale of the sheet is $\tilde{t}_\star = (\tilde{\rho}_{sh}\tilde{h}\tilde{L}^4/\tilde{B})^{1/2} \simeq 10^{-3}$ s, and the structure-to-fluid mass ratio is given by $\lambda \simeq 0.03$, i.e. the system is in the fluid-dominated region. Since our theory is limited to inviscid fluids, it is reasonable to assume that the theory should agree with the solution of the more general, viscous equations, in the limit of high Reynolds numbers, where energy dissipation is rather small. Estimating the Reynolds number as $Re \sim \tilde{\rho}_\ell \tilde{\bar{v}}(\tilde{t}_p)\tilde{L}/\tilde{\mu}$, where $\tilde{\mu} \simeq 10^{-3}$ Pa s is the dynamic viscosity and $\tilde{\bar{v}}(\tilde{t}_p) \sim (\lambda\tilde{\Delta}/\tilde{L}_y)^{1/2}(\tilde{L}/\tilde{t}_\star)$ is our scaling for the fluid's velocity at time $\tilde{t}_p$ in the fluid-dominated region (see § 4.1), we find that $Re \sim 10^3$, i.e. it is relatively high. Yet, we are aware that higher Reynolds numbers should possibly be considered to reveal a convergence to the inviscid limit. Using these parameters, we have from (5.1*a*) and (5.2) that the growth rate and the frequency of the oscillations are $\tilde{\sigma} \simeq 3.2/\tilde{t}_\star$ and $\tilde{\omega} \simeq 8.5/\tilde{t}_\star$, respectively. In addition, given an initial volume difference, the peak time is obtained from (5.1*b*). This gives $\tilde{t}_p \simeq 3.1\tilde{t}_\star$ if $\tilde{v}_{du}(0)/\tilde{v}_{du}^{cr} = 10^{-4}$, and $\tilde{t}_p \simeq 1.7\tilde{t}_\star$ if $\tilde{v}_{du}(0)/\tilde{v}_{du}^{cr} = 10^{-2}$. At that moment, the average backward pressure difference on the sheet is given by $\tilde{\bar{p}}_{ud}(t_p) \simeq -160$ kPa; see (4.5).

However, when attempting to predict the behaviour of an experimental system using our solution, it is important to keep in mind the assumptions made in the formulation. For example, we assumed that the fluid exchange between the two parts of the chamber occurs through the upper and lower walls, $y = \pm L_y/2$, but, in practice, this fluid exchange is likely to occur through a connecting channel, as shown in figure 1. In this case, the analytical analysis must take into account the geometry of the transition region and its associated pressure drop. For example, we anticipate that a narrow transition channel will slow down the dynamics and decrease the growth rate of the instability. Additionally, we expect that if the pressure drop in the channel is much smaller than $\bar{p}_{ud}(t_p)$, it will have a negligible effect on the dynamics.

6. Concluding remarks

We investigated the dynamic interaction between a thin sheet and an inviscid fluid that are confined in a closed rectangular chamber. Our investigation focused on two different regions of the system: the early time evolution, where nonlinear effects are negligible, and the evolution at moderate times, where nonlinearity plays a crucial role in the solution. To analyse the dynamics at $t \ll 1$, we employed a linear stability analysis around the second and first buckling modes. While the second mode is always an unstable state whose highest growth rate is a positive number, the first mode is always stable and yields an imaginary growth rate, i.e. periodic oscillations. In the small-amplitude approximation, $\Delta \ll 1$, we obtained analytical solutions for the highest growth rate and the smallest oscillation frequency (3.6) and (3.8) respectively, which agree well with the numerical solutions. Yet, experimental data are needed to validate these central analytical predictions. To facilitate comparisons with experiments, we repeated these results in dimensional form in § 5.

Given the chamber's dimensions, we showed that both σ and ω converge to constants in the solid-dominated region and exhibit $\lambda^{1/2}$ scaling in the fluid-dominated region. This scaling highlights the effect of the fluid on the sheet's motion. When $\lambda \gg 1$, the elastic forces are primarily balanced by the inertia of the sheet, and the fluid has minimal effect on the dynamics. On the other hand, when $\lambda \ll 1$, the elastic forces are mainly balanced by the hydrodynamic pressure difference, and the sheet's inertia has a limited effect on the dynamics. The differences between these two regions are further manifested in the eigenfunctions of the linear stability solution. In the solid-dominated region only one

mode of the sheet is excited, i.e. the other modes fall to zero as $1/\lambda$, while an infinite number of modes are excited in the fluid-dominated region. While this difference did not affect the system's behaviour at moderate times, since in the leading order the dynamics is governed by the first two modes, we conjecture that it can influence the system's behaviour at $t \gg 1$; namely, beyond moderate times when higher modes have an increasing effect on the dynamics, we would expect the fluid-dominated solution to be less ordered than the solution in the solid-dominated region.

In addition, we focused on how the sheet escapes from the second buckling mode at moderate times. Key to this analysis is the two-mode approximation that allowed us to analytically analyse the energetic interplay between the sheet and the fluid; see (4.2) and figure 10. This energetic interplay is based on the fact that our model incorporates an elastic sheet and an inviscid fluid, which ensures that the system's total energy is always conserved. At each moment in time, the total energy is distributed between the kinetic energy of the sheet, the potential energy of the sheet and the energy of the fluid, in different proportions. In the solid-dominated region, the sheet's initial potential energy is converted to the sheet's kinetic energy, and only a small fraction, of order λ^{-1}, is converted to the energy of the fluid. However, the picture is reversed in the fluid-dominated region, where most energy is used to displace the fluid.

The time at which the potential energy of the sheet reaches a minimum (4.4) constitutes another central result of our theory, which can be verified experimentally. In particular, we showed that σt_p is almost independent of the parameter λ, and in the limit $v_{du}(0) \ll 1$ it diverges logarithmically.

During the dynamic evolution at moderate times, we observed that the sheet–fluid interplay experiences a transition from negative to positive feedback. Initially, the fluid resists the sheet's motion, but at later times, the hydrodynamic pressure difference acts in the direction of the sheet's motion and promotes the sheet's dynamics. The positive feedback ends at $t = t_p$, when the volume difference reaches its maximum value, dictated by the inextensibility of the sheet. At that moment, the pressure difference on the sheet, $\bar{p}_{ud}$, reaches its peak value.

An important extension of the present theory is the inclusion of viscosity in the mathematical formulation of the fluid. This extension will allow us to investigate the behaviour of the sheet at both high and low Reynolds numbers and thus look for the elastohydrodynamic instabilities caused by viscous effects. It will also allow us to investigate the formation of boundary layers and examine their impact on the dynamics of the system. We will pursue this extension in a future study.

Acknowledgements. We thank O. Shoshani and Y. Green for helpful discussions.

Funding. This research was partially supported by the Israel Science Foundation (grant no. 950/22).

Declaration of interests. The authors report no conflict of interest.

Author ORCIDs.
Kirill Goncharuk https://orcid.org/0000-0002-3857-8444;
Yuri Feldman https://orcid.org/0000-0001-9143-9382;
Oz Oshri https://orcid.org/0000-0003-1782-4105.

Appendix A. Derivation of (2.10)

Equations (2.2)–(2.9) have a conserved first integral that corresponds to the total energy in the system. To derive this conserved quantity, we multiply (2.8*a*) by $\partial\theta/\partial t$ and (2.8*b*) by $\partial \boldsymbol{x}_{sh}/\partial t$, and subtract the second equation from the first. Then, we integrate the resulting

equation between $s \in [0, 1]$, and use integration by parts and the geometric constraints (2.6) to simplify the result. This gives

$$\frac{\mathrm{d}}{\mathrm{d}t}\left[E^k_{sh}(t) + E^p_{sh}(t)\right] = -\int_0^1 \frac{\partial}{\partial s}\left(\frac{\partial \boldsymbol{x}_{sh}}{\partial t}\cdot\boldsymbol{F} - \frac{\partial\theta}{\partial t}\frac{\partial\theta}{\partial s}\right)\mathrm{d}s - \int_0^1 (p_u - p_d)\frac{\partial \boldsymbol{x}_{sh}}{\partial t}\cdot\hat{\boldsymbol{n}}_d\,\mathrm{d}s, \tag{A1}$$

where $E^k_{sh}(t) = \frac{1}{2}\int_0^1 |\partial \boldsymbol{x}_{sh}/\partial t|^2\,\mathrm{d}s$ and $E^p_{sh}(t) = \frac{1}{2}\int_0^1 (\partial\theta/\partial s)^2\,\mathrm{d}s$ are readily identified as the kinetic and potential energies of the sheet, respectively. Given the boundary conditions on the sheet's edges (2.9), the first term on the right-hand side of (A1) vanishes. Therefore, to complete the derivation, it remains to show that the second term on the right-hand side of (A1) equals $-\mathrm{d}E_f(t)/\mathrm{d}t$.

Following Lamb (1945), the kinetic energy of an incompressible fluid is given by

$$\frac{\mathrm{d}}{\mathrm{d}t}\left(\frac{1}{2\lambda}\iint_{v_i(t)} |\nabla\phi_i|^2\,\mathrm{d}x\,\mathrm{d}y\right) = -\oint_{\delta v_i(t)} p_i\nabla\phi_i\cdot\hat{\boldsymbol{n}}_i\,\mathrm{d}\tilde{s}, \tag{A2}$$

where $\delta v_i(t)$ are the perimeters of the upper or the lower parts of the chamber, $\mathrm{d}\tilde{s}$ is an infinitesimal element on $\delta v_i(t)$ (on the sheet $\mathrm{d}\tilde{s} = \mathrm{d}s$) and $\hat{\boldsymbol{n}}_i(\tilde{s}, t)$ are the corresponding local unit normal vectors on $\delta v_i(t)$. Since $(\nabla\phi_i\cdot\hat{\boldsymbol{n}}_i)_{x=0,1} = 0$ on the sidewalls of the chamber, in accordance with (2.4*b*), and since we have periodic boundary conditions on the upper and lower walls, the right-hand side of (A2) reduces to an integral over the configuration of the sheet. When summed over the two parts of the chamber this gives

$$\frac{\mathrm{d}E_f(t)}{\mathrm{d}t} = -\sum_{i=u,d}\int_0^1 p_i\nabla\phi_i\cdot\hat{\boldsymbol{n}}_i\,\mathrm{d}s = -\sum_{i=u,d}\int_0^1 p_i\frac{\partial \boldsymbol{x}_{sh}}{\partial t}\cdot\hat{\boldsymbol{n}}_i\,\mathrm{d}s. \tag{A3}$$

Here, $E_f(t) = \sum_{i=u,d}(1/2\lambda)\iint_{v_i(t)}|\nabla\phi_i|^2\,\mathrm{d}x\,\mathrm{d}y$ is the energy of the fluid, and in the second equality we used the kinematic boundary condition (2.7*a*,*b*), to replace the normal velocity of the fluid with the normal velocity of the sheet. Finally, note that on the sheet the normal vectors are related by $\hat{\boldsymbol{n}}_u(s, t) = -\hat{\boldsymbol{n}}_d(s, t)$. Using this relation and (A3), we obtain that

$$\frac{\mathrm{d}E_f(t)}{\mathrm{d}t} = \int_0^1 (p_u - p_d)\frac{\partial \boldsymbol{x}_{sh}}{\partial t}\cdot\hat{\boldsymbol{n}}_d\,\mathrm{d}s. \tag{A4}$$

Substituting (A4) into (A1) and integrating once with respect to time completes the derivation.

Appendix B. Minimization of the action

In this appendix, we show that the minimization of the action $\mathcal{S} = \int_0^{\mathrm{T}}\mathcal{L}\,\mathrm{d}t$, where $\mathcal{L}$ is given by (2.14), yields the complete set of equilibrium equations in the small-amplitude approximation (2.11)–(2.13). To do so, we minimize the action with respect to the elastic fields, $y_{sh}(x, t)$ and $F_x(t)$, and the hydrodynamic fields, $\phi_u(x, y, t)$ and $\phi_d(x, y, t)$, in the standard way. We consider a small perturbation in each of these variables, for example, $y_{sh} \to y_{sh} + \delta y_{sh}$, and then expand the action to linear order in the perturbation, $\delta y_{sh}(x, t)$.

This procedure gives, after integration by parts, the variation

$$\begin{aligned}\delta\mathcal{S} = &\int_0^1 \left[\left(\frac{\partial y_{sh}}{\partial t} + \frac{\phi_d(x,0,t) - \phi_u(x,0,t)}{\lambda}\right)\delta y_{sh}\right]_{t=0}^{\mathrm{T}} \mathrm{d}x \\ &+ \int_0^{\mathrm{T}} \left[-\frac{\partial^2 y_{sh}}{\partial x^2}\frac{\partial \delta y_{sh}}{\partial x} + \left(\frac{\partial^3 y_{sh}}{\partial x^3} + F_x\frac{\partial y_{sh}}{\partial x}\right)\delta y_{sh}\right]_{x=0}^{x=1} \mathrm{d}t \\ &- \int_0^{\mathrm{T}}\int_0^1 \left(\frac{\partial^2 y_{sh}}{\partial t^2} + \frac{\partial^4 y_{sh}}{\partial x^4} + F_x(t)\frac{\partial^2 y_{sh}}{\partial x^2} + [p_u(x,0,t) - p_d(x,0,t)]\right)\delta y_{sh}\,\mathrm{d}x\,\mathrm{d}t \\ &+ \int_0^{\mathrm{T}}\int_0^1 \left(\frac{1}{2}\left(\frac{\partial y_{sh}}{\partial x}\right)^2 - \Delta\right)\delta F_x\,\mathrm{d}x\,\mathrm{d}t \\ &+ \frac{1}{\lambda}\int_0^{\mathrm{T}}\int_0^1 [\delta\phi_d(x,0,t) - \delta\phi_u(x,0,t)]\frac{\partial y_{sh}}{\partial t}\mathrm{d}x\,\mathrm{d}t \\ &- \frac{1}{\lambda}\sum_{i=u,d}\left(\int_0^{\mathrm{T}}\oint_{\delta v_i}\nabla\phi_i\cdot\hat{\boldsymbol{n}}_i\delta\phi_i\,\mathrm{d}\tilde{s}\,\mathrm{d}t - \int_0^{\mathrm{T}}\int_{v_i}\nabla^2\phi_i\delta\phi_i\,\mathrm{d}x\,\mathrm{d}y\,\mathrm{d}t\right), \end{aligned} \tag{B1}$$

where v_i are the volumes of the chamber above and below the sheet in the small-amplitude approximation, δv_i are the perimeters of the upper and lower volumes, $\hat{\boldsymbol{n}}_i$ are the unit normal vectors on δv_i and $\mathrm{d}\tilde{s}$ is an infinitesimal line element on δv_i (on the sheet $\mathrm{d}\tilde{s} = \mathrm{d}s$).

The initial conditions of the system and the boundary conditions that we imposed (2.9*b*) and (2.9*c*) imply that the first and second lines in (B1) vanish altogether. The third and fourth lines in (B1) vanish if the force balance equation (2.12) and (2.13*a*), and the geometric constraint (2.11), are both satisfied. In the last line, the two integrals over the upper and lower volumes of the chamber, v_i, vanish if the continuity equations (2.2*a*) are satisfied. Therefore, it remains to show that the fifth line and the penultimate term in the last line of (B1) are equal to zero. To do so, we note that $(\nabla\phi_i\cdot\hat{\boldsymbol{n}}_i)_{x=0,1} = 0$, and that we assumed periodic boundary conditions at $y = \pm L_y/2$ (2.4*a*). As a result, the integrals over the perimeters δv_i reduce to integrals over the sheet–fluid interfaces. In that case, the remaining part of the variation of $\delta\mathcal{S}$ reads

$$\begin{aligned}\delta\mathcal{S} = &\frac{1}{\lambda}\int_0^{\mathrm{T}}\int_0^1 [\delta\phi_d(x,0,t) - \delta\phi_u(x,0,t)]\frac{\partial y_{sh}}{\partial t}\mathrm{d}x\,\mathrm{d}t \\ &- \frac{1}{\lambda}\int_0^{\mathrm{T}}\int_0^1 \left[\left(\frac{\partial\phi_d}{\partial y}\delta\phi_d\right)_{y=0} - \left(\frac{\partial\phi_u}{\partial y}\delta\phi_u\right)_{y=0}\right]\mathrm{d}x\,\mathrm{d}t. \end{aligned} \tag{B2}$$

Collecting the terms that are proportional to $\delta\phi_i(x,0,t)$, we find that the integrands in (B2) vanish when the kinematic boundary conditions (2.13*b*) are satisfied.

This completes the proof that the force balance equations and their corresponding boundary conditions in the small-amplitude approximation both emanate from the minimization of the action.

Appendix C. Derivation of (2.17) and (2.18)

In this appendix, we derive (2.17) and (2.18) in the main text. To do so, we first express the Lagrangian (2.14) in terms of the unknown time-dependent coefficients $A_n(t)$, $a_m(t)$ and

$c_m(t)$. Substituting the normal mode expansion of the sheet's height function (2.16) and the potential functions (2.15) into the Lagrangian (2.14) and integrating over the spatial coordinates gives

$$\begin{aligned}\mathcal{L} = &\sum_{n=1}^{N} \frac{1}{4}\left[\left(\frac{\mathrm{d}A_n}{\mathrm{d}t}\right)^2 + \pi^2 n^2\left(F_x(t) - \pi^2 n^2\right)A_n^2\right] - F_x(t)\Delta \\ &+ \frac{L_y}{\lambda}a_0\sum_{n=1}^{N} W(n,0)\frac{\mathrm{d}A_n}{\mathrm{d}t} + \sum_{n=1}^{N}\sum_{m=1}^{N-1}\frac{2}{\lambda}W(n,m)\sinh\left(\frac{\pi m L_y}{2}\right)(a_m - c_m)\frac{\mathrm{d}A_n}{\mathrm{d}t} \\ &- \frac{L_y}{2\lambda}a_0^2 - \sum_{m=1}^{N-1}\frac{\pi m}{2\lambda}\sinh(\pi m L_y)\left(a_m^2 + c_m^2\right). \end{aligned} \tag{C1}$$

While the first line in this equation describes the kinetic and the potential energies of the sheet and the geometric constraint, the second and third lines emanate, respectively, from the mixed term, $\phi_i(x, 0, t)\partial y_{sh}/\partial t$, and the kinetic energies of the fluid.

The next step is to express the coefficients of the hydrodynamic potentials, $a_m(t)$ and $c_m(t)$, in terms of the elastic coefficients, $A_n(t)$. Minimizing (C1) with respect to $a_m(t)$ and $c_m(t)$, we obtain

$$a_0(t) = \sum_{k=1}^{N} W(k,0)\frac{\mathrm{d}A_k}{\mathrm{d}t}, \tag{C2a}$$

$$a_m(t) = -c_m(t) = \sum_{k=1}^{N}\frac{2}{\pi m}\frac{\sinh(\pi m L_y/2)}{\sinh(\pi m L_y)}W(k,m)\frac{\mathrm{d}A_k}{\mathrm{d}t} \quad (m = 1, 2, \ldots, N-1), \tag{C2b}$$

where $W(n, m) = (n/\pi)((1 - (-1)^{n+m})/(n^2 - m^2))$ for $n \neq m$ and zero otherwise, as is defined immediately following (2.18). Finally, we substitute (C2) back into the Lagrangian (C1), and collect together terms that are proportional to $(\mathrm{d}A_n/\mathrm{d}t)(\mathrm{d}A_k/\mathrm{d}t)$, the lateral compression $F_x(t)$ and A_nA_k. This yields (2.17) and (2.18) in the main text.

Appendix D. Linear stability analysis at a finite excess length

When the excess length of the sheet compared with the lateral dimension of the chamber is finite, rather than $\Delta \ll 1$, as assumed in § 2.1, the linear stability analysis is obtained from the linearization of (2.2)–(2.9). In this appendix, we obtain a closed set of equations for the linearization of the system in this, more general, case and explain the direction we take to obtain the numerical solution.

To linearize (2.2)–(2.9), we first expand the elastic and the hydrodynamic fields around their base solutions; for example, $y_{sh}(s, t) = y_{sh}(s, 0) + \epsilon\, \mathrm{e}^{\sigma t}\hat{y}_{sh}(s)$, where $\hat{y}_{sh}(s)$ is a yet-to-be-determined eigenfunction and ϵ is an arbitrary small parameter. Similarly, we define the eigenfunctions $\{\hat{x}_{sh}(s), \hat{\theta}(s), \hat{F}_x(s), \hat{F}_y(s)\}$ for the elastic sheet and $\{\hat{\phi}_i(x, y), \hat{p}_i(x, y)\}$ for the fluid. We keep in mind that the fluid starts from rest, and therefore the base solutions for the hydrodynamic fields are equal to zero. Thereafter, we substitute these expansions in the continuity and Bernoulli equations (2.2), and expand them to a

linear order in ϵ. This expansion reads

$$\nabla^2 \hat{\phi}_i = 0, \tag{D1a}$$

$$\hat{p}_i(x, y) = -\frac{\sigma}{\lambda}\left[\hat{\phi}_i(x, y) - \hat{\phi}_d\left(\frac{1-\Delta}{2}, -\frac{L_y}{2}\right)\right], \tag{D1b}$$

where in the last equation we determine the constant $c_i(t)$ such that (2.5) is satisfied. Similarly, an expansion of the geometric constrains (2.6), and the force balance equations on the sheet (2.8), gives

$$\frac{\mathrm{d}\hat{x}_{sh}}{\mathrm{d}s} = -\hat{\theta}\sin\theta(s, 0), \tag{D2a}$$

$$\frac{\mathrm{d}\hat{y}_{sh}}{\mathrm{d}s} = \hat{\theta}\cos\theta(s, 0), \tag{D2b}$$

$$\frac{\mathrm{d}^2\hat{\theta}}{\mathrm{d}s^2} = \left[-F_x(s, 0)\hat{\theta} + \hat{F}_y\right]\cos\theta(s, 0) - \left[\hat{F}_x + F_y(s, 0)\hat{\theta}\right]\sin\theta(s, 0), \tag{D2c}$$

$$\sigma^2\hat{x}_{sh} = -\frac{\mathrm{d}\hat{F}_x}{\mathrm{d}s} + \left[\hat{p}_u(x_{sh}(s, 0), y_{sh}(s, 0)) - \hat{p}_d(x_{sh}(s, 0), y_{sh}(s, 0))\right]\sin\theta(s, 0), \tag{D2d}$$

$$\sigma^2\hat{y}_{sh} = -\frac{\mathrm{d}\hat{F}_y}{\mathrm{d}s} - \left[\hat{p}_u(x_{sh}(s, 0), y_{sh}(s, 0)) - \hat{p}_d(x_{sh}(s, 0), y_{sh}(s, 0))\right]\cos\theta(s, 0). \tag{D2e}$$

Equations (D1) and (D2) form a closed system of equations once they are supplemented with the linearized form of the boundary conditions (2.4), (2.7*a*,*b*) and (2.9). While at the fluid–chamber and the fluid–sheet interfaces we have

$$\frac{\partial\hat{\phi}_i}{\partial x}(0, y) = \frac{\partial\hat{\phi}_i}{\partial x}(1-\Delta, y) = 0, \tag{D3a}$$

$$\hat{\phi}_d(x, -L_y/2) = \hat{\phi}_u(x, L_y/2), \tag{D3b}$$

$$\frac{\partial\hat{\phi}_d}{\partial y}(x, -L_y/2) = \frac{\partial\hat{\phi}_u}{\partial y}(x, L_y/2), \tag{D3c}$$

$$\sigma\hat{y}_{sh} + \frac{\partial\hat{\phi}_i}{\partial x}\left[\frac{\partial y_{sh}}{\partial x}(s, 0)\right] = \frac{\partial\hat{\phi}_i}{\partial y}, \tag{D3d}$$

at the edges of the sheet, the boundary conditions are

$$\hat{x}_{sh}(0) = 0, \quad \hat{x}_{sh}(1) = 0, \tag{D4a}$$

$$\hat{y}_{sh}(0) = 0, \quad \hat{y}_{sh}(1) = 0, \tag{D4b}$$

$$\frac{\mathrm{d}\hat{\theta}}{\mathrm{d}s}(0) = 0, \quad \frac{\mathrm{d}\hat{\theta}}{\mathrm{d}s}(1) = 0. \tag{D4c}$$

This completes the linearization of (2.2)–(2.9). The linearized equations (D1)–(D4) always admit the trivial solution, where the eigenfunctions vanish altogether, unless their determinant is equal to zero.

To solve this set of equations for given L_y, Δ and λ, we first obtain numerically the base solution for the position of the sheet, i.e. $\boldsymbol{x}_{sh}(s, 0)$ and $\theta(s, 0)$. Then, we substitute this solution into the linearized equations and discretize them. The discrete equations are solved using a finite-difference scheme for the elastic sheet and a finite-element scheme for the solution of (D1) in the bulk of the fluid.

References

Alben, S. 2008 Optimal flexibility of a flapping appendage in an inviscid fluid. *J. Fluid Mech.* **614**, 355–380.

Alben, S. & Shelley, M.J. 2008 Flapping states of a flag in an inviscid fluid: bistability and the transition to chaos. *Phys. Rev. Lett.* **100**, 074301.

Argentina, M. & Mahadevan, L. 2005 Fluid-flow-induced flutter of a flag. *Proc. Natl Acad. Sci. USA* **102** (6), 1829–1834.

Box, F., O'Kiely, D., Kodio, O., Inizan, M., Castrejón-Pita, A.A. & Vella, D. 2019 Dynamics of wrinkling in ultrathin elastic sheets. *Proc. Natl Acad. Sci. USA* **116** (42), 20875–20880.

Boyko, E., Eshel, R., Gommed, K., Gat, A.D. & Bercovici, M. 2019 Elastohydrodynamics of a pre-stretched finite elastic sheet lubricated by a thin viscous film with application to microfluidic soft actuators. *J. Fluid Mech.* **862**, 732–752.

Butikov, E.I. 1999 The rigid pendulum – an antique but evergreen physical model. *Eur. J. Phys.* **20** (6), 429–441.

Chopin, J., Dasgupta, M. & Kudrolli, A. 2017 Dynamic wrinkling and strengthening of an elastic filament in a viscous fluid. *Phys. Rev. Lett.* **119**, 088001.

Christov, I.C., Cognet, V., Shidhore, T.C. & Stone, H.A. 2018 Flow rate–pressure drop relation for deformable shallow microfluidic channels. *J. Fluid Mech.* **841**, 267–286.

Coene, R. 1992 Flutter of slender bodies under axial stress. *Appl. Sci. Res.* **49** (2), 175–187.

Connel, B.S.H. & Yue, D.K.P. 2007 Flapping dynamics of a flag in a uniform stream. *J. Fluid Mech.* **581**, 33–67.

Diamant, H. 2021 Parametric excitation of wrinkles in elastic sheets on elastic and viscoelastic substrates. *Eur. Phys. J.* E **44** (6), 78.

Drotman, D., Jadhav, S., Sharp, D., Chan, C. & Tolley, M.T. 2021 Electronics-free pneumatic circuits for controlling soft-legged robots. *Sci. Robot.* **6** (51), eaay2627.

Fargette, A., Neukirch, S. & Antkowiak, A. 2014 Elastocapillary snapping: capillarity induces snap-through instabilities in small elastic beams. *Phys. Rev. Lett.* **112**, 137802.

Gomez, M., Moulton, D.E. & Vella, D. 2017 Passive control of viscous flow via elastic snap-through. *Phys. Rev. Lett.* **119**, 144502.

Goriely, A. 2017 *The Mathematics and Mechanics of Biological Growth*, 1st edn. Springer.

Grotberg, J.B. & Jensen, O.E. 2004 Biofluid mechanics in flexible tubes. *Annu. Rev. Fluid Mech.* **36** (1), 121–147.

Guan, X., Nguyen, N., Pocivavsek, L., Cerda, E. & Velankar, S.S. 2023 Flat, wrinkled, or ridged: relaxation of an elastic film on a viscous substrate undergoing continuous compression. *Intl J. Solids Struct.* **275**, 112242.

Guan, X., Sarma, A.P., Hamesh, E.K., Yang, J., Nguyen, N., Cerda, E., Pocivavsek, L. & Velankar, S.S. 2022 Compression-induced buckling of thin films bonded to viscous substrates: uniform wrinkles vs localized ridges. *Intl J. Solids Struct.* **254**, 111843.

Holmes, D.P., Tavakol, B., Froehlicher, G. & Stone, H.A. 2013 Control and manipulation of microfluidic flow via elastic deformations. *Soft Matt.* **9**, 7049–7053.

Hosoi, A.E. & Mahadevan, L. 2004 Peeling, healing, and bursting in a lubricated elastic sheet. *Phys. Rev. Lett.* **93**, 137802.

Ishizaka, K. & Flanagan, J.L. 1972 Synthesis of voiced sounds from a two-mass model of the vocal cords. *Bell Syst. Tech. J.* **51** (6), 1233–1268.

Jiao, S. & Liu, M. 2021 Snap-through in graphene nanochannels: with application to fluidic control. *ACS Appl. Mater. Interfaces* **13** (1), 1158–1168.

Kim, S., Laschi, C. & Trimmer, B. 2013 Soft robotics: a bioinspired evolution in robotics. *Trends Biotechnol.* **31** (5), 287–294.

King, J.R. 1989 The isolation oxidation of silicon. *SIAM J. Appl. Maths* **49** (1), 264–280.

Kodio, O., Goriely, A. & Vella, D. 2020 Dynamic buckling of an inextensible elastic ring: linear and nonlinear analyses. *Phys. Rev.* E **101**, 053002.

Kodio, O., Griffiths, I.M. & Vella, D. 2017 Lubricated wrinkles: imposed constraints affect the dynamics of wrinkle coarsening. *Phys. Rev. Fluids* **2**, 014202.

Krylov, S., Ilic, B.R., Schreiber, D., Seretensky, S. & Craighead, H. 2008 The pull-in behavior of electrostatically actuated bistable microstructures. *J. Micromech. Microengng* **18** (5), 055026.

Lamb, H. 1945 *Hydrodynamics*. Dover.

Landau, L.D. & Lifshitz, E.M. 1986 *Theory of Elasticity*, 3rd edn. Butterworth-Heinemann.

Laskar, A., Manna, R.K., Shklyaev, O.E. & Balazs, A.C. 2022 Computer modeling reveals modalities to actuate mutable, active matter. *Nat. Commun.* **13** (1), 2689.

LEE, C.-Y., CHANG, C.-L., WANG, Y.-N. & FU, L.-M. 2011 Microfluidic mixing: a review. *Intl J. Mol. Sci.* **12** (5), 3263–3287.

LIGHTHILL, M.J. 1960 Note on the swimming of slender fish. *J. Fluid Mech.* **9** (2), 305–317.

LIU, Y.Z., KIM, B.J. & SUNG, H.J. 2004 Two-fluid mixing in a microchannel. *Intl J. Heat Fluid Flow* **25** (6), 986–995.

MANNA, R.K., LASKAR, A., SHKLYAEV, O.E. & BALAZS, A.C. 2022 Harnessing the power of chemically active sheets in solution. *Nat. Rev. Phys.* **4** (2), 125–137.

MATIA, Y. & GAT, A.D. 2015 Dynamics of elastic beams with embedded fluid-filled parallel-channel networks. *Soft Robot.* **2** (1), 42–47.

MUNK, M.M. 1924 The aerodynamic forces on airship hulls. *NACA Tech. Rep.* TR-184.

NEUKIRCH, S., FRELAT, J., GORIELY, A. & MAURINI, C. 2012 Vibrations of post-buckled rods: the singular inextensible limit. *J. Sound Vib.* **331** (3), 704–720.

O'KIELY, D., BOX, F., KODIO, O., WHITELEY, J. & VELLA, D. 2020 Impact on floating thin elastic sheets: a mathematical model. *Phys. Rev. Fluids* **5**, 014003.

OSHRI, O. 2021 Volume-constrained deformation of a thin sheet as a route to harvest elastic energy. *Phys. Rev.* E **103**, 033001.

PANDEY, A., MOULTON, D.E., VELLA, D. & HOLMES, D.P. 2014 Dynamics of snapping beams and jumping poppers. *Europhys. Lett.* **105** (2), 24001.

PEDLEY, T.J., BROOK, B.S. & SEYMOUR, R.S. 1996 Blood pressure and flow rate in the giraffe jugular vein. *Phil. Trans. R. Soc. Lond.* B **351** (1342), 855–866.

POCIVAVSEK, L., YE, S.-H., PUGAR, J., TZENG, E., CERDA, E., VELANKAR, S. & WAGNER, W.R. 2019 Active wrinkles to drive self-cleaning: a strategy for anti-thrombotic surfaces for vascular grafts. *Biomaterials* **192**, 226–234.

PRESTON, D.J., JIANG, H.J., SANCHEZ, V., ROTHEMUND, P., RAWSON, J., NEMITZ, M.P., LEE, W.-K., SUO, Z., WALSH, C.J. & WHITESIDES, G.M. 2019 A soft ring oscillator. *Sci. Robot.* **4** (31), eaaw5496.

ROTHEMUND, P., AINLA, A., BELDING, L., PRESTON, D.J., KURIHARA, S., SUO, Z. & WHITESIDES, G.M. 2018 A soft, bistable valve for autonomous control of soft actuators. *Sci. Robot.* **3** (16), eaar7986.

STROOCK, A.D., DERTINGER, S.K.W., AJDARI, A., MEZIĆ, I., STONE, H.A. & WHITESIDES, G.M. 2002 Chaotic mixer for microchannels. *Science* **295** (5555), 647–651.

THORSEN, T., MAERKL, S.J. & QUAKE, S.R. 2002 Microfluidic large-scale integration. *Science* **298** (5593), 580–584.

WOLFRAM RESEARCH 2018 *Mathematica, Version 11.0*.

ZHANG, W.-M., YAN, H., PENG, Z.-K. & MENG, G. 2014 Electrostatic pull-in instability in MEMS/NEMS: a review. *Sensors Actuators* A **214**, 187–218.

Chapter 3

Semi-implicit IBM within SIMPLE

This chapter is based on: Goncharuk, K., Feldman, Y., & Oshri, O. (2023). *The immersed boundary method: A SIMPLE approach. Journal of Computational Physics*, **487**, 112148.

A semi-implicit direct-forcing immersed boundary method (IBM) is incorporated into the SIMPLE pressure–velocity coupling by treating the body force as a *correction* within the SIMPLE pressure-correction step. This placement exposes a special algebraic structure: the interpolation–spreading composition IR appears in a form that can be approximated efficiently using the locality of the regularised delta and the compact Lagrangian stencil. With this IR simplification, the IBM constraint is enforced while retaining the standard SIMPLE solve sequence and linear operators, so that implementation overhead and cost remain close to a baseline SIMPLE scheme.

The governing equations are the incompressible Navier–Stokes equations in non-dimensional form on a staggered finite-volume grid. Lagrangian markers define the immersed geometry; interpolation I maps Eulerian velocities to the interface and spreading R returns the corrected forces to the grid. Embedding the force update in the pressure-correction stage reduces interfacial leakage and sharpens pressure–boundary coupling without introducing a full implicit monolithic solve. The approach remains robust at practical Courant numbers and is straightforward to integrate into existing SIMPLE codes.

Verification and applicability are demonstrated on two- and three-dimensional benchmarks, including moving bodies. Grid-refinement studies quantify bulk accuracy and interfacial errors, and comparisons with explicit direct forcing show markedly reduced leakage at similar cost. These results motivate the fully implicit

development in Chapter 4, where a Vanka-type smoother and multigrid acceleration are introduced for stronger coupling.

Structure of the article.

1. **Introduction.** Context and motivation for embedding IBM as a force correction inside SIMPLE.
2. **Theoretical background.** Non-dimensional governing equations; Lagrangian–Eulerian coupling; derivation of the SIMPLE-IBM force-correction step with the IR approximation.
3. **Results and discussion.** Applicability on various 2D/3D benchmarks, including moving bodies; accuracy, leakage, and cost relative to explicit forcing.

Journal of Computational Physics 487 (2023) 112148

Contents lists available at ScienceDirect

Journal of Computational Physics

journal homepage: www.elsevier.com/locate/jcp

The immersed boundary method: A SIMPLE approach

Kirill Goncharuk, Oz Oshri, Yuri Feldman *

Department of Mechanical Engineering, Ben-Gurion University of the Negev, P.O. Box 653, Beer-Sheva 84105, Israel

ARTICLE INFO

Article history:
Received 8 September 2022
Received in revised form 29 January 2023
Accepted 11 April 2023
Available online 18 April 2023

Keywords:
Implicit immersed boundary method
Distributed Lagrange multiplier
Schur complement

ABSTRACT

A novel formulation of the direct forcing immersed boundary (IB) method, that treats it as an integral part of a SIMPLE method is presented for the simulation of incompressible flows. The incompressibility and no-slip kinematic constraints are treated implicitly as distributed Lagrange multipliers and are fully coupled with each other by combining them into a single Poisson-body forces system of equations that constitutes a regularized saddle point problem. A physically justified approximation of the system, resembling a technique typical of the penalty method, is carried out to facilitate the solution. By utilizing the Schur complement approach, the approximated system is decomposed into two separate systems of equations, allowing us to compute the values for the volumetric force and pressure corrections. The first system, which is characterized by a small (only $O(10)$) value of the condition number, is conveniently solved by the BiCgStab method [1], converging within 2-3 iterations, while the second system is addressed by the direct TPF solver [2], characterized by $O(N^{4/3})$ complexity. The entire methodology is designed to be highly portable, which facilitates the use of any available solver that was designed to simulate incompressible flows governed by the Helmholtz and Laplace operators but could not benefit from the immersed boundary formalism. The capabilities of the developed methodology applied to the simulation of representative shear- and buoyancy-driven confined flows developing in the presence of stationary immersed bodies are demonstrated. A further application of the developed approach to moving boundary and two-way coupled fluid-structure interaction problems is discussed.

1. Introduction

The immersed boundary (IB) method, initially introduced by Peskin [3] about half a century ago, may perhaps be regarded as the start of the rapidly growing field of computational science that facilitates the numerical simulation of a wide range of physical phenomena, including thermally driven flows, flows developing around solid bodies (either stationary or moving with prescribed kinematics), flows around elastic bodies and within elastic confinements, particulate flows, and two-phase flows, to name but a few. A full list of the application areas of the IB method is far more extensive, and thus, rather than enumerating them, we refer the interested reader to a number of recent review papers [4–7]. Over the years, the IB method has evolved into a number of branches, which can be classified into ghost-cell [8,9], cut-cell [10], sharp interface [11], cut-stencil [12], iso-geometric [13] IB methods, as well as the recently developed shifted boundary method [14,15].

* Corresponding author.
E-mail address: yurifeld@bgu.ac.il (Y. Feldman).

https://doi.org/10.1016/j.jcp.2023.112148
0021-9991/

While some of the above branches resemble the original IB method only vaguely (if at all), in the current paper we focus on the family of IB methods based on the same concepts as those elaborated in the study of [3]. The method, originally designed for the simulation of the fluid-structure interactions (FSI), is based on a number of fundamental concepts. First, two separate grids are defined—a Lagrangian grid for the body surface and a Eulerian grid for the surrounding fluid. Second, the impact of the body on the surrounding flow is reflected by the dynamical response of the body surface obtained by applying constitutive laws, for example, linear springs connecting the Lagrangian points of the surface. As a result, the surface of an immersed body exerts forces on the surrounding fluid, constituting dynamic constraints on the flow. To impose the same velocity on the solid boundary and the fluid adjacent to it, the kinematic constraint of no-slip should be imposed on the surface of the immersed body. Third, as the two grids are not necessarily superimposable, two adjoint operators, namely, the interpolation and the regularization operators, are introduced to convey information on the dynamic and kinematic constraints between the two grids. Both operators are implemented by utilizing discrete Dirac delta functions that satisfy a number of properties so as to provide conservation of the fluid dynamics laws [16]. Finally, the flow field is resolved outside and within the body, although for most configurations flow within the body is considered nonphysical. Again, we refer the interested reader to the excellent review of Mittal and Iaccarino [17], which provides a comprehensive picture of the developments in the field.

Unfortunately, the original IB method [3] cannot be straightforwardly applied to the simulation of the flow around rigid non-deformable immersed bodies. Simply assigning large enough values to the stiffness coefficients of the linear springs connecting the Lagrangian points of the body surface significantly increases the stiffness of the problem, leading to convergence problems and to inaccurate results. The remedy derives from the direct forcing approach, initially introduced by Mohd-Yusof and co-authors [18,19], that allows the kinematic constraint of no-slip to be directly imposed on the immersed boundary without making any assumptions about the dynamics of the system. We note that the earlier versions of the direct forcing approach had relied mostly on the explicit calculation of the forces exerted by the immersed body on the surrounding flow, as this approach requires the introduction of only minimal changes into the solvers of Navier-Stokes (NS) equations. Conceptually, the explicit formulation required applying the available solvers, which were not originally equipped with the IB functionality, in a predictor–corrector manner. The drawbacks of this approach derive from three main factors, namely, the need to proceed in very small time steps to avoid nonphysical flow leaks through the surface of the immersed body, the imposition of the no-slip constraint on the predicted, rather than on the corrected, flow field, and, most importantly, the very fact of violating the elliptic physics of the NS equations. In the original explicit formulation, each force is calculated locally for each Lagrangian point. As a result, the force value is not immediately affected by far distant velocities and, in turn, cannot affect the balance of momentum in far distant locations of the computational domain. The problem becomes critical for unsteady flows characterized by low, $O(10^2)$ and moderate $O(10^3)$ values of the Reynolds number and also in the simulation of dense particulate flows characterized by a large number of collisions between particles taking place in a short period of time.

To address the challenges posed by the explicit formulation of the direct forcing approach, research dedicated to developing its semi- or fully implicit counterparts has been conducted in recent decades. Worth mentioning in this context is the study of Wu and Shu [20], who developed an implicit IB formulation incorporated within the lattice-Boltzmann (LB) method. The authors successfully addressed the elliptic physics of the NS equations by coupling all the Lagrangian forces. At the same time, the calculation of the forces was based entirely on the predicted value of the velocity. In contrast, Taira and Colonius [21] developed a fully implicit IB method. The key idea was to formulate a saddle point problem in which the velocity field is coupled to both the pressure and the Lagrangian forces fields constituting distributed Lagrange multipliers (DLMs) to simultaneously impose incompressibility and no-slip constraints. The system was solved by applying the projection method. That study was then paired with the lattice Green's function to efficiently simulate external flows [22], and more recently it was extended to simulate FSI flows [23]. A similar saddle point formulation was also used for simulating flows around rigid bodies [24–27] and two-phase flows [28,29] and for addressing the FSI configurations of thick deformable bodies [30]. A slightly different semi-implicit formulation coupling Lagrangian forces and heat fluxes with a predicted (i.e. non-divergence free) velocity field was proposed in [31], and subsequently it was used for the investigation of $3D$ moving boundary flows [32] and natural convection confined flows developing around hot and cold cylinders [33,34].

The current study aims at extending the toolbox of available numerical IB frameworks by providing an alternative way of fully coupling between the flow properties and the Lagrangian forces introduced to impose the kinematic constraints of no-slip on the surface of an immersed body. The novel IB formulation described herein shares ideas with the study of Taira and Colonius [21] but at the same time gives a new perspective for the coupling of DLMs and primitive flow variables by adopting the well-known SIMPLE approach of Patankar and Spalding [35]. The key idea is to regard the entire IB method as a SIMPLE approach by coupling between the *corrections* of pressure, velocity and the Lagrangian forces and then utilizing them for imposing both incompressibility and no-slip constraints. As a novel aspect, the developed formulation is reduced to the solution of a Poisson-body forces system of equations constituting a *regularized* saddle point, that can be conveniently transformed into equivalent positive definite system [36]. We then propose a physically justified approximation of the system allowing for immense decrease in memory consumption compared to the previously developed numerical methodologies [31,32]. Additionally, we put an emphasis on the portability of the developed methodology to provide its convenient embedding into any available solvers of the Laplace and Helmholtz equations. A comprehensive verification study was next performed by applying the developed method to the simulation of representative $2D$ and $3D$ steady and supercritical flows. The study is summarized by presenting the efficiency characteristics of the developed methodology and

discussing the steps to be taken for further adapting it for the simulation of moving boundary and two-way coupled FSI configurations.

2. Theoretical background

2.1. Governing non-dimensional equations

We start with a brief formulation of the NS equations governing the incompressible shear- and thermally driven flows considered in the current study. According to the formalism of the IB method, additional volumetric body forces and heat fluxes are introduced into the momentum and energy equations, respectively, constituting the dynamic conditions imposed by the immersed body on the surrounding flow. The equations governing the kinematic constraints of no-slip and a prescribed temperature are then formulated on the surface of the immersed body to achieve closure of the overall system. In summary, the incompressible isothermal shear-driven flow is governed by a system of continuity and NS Eqs. (1):

$$\begin{cases} \nabla\cdot\boldsymbol{u}=0, \\ \dfrac{\partial\boldsymbol{u}}{\partial t}+(\boldsymbol{u}\cdot\nabla)\boldsymbol{u}=-\nabla p+\dfrac{1}{Re}\nabla^2\boldsymbol{u}+\boldsymbol{f}, \\ \boldsymbol{u}_s=\boldsymbol{U}^{\Gamma}, \end{cases} \tag{1}$$

the non-isothermal natural convection flow is governed by a system of continuity, NS and energy Eqs. (2):

$$\begin{cases} \nabla\cdot\boldsymbol{u}=0, \\ \frac{\partial\boldsymbol{u}}{\partial t}+(\boldsymbol{u}\cdot\nabla)\boldsymbol{u}=-\nabla p+\sqrt{\frac{Pr}{Ra}}\nabla^2\boldsymbol{u}+\theta\vec{e}_z+\boldsymbol{f}, \\ \frac{\partial\theta}{\partial t}+(\boldsymbol{u}\cdot\nabla)\theta=\frac{1}{\sqrt{PrRa}}\nabla^2\theta+q, \\ \boldsymbol{u}_s=\boldsymbol{U}^{\Gamma},\theta_s=\theta^{\Gamma}, \end{cases} \tag{2}$$

and the non-isothermal forced convection flow is governed by a system of continuity, NS and energy Eqs. (3):

$$\begin{cases} \nabla\cdot\boldsymbol{u}=0, \\ \frac{\partial\boldsymbol{u}}{\partial t}+(\boldsymbol{u}\cdot\nabla)\boldsymbol{u}=-\nabla p+\frac{1}{Re}\nabla^2\boldsymbol{u}+\frac{Ra}{PrRe^2}\theta\vec{e}_z+\boldsymbol{f}, \\ \frac{\partial\theta}{\partial t}+(\boldsymbol{u}\cdot\nabla)\theta=\frac{1}{PrRe}\nabla^2\theta+q, \\ \boldsymbol{u}_s=\boldsymbol{U}^{\Gamma},\theta_s=\theta^{\Gamma}. \end{cases} \tag{3}$$

The unknown functions introduced into the system of Eqs. (1) are the non-dimensional velocity vector field $\boldsymbol{u}=(u,v,w)$, the pressure field p, and the volumetric force field $\boldsymbol{f}$ exerted by the immersed body on the surrounding flow. $\boldsymbol{u}_s$ corresponds to the values of the velocity components interpolated from the surrounding field $\boldsymbol{u}$ to the surface of the immersed body, $\boldsymbol{U}^{\Gamma}$ is the value of the prescribed non-dimensional velocity of the surface of the immersed body, and t is non-dimensional time. Note that for the rigid stationary immersed bodies considered in the current study, $\boldsymbol{U}^{\Gamma}=0$ on the entire surface of the body. Compared to the system of Eqs. (1), the system of Eqs. (2)-(3) include additional unknown functions θ and q corresponding to the non-dimensional temperature and volumetric heat flux, respectively. $\vec{e}_z$ is a unit vector in the vertical (z) direction. The source term $\theta\vec{e}_z$ appearing in the right-hand side (RHS) of the momentum equation of both systems reflects the effects of buoyancy, as follows from the Boussinesq approximation; θ_s corresponds to the temperature values interpolated from the surrounding field θ to the surface of the immersed body; and θ^{Γ} is the value of the prescribed non-dimensional temperature of the surface of the immersed body.

The normalized system of Eqs. (1) is governed by a single non-dimensional parameter, namely, the Reynolds number, $Re=LU_0/\nu$ (where ν is the liquid kinematic viscosity), resulting from utilizing L, U_0, L/U_0, $\rho{U_0}^2$, and $\rho{U_0}^2/L$ scales for normalizing the length, velocity, time, pressure and force density, respectively. The normalized system of Eqs. (2) is governed by two non-dimensional parameters, namely, the Rayleigh number, $Ra=\frac{g\beta}{\nu\alpha}\Delta TL^3$ (where g is the gravitational acceleration, β is the liquid coefficient of thermal expansion, ΔT is the temperature difference between the maximal and the minimal temperatures of the liquid, and α is the liquid thermal diffusivity) and the Prandtl number, $Pr=\nu/\alpha$, where both numbers are obtained by utilizing L, $\sqrt{g\beta L\Delta T}$, L/U, ρU^2, $\rho U^2/L$ and $\rho C_p\Delta T/(L/U)$ (where C_p is the liquid specific heat capacity) scales for normalizing the length, velocity, time, pressure, and force and heat flux densities, respectively. The normalized system of Eqs. (3) is governed by three non-dimensional parameters, namely, the Reynolds number Re, the Prandtl number Pr, and the Rayleigh number Ra, as defined above, which were obtained by utilizing L, U_0, L/U_0, $\rho{U_0}^2$, $\rho{U_0}^2/L$, and $\rho C_p\Delta T/(L/U_0)$ scales for normalizing the length, velocity, time, pressure, and force and heat flux densities, respectively. For all the simulations presented in this study, a constant value of $Pr=0.7$, corresponding to air, was used.

2.2. Immersed boundary functionality built into the SIMPLE approach

The numerical solution of any system governed by incompressible continuity and NS equations begins with choosing a strategy for pressure-velocity coupling and with the temporal and spatial discretization of the corresponding differential operators. Systems incorporating the IB method functionality must also be provided with ways to calculate additional volumetric body forces and heat fluxes. We first give all the details of the steps taken to solve the system of Eqs. (1) and then continue the discussion by pointing out what needs to be done to extend the developed methodology for solving the systems of Eqs. (2) and (3).

The SIMPLE algorithm [35] (see also Appendix A for a brief description of the SIMPLE algorithm) was used for pressure-velocity coupling and was extended further with a built-in IB method functionality, leading to reformulating the momentum and kinematic constraint equations as:

$$\frac{3\boldsymbol{u}^* - 4\boldsymbol{u}^n + \boldsymbol{u}^{n-1}}{2\Delta t} = -\nabla p^n + \frac{1}{Re}\nabla^2\boldsymbol{u}^* + \boldsymbol{R}[\boldsymbol{F}^n] - (\boldsymbol{u}\cdot\nabla\boldsymbol{u})^n, \tag{4}$$

$$\frac{3\boldsymbol{u}'}{2\Delta t} = -\nabla p' + \boldsymbol{R}[\boldsymbol{F}'], \tag{5}$$

$$\boldsymbol{I}[\boldsymbol{u}^{n+1}] = \boldsymbol{U}^{\Gamma}, \tag{6}$$

where the standard second-order finite volume method [37] and the second-order backward finite difference were utilized for the spatial and temporal discretizations, respectively, and $\boldsymbol{u}'$, p' and $\boldsymbol{F}'$ correspond to corrections of the velocity, pressure, and volumetric force fields, respectively. Compared to the original SIMPLE algorithm [35], the current formulation is extended by the $\boldsymbol{R}[\boldsymbol{F}^n]$ and $\boldsymbol{R}[\boldsymbol{F}']$ terms now included in the RHS of Eq. (4) and Eq. (5), respectively, and by introducing an additional equation, Eq. (6), constituting a kinematic no-slip constraint on the surface of the immersed body. In this extended formulation, $\boldsymbol{R}$ and $\boldsymbol{I}$ correspond to two adjoint operators, namely, the regularization and interpolation operators, introduced to exchange information between the Lagrangian grid (given by a series of Lagrangian points, determining the surface of the immersed body) and the underlying Eulerian grid (typically constituting a uniform structured grid), on which the solution of discretized Eqs. (4) – (6) is obtained. The formal definition of the $\boldsymbol{R}$ and $\boldsymbol{I}$ operators smearing the Lagrangian forces over the underlying Eulerian grid and interpolating velocity components from the Eulerian grid to the Lagrangian points of the immersed body can vary, depending on the specific configuration. We determine the $\boldsymbol{R}$ and $\boldsymbol{I}$ operators by utilizing the discrete Dirac delta functions introduced in [16], as detailed in Appendix B.

Similarly to the original SIMPLE algorithm, $\boldsymbol{u}^*$ is the predicted velocity field obtained by the solution of Eq. (4) utilizing the pressure and volumetric force fields taken from the previous time step. For this reason, the predicted velocity field is non-solenoidal and also does not satisfy the kinematic constraint of no-slip on the surface of the immersed body, so that to proceed to the next time step all the flow fields should be corrected as $\boldsymbol{u}^{n+1} = \boldsymbol{u}^* + \boldsymbol{u}'$, $p^{n+1} = p^n + p'$, and $\boldsymbol{F}^{n+1} = \boldsymbol{F}^n + \boldsymbol{F}'$ to satisfy the fully constrained system of continuity and NS equations. The standard step of the original SIMPLE algorithm [35] is then replaced to convert the continuity equation into an equation for pressure and Lagrangian forces corrections. By taking the divergence of both sides of Eq. (5) and by using $\nabla\cdot\boldsymbol{u}^{n+1} = 0$, we obtain:

$$-\nabla^2 p' + \nabla\cdot\left(\boldsymbol{R}[\boldsymbol{F}']\right) = -\frac{3}{2\Delta t}\nabla\cdot\boldsymbol{u}^*. \tag{7}$$

Eq. (7), obtained in this way, constitutes a modified Poisson equation, which is unclosed, since it contains both p' and $\boldsymbol{F}'$ as unknown fields. Closure is achieved by combining it with the kinematic constraint of no-slip, formulated by Eq. (6), which now requires us to express $\boldsymbol{u}^{n+1}$ in terms of p' and $\boldsymbol{F}'$. The procedure is performed in two steps. In the first step, Eq. (5) is rewritten to express the velocity correction field as:

$$\boldsymbol{u}' = -\frac{2}{3}\Delta t\left(\nabla p' - \boldsymbol{R}[\boldsymbol{F}']\right). \tag{8}$$

In the second step, we exploit the linearity of the interpolation operator $\boldsymbol{I}$ (see Appendix B) with respect to the interpolated fields, so that $\boldsymbol{I}[\boldsymbol{u}^{n+1}] = \boldsymbol{I}[\boldsymbol{u}^*] + \boldsymbol{I}[\boldsymbol{u}']$ and $\boldsymbol{I}\left[-\nabla p' + \boldsymbol{R}[\boldsymbol{F}']\right] = -\boldsymbol{I}[\nabla p'] + \boldsymbol{I}\boldsymbol{R}[\boldsymbol{F}']$. We then reformulate Eq. (6) as:

$$-\boldsymbol{I}[\nabla p'] + \boldsymbol{I}\boldsymbol{R}[\boldsymbol{F}'] = \frac{3}{2}\frac{\boldsymbol{U}^{\Gamma} - \boldsymbol{I}[\boldsymbol{u}^*]}{\Delta t}. \tag{9}$$

Finally, the closed Poisson-body forces system of equations is formulated, and is written in block-matrix form as:

$$\begin{bmatrix} -\nabla^2(\ ) & \nabla\cdot(\boldsymbol{R}[\ ]) \\ \boldsymbol{I}[\nabla(\ )] & -\boldsymbol{I}\boldsymbol{R}[\ ] \end{bmatrix}\begin{bmatrix} p' \\ \boldsymbol{F}' \end{bmatrix} = \begin{bmatrix} -\frac{3}{2\Delta t}\nabla\cdot\boldsymbol{u}^* \\ \frac{3}{2}\frac{\boldsymbol{I}[\boldsymbol{u}^*]-\boldsymbol{U}^{\Gamma}}{\Delta t} \end{bmatrix}. \tag{10}$$

The sequence of operations of the developed algorithm, in order of their execution, is summarized in Table 1.

Note, it is assumed that a single correction of the predicted p^n, $\boldsymbol{u}^n$, and $\boldsymbol{F}^n$ fields at time step n is sufficient to obtain the divergence-free velocity field $\boldsymbol{u}^{n+1}$ and the converged values of both the pressure field p^{n+1} and the Lagrangian forces

Table 1
Sequence of operations for proceeding by a single time step.

1.	Guess or take from the previous time steps p^n, $\boldsymbol{u}^{n,n-1}$, and $\boldsymbol{F}^n$.
2.	Solve the momentum Eq. (4) to obtain $\boldsymbol{u}^*$.
3.	Solve the system of Eqs. (10) to *simultaneously* obtain p' and $\boldsymbol{F}'$ fields.
4.	Calculate $\boldsymbol{u}'$ by using Eq. (8).
5.	Proceed to the next time step by assigning $p^{n+1} = p^n + p'$, $\boldsymbol{u}^{n+1} = \boldsymbol{u}^n + \boldsymbol{u}'$, $\boldsymbol{F}^{n+1} = \boldsymbol{F}^n + \boldsymbol{F}'$.

$\boldsymbol{F}^{n+1}$, as follows from Step 5 of the developed algorithm (see Table 1). This assumption is reasonable for sufficiently small time steps $\Delta t \sim O(10^{-3})$, and initial conditions for the pressure and the velocity fields that would satisfy the momentum and the continuity equations (e.g., assigning zero values to all the flow fields). In fact, for all the configurations analyzed in the current study, the maximum value of $\nabla \cdot \boldsymbol{u}^{n+1}$ was less than 10^{-13}, while the kinematic constraint of no-slip was met up to the value[1] of 10^{-6} immediately after the first correction in any given time step. At the same time for larger time steps or for the direct numerical simulation (DNS) of turbulent flows, it may be necessary to introduce underrelaxation factors along with internal iterations and to repeat steps 1–5 of the algorithm to meet the divergence-free and kinematic constraints of no-slip with the specified accuracy before proceeding to the next time step. For a more explicit discussion regarding the limitations that should be imposed on the time step and underrelaxation values to optimize the convergence of the SIMPLE-family algorithms, Refs. [38,39] should be consulted. It should also be noted that the currently developed methodology allowing us to obtain the pressure and volumetric force corrections in a coupled manner can be adapted with reasonable effort to any derivatives of the SIMPLE approach, e.g., the SIMPLEC, SIMPLER or PISO algorithms described in [40].

2.3. Solution of the momentum equation

Momentum equation Eq. (4) was solved by a solver based on an algorithm implementing the tensor product factorization (TPF) method combined with the Thomas solver [2]. The latter, which is a direct solver, is superior to the commonly used iterative BiCgStab [1] algorithm, when used for obtaining the matrix-vector product of the inverse Helmholtz operator; it has been extensively verified in our previous studies [41,31,32]. With emphasis on the portability of the developed methodology, the solver is utilized in this study in a black-box manner by modifying only the RHS of Eq. (4). In practice, any other solver capable of giving the matrix-vector product of the inverse Helmholtz operator (either exact, e.g. [42], or approximate, e.g. [43]) can be utilized instead.

2.4. Solution of the Poisson-body forces system

The Poisson-body forces system presented in Eq. (10) is similar to that obtained in the study of [21], in the sense that it couples the pressure and the force correction fields, both treated as DLMs to simultaneously satisfy the incompressibility and no-slip constraints, respectively. Nonetheless, there is a major difference between the two approaches in that the system developed in this study contains an operator $\boldsymbol{IR}$ located in the right bottom corner of the system of Eq. (10) and acting on the force corrections $\boldsymbol{F}'$. Thus, the current formulation constitutes a regularized saddle point problem, with a convenient solution to this problem being the most important contribution of the developed methodology. The role of the $\boldsymbol{IR}$ operator will be discussed in detail below (we note here that the presence of this operator significantly facilitates the solution of the problem).

We also note that the specific aim of the current study is to address the most challenging configuration arising when simulating confined flows. In this case, the Neumann boundary conditions are imposed on the pressure (or pressure correction) fields at the solid boundaries. As a result, the Poisson-body forces system is, on the one hand, too poorly conditioned to be efficiently solved by using Krylov space iterative methods (e.g., BiCgStab [1]), and, on the other hand, too large to be handled by a sparse direct solver (e.g., MUMPS [44,45]) for realistic 3D configurations. An additional challenge is that the problem is stationary, so that the Tailor series expansion of the inverse Laplacian in Δt, as discussed in [43] for the simulation of general incompressible flows and further extended in [21] by coupling it with the IB method formalism, cannot be directly implemented. The solution to this problem lies in preconditioning the Laplacian with its approximate inverse, as was proposed by [43] and successfully implemented by [25]. Recalling, however, that in the framework of the current study the focus is on the portability of the developed IB method (i.e., the use of previously developed solvers that do not have the immersed boundary capability in a black-box manner), we propose an alternative way of solving the Poisson-body forces system of equations based on a physically justified approximation of the matrix-vector product of operator $\boldsymbol{IR}$.

2.4.1. Approximation of the matrix-vector product of operator $\boldsymbol{IR}$

The impact of the $\boldsymbol{IR}$ operator can be quantified by obtaining the product of matrix $\boldsymbol{I}$ by matrix $\boldsymbol{R}$, each containing the "weights" determined by the distances between the corresponding locations of the Lagrangian and Eulerian grid points and

[1] Additional details for meeting the kinematic constraint of no-slip are given in section 2.4.2.

calculated by utilizing the discrete Dirac delta function [16]. Note that despite the fact that $\boldsymbol{I}$ and $\boldsymbol{R}$ operators are adjoint to each other, the two matrices are not reciprocal, so their product is not an identity matrix. In reality, however, it would be preferable to avoid explicit building and multiplication of the $\boldsymbol{I}$ and $\boldsymbol{R}$ matrices when calculating the product of $\boldsymbol{IR}$ by the vector of force corrections $\boldsymbol{F}'$; such a calculation could be very costly for realistic $3D$ configurations containing $O(10^5)$ or even more Lagrangian points. To develop a formally justified approximation of the above matrix-vector product, we next focus on the fact that if the same discrete Dirac delta functions are used in the interpolation $\boldsymbol{I}$ and regularization $\boldsymbol{R}$ operators, the sum of each row (or each column) of the matrix $\boldsymbol{IR}$ is equal to some constant λ. This property is a direct consequence of the so-called "sum of squares rule" imposed by [46] when constructing any discrete Dirac delta function:

$$\Sigma_i[\phi(r-i)]^2 = \lambda, \forall r, \tag{11}$$

where all the summations are performed for the integers i, such that $-\infty < i < +\infty$ and λ is some constant. The need for Eq. (11) arises in situations where a quantity in a specific Lagrangian point is first regularized to the underlying Eulerian grid and the resulting field is interpolated back to the same Lagrangian point. The rule grantees that the result is independent of the position of the Lagrangian point relative to the Eulerian grid. For the currently used discrete Dirac delta function [16], this constant is equal to $\lambda = 0.5$.[2] Note, too, that the above rule is also preserved when function ϕ is utilized in $2D$ and $3D$ discrete Dirac delta functions. Therefore, the result of applying the operator $\boldsymbol{IR}$ to any uniform field is the field itself multiplied by a factor of 0.5, as follows straight forwardly from Eq. (11). Although the realistic force corrections vector $\boldsymbol{F}'$ is not uniform, it is still possible to use the above property and to approximate the product $\boldsymbol{IR} \times \boldsymbol{F}'$ based on the following observations:

- **Compact support of the *IR* operator.** As a result of the compact support of ϕ (only one and a half grid points in each direction), matrices $\boldsymbol{I}$ and $\boldsymbol{R}$ are extremely sparse, with a typical row containing only a few hundred non-zero entries, while the dimension of a typical row of the $\boldsymbol{IR}$ matrix is $O(10^5)$ for realistic $3D$ configurations. The matrix $\boldsymbol{IR}$, which couples between all the Lagrangian quantities, is also sparse, because only a very narrow neighborhood of the Eulerian grid is affected by the regularized Lagrangian quantities that are in close proximity to each other (since $\boldsymbol{R}$ is sparse) and, in turn, a very limited number of the Eulerian quantities simultaneously affect the given Lagrangian point by interpolation (since $\boldsymbol{I}$ is sparse).
- **Smoothing properties of the *IR* operator.** When calculated implicitly, the kinematic constraints suffer from spurious oscillations in the volumetric (or surface) forces (or heat fluxes). The observed inaccuracies stem from the ill-posed integral equation of the first kind for the surface stresses utilizing discrete smeared Dirac delta functions, as detailed in [23]. The same study proposed an efficient technique to filter out high frequencies and to converge the surface stresses and forces to physically correct parameters acting on the surface of the immersed body. Remarkably, an effect similar to filtering out the high-frequency oscillations can be achieved by applying the product of the $\boldsymbol{IR}$ operator to the vector of kinematic constraints. To demonstrate this effect, we analyzed the representative fields of the force density corrections F'_x and F'_y by taking a snapshot of the flow developing around a cylinder placed within the lid-driven cavity (one of the numerical experiments described below) at $Re = 100$ obtained on 100^2 grid with $\Delta x = \Delta y = 10^{-2}$. The fields represented by black solid lines in Figs. 1 (a) and (b), suffer from spurious oscillations. In addition to the obtained F'_x and F'_y distributions, we present their smoothed counterparts (both indicated by solid red lines) obtained by calculating the $2\boldsymbol{IR} \times F'_x$ and $2\boldsymbol{IR} \times F'_y$ products.[3] These products determine the actual (physically correct) contribution of the Lagrangian quantities to the $\boldsymbol{IR} \times \boldsymbol{F}'$ term, entering Eq. (10), discretized on the Eulerian grid; i.e. due to the inclusion of the $\boldsymbol{IR}$ term into the currently developed IB formulation, the field actually contributed by the force density corrections is smooth (for sufficiently regular geometries) and can be approximately considered as piece-wise constant in the vicinity of each Lagrangian point for a reasonably dense grid resolution.

As follows from the above discussion, the action operator $\boldsymbol{IR}$ is local (i.e., affects only the quantities in a small number of neighboring Lagrangian points), and its product by the implicitly obtained field of kinematic constraints containing high-frequency oscillations can be approximated by replacing the original field with its smoothed counterpart. In practice, this allows us to replace the operator $\boldsymbol{IR}$ with a $\frac{1}{2}\mathbf{I}$ matrix (where $\mathbf{I}$ is the identity matrix) by assuming that the values of the smoothed Lagrangian quantities located in close proximity are approximately the same. Note that the obtained result can be seen as a generalization of the approximation recently proposed in [47,48] for the explicit formulation of the IB method. The approximate form of the Poisson-body forces system can thus be written as:

$$\begin{bmatrix} -\nabla^2(\ ) & \nabla\cdot(\boldsymbol{R}[\ ]) \\ \boldsymbol{I}[\nabla(\ )] & -\frac{1}{2}\mathbf{I} \end{bmatrix} \begin{bmatrix} p' \\ \boldsymbol{F}' \end{bmatrix} = \begin{bmatrix} -\frac{3}{2\Delta t}\nabla\cdot\boldsymbol{u}^* \\ \frac{3}{2}\frac{\boldsymbol{I}[\boldsymbol{u}^*]-\boldsymbol{U}^\Gamma}{\Delta t} \end{bmatrix}. \tag{12}$$

[2] See Refs. [46,16] for the full list of rules that should be imposed when constructing discrete Dirac delta function.

[3] The results were multiplied by a factor of 2 to make the visual comparisons easier.

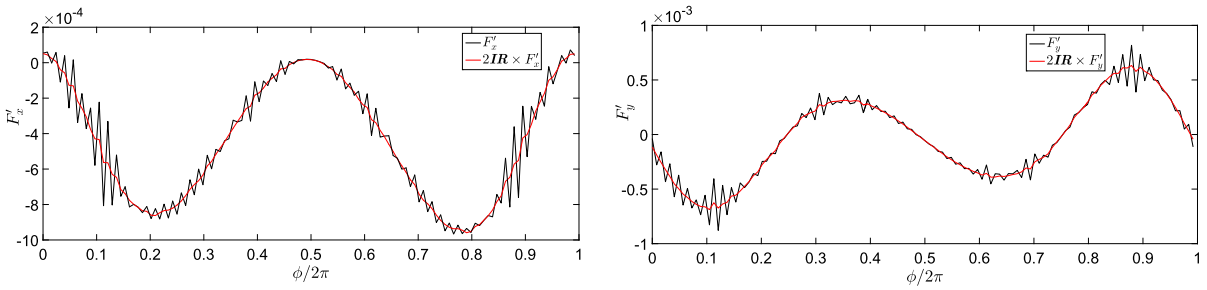

Fig. 1. The force correction density as a function of the angle on the surface of the cylinder immersed within lid-driven cavity flow: (a) in the x direction; (b) in the y direction. Black solid lines correspond to the original force correction density values, as obtained from the simulation. Red solid lines correspond to a processed force correction density field obtained by doubling the product of the $\boldsymbol{IR}$ operator by the original F'_x and F'_y fields. (For interpretation of the colors in the figure(s), the reader is referred to the web version of this article.)

Note that the structure of the system of Eqs. (12) is typical of the systems solved by the penalty method. However, unlike the penalty method, which replaces the solution of an originally constrained problem with a series of solutions of unconstrained problems and for which the value of the constant multiplying the identity matrix is not obvious, the system of Eq. (12) is constrained, albeit approximated, and the $-\frac{1}{2}\mathbf{I}$ term has a physical basis. In all numerical experiments performed in the framework of the current study, the solution of both forms of the Poisson-body forces system, i.e., Eq. (10) and Eq. (12), yielded similar results, although the solution of the approximated system was characterized by much lower memory consumption and much faster convergence, as detailed below.

2.4.2. Numerical procedure

An important feature of the developed algorithm is that discretization of both $\nabla \cdot (\boldsymbol{R}[\,])$ and $\boldsymbol{I}[\nabla(\,)]$ operators is implemented implicitly, thereby constituting an additional challenge compared, for example, to implicit implementation of the interpolation $\boldsymbol{I}$ and regularization $\boldsymbol{R}$ operators commonly used in previous studies, see e.g. [21,25,31]. Implicit discretization of the $\nabla \cdot (\boldsymbol{R}[\,])$ and $\boldsymbol{I}[\nabla(\,)]$ operators can be implemented by using different strategies. The strategy implemented by us for simulating a 2D lid-driven cavity flow with an embedded cylinder, as appears in the complementary material, is based on the subtraction of two matrices. The key idea is to arrange the force weights contributed by each Lagrangian point into a single matrix, the first dimension of which is equal to the total number of Lagrangian points, and the second dimension, is equal to the total number of Eulerian cells. The divergence can then be conveniently obtained by subtracting the corresponding rows (in accordance with the global numbering of the velocity field) of the matrices so constructed. Note that the above procedure must be repeated for each velocity component. Utilizing the above strategy for a 3D configuration can be very costly in terms of memory consumption. The straightforward way to remedy the memory limitation, in this case, is to decompose the 3D domain into 2D sections and repeat the procedure described above separately for each section.

For the sake of conciseness, let us now denote the following: the Laplace operator acting on the pressure corrections field and taken with a negative sign as $-\nabla^2(\,) \equiv \boldsymbol{L}$; the divergence acting on the force corrections field regularized from the surface of the immersed body as $\nabla \cdot (\boldsymbol{R}[\,]) \equiv \boldsymbol{B}^T$; and the $-\boldsymbol{IR}$ operator acting on the regularized force corrections field and its approximation entering Eq. (12) as $-\boldsymbol{IR}[\,] \equiv \boldsymbol{C}$ and $-\frac{1}{2}\mathbf{I} \equiv \boldsymbol{C}$, respectively. It should be noted that $\nabla \cdot (\boldsymbol{R}[\,])$ and $\boldsymbol{I}[\nabla(\,)]$ are determined by transpose matrices when the same discrete Dirac delta functions are used by the regularization and interpolation operators. By following the above notation, the Poisson-body forces system can be reformulated as:

$$\begin{bmatrix} \boldsymbol{L} & \boldsymbol{B}^T \\ \boldsymbol{B} & \boldsymbol{C} \end{bmatrix} \begin{bmatrix} p' \\ \boldsymbol{F}' \end{bmatrix} = \begin{bmatrix} RHS_{p'} \\ RHS_{\boldsymbol{F}'} \end{bmatrix}. \tag{13}$$

For $2D$ configurations, the system of Eqs. (13) can be conveniently solved by utilizing a direct sparse solver, e.g., by performing LU decomposition, as demonstrated by the MATLAB script provided in the complementary material. For $3D$ configurations, however, the above system is severely ill conditioned, and thus cannot be solved by the direct solver. Instead, we utilize a Schur complement approach to decompose the system of Eqs. (13) and to separately calculate the $\boldsymbol{F}'$ and p' fields by:

$$\begin{cases} \boldsymbol{F}' = (\boldsymbol{B}\boldsymbol{L}^{-1}\boldsymbol{B}^T - \boldsymbol{C})^{-1}(\boldsymbol{B}\boldsymbol{L}^{-1}RHS_{p'} - RHS_{\boldsymbol{F}'}), \\ p' = \boldsymbol{L}^{-1}(RHS_{p'} - \boldsymbol{B}^T\boldsymbol{F}'). \end{cases} \tag{14}$$

It should be stressed that there is no need to explicitly calculate an inverse of any matrix at any stage of the solution. In fact, $\boldsymbol{B}\boldsymbol{L}^{-1}\boldsymbol{B}^T$ is built by solving a Laplace problem for each column of $\boldsymbol{B}^T$ and then immediately multiplying matrix $\boldsymbol{B}$ by the obtained vector. In this way, the building of intermediate large matrix $\boldsymbol{L}^{-1}\boldsymbol{B}^T$ is avoided [31]. Note that this most time-

consuming part of the algorithm can be pre-computed once at the beginning of the simulation.[4] This part of the algorithm is also "embarrassingly parallel" in the sense that the $\boldsymbol{BL}^{-1}\boldsymbol{B}^T$ product can be calculated independently for different columns of $\boldsymbol{B}^T$ on different servers without the need for the explicit use of MPI, so that the overall process speedup is linear if the same hardware is used. Although the resulting small matrix $\boldsymbol{BL}^{-1}\boldsymbol{B}^T$ should be collected in a single server at the end of the calculation, this procedure is performed only once before the time integration process starts. The products $\boldsymbol{BL}^{-1}RHS_{p'}$ and $\boldsymbol{L}^{-1}(RHS_{p'}-\boldsymbol{B}^T\boldsymbol{F}')$ are again calculated by solving the Laplace problem and by utilizing sparse matrix-vector multiplications, as detailed in [31,32]. In all the currently performed numerical experiments, the Laplace problem was solved by applying the TPF solver[5] [2].

We now discuss a strategy for solving a system of equations containing the $[(\boldsymbol{BL}^{-1}\boldsymbol{B}^T-\boldsymbol{C})]$ operator. According to our previous experience [31], the matrix $[(\boldsymbol{BL}^{-1}\boldsymbol{B}^T]$ is always full of non-zero entries, the vast majority of which are very small ($O(10^{-16})$ and smaller). Storing all these entries is prohibitively expensive for realistic $3D$ configurations. For this reason, a sparsing threshold was set such that values below it are not stored in the $[\boldsymbol{BL}^{-1}\boldsymbol{B}^T]$ matrix. The value of the sparsing threshold can vary for each problem and depends on the specific discrete Dirac delta functions utilized. As a rule of thumb, the sparsing threshold should be at least 4–5 orders of magnitude less than the absolute value of the maximal entry of the matrix $[\boldsymbol{BL}^{-1}\boldsymbol{B}^T]$. For a more formal choice of the sparsity threshold value, one should make sure that the error of meeting the kinematic constraint of no-slip is less than the discretization error of the currently used method. In fact, in all the numerical experiments performed in the current study, the threshold value for the solution of the system of Eq. (14) was set to 10^{-3}. For this threshold, the kinematic constraint of no-slip was met up to 10^{-6} and 10^{-7} for $\Delta t=5\times10^{-3}$ and $\Delta t=10^{-3}$, respectively, so that it is indeed bounded by the discretization error of the currently utilized second-order (in time and in space) finite volume method.

After the matrix $[\boldsymbol{BL}^{-1}\boldsymbol{B}^T]$ has been built, the operator $[\boldsymbol{BL}^{-1}\boldsymbol{B}^T-\boldsymbol{C}]$ can be calculated by simply subtracting the two matrices. A very important observation here is that a non-zero matrix $\boldsymbol{C}$ allows for stabilization of the above system. Further approximation of $\boldsymbol{C}$ as $\boldsymbol{C}=-\frac{1}{2}\boldsymbol{I}$ allows to significantly increase the main diagonal of the operator $[(\boldsymbol{BL}^{-1}\boldsymbol{B}^T-\boldsymbol{C})]$, which turns it into well-conditioned matrix, characterized by a small (only $O(10)$) value of the condition number. As a result, the system of equations can be conveniently solved by applying the BiCgStab [1] method, which converges in no more than 3 iterations to the value of $l_\infty\le10^{-9}$ of the infinity norm of the error. Another alternative for the solution of the above system is to apply the MUMPS [44,45] direct solver for performing the LU decomposition of the $[\boldsymbol{BL}^{-1}\boldsymbol{B}^T-\boldsymbol{C}]$ matrix. The LU factors can be then stored on the computer hard disk and read when necessary by employing the MUMPS functionality. As a result of the intrinsically sequential nature of the back substitution procedure, as implemented in MUMPS, this strategy has been found attractive only for moderate grid resolutions, not exceeding 200 grid points in each direction.

Summarizing the above discussion, we note that the approximation $\boldsymbol{C}=-\frac{1}{2}\boldsymbol{I}$ both provided an accurate meeting of all no-slip kinematic constraints and resulted in adequate sparsity of both the $[\boldsymbol{BL}^{-1}\boldsymbol{B}^T-\boldsymbol{C}]$ matrix and its LU factors. In addition, the first equation of the system of Eqs. (14) can be conveniently solved by applying the BiCgStab method, which demonstrates rapid convergence when the above approximation of matrix $\boldsymbol{C}$ is utilized. This is in contrast to the exact implementation $\boldsymbol{C}=\boldsymbol{IR}$, which, on the one hand, resulted in very high memory consumption when storing the corresponding LU factors required by the direct solver and, on the other hand, suffered from a poor convergence of the iterative solution performed by the BiCgStab method.

2.5. Simulation of natural convection flow

In this section, we briefly describe the procedure that must be followed to solve a system of equations Eqs. (2) and (3). We detail the steps that must be taken to solve the system of Eqs. (2). The system of Eqs. (3) is solved analogously. Following the same procedure as that performed for the NS equations governing isothermal flow (see Eq. (1)), Eqs. (2) governing natural convection flow may be rewritten in the semi-discrete form as:

$$\frac{3\theta^{n+1}-4\theta^n+\theta^{n-1}}{2\Delta t}=\frac{1}{\sqrt{PrRa}}\nabla^2\theta^{n+1}+\boldsymbol{R}(Q^{n+1})-(\boldsymbol{u}\cdot\nabla\theta)^n, \tag{15}$$

$$\boldsymbol{I}[\theta^{n+1}]=\Theta^{\Gamma}, \tag{16}$$

$$\frac{3\boldsymbol{u}^*-4\boldsymbol{u}^n+\boldsymbol{u}^{n-1}}{2\Delta t}=-\nabla p^n+\sqrt{\frac{Pr}{Ra}}\nabla^2\boldsymbol{u}^*+\boldsymbol{R}[\boldsymbol{F}^n]+\theta^{n+1}\vec{e}_z-(\boldsymbol{u}\cdot\nabla\boldsymbol{u})^n, \tag{17}$$

$$\frac{3\boldsymbol{u}'}{2\Delta t}=-\nabla p'+\boldsymbol{R}[\boldsymbol{F}'], \tag{18}$$

$$\boldsymbol{I}[\boldsymbol{u}^{n+1}]=\boldsymbol{U}^{\Gamma}, \tag{19}$$

where Eqs. (15) and (16) govern for the energy equation and the kinematic constraint of the temperature prescribed on the surface of the immersed body, and Eqs. (17)–(19) govern the momentum equation in the SIMPLE [35] formulation and the

[4] The pre-computing can be done for stationary geometries. For moving bodies, different strategies can be adopted, see e.g. [32]).

[5] Any other Laplace equation solver (exact or approximate, direct or iterative) can be used instead.

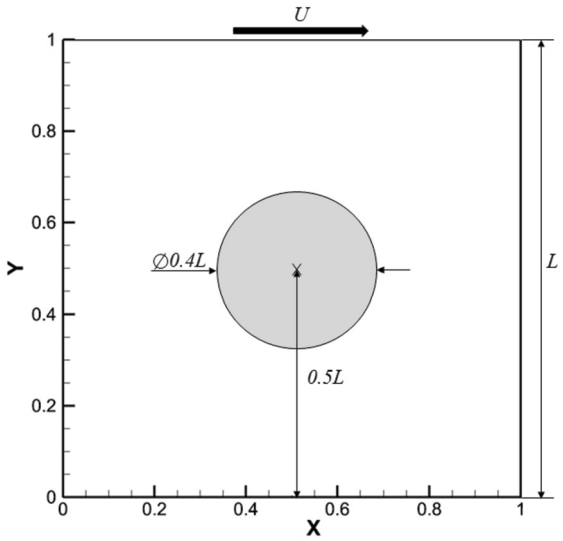

Fig. 2. $2D$ lid-driven cavity with an embedded cylinder in the center – physical model.

kinematic constraint of no-slip on the surface of the immersed body. Note that utilizing the above temporal discretization allows us to decouple the energy and the momentum equations and to solve them separately in each time step. Similarly to the isothermal configuration, the standard second-order finite volume method [37] and the second-order backward finite difference were utilized for the spatial and temporal discretizations, respectively. Eqs. (15) and (16) can be written in a compact block-matrix form as:

$$\begin{bmatrix} \boldsymbol{H} & \boldsymbol{R} \\ \boldsymbol{I} & 0 \end{bmatrix} \begin{bmatrix} \theta^{n+1} \\ Q \end{bmatrix} = \begin{bmatrix} RHS^{n-1,n} \\ \Theta^{\Gamma} \end{bmatrix}, \tag{20}$$

where $\boldsymbol{H} = (\frac{3}{2\Delta t}(\theta^{n+1}) - \frac{1}{\sqrt{PrRa}}\nabla^2(\theta^{n+1}))$ is the Helmholtz operator. The saddle node problem governed by Eq. (20) is then solved by applying Schur complement decomposition, leading to:

$$\begin{cases} Q = [\boldsymbol{I}\boldsymbol{H}^{-1}\boldsymbol{R}]^{-1}[\boldsymbol{I}\boldsymbol{H}^{-1}RHS^{n-1,n} - \Theta^{\Gamma}], \\ \theta = \boldsymbol{H}^{-1}[RHS^{n-1,n} - \boldsymbol{R}[Q]]. \end{cases} \tag{21}$$

As described above, the TPF method combined with the Thomas solver [2] is utilized for obtaining all the required matrix-vector products of the inverse Helmholtz operator and for pre-computing the $[\boldsymbol{I}\boldsymbol{H}^{-1}\boldsymbol{R}]$ matrix. In this case, the sparsing threshold was set to 10^{-10} when filling the $[\boldsymbol{I}\boldsymbol{H}^{-1}\boldsymbol{R}]$ matrix. In all the currently performed numerical experiments, it was verified that the infinity norm of the error obtained when enforcing the kinematic constraint of the temperature prescribed on the surface of the immersed body was $l_\infty \leq 10^{-8}$, which is bounded by the temporal and the spatial discretization errors of the applied finite volume method. The subsequent solution steps employed LU factorization of the pre-computed $[\boldsymbol{I}\boldsymbol{H}^{-1}\boldsymbol{R}]$ matrix, which was performed by utilizing the MUMPS solver. For a more detailed description of all the stages involved in solving the system of Eqs. (20), our previous study [31] should be consulted. After the temperature field θ^{n+1} had been obtained by the solution of the system of Eqs. (20), it was then used when building the RHS of Eq. (17). In the subsequent step, Eqs. (17)–(19) were solved in the same sequence as that used when solving Eqs. (4)–(6), as described above.

3. Results and discussion

3.1. 2D lid-driven cavity with an embedded cylinder

The flow developing within square lid-driven cavity of side L with a cylinder of diameter $0.4L$ placed in the geometrical center of the cavity is examined (see Fig. 2). The top lid of the cavity moves with constant velocity U in the x direction, while all other cavity boundaries and the cylinder are stationary. Table 2 summarizes the verification study of the developed $2D$ solver applied to the simulation of lid-driven cavity flow (without an embedded cylinder) at $Re = 1000$. The obtained flow characteristics are compared with the data available in the literature. The criterion for reaching the steady-state solution was $l_\infty \leq 10^{-5}$ of the infinity norm calculated for the relative deviation between two consecutive time steps for all the flow variables. It can be seen that the obtained values of the maximal and minimal velocities and their spatial locations are in excellent agreement with the independent results, which successfully verifies the developed $2D$ solver.

We next present the results of the grid independence study for the lid-driven cavity with an embedded cylinder of diameter $0.4L$ placed in the cavity center. The simulations were performed for three different Re values on three different

Table 2
Comparison of the flow characteristics obtained for the flow within 2D lid-driven cavity, $Re = 1000$.

	Grid	u_{min}	y_{min}	v_{max}	x_{max}	v_{min}	x_{min}
Ref. [49]	128^2	-0.3653	0.1744	0.3547	0.1506	-0.4824	0.9037
Ref. [50]	129^2	-0.3829	0.1719	0.3710	0.1563	-0.5155	0.9063
Ref. [51]	256^2	-0.3883	0.1698	0.3768	0.1564	-0.5270	0.9088
Current study	512^2	-0.3865	0.1719	0.3749	0.1582	-0.5247	0.9082

Table 3
Results of a grid independence study performed for $2D$ lid driven-cavity flow with a cylinder of diameter $D = 0.4$ embedded in the center at three different Re values.

	Re=1000			Re=5000			Re=8000		
Grid	u_{min}	v_{min}	v_{max}	u_{min}	v_{min}	v_{max}	u_{min}	v_{min}	v_{max}
128^2	-0.3382	-0.4568	0.3253	-0.4057	-0.5142	0.3913	-0.4017	-0.5002	0.3920
256^2	-0.3434	-0.4638	0.3297	-0.4290	-0.5426	0.4125	-0.4358	-0.5435	0.4238
512^2	-0.3448	-0.4651	0.3309	-0.4357	-0.5508	0.4189	-0.4469	-0.5570	0.4336

Table 4
Comparison of the oscillation frequencies f obtained for different Re values.

	$Re = 8600$	$Re = 8700$	$Re = 8800$
Current	0.491	0.489	0.489
Ref. [51]	0.519	0.519	0.519
Rel. Dev. [%]	5.395	5.780	5.780

grids, with grid resolution being doubled each time. It can be seen that the relative deviations between the corresponding extreme values of all the velocity components obtained on 256^2 and 512^2 grids do not exceed 0.5%, 1.5% and 2.5% for the values of $Re = 1000, 5000$, and 8000, respectively, which successfully verifies the grid independence of the results obtained on both grids. See Table 3.

Based on the above analysis, all the time consuming simulations of supercritical flow regimes were performed on a uniform 256^2 grid, while less time consuming simulations of steady state flows, were conducted on a 512^2 grid.

To prevent ill-conditioning, the space between the Lagrangian points on the cylinder surface was almost the same (to within 5%) as that of the Eulerian grid. The obtained characteristics of the steady-state flow are presented in Fig. 3 in terms of streamlines and contours of the velocity magnitude for the values of $Re = 100, 500, 1000, 5000$ and 8000. Both flow characteristics are similar qualitatively and quantitatively to the corresponding data reported in Refs. [51,52].

Thereafter, we calculated the vorticity fields $\boldsymbol{\omega} = \nabla \times \boldsymbol{u}$ for $Re = 1000, 5000$ and 8000. Those vorticity fields, presented in Fig. 4, are in good qualitative agreement with the corresponding data reported in [51,53]. We confirmed the presence of a number of secondary eddies at the top left corner and both bottom corners of the cavity. Unfortunately, it was impossible to conduct a quantitative comparison of extreme vorticity values, since the data presented in [51] is not grid independent. In addition, we performed a quantitative comparison between the values of the u_x and u_y velocity components along the vertical and horizontal centerlines of the cavity, respectively, as obtained in this study for the value of $Re = 1000$, and the corresponding values reported in [52,54], which were acquired by photogrammetry. The data shown in Fig. 5 shows excellent agreement between our results and the independent results of both studies. The work performed in this section is summarized by comparison between our results and the independent results obtained in Ref. [51] for supercritical flow regimes. Fig. 6 presents the time evolutions of the u_x velocity component and the corresponding frequency spectra measured at the control point (0.9,0.1) for the values of $Re = 8600, 8700$, and 8800. The supercritical flow is governed by single oscillating harmonics, indicating that the flow undergoes Hopf bifurcation during the transition from subcritical to supercritical flow regimes. The multipliers of the main harmonics, resulting from the non-linearity of the supercritical flow, are clearly recognizable. Remarkably, there was a small decrease in the oscillating frequency value when moving from $Re = 8600$ to $Re = 8700$. A further increase to $Re = 8800$ did not result in any variation of the oscillating frequency value of the main harmonics. Surprisingly, there were large differences between our results and the values of the u_x signals acquired at the control point (0.9,0.1) reported in [51]. Despite this unexplained observation, acceptable agreement (no more than 6% discrepancy) was obtained between the two sets of results with respect to the frequency spectra values (see Table 4), as expected for slightly supercritical flows; this agreement successfully verifies the developed solver.

3.2. 2D laminar mixed convection flow in a lid-driven cavity with an embedded cylinder

Mixed convection flow in a square lid-driven cavity of side L with an embedded circular cylinder of diameter $0.4L$ placed in the center of the cavity is considered (see Fig. 7). The top lid of the cavity moves with a constant horizontal velocity

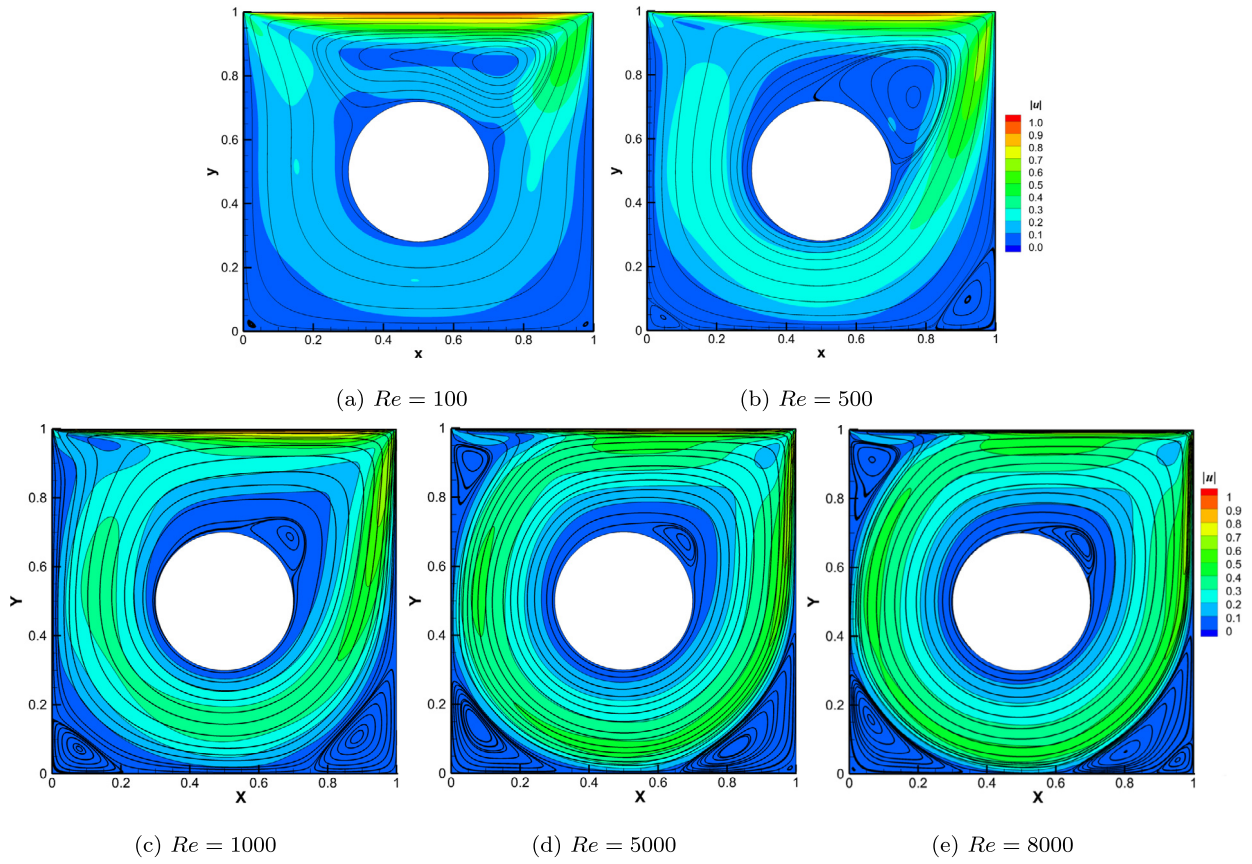

(a) $Re = 100$ (b) $Re = 500$

(c) $Re = 1000$ (d) $Re = 5000$ (e) $Re = 8000$

Fig. 3. Streamlines and contours of the velocity magnitude obtained for five different Re values, $Re = 100, 500, 1000, 5000, 8000$.

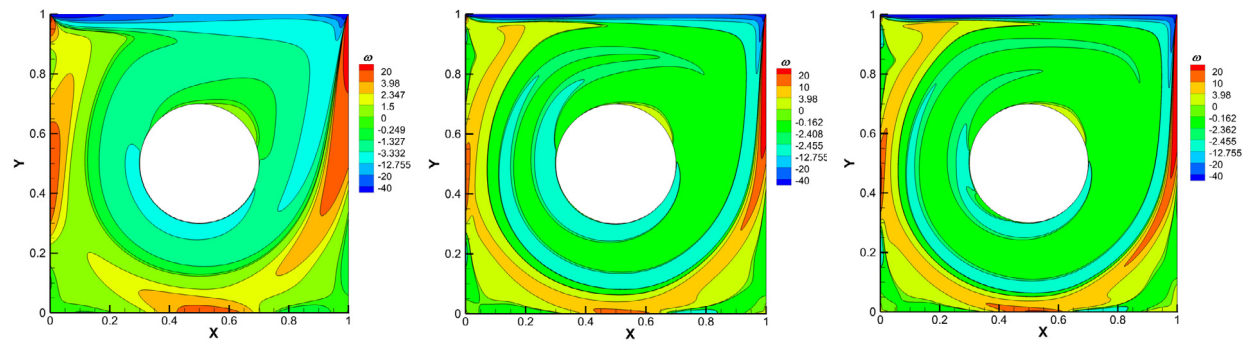

(a) $Re = 1000$ (b) $Re = 5000$ (c) $Re = 8000$

Fig. 4. Vorticity contours obtained for three different Re values.

U, while all other walls are stationary. In addition, the bottom and the top walls of the cavity are held at constant hot θ_H and cold θ_C temperatures, respectively, while both vertical walls are thermally insulated. Gravity acts in the negative direction of the y axis. The cylinder surface is either held at constant cold temperature θ_C or thermally insulated. Starting with performing a grid independence study, we conducted the simulations on 50^2, 100^2 and 200^2 grids for the isothermal cold cylinder. The grid convergence of the results was verified in terms of comparison of the values of the $\overline{Nu}$ number averaged over the surface of the cylinder, as presented in Table 5. The results were obtained for four different values of the Richardson, $Ri = Ra/PrRe^2$, number, $Ri = 0.01, 1, 5$, and 10. It can be seen that the maximal deviation of the $\overline{Nu}$ values obtained on 100^2 and 200^2 grids does not exceed 0.4%, which successfully verifies the grid independence of the results. Therefore, all the results presented in this section for a cylinder with an isothermal surface were obtained on a 200^2 grid. For the adiabatic cylinder configuration, whose simulation requires an explicit calculation of the temperature gradient on the surface of the cylinder [55], we used even denser 300^2 grids. The contours of the temperature obtained for the isothermal

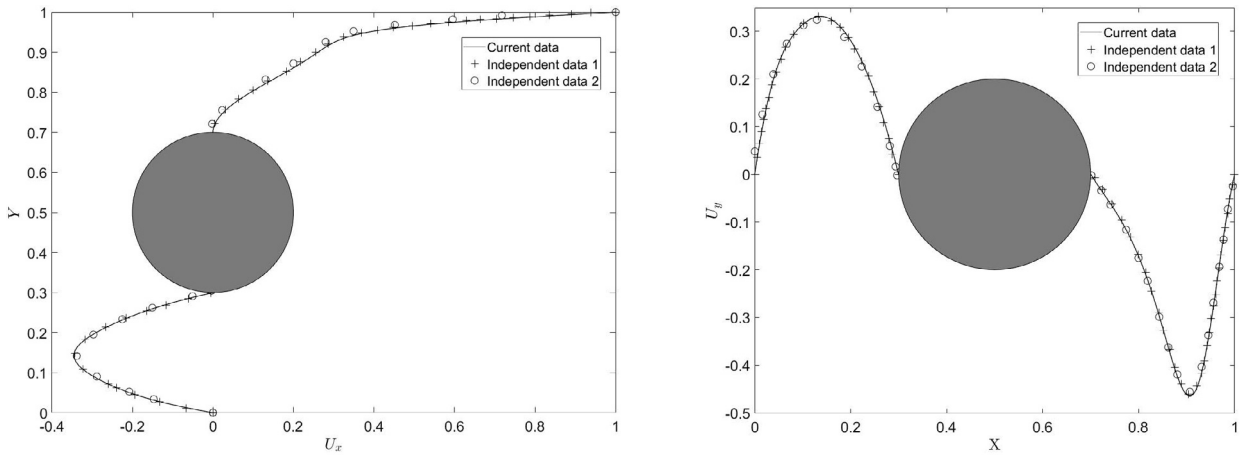

(a) (b)

Fig. 5. Velocity components measured along the cavity centerlines, $Re = 1000$: (a) u_x velocity component measured along the vertical centerline; (b) u_y velocity component measured along the horizontal centerline. Solid line corresponds to the currently obtained data, ∘ symbols correspond to the data reported in [52], and + symbols correspond to the data reported in [54].

Table 5
Results of the grid independence study.

	$\overline{Nu}$		
$Ri/Grid$	50^2	100^2	200^2
0.01	2.9251	2.9340	2.9381
1	3.4707	3.4920	3.5026
5	4.7184	4.7099	4.7061
10	5.0906	5.0688	5.0641

Table 6
Comparison between the $\overline{Nu}$ values averaged over the lower surface of a lid driven cavity calculated for $Re = 100$.

	$\overline{Nu}$			
Ri	Isothermal	Isothermal, Ref. [56]	Adiabatic	Adiabatic, Ref. [56]
0.01	2.9381	2.92	2.2650	2.24
1	3.5026	3.5	3.3669	3.33
5	4.7061	4.69	4.0988	4.06
10	5.0641	5.04	4.4866	4.50

and the adiabatic cylinders presented in Figs. 8 and 9, respectively, are in good qualitative agreement with the data available in the literature [56] for the entire range of the Richardson numbers. As expected, the configuration with adiabatic cylinder is characterized by a more uniform temperature distribution over the cavity compared to that with the isothermal cold cylinder. A quantitative comparison between the currently obtained and the independent [56] $\overline{Nu}$ values averaged over the lower surface of a lid-driven cavity is summarized in Table 6. The results demonstrate a high degree of agreement for both isothermal and adiabatic cylinders for the entire range of Ri numbers, with a maximum deviation of 1.3%.

In what follows, we focus on the local flow characteristics obtained for a lid-driven cavity with an embedded adiabatic cylinder. A comparison between the currently obtained and the independent values of the local Nu values calculated along the bottom wall of the cavity and the temperature values measured on the cylinder surface for three different Ri values is presented in Figs. 10 (a) and (b), respectively. The results are in acceptable qualitative agreement with the corresponding independent data and successfully capture the trends of the heat flux enhancement through the right half of the cavity bottom over the entire range of Ri values (see Fig. 10 (a)) as well as the temperature distribution polarization along the cylinder surface as the Ri number decreases (see Fig. 10 (b)).

3.3. 3D lid-driven cavity with an embedded sphere

In this and the following sections we present the $3D$ results obtained when analyzing shear- and thermally driven confined flows around immersed bodies of spherical shape. To achieve the best accuracy of the IB method, all the spheres were built of equispaced Lagrangian points characterized by a distance equal to that of the grid size of the corresponding

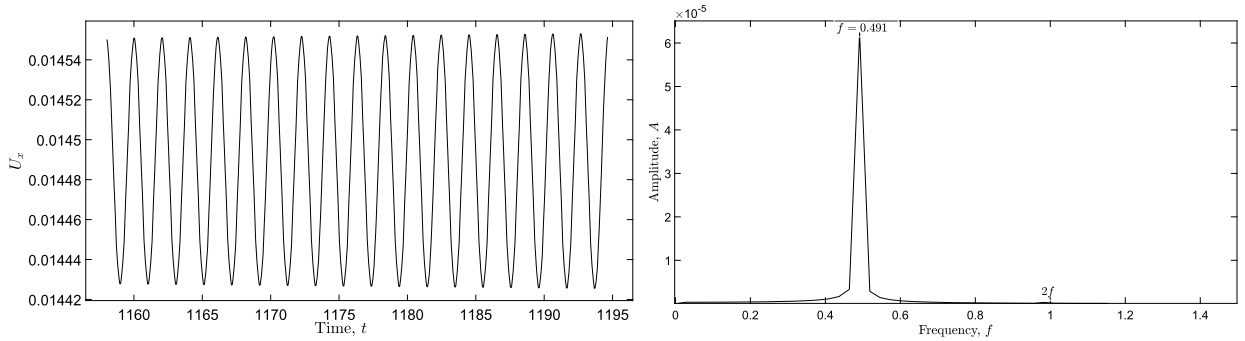

(a) Time evolution and spectra, $Re = 8600$

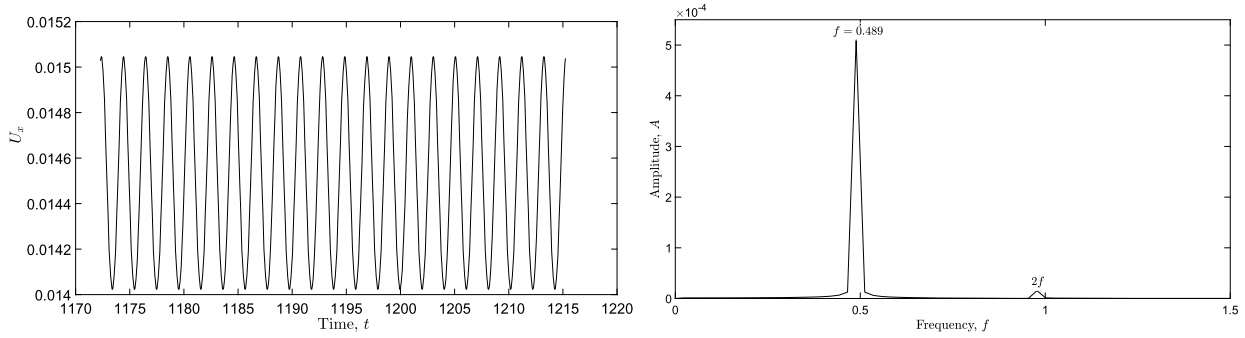

(b) Time evolution and spectra, $Re = 8700$

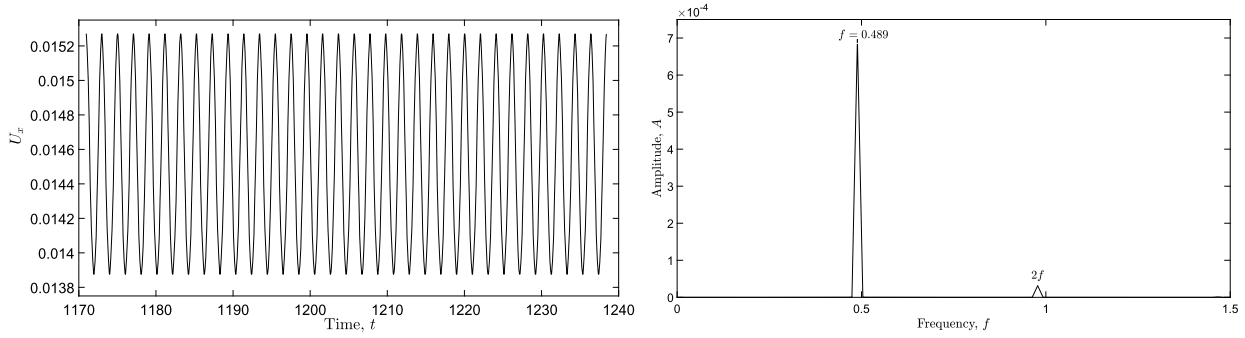

(c) Time evolution and spectra, $Re = 8800$

Fig. 6. Time evolution and spectra of the u_x velocity component measured at the control point (0.9, 0.1) for different Re values.

Eulerian grid. The mapping of the spherical surfaces was implemented by utilizing the non-iterative method of Leopardi [59]. The flow within a cubic lid-driven cavity of side L with a sphere of diameter αL placed in the geometric center of the cavity was investigated (see Fig. 11). The top lid of the cavity moves with a constant velocity U in the x direction, while all the other boundaries and the sphere are stationary. All the simulations were performed on a 200^3 grid.

3.3.1. *Sphere of diameter* $0.25L$

To ensure the accuracy of our results, we performed a grid independence study for the flow within the given configuration. We conducted simulations on grids of sizes 100^3, 150^3, and 200^3 at Reynolds numbers of 1, 100, and 400. The values of the u_x and u_y velocity components along the vertical and horizontal centerlines are presented in Table 7. Our analysis showed that the velocities obtained on the 150^3 and 200^3 grids were in agreement, to within 3 decimal digits, for most points, with maximum relative deviations of 2.5% occurring in regions of low velocity. These results demonstrate the grid independence of the obtained results, and we therefore conducted all further analysis using a 200^3 grid.

The contours of the u_x velocity component in the mid-cross section of the cavity for three different Re numbers are presented in Fig. 12. It may be seen that the distribution of the u_x velocity component maintains symmetry about the vertical centerline for all Re values. As expected, the velocity gradients increase in the vicinity of the moving lid as the Re

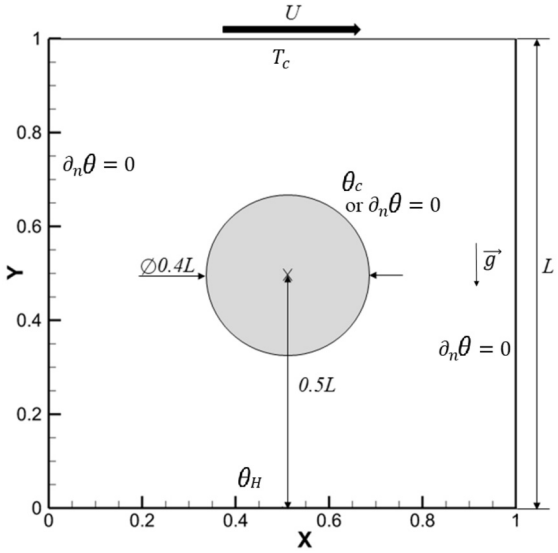

Fig. 7. Laminar mixed convection flow in a lid driven cavity with an embedded cylinder – physical model.

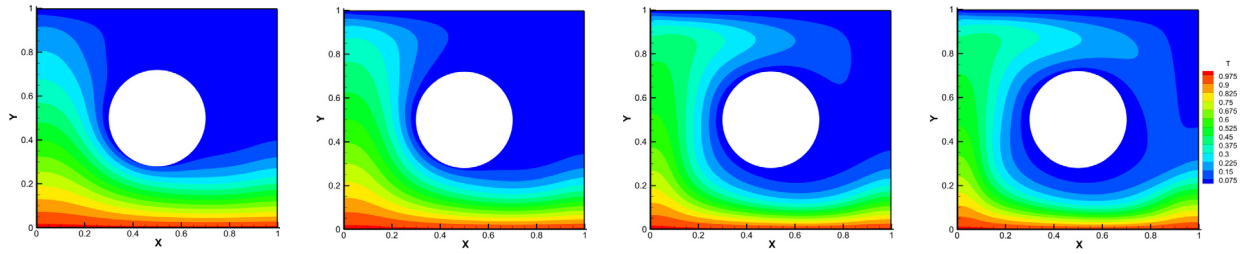

(a) $Ri = 0.01$ (b) $Ri = 1$ (c) $Ri = 5$ (d) $Ri = 10$

Fig. 8. Temperature distribution obtained for the isothermal cylinder.

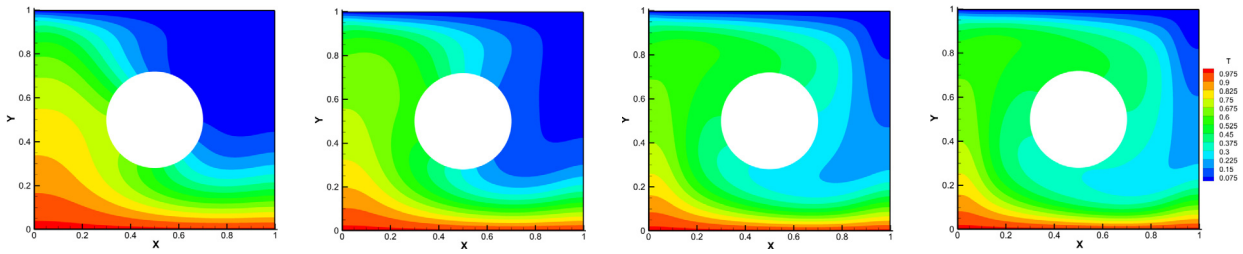

(a) $Ri = 0.01$ (b) $Ri = 1$ (c) $Ri = 5$ (d) $Ri = 10$

Fig. 9. Temperature distribution obtained for the adiabatic cylinder.

values increase. These contours are in good qualitative agreement with the data reported in reference [60]. Table 8 presents a quantitative comparison of the values of u_x and u_z obtained along the vertical and horizontal centerlines, respectively, for three different values of $Re = 1, 100$, and 400 with the corresponding data reported in [60], which was acquired by photogrammetry. It can be seen that for the vast majority of measurements the results are in good agreement, with a maximal relative deviation of 6%. For a small number of control points, characterized by a close-to-zero value of u_z, the relative deviation between the corresponding values is close to 10%.

3.3.2. Sphere of diameter 0.4*L*

The steady state and supercritical flows were then investigated for the 3*D* lid-driven cavity flow in a cube with a sphere of diameter $0.4L$ placed in the center of the cube. The steady-state flow was simulated for $Re = 100, 400, 1000$ and 1500 values. The obtained flow characteristics are presented in Fig. 13 in terms of the iso-contours of the u_x, u_y and u_z velocity components in the mid-cross-section of the cavity for the values of $Re = 100, 400$ and 1000. The calculated iso-

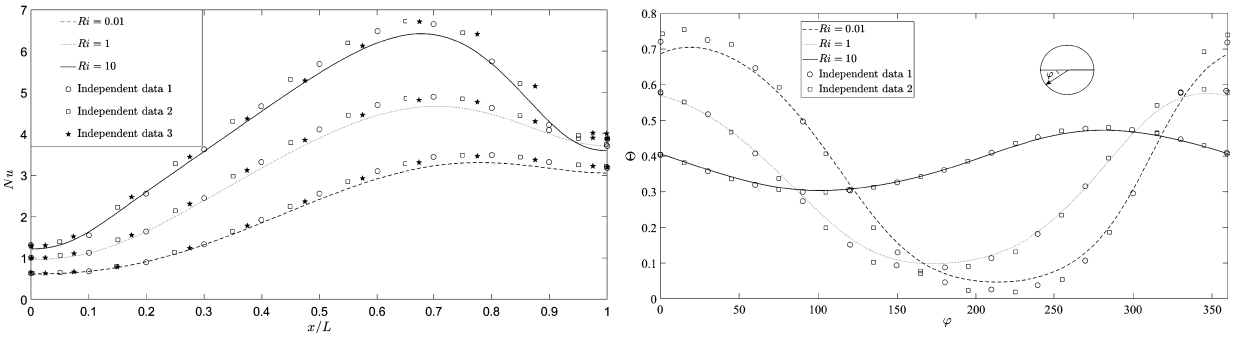

(a) Local Nusselt number at $y = 0$ (b) Temperature along the cylinder surface

Fig. 10. Comparison of the local Nu and the temperature values along the surface of adiabatic cylinder placed in the center of a lid-driven cavity obtained for three different Richardson numbers $Ri = 0.01$, $Ri = 1$ and $Ri = 10$. Dashed, dotted and solid lines correspond to the currently obtained data, ★ symbols correspond to the data reported in [56] ∘ symbols correspond to the data reported in [57], and □ symbols correspond to the data reported in [58].

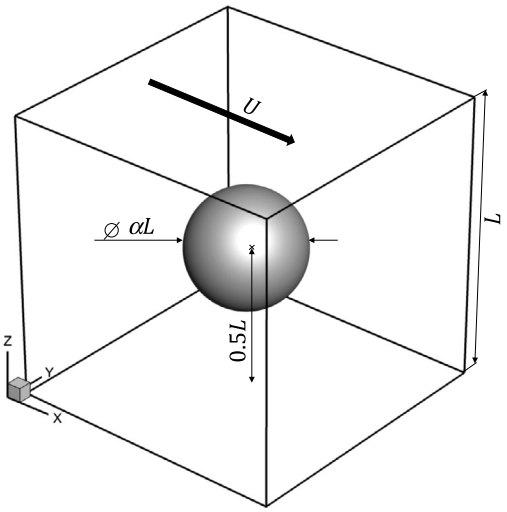

Fig. 11. Cubic lid-driven cavity with an embedded sphere in the center – physical model.

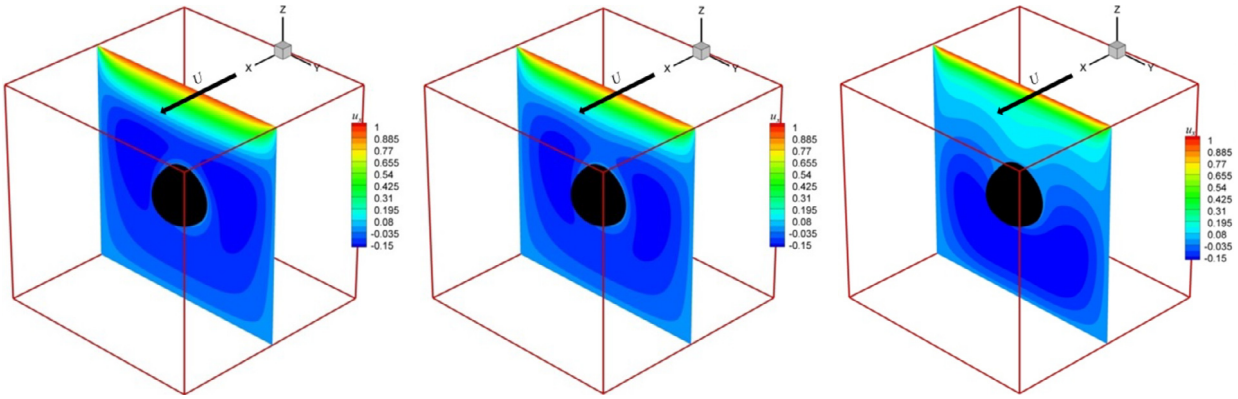

(a) $Re = 1$ (b) $Re = 100$ (c) $Re = 400$

Fig. 12. Contours of u_x for the lid driven cavity flow with an embedded in the center sphere of diameter $D = 0.25L$.

Table 7
Summary of grid independence study. The data corresponds to the values of u_x and u_z velocity components collected along the vertical and horizontal centerlines, respectively.

$Re = 1$				$Re = 100$				$Re = 400$			
$z/_{Grid}$	u_x			$z/_{Grid}$	u_x			$z/_{Grid}$	u_x		
	100^3	150^3	200^3		100^3	150^3	200^3		100^3	150^3	200^3
0.95195	0.68862	0.68973	0.68966	0.95423	0.65728	0.65821	0.65804	0.95423	0.47726	0.47887	0.49609
0.90160	0.40895	0.41050	0.41049	0.90389	0.35729	0.35845	0.35815	0.90389	0.23154	0.23234	0.23759
0.85355	0.19340	0.19505	0.19508	0.85355	0.15682	0.15802	0.15789	0.85355	0.15959	0.16010	0.16018
0.80320	0.02546	0.02672	0.02666	0.80320	0.03200	0.03318	0.03315	0.80320	0.12652	0.12702	0.12721
0.75057	-0.08568	-0.08551	-0.08581	0.75286	-0.04202	-0.04134	-0.04143	0.75286	0.09885	0.09964	0.10109
0.70023	-0.12603	-0.12825	-0.12912	0.70252	-0.07351	-0.07446	-0.07490	0.70252	0.06920	0.07071	0.07254
0.30206	-0.09859	-0.10144	-0.10209	0.30206	-0.10661	-0.11032	-0.11114	0.30206	-0.16812	-0.17320	-0.17455
0.25172	-0.11808	-0.11924	-0.11953	0.25172	-0.12815	-0.13005	-0.13048	0.25172	-0.21185	-0.21502	-0.21603
0.20366	-0.11799	-0.11825	-0.11831	0.20137	-0.12750	-0.12829	-0.12851	0.19908	-0.21639	-0.21862	-0.21813
0.14874	-0.10383	-0.10357	-0.10357	0.15103	-0.11317	-0.11332	-0.11341	0.15103	-0.18980	-0.19112	-0.19332
0.10069	-0.08148	-0.08109	-0.08106	0.10069	-0.08799	-0.08783	-0.08785	0.10069	-0.14754	-0.14822	-0.14852
0.05263	-0.04934	-0.04902	-0.04900	0.05263	-0.05335	-0.05315	-0.05315	0.05034	-0.08970	-0.08992	-0.08680
$Re = 1$				$Re = 100$				$Re = 400$			
$x/_{Grid}$	u_z			$x/_{Grid}$	u_z			$x/_{Grid}$	u_z		
	100^3	150^3	200^3		100^3	150^3	200^3		100^3	150^3	200^3
0.05721	0.09030	0.09007	0.09016	0.05734	0.08944	0.08938	0.08955	0.05023	0.13483	0.13599	0.13675
0.10755	0.14447	0.14431	0.14440	0.10550	0.13530	0.13536	0.13545	0.10046	0.19602	0.19755	0.19826
0.15789	0.17390	0.17393	0.17406	0.15596	0.16021	0.16042	0.16056	0.14840	0.21368	0.21496	0.21555
0.20824	0.17969	0.18010	0.18027	0.20642	0.16593	0.16644	0.16663	0.20091	0.20982	0.21089	0.21137
0.25858	0.16333	0.16445	0.16476	0.25688	0.15397	0.15516	0.15546	0.24886	0.19194	0.19321	0.19371
0.30892	0.12253	0.12544	0.12612	0.30734	0.11927	0.12226	0.12294	0.29909	0.15367	0.15645	0.15724
0.70709	-0.13910	-0.14129	-0.14170	0.70872	-0.15334	-0.15570	-0.15625	0.70091	-0.06086	-0.06351	-0.06393
0.75744	-0.17145	-0.17234	-0.17255	0.75917	-0.20512	-0.20677	-0.20726	0.75114	-0.17000	-0.17226	-0.17276
0.80778	-0.18095	-0.18129	-0.18141	0.80963	-0.22841	-0.22958	-0.23000	0.80137	-0.28543	-0.28791	-0.28882
0.85812	-0.16777	-0.16781	-0.16790	0.86009	-0.21376	-0.21446	-0.21477	0.84932	-0.35992	-0.36274	-0.36419
0.90389	-0.13477	-0.13459	-0.13466	0.90826	-0.16230	-0.16266	-0.16284	0.90183	-0.32061	-0.32236	-0.32367
0.95652	-0.07144	-0.07132	-0.07127	0.96101	-0.07428	-0.07436	-0.07442	0.94977	-0.16749	-0.16868	-0.16906

contours bear a striking resemblance (both qualitatively and quantitatively) to the corresponding independent data available in literature [51]. The same trends were observed with respect to the symmetry preserving of all the velocity components relative to the vertical centerline and to the presence of numerous secondary eddies in the bottom region of the cavity. The acceptable quantitative agreement between the maximal values of the velocity components obtained in this study and those obtained in Ref. [51] as summarized in Table 9, verifies the correctness of our steady-state results.

The characteristics of the supercritical flow developing for the values of $Re = 1790, 1810, 1820$ and 1850 were then compared with the corresponding results reported in [51]. The time evolutions of the v_z velocity component collected at the control point $(0.85, 0.5, 0.5)$ for all the simulated periodic flows, along with the corresponding frequency spectra, are shown in Fig. 14. The main harmonic and its multipliers typical of non-linear supercritical flow regimes can be clearly recognized. The values of the obtained main harmonics for all the Re values are close to each other and are in good agreement with the corresponding values reported in [51]. The time evolutions of signals obtained in this study are, however, characterized by higher amplitudes and a more pronounced impact of the multiplied harmonics—characteristics that were apparently under-resolved in [51] as a result of insufficient grid resolution (the calculations were performed on a 80^3 grid).

The phase plots obtained by plotting the time evolutions of u_z versus u_x collected at the control point (0.85, 0.5, 0.5) for different Re values are shown in Fig. 15. There is good agreement between our data and the corresponding data reported in [51] in terms of extreme values of the measured u_z and u_x velocities for the entire range of Re values. Nonetheless, the shape of our phase plot curves is more complicated than that in [51] which, again, is a consequence of the more pronounced impact of the multiplied harmonics characterizing our simulated flow fields.

3.4. Diagonally 3D lid-driven cavity with an embedded sphere

We examine the configuration of a cubic diagonally lid-driven cavity of side L in which the lid moves along the main diagonal with constant velocity $U(cos(\frac{\pi}{4}), sin(\frac{\pi}{4}), 0)$ and in which a sphere of diameter $L/4$ is placed in the cavity center (see Fig. 16). The diagonally lid-driven cavity has attracted interest due to the complex separation flows developing within it, in both the subcritical and supercritical regimes (see e.g. [61], [62]). We currently extend the state of the art on the above complex flow by investigating the characteristics of the subcritical flow regime developing within the diagonally lid-driven cavity hosting a stationary no-slip sphere at its center. All the simulations were performed on a 200^3 grid.

Table 8
Comparison between the values of u_x and u_z velocities currently calculated along the vertical and horizontal centerlines and the corresponding data reported in [60]. The values are compared in terms of relative deviation between the results.

$Re = 1$						$Re = 100$						$Re = 400$					
$Rel.Dev.$[%]			$Rel.Dev.$[%]			$Rel.Dev.$[%]			$Rel.Dev.$[%]			$Rel.Dev.$[%]			$Rel.Dev.$[%]		
z	u_x [60]	u_x	x	u_z [60]	u_z	z	u_x [60]	u_x	x	u_z [60]	u_z	z	u_x [60]	u_x	x	u_z [60]	u_z
0.95195	2.117	0.68966	0.05721	1.016	0.09016	0.95423	2.407	0.65804	0.05734	0.345	0.08955	0.95423	2.672	0.49609	0.05023	2.075	0.13675
0.90160	3.559	0.41049	0.10755	3.004	0.14440	0.90389	2.659	0.35815	0.10550	0.325	0.13545	0.90389	0.797	0.23759	0.10046	0.414	0.19826
0.85355	4.798	0.18508	0.15789	1.232	0.17406	0.85355	4.126	0.15789	0.15596	1.193	0.16056	0.85355	1.434	0.16018	0.14840	2.976	0.21555
0.80320	3.826	0.01666	0.20824	2.821	0.18027	0.80320	8.772	0.03015	0.20642	0.250	0.16663	0.80320	2.533	0.12721	0.20091	2.848	0.21137
0.75057	3.998	-0.08581	0.25858	1.386	0.16476	0.75286	10.702	-0.04143	0.25688	1.380	0.15546	0.75286	1.861	0.10109	0.24886	0.414	0.19371
0.70023	2.528	-0.12912	0.30892	0.208	0.12612	0.70252	2.010	-0.07490	0.30734	1.346	0.12294	0.70252	2.210	0.07254	0.29909	0.417	0.15724
0.30206	3.620	-0.10209	0.70709	1.491	-0.14170	0.30206	5.068	-0.11114	0.70872	1.874	-0.15625	0.30206	4.300	-0.17455	0.70091	9.094	-0.06293
0.25172	2.359	-0.11953	0.75744	0.537	-0.17255	0.25172	5.078	-0.13048	0.75917	3.943	-0.20726	0.25172	1.486	-0.21603	0.75114	3.306	-0.17276
0.20366	2.514	-0.11831	0.80778	0.346	-0.18141	0.20137	3.621	-0.12851	0.80963	1.503	-0.23000	0.19908	0.338	-0.21813	0.80137	0.624	-0.28882
0.14874	3.842	-0.10357	0.85812	0.509	-0.16790	0.15103	2.922	-0.11341	0.86009	3.042	-0.21477	0.15103	0.616	-0.19332	0.84932	0.095	-0.36419
0.10069	4.454	-0.08106	0.90389	6.537	-0.13466	0.10069	0.794	-0.08785	0.90826	5.849	-0.16284	0.10069	3.228	-0.14852	0.90183	1.728	-0.32367
0.05263	7.412	-0.04900	0.95652	10.807	-0.06927	0.05263	3.564	-0.05315	0.96101	4.680	-0.07442	0.05034	2.453	-0.08680	0.94977	3.895	-0.16906

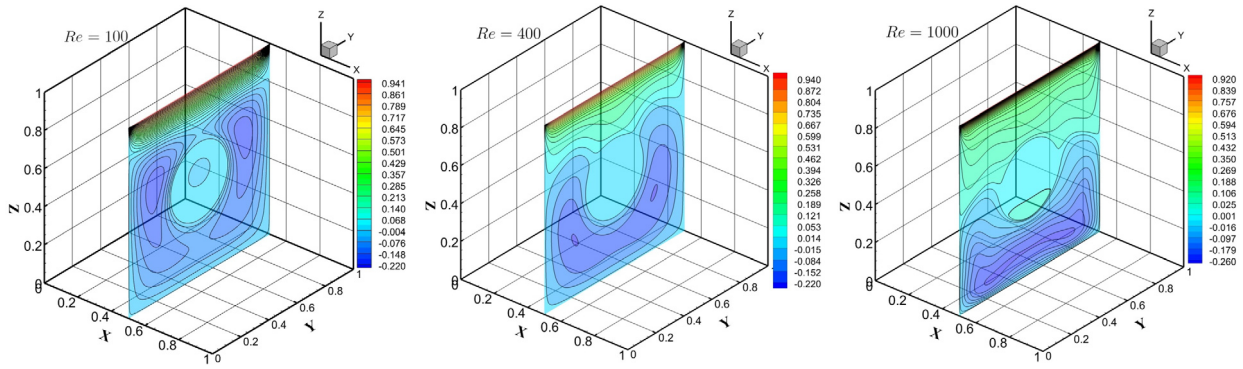

(a) Iso-contours of u_x velocity

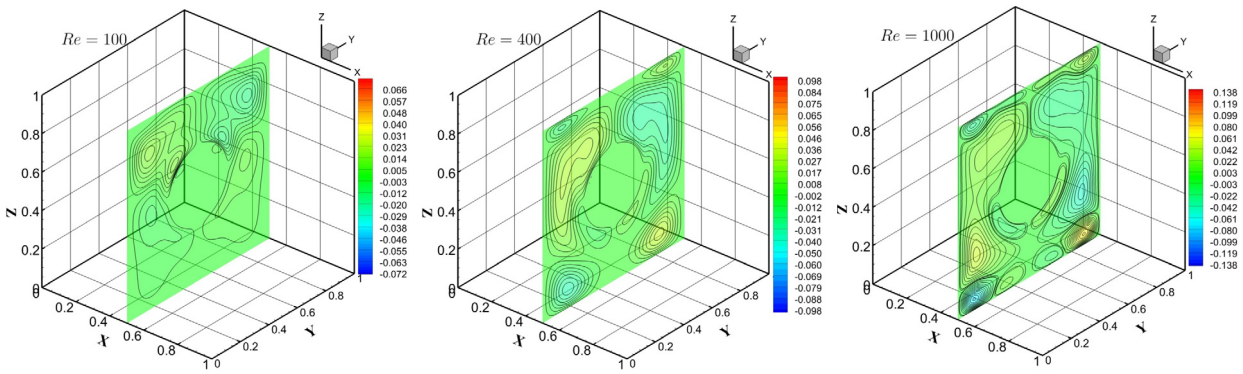

(b) Iso-contours of u_y velocity

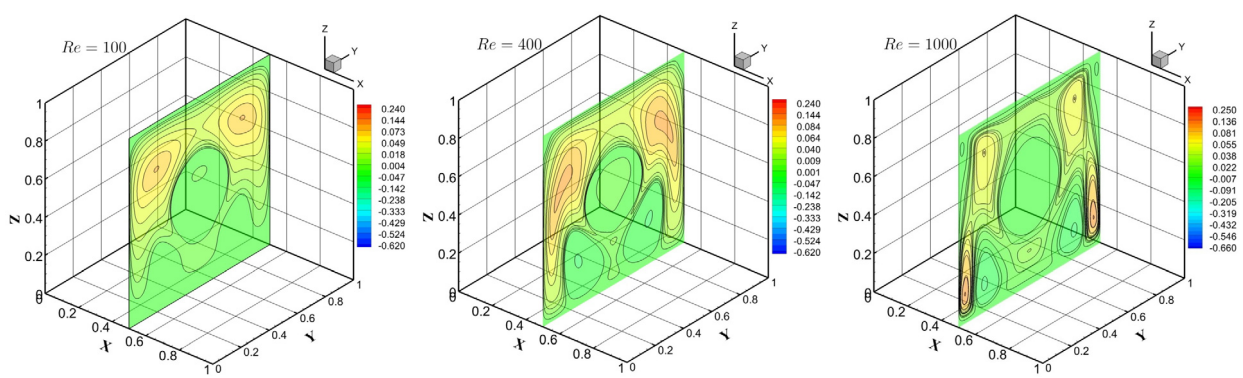

(c) Iso-contours of u_z velocity

Fig. 13. Iso-contours of the velocity components in a mid cross-section of the cavity obtained for three different *Re* values.

Table 9
Comparison between extreme values of the velocity components obtained for different *Re* values.

Re	u_{xmin}		u_{ymin}		u_{ymax}		u_{zmin}		u_{zmax}	
	Ref. [51]	Current	Ref. [51]	Current	Ref. [51]	Current	Ref. [51]	Current	Ref. [51]	Current
100	-0.22311	-0.22421	-0.07437	-0.07598	0.07415	0.07603	-0.50933	-0.51036	0.23871	0.34058
400	-0.22724	-0.22795	-0.09827	-0.09699	0.09827	0.09699	-0.62632	-0.63243	0.24277	0.28287
1000	-0.26324	-0.26667	-0.13936	-0.13423	0.13936	0.13423	-0.66759	-0.67588	0.24654	0.24962
1500	-0.28349	-0.28920	-0.18533	0.14843	0.18533	0.14843	-0.66857	-0.69072	0.24565	0.25013

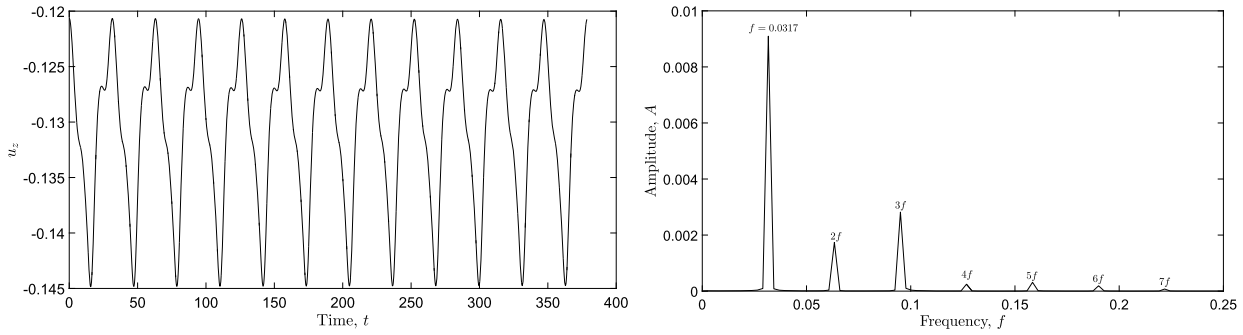

(a) Time evolution and spectra, $Re = 1790$

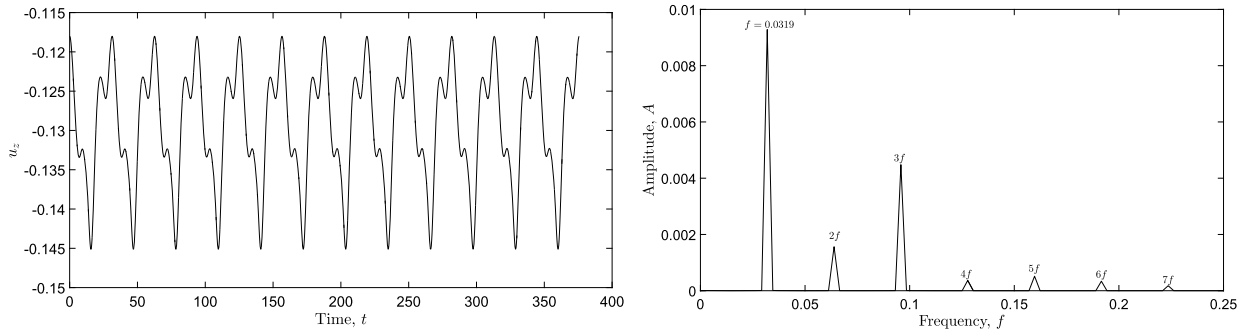

(b) Time evolution and spectra, $Re = 1810$

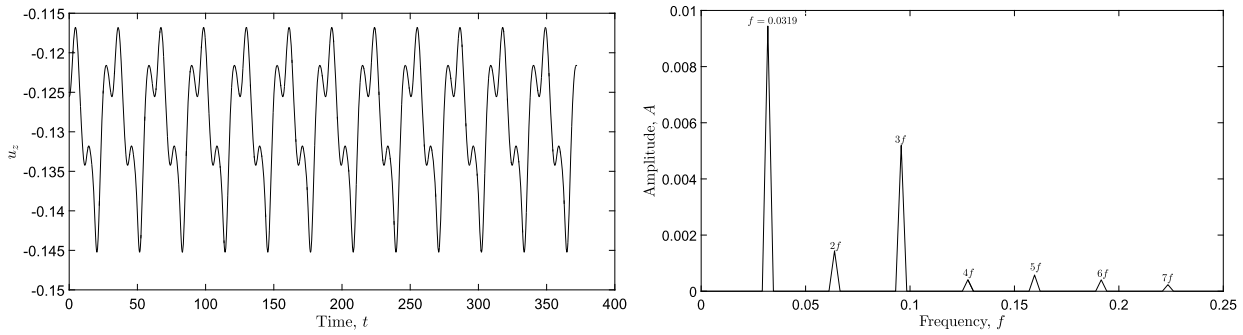

(c) Time evolution and spectra, $Re = 1820$

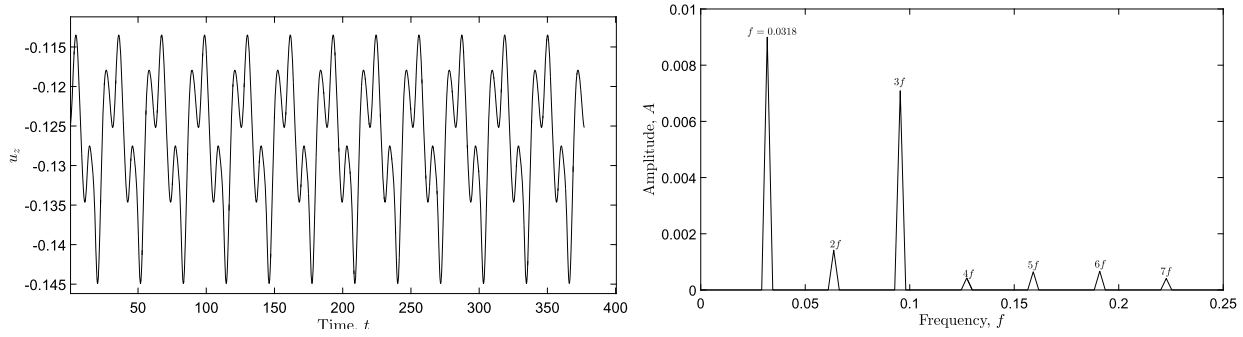

(d) Time evolution and spectra, $Re = 1850$

Fig. 14. Time evolution and spectra of the u_z velocity component, as measured at control point (0.85, 0.5, 0.5) for different Re values.

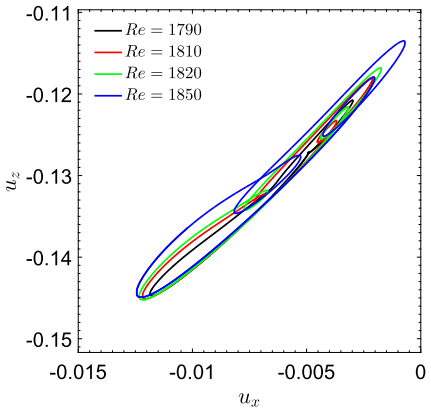

Fig. 15. Phase plots of the u_z velocity component versus the u_x velocity component, as measured at the control point (0.85, 0.5, 0.5) for different Re values.

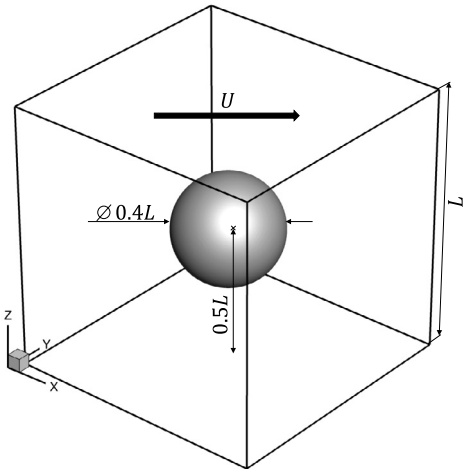

Fig. 16. Cubic diagonally lid-driven cavity with an embedded sphere in the center – physical model.

The iso-contours of the $u_d = u_x cos(\frac{\pi}{4}) + u_y sin(\frac{\pi}{4})$ and u_z velocity components with superimposed flow pathlines projected on the main diagonal and horizontal cross-sections are shown in Fig. 17. The steady-state flow was calculated for $Re = 2800$. The steady-state flow preserves the symmetry relatively to the main diagonal plane. Remarkably, in contrast to the "classical" lid-driven cavity configuration, embedding the sphere in the center of the cavity suppresses the transition to unsteadiness. We note that without the embedded spheres the transition to unsteadiness in "classical" and diagonally lid-driven cavities sets in at $Re \approx 1920$ and $Re \approx 2300$, respectively [63,62,64]; in contrast to the spheres placed in the center of the cavities, supercritical flow is already observed at $Re = 1810$ for the "classical" lid-driven cavity, whereas the flow remains steady even at $Re = 2800$ for the diagonally lid-driven cavity. The observed phenomenon can be explained by the fact that in the diagonally lid-driven cavity the embedded sphere splits the primary vortex into two counter-rotating vortices. As a result, the interaction between the primary and the secondary vortices, constituting the primary source of the instability onset [64], weakens and, consequently, the transition to instability sets in at higher Re values. We conclude this section by summarizing in Table 10 the values of all the velocity components along the vertical centerline of the cavity, which may be useful for comparison with independently obtained results in the future.

3.5. Hot sphere within a cold cubic container

The natural convection flow developing around a hot sphere of diameter $D = 0.4L$ placed inside a cold cubic container of side L (see Fig. 18) is examined. The center of the sphere is placed on the vertical centerline at height H from the cavity bottom. The gravity force acts in the $-\hat{z}$ direction. We now define a normalized distance between the sphere and the cubic container centers as $\kappa = (H - 0.5L)/L$. To quantify the heat transfer rate from the surface of the hot sphere and from the surfaces of the cold cubic cavity, we also define two values of the Nusselt number, $\overline{Nu} = \overline{PrRa}\Delta x\overline{Q}$ and $\overline{Nu}_G = \frac{1}{N}\sum_{i=1}^{N}\frac{\overline{\partial\theta}}{\partial \mathbf{n}}$, averaged over the surfaces of the sphere and the cubic container, respectively. Here $\overline{Q}$ is simply the arithmetic mean of all the heat fluxes Q_k at each Lagrangian point k of the sphere obtained directly by the solution of Eqs. (20), and N corresponds to the total number of thermally non-insulated faces of the cubical container ($N = 6$ for

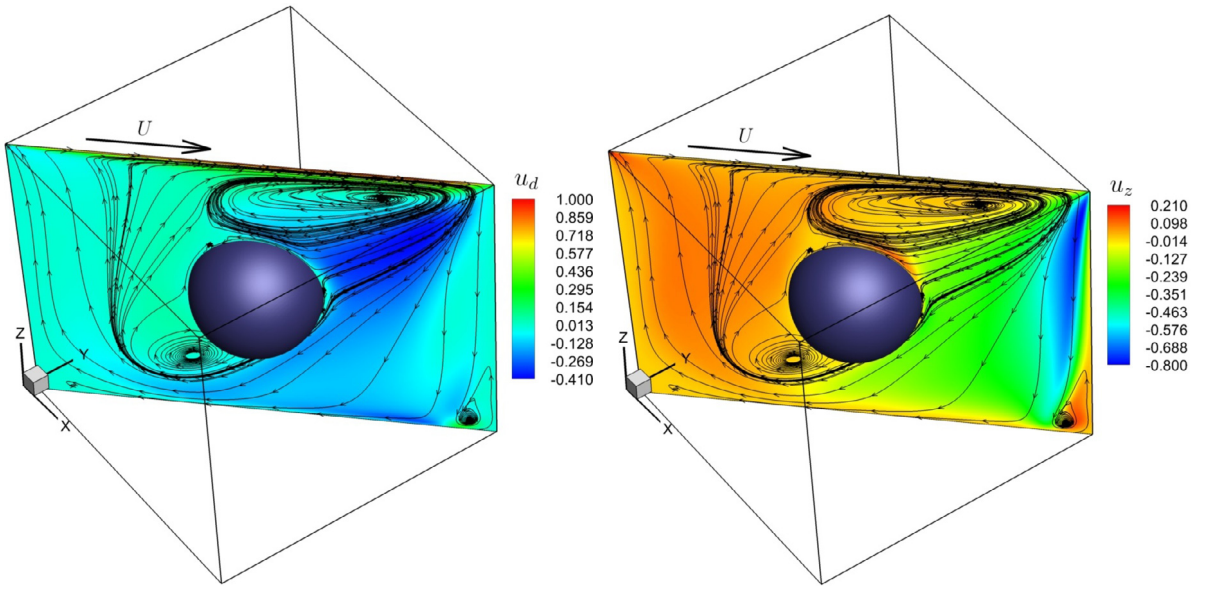

(a) Projection of the flow pathlines on the diagonal cross-section superimposed on contours of the u_d and u_z velocity components.

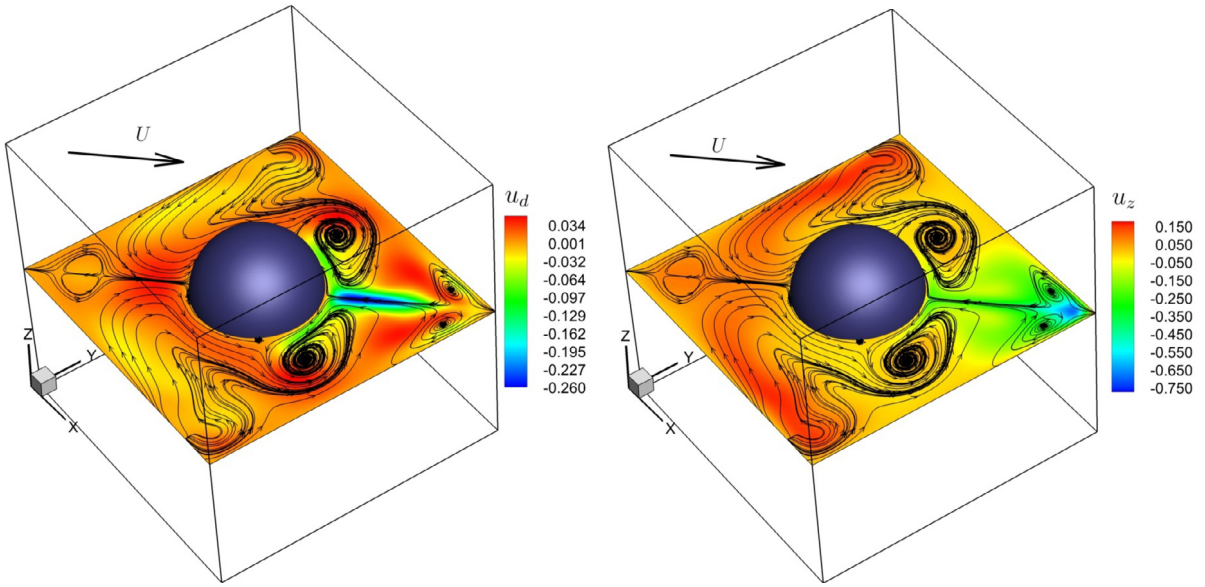

(b) Projection of the flow pathlines on the horizontal cross-section superimposed on contours of the u_d and u_z velocity components.

Fig. 17. Characteristics of the steady-state flow typical of a diagonally lid-driven cavity with an embedded sphere obtained for $Re = 2800$.

the configuration under consideration). The values $\overline{Nu}$ and $\overline{Nu}_G$ calculated for the steady-state natural convection flow developing at $Ra = 10^5$ and $Ra = 10^6$ values and their comparison with the corresponding results available in the literature are summarized in Table 11.

As can be seen from the Table 11, there is acceptable agreement (a maximal value of the relative deviation does not exceed 9%) between the currently obtained values and the independent data for the entire range of Ra and κ values. For additional verification of the conservation of the global heat flux of the system, we compared the values of $\overline{Nu}$ and $N/\pi D^2 \overline{Nu}_G$, corresponding to the average area specific heat fluxes from the surfaces of the hot sphere and the cold cubic container, respectively. The relative deviation between the values was less than 0.5% for the entire range of Ra and κ values,

Table 10
Numerical values of all the velocity components obtained along the vertical centerline for different Re values.

z	$Re = 2400$		$Re = 2600$		$Re = 2800$	
	u_x, u_y	u_z	u_x, u_y	u_z	u_x, u_y	u_z
0.002489	-1.3611E-02	-5.5481E-04	-1.3732E-02	-5.9578E-04	-1.3919E-02	-6.3865E-04
0.061991	-1.0740E-01	-6.7994E-02	-1.0350E-01	-6.9455E-02	-1.0054E-01	-7.0909E-02
0.121493	-1.1728E-01	-1.3213E-01	-1.1542E-01	-1.3371E-01	-1.1363E-01	-1.3460E-01
0.180996	-1.0329E-01	-1.1703E-01	-1.0665E-01	-1.2232E-01	-1.1002E-01	-1.2723E-01
0.240499	-3.8603E-02	-3.5437E-02	-3.9955E-02	-3.7081E-02	-4.1536E-02	-3.8880E-02
0.759502	-8.9426E-02	3.9756E-02	-9.1101E-02	3.2964E-02	-9.1534E-02	2.5465E-02
0.819004	-3.3817E-02	2.7711E-02	-3.6154E-02	2.0284E-02	-3.8896E-02	1.4138E-02
0.878507	2.5904E-02	3.5641E-02	2.0932E-02	2.9248E-02	1.5168E-02	2.3410E-02
0.938009	8.6466E-02	2.9329E-02	8.4158E-02	2.8013E-02	8.1903E-02	2.6226E-02
0.997511	6.5758E-01	2.2253E-04	6.5574E-01	2.2055E-04	6.5399E-01	2.1611E-04

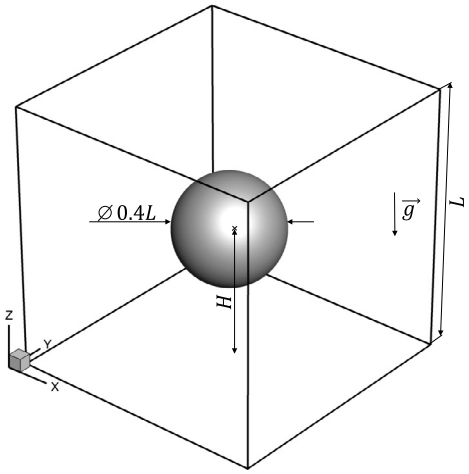

Fig. 18. Hot sphere placed inside a cold cubic container along its vertical centerline – physical model.

Table 11
Comparison between the values obtained in this study and those in the literature for $\overline{Nu}$ and $\overline{Nu}_G$ averaged over the surfaces of a hot sphere and a cold cube, respectively. The values are compared in terms of relative deviation between the results.

	$\overline{Nu}$								$\overline{Nu}_G$					
	$Ra = 10^5$				$Ra = 10^6$				$Ra = 10^5$			$Ra = 10^6$		
	$Rel.Dev.$[%]				$Rel.Dev.$[%]				$Rel.Dev.$[%]			$Rel.Dev.$[%]		
κ	Ref. [65]	Ref. [41]	Ref. [31]	Present	Ref. [65]	Ref. [41]	Ref. [31]	Present	Ref. [65]	Ref. [31]	Present	Ref. [65]	Ref. [31]	Present
-0.25	4.674	3.913	5.902	14.335	4.288	0.765	5.567	21.826	0.217	7.152	1.1969	0.602	5.563	1.8262
-0.2	4.307	3.367	5.513	13.513	4.256	1.457	4.785	21.548	0.632	6.886	1.1284	0.582	7.488	1.8030
-0.1	4.091	1.258	3.413	13.272	4.360	2.049	2.316	21.719	0.235	4.890	1.1084	0.341	5.075	1.8168
0	4.062	1.675	0.258	13.194	4.282	7.939	0.176	21.627	0.272	1.752	1.1014	0.520	3.075	1.8080
0.1	3.838	4.687	3.005	12.844	4.101	6.060	2.053	21.238	0.690	1.417	1.0728	0.327	1.329	1.7758
0.2	4.236	6.557	5.205	12.796	4.181	8.216	4.702	20.522	0.655	3.677	1.0689	0.379	1.200	1.7162
0.25	4.289	6.670	5.568	13.524	4.341	8.620	5.535	20.616	0.903	4.214	1.1295	0.099	2.024	1.7239

which proves the accurate preservation of the total thermal balance between the emanating surface of the hot sphere and the absorbing surfaces of the cold cubic container.

We now present the qualitative characteristics of the simulated steady-state flow in terms of the iso-surfaces of the λ_2 criterion [66] corresponding to the outermost surface of the vortical structures evolving in the flow. The value of $\lambda_2 = -0.1$ was chosen for visualization purposes in accordance with the works of [67,31]. The iso-surfaces presented in Fig. 19 are in good agreement with the corresponding data presented in [31]. Noticeably, in agreement with the observations made in [31], the flow vortical structures are symmetric relative to the $X - Z$ and $Y - Z$ centerplanes and to both main diagonal planes of the cubic container. A large circumferential convection cell located close to the top boundary of the cube is clearly recognizable for the entire range of Ra and κ values. For negative κ values, the convection cell acquires a mushroom-like shape, while for positive values of κ the convective cell acquires a torus shape, as was reported in [31].

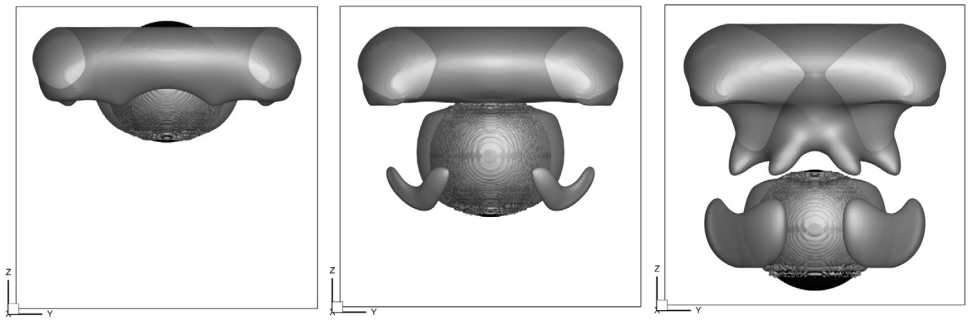

(a) Front view of $\lambda_2 = -0.1$ iso-surfaces obtained for $Ra = 10^5$, and $\kappa = 0.25, 0, -0.25$.

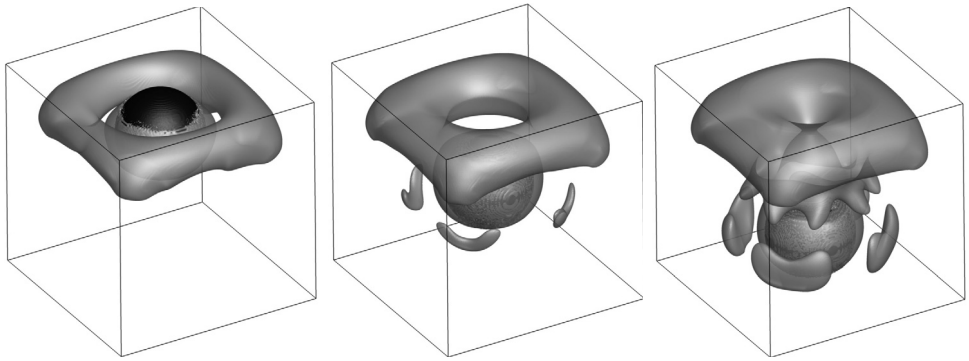

(b) Isometric view of $\lambda_2 = -0.1$ iso-surfaces obtained for $Ra = 10^5$, and $\kappa = 0.25, 0, -0.25$.

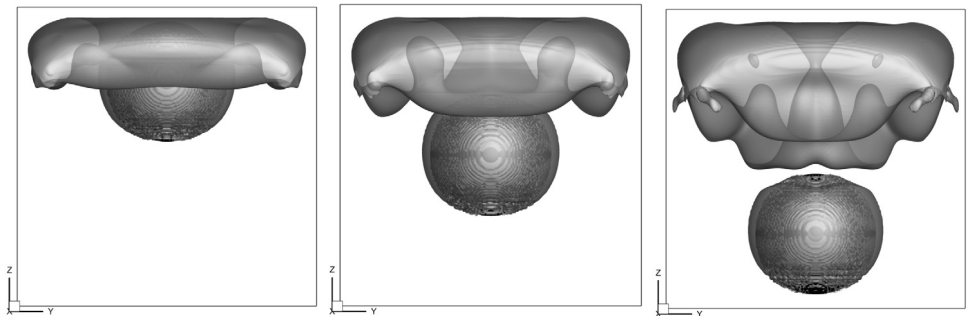

(c) Front view of $\lambda_2 = -0.1$ iso-surfaces obtained for $Ra = 10^6$, and $\kappa = 0.25, 0, -0.25$.

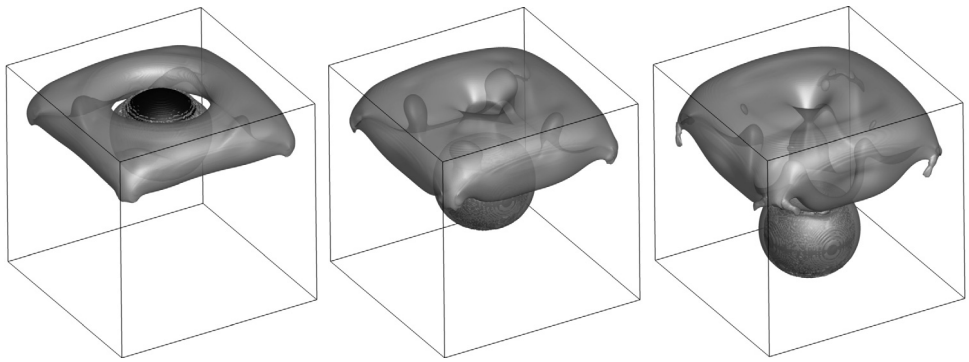

(d) Isometric view of $\lambda_2 = -0.1$ iso-surfaces obtained for $Ra = 10^6$, and $\kappa = 0.25, 0, -0.25$.

Fig. 19. Iso-surfaces of the λ_2 criterion.

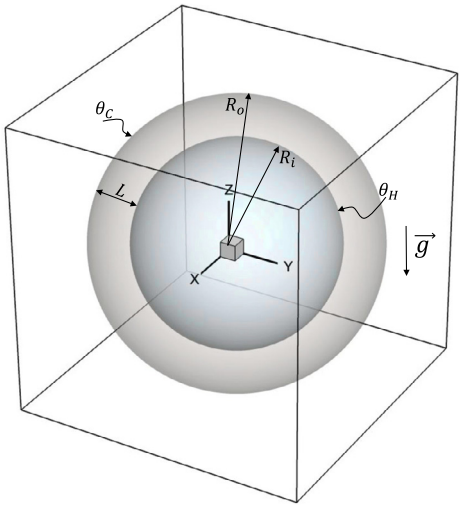

Fig. 20. Hot internal sphere of radius R_i placed within a cold outer sphere of radius R_o – physical model. The two spheres are placed within a cold cubic container in accordance with the formalism of the IB method.

3.6. Natural convection between two concentric spheres

The natural convection within a spherical shell confined by hot and cold spheres of radii R_i and R_o, respectively, is examined. The surfaces of the hot and cold spheres are held at constant temperatures θ_c and θ_h, respectively. According to the formalism of the IB method, the simulations were conducted on a uniform structured grid, and therefore both spheres were placed at the center of the cubic cavity, although the domain of interest is restricted to the region confined by the two spheres (see Fig. 20). The container walls were held at a constant cold temperature θ_c. The distance between the surfaces of the outer and inner spheres, L, was used to normalize the length scales. An additional non-dimensional parameter determining the geometry of the configuration under consideration was $\phi = R_i/R_o$. The dimensions of the cubic container were chosen in such a way that at least 10 grid points separated the container walls from the surface of the external sphere, so as to facilitate an adequate adjustment of the flow between them.

We then set the values of $Ra = 4.6 \times 10^4$ to enable us to perform an analysis of the slightly supercritical flow developing within the spherical gap characterized by the value of $\phi = 0.774$. The bifurcated flow regime is characterized by complex multi-cellular dynamics in the form of either pulsating or traveling waves, as detailed in [68–70,31]. Figs. 21 (a) and (b) present a snapshot of the contours of the radial velocity u_r interpolated onto the mid-sphere surface between the hot and the cold spheres. The obtained results are in excellent agreement with those reported in [70], which used linear stability analysis to predict that the traveling wave instability sets in at $Ra_{cr} = 3.9562 \times 10^4$ and is characterized by a wave number of $m = 10$ of the leading eigenmode. In that study, the critical value of the angular frequency for this regime was found to be $\omega_{cr} = 0.389$.[6] This value is in excellent agreement with our results, which for the slightly supercritical flow simulated for $Ra = 4.6 \times 10^4$ predicted a traveling wave solution characterized by a wave number of $m = 10$ and a value of $w_{cr} = 0.387$ for the angular frequency. Note that the value of the angular frequency of the flow can be obtained simply by dividing by 2 the value of the angular frequency of the time evolution of the Nusselt number, $\overline{Nu}_o$ averaged over the surface of the outer sphere, as presented in Figs. 21 (c) and (d) (see e.g. [31,68]).

3.7. Memory consumption and time step and scaling

To further evaluate the efficiency characteristics of the solver developed in this study, we examined the way in which the memory consumption and the duration of a single time step scale with the total number of Lagrangian points, N_s and with the total number of grid points, N_g. All the characteristics were obtained on a standard Linux server having 128 GB DDR3 shared memory and 2 Intel Xeon 12C processors, 24 threads each (48 threads in total). Shared memory openMP parallelization was used. The data was acquired for the grid resolutions starting from 50^3 and ending with 300^3 grid points when simulating natural convection flow developing between two concentric spheres for the values of $Ra = 4.6 \times 10^4$ and $\phi = 0.714$ (see Figs. 22-(a) and (b)), and the $3D$ lid-driven cavity flow with a sphere of diameter $0.4L$ placed in the cavity center for $Re = 400$ (see Figs. 22-(c) and (d)). For the first configuration, the number of Lagrangian points varied from 10,039 points for the coarsest grid resolution to 371,121 points for the finest grid resolution of the Eulerian grid. For the second configuration, the number of Lagrangian points varied from 491 to 17,675 points for the coarsest and the finest grid

[6] The value of $\omega_{cr} = 92.5$ reported in [70] was divided by $(Pr/Ra)^{0.5}$ for fitting the scaling of the current work.

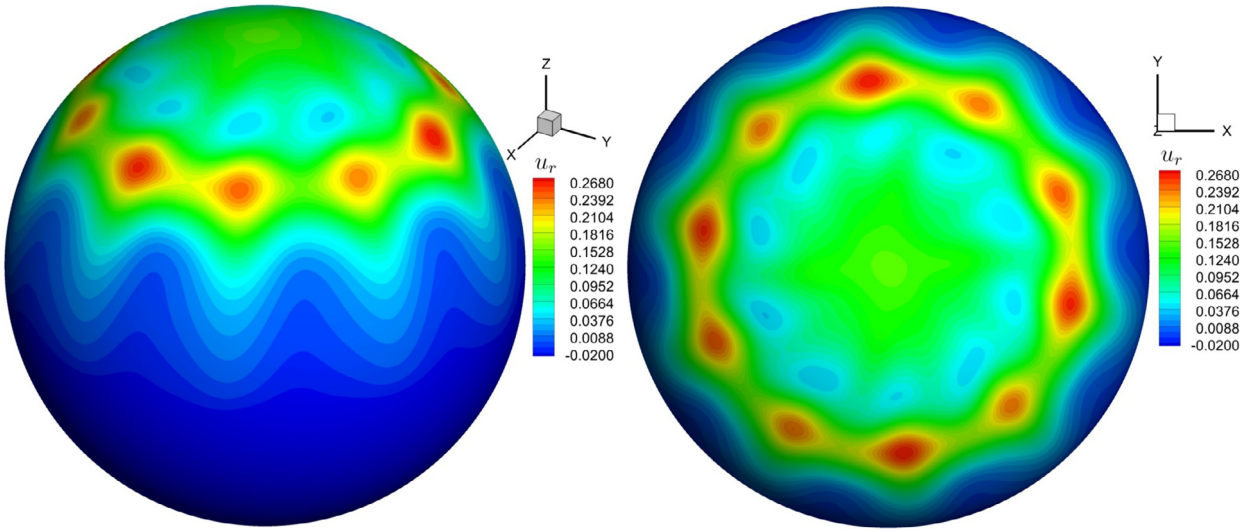

(a) Snapshot of the v_r velocity component interpolated onto the mid-sphere surface, $R = (R_i + R_o)/2$: isometric and top views.

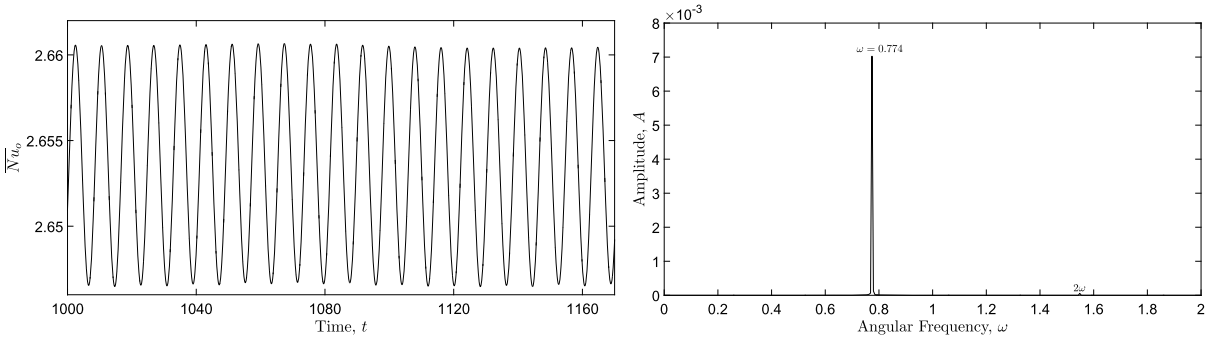

(b) Time evolution and frequency spectra of the Nusselt number, $\overline{Nu_o}$ averaged over the surface of the outer sphere.

Fig. 21. Characteristics of the periodic natural convection flow developing between two concentric spheres for the values of $Ra = 4.6 \times 10^4$ and $\phi = 0.714$.

resolutions, respectively. In both cases the number of Lagrangian points was dictated by the necessity to preserve the same spacing for the Eulerian and Lagrangian grids.

For natural convection flow, the memory consumption and the time step duration scale as $N_s^{1.09}$ and $N_s^{1.37}$, respectively, with the total number of Eulerian points, N_s, as follows from Fig. 22-(a). Maximum values of about 17 Gb RAM and 6 s of memory consumption and duration of the time step, respectively, were obtained for the finest 300^3 grid resolution. Remarkably, the memory consumption and the time step duration scale as $N_g^{0.72}$ and $N_g^{0.91}$, respectively, with the total number of grid points, as follows from Fig. 22 (b). The obtained result is not surprising, since for the equally spaced grids the total number of Eulerian grid points scales as $\Delta x^{1.5}$ to the total number of Lagrangian grid points, in keeping with the corresponding exponent values of N_s and N_g. Note that the same trend is also observed for the lid-driven cavity configuration, for which the ratio between the corresponding exponents of N_s and N_g is also maintained at 1.5 (see Figs. 22-(c) and (d)). At the same time, there are two clearly observed differences between the corresponding efficiency characteristics typical of the two configurations. First, for the natural convection flow, the slopes characterizing the power law functionality of the memory consumption and the time step duration are different, while for the lid-driven cavity flow the two slopes are nearly the same. Second, the exponent values characterizing the time step duration scaling typical of the natural convection configuration are lower compared to the corresponding values obtained for the lid-driven cavity flow. The first difference can apparently be attributed to the fact that for the natural convection flow the time duration step consists of the sum of the times required for the solution of both the energy and the NS equations, while for the lid-driven cavity flow the time duration step includes only the time required for the solution of the NS equations. The second difference can be explained by the fact that the natural convection configuration is characterized by an order of magnitude higher number of Lagrangian points, N_s, and is thus advantageous for strong scaling by the currently utilized openMP parallelization. In general, the upper limit of the exponent value characterizing the scalability of the developed approach as a function of the Eulerian and

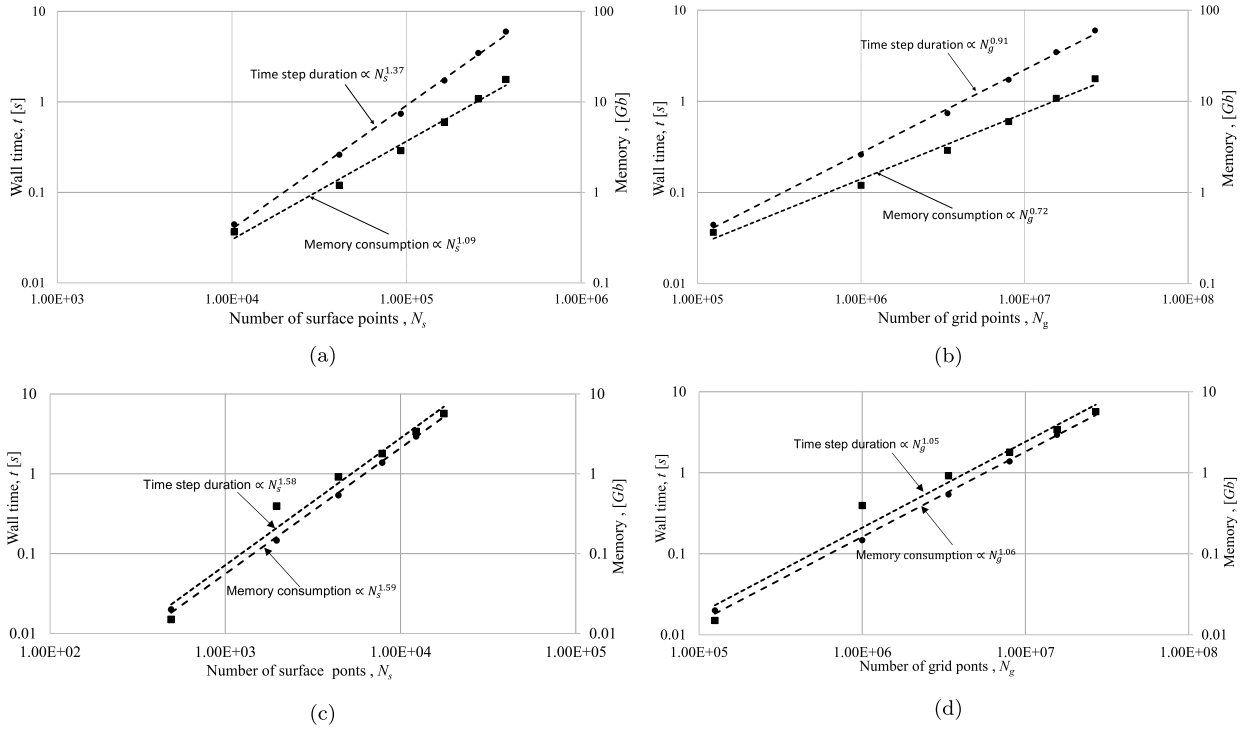

Fig. 22. Memory consumption and duration of a single time step as a function of the number of points on the surfaces of both spheres, N_s, and the total number of grid points, N_g obtained when simulating: natural convection flow developing between two concentric spheres for the values of $Ra = 4.6 \times 10^4$ and $\phi = 0.714$ (a-b); or lid-driven cavity flow within a cube with an embedded sphere of diameter $0.4L$ placed at the center of the cavity for the value of $Re = 400$ (c-d).

Lagrangian grid points is limited to 1.6, which is close to the $O(N^{4/3})$ complexity of the original solver [2], not upgraded with the IB capability; this indicates the high efficiency of the currently developed approach.

3.8. Future potential of the developed methodology

Adapting the developed IB methodology to the simulation of incompressible flows in the presence of non-stationary immersed bodies (e.g., moving boundary and two-way coupled FSI configurations) is a promising direction that has yet to be developed. The key idea is to exploit the fact that the Poisson-body forces system of Eqs. (13) constitutes a regularized saddle point problem in which the non-zero matrix $\boldsymbol{C}$ and its inverse $\boldsymbol{C}^{-1}$ can be approximated as $\boldsymbol{C} = -\frac{1}{2}\mathbf{I}$ and $\boldsymbol{C}^{-1} = -2\mathbf{I}$, respectively. As a result, the order in the Schur complement decomposition of the system of Eqs. (13) can be switched to proceed first with finding the pressure corrections field and then to continue with obtaining a solution for the Lagrangian force corrections field as:

$$\begin{cases} p' = (\boldsymbol{L} + 2\boldsymbol{B}^T\boldsymbol{B})^{-1}(RHS_{p'} + 2\boldsymbol{B}^T RHS_{\boldsymbol{F}'}), \\ \boldsymbol{F}' = 2(\boldsymbol{B}p' - RHS_{\boldsymbol{F}'}). \end{cases} \tag{22}$$

Note that for the above formulation the matrix $(\boldsymbol{L} + 2\boldsymbol{B}^T\boldsymbol{B})$ can be rebuilt very rapidly, as only $\boldsymbol{B}^T$ and $\boldsymbol{B}$ need to be updated and multiplied in each time step. The updating of the above matrices is "embarrassingly" parallel and can be conveniently implemented by employing either distributed or shared parallelization, while the multiplication of the two matrices can be implemented by employing the standard routines of any available linear algebra (e.g. LAPACK) library. The drawbackof the above formulation derives from the fact that in this case the matrix-vector product of the operator $(\boldsymbol{L} + 2\boldsymbol{B}^T\boldsymbol{B})^{-1}$ cannot be implemented by the available solvers of Laplace or Helmholts equations, which implies the necessity to develop a solver specifically dedicated to the solution of system (13). This development will require an in-depth investigation of the structure and properties of the above operator and is currently under investigation by us.

4. Conclusions

In this study, a new implicit formulation of the IB method, based on the SIMPLE algorithm adapted for coupling between velocity, pressure, and Lagrangian forces was developed. In this methodology, the pressure and Lagrangian forces fill the role of the DLMs imposing the incompressibility and the kinematic no-slip constraints, respectively. The developed methodology

Table A.12
Sequence of operations for proceeding by a single time step.

1.	Initialize the velocity $\boldsymbol{u}^{n,n-1}$ and pressure p^n fields with initial values or use them from the previous time steps.
2.	Calculate the intermediate velocity field by solving the momentum equation and the values of the velocity and pressure fields from the previous time steps: $\frac{3\boldsymbol{u}^*-4\boldsymbol{u}^n+\boldsymbol{u}^{n-1}}{2\Delta t} = -\nabla p^n + \frac{1}{Re}\nabla^2\boldsymbol{u}^* - (\boldsymbol{u}\cdot\nabla\boldsymbol{u})^n$.
3.	Calculate the pressure correction term by employing the continuity equation and solving the Poisson equation: $\nabla^2 p' = \frac{3}{2\Delta t}\nabla\cdot\boldsymbol{u}^*$.
4.	Calculate the velocity correction field: $\boldsymbol{u}' = -\frac{2}{3}\Delta t\nabla p'$.
5.	Proceed to the next time step by assigning $p^{n+1} = p^n + p'$, $\boldsymbol{u}^{n+1} = \boldsymbol{u}^* + \boldsymbol{u}'$.

formulates the Poisson-body force system of equations constituting the regularized saddle point problem, the solution of which yields coupled fields of pressure and Lagrangian forces corrections. The corrections are then used to obtain the velocity field, which simultaneously meets the incompressibility and the no-slip constraints.

A physically justified approximation of the Poisson-body force system of equations was developed. On the one hand, the structure of the approximated Poisson-body force system of equations resembles that obtained when applying the penalty method. On the other hand, in contrast to the penalty method, which relaxes a constrained problem by solving a series of unconstrained problems with a gradually decreasing penalty parameter, the approximated Poisson-body force system is an a priori-constrained, albeit approximated, system. The approximated Poisson-body force system was solved by a direct solver for the $2D$ configuration and by an iterative BiCgStab solver for a number of realistic $3D$ configurations. The BiCGStab algorithm was applied to the Schur complement of the top left block of the Poisson-body force system constituting the Laplace operator. The very structure of the Schur complement, provided a high convergence rate (no more than three iterations at any time step) of the BiCGStab algorithm.

The methodology developed in this study extends the state-of-the-art toolbox of available semi- and fully implicit IB methods. The method was successfully verified by applying it to the analysis of a number of representative $2D$ and $3D$ shear- and thermally driven confined steady-state and supercritical flows. The efficiency of the method was quantified by means of scaling its time step and memory consumption characteristics. In light of the fact that the Poisson-body forces system of equations constitutes a regularized saddle point problem, the potential of the developed methodology in its further adaptation to the simulation of moving boundary and two-way coupled FSI configurations is discussed, and a number of promising directions worthy of further research are opened.

CRediT authorship contribution statement

Conceptualization: Yuri Feldman, Oz Oshri, Kirill Goncharuk; Methodology: Yuri Feldman, Kirill Goncharuk; Software: Yuri Feldman, Kirill Goncharuk; Validation: Kirill Goncharuk; Data Curation: Yuri Feldman, Oz Oshri; Writing – Original Draft: Kirill Goncharuk; Writing – Review & Editing: Yuri Feldman, Oz Oshri; Project administration: Yuri Feldman, Oz Oshri; Funding acquisition: Yuri Feldman, Oz Oshri.

Declaration of competing interest

The authors declare that they have no known competing financial interests or personal relationships that could have appeared to influence the work reported in this paper.

Data availability

No data was used for the research described in the article.

Acknowledgement

This research was partially supported by the Israel Science Foundation (grant No. 950/22).

Appendix A. Brief description of the SIMPLE algorithm

The SIMPLE algorithm [37] is a widely used numerical method for solving incompressible NS equations. The algorithm is based on a pressure-correction approach, in which the velocity and pressure fields are iteratively corrected until a converged solution is obtained. The SIMPLE algorithm has been successfully applied to a wide range of problems in fluid dynamics. The sequence of operations of the algorithm for proceeding by a single time step in order of execution is summarized in Table 1. Note that a number of iterations can be required to provide a divergence-free velocity field up to a given precision prior to proceeding to the next time step. In this case, the Steps 2-5 should be reiterated, while Step 2 uses the updated pressure field to recalculate the predicted velocity $\boldsymbol{u}^*$ and this, in turn, is used in Step 3 to recalculate the pressure correction field p'. See Table A.12.

Appendix B. Interpolation and regularization operators

Following the formalism of the originally developed IB method [3], the surface of the immersed body is determined by a set of Lagrangian points not necessarily coinciding with an underlying Eulerian grid on which the continuity, NS, and energy equations are discretized and solved. For this reason, two adjoint operators, namely, the interpolation operator $\boldsymbol{I}$ and the regularization operator $\boldsymbol{R}$, are introduced. The interpolation operator $\boldsymbol{I}$ interpolates the Eulerian velocities and temperatures on the Lagrangian points, whereas the regularization operator $\boldsymbol{R}$ smears the Lagrangian volumetric forces and heat fluxes to the neighboring Eulerian grid. The interpolated velocities and temperatures are then used in the equations responsible for imposing the kinematic constraints of no-slip and prescribed temperature, respectively. The smeared volumetric forces and heat fluxes are, in turn, introduced as sources into the corresponding NS and energy equations.

Both the interpolation and the regularization operators used in this study utilize the discrete Dirac delta function proposed by Roma et al. [16]:

$$\delta(r) = \begin{cases} \frac{1}{6\Delta r}\left[5 - 3\frac{|r|}{\Delta r} - \sqrt{-3\left(1 - \frac{|r|}{\Delta r}\right)^2 + 1}\right] & \text{for } 0.5\Delta r \le |r| \le 1.5\Delta r, \\ \frac{1}{3\Delta r}\left[1 + \sqrt{-3\left(\frac{|r|}{\Delta r}\right)^2 + 1}\right] & \text{for } |r| \le 0.5\Delta r, \\ 0 & \text{otherwise}, \end{cases} \tag{B.1}$$

where Δr is the cell width in the r direction. This delta function has a compact support (only three grid cells in each direction), and obeys five basic rules (see Ref. [16] for additional details), which provide proper smoothness and conservation of the smeared/interpolated fields and makes the delta function applicable for the use on staggered grids. However, these rules can be met exactly only when the delta function is applied to equally spaced Eulerian grids and Lagrangian markers, while violation of these rules may result in increased stiffness of the interpolation and regularization operators.

The regularization and interpolation operators are defined as convolutions of the corresponding smeared or interpolated function with two- or three-dimensional discrete Dirac delta functions:

$$\boldsymbol{R}(\boldsymbol{F}^k(\boldsymbol{X}^k), Q^k(\boldsymbol{X}^k)) = \int_S (\boldsymbol{F}^k(\boldsymbol{X}^k), Q^k(\boldsymbol{X}^k)) \cdot \delta(\boldsymbol{x}_i - \boldsymbol{X}^k) dV_S^k, \tag{B.2a}$$

$$\boldsymbol{I}(\boldsymbol{u}(\boldsymbol{x}_i), \theta(\boldsymbol{x}_i)) = \int_\Omega (\boldsymbol{u}(\boldsymbol{x}_i), \theta(\boldsymbol{x}_i)) \cdot \delta(\boldsymbol{X}^k - \boldsymbol{x}_i) dV_{\Omega_i}, \tag{B.2b}$$

where dV_S^k corresponds to the finite volume of the thin shell surrounding the k^{th} Lagrangian point of the immersed body surface and dV_{Ω_i} corresponds to the i^{th} finite volume of the Eulerian grid. Note that to provide the best accuracy of the results, the two finite volumes should be close to each other.

Appendix C. Supplementary material

Supplementary material related to this article can be found online at https://doi.org/10.1016/j.jcp.2023.112148.

References

[1] W. Press, S. Teukolsky, W. Vetterling, B. Flannery, Numerical Recipes in Fortran 77: The Art of Scientific Computing, Cambridge University Press, 1989.
[2] H. Vitoshkin, A.Y. Gelfgat, On direct inverse of Stokes, Helmholtz and Laplacian operators in view of time-stepper-based Newton and Arnoldi solvers in incompressible CFD, Commun. Comput. Phys. 14 (2013) 1103–1119.
[3] C.S. Peskin, Flow patterns around heart valves: a numerical method, J. Comput. Phys. 10 (1972) 252–271.
[4] F. Sotiropoulos, X. Yang, Immersed boundary methods for simulating fluid-structure interaction, Prog. Aerosp. Sci. 65 (2014) 1–21.
[5] W. Hang, F. Tian, Recent trends and progress in the immersed boundary method, Proc. Inst. Mech. Eng., Part C, J. Mech. Eng. Sci. 223 (2019) 7617–7636.
[6] W. Kim, H. Choi, Immersed boundary methods for fluid-structure interaction: a review, Int. J. Heat Fluid Flow 75 (2019) 301–3–09.
[7] W. Xiao, H. Zhang, K. Luo, C. Mao, J. Fan, Immersed boundary method for multiphase transport phenomena, Rev. Chem. Eng. 38 (2022) 363–405.
[8] Y. Tseng, J. Ferziger, A ghost-cell immersed boundary method for flow in complex geometry, J. Comput. Phys. 192 (2003) 593–623.
[9] J. Lee, D. You, An implicit ghost-cell immersed boundary method for simulations of moving body problems with control of spurious force oscillations, J. Comput. Phys. 233 (2013) 295–314.
[10] D.M. Ingram, D.M. Causon, C.G. Mingham, Developments in cartesian cut cell methods, Math. Comput. Simul. 61 (2003) 561–572.
[11] R. Mittal, H. Dong, M. Bozkurttas, F.M. Najjar, A. Vargas, A. von Loebbecke, A versatile sharp interface immersed boundary method for incompressible flows with complex boundaries, J. Comput. Phys. 227 (2008) 4825–4852.
[12] L. Duan, H. Wang, X. Zhong, A high-order cut-cell method for numerical simulation of hypersonic boundary-layer instability with surface roughness, J. Comput. Phys. 229 (2010) 7207–7237.
[13] D. Schillinger, L. Dede, M.A. Scott, J.A. Evans, M. Borden, E. Rank, T.J.R. Hughes, An isogeometric design-through-analysis methodology based on adaptive hierarchical refinement of NURBS, immersed boundary methods, and T-spline CAD surfaces, Comput. Methods Appl. Mech. Eng. 249 (2012) 116–150.
[14] A. Main, G. Scovazzi, The shifted boundary method for embedded domain computations. Part I: Poisson and Stokes problems, J. Comput. Phys. 372 (2018) 972–995.

[15] A. Main, G. Scovazzi, The shifted boundary method for embedded domain computations. Part II: Linear advection-diffusion and incompressible Navier-Stokes equations, J. Comput. Phys. 372 (2018) 996–1026.
[16] A. Roma, C.S. Peskin, M.J. Berger, An adaptive version of the immersed boundary method, J. Comput. Phys. 153 (1999) 509–534.
[17] R. Mittal, G. Iaccarino, The immersed boundary method, Annu. Rev. Fluid Mech. 37 (2005) 239–261.
[18] J. Mohd-Yusof, Combined Immersed-Boundary/B-Spline Methods for Simulations of Flow in Complex Geometries, Center for Turbulence Research, Annual Research Briefs, 1997, pp. 317–327.
[19] E.A. Faldun, R. Verzicco, P. Orlandi, J. Mohd-Yusof, Combined immersed-boundary finite-difference methods for three-dimensional complex flow simulations, J. Comput. Phys. 161 (2000) 35–60.
[20] J. Wu, C. Shu, Implicit velocity correction-based immersed boundary-lattice Boltzmann method and its applications, J. Comput. Phys. 228 (2009) 1963–1979.
[21] K. Taira, T. Colonius, The immersed boundary method: a projection approach, J. Comput. Phys. 225 (2007) 3121–3133.
[22] S. Liska, T. Colonius, A fast immersed boundary method for external incompressible viscous flows using lattice Green's functions, J. Comput. Phys. 331 (2016) 257–279.
[23] A. Goza, T. Colonius, A strongly-coupled immersed-boundary formulation for thin elastic structures, J. Comput. Phys. 336 (2017) 401–411.
[24] D. Stein, R. Guy, B. Thomases, Immersed Boundary Smooth Extension (IBSE): a high-order method for solving incompressible flows in arbitrary smooth domains, J. Comput. Phys. 335 (2017) 155–178.
[25] B. Kallemov, A. Bhalla, B. Griffith, A. Donev, An immersed boundary method for rigid bodies, Commun. Appl. Math. Comput. Sci. 11 (2016) 79–141.
[26] Y. Feldman, Y. Gulbeg, An extension of the immersed boundary method based on the distributed Lagrange multiplier approach, J. Comput. Phys. 322 (2016) 248–266.
[27] Y. Feldman, Oscillatory instability of 2D natural convection flow in a square enclosure with a tandem of vertically aligned cylinders, Fluid Dyn. Res. 50 (2018) 051410.
[28] M. Huang, M. Shelley, D. Stein, A stable and accurate scheme for solving the Stefan problem coupled with natural convection using the immersed boundary smooth extension method, J. Comput. Phys. 432 (2021) 110162.
[29] A. Spizzichino, S. Goldring, Y. Feldman, The immersed boundary method: application to two-phase immiscible flows, Commun. Comput. Phys. 25 (2019) 107–134.
[30] J. Eldredge, A method of immersed layers on Cartesian grids, with application to incompressible flows, J. Comput. Phys. 448 (2022) 110716.
[31] Y. Feldman, Semi-implicit direct forcing immersed boundary method for incompressible viscous thermal flow problems: a Schur complement approach, Int. J. Heat Mass Transf. 127 (2018) 1267–1283.
[32] R. Sela, E. Zemach, Y. Feldman, A semi-implicit direct forcing immersed boundary method for periodically moving immersed bodies: a Schur complement approach, Comput. Methods Appl. Mech. Eng. 373 (2021) 113498.
[33] A. Spizzichino, E. Zemach, Y. Feldman, Oscillatory instability of a 3d natural convection flow around a tandem of cold and hot vertically aligned cylinders placed inside a cold cubic enclosure, Int. J. Heat Mass Transf. 141 (2019) 327–345.
[34] E. Zemach, A. Spizzichino, Y. Feldman, Instability characteristics of a highly separated natural convection flow: configuration of a tandem of cold and hot horizontally oriented cylinders placed within a cold cubic enclosure, Int. J. Therm. Sci. 159 (2021) 106606.
[35] S.V. Patankar, D.B. Spalding, A calculation procedure for heat, mass and momentum in three-dimensional parabolic flows, Int. J. Heat Mass Transf. 15 (1972) 1787–1806.
[36] M. Benzi, G.H. Golub, J. Liesen, Numerical solution of saddle point problems, Acta Numer. 14 (2005) 1–137.
[37] S.V. Patankar, Numerical Heat Transfer and Fluid Flow, McGraw-Hill, 1980.
[38] J. Van Doormal, G. Raithby, Enhancements of the simple method for predicting incompressible fluid flows, Numer. Heat Transf. 7 (1984) 147–163.
[39] W. Zeng, W. Tao, A comparison study of the convergence characteristics and robusteness for four variants of SIMPLE-family at fine grids, Eng. Comput. 20 (2003) 320–340.
[40] T.J. Chung, Computational Fluid Dynamics, Cambridge University Press, 2010.
[41] Y. Gulberg, Y. Feldman, On laminar natural convection inside multi-layered spherical shells, Int. J. Heat Mass Transf. 91 (2015) 908–921.
[42] H.G. Weller, G. Tabor, H. Jasak, C. Fureby, A tensorial approach to computational continuum mechanics using object-oriented techniques, Comput. Phys. 12 (1998) 620–631.
[43] J. Perot, An analysis of the fractional step method, J. Comput. Phys. 108 (1993) 51–58.
[44] P. Amestoy, I. Duff, J. LÉxcellent, J. Koster, Multifrontal parallel distributed symmetric and unsymmetric solvers, Comput. Methods Appl. Mech. Eng. 184 (1998) 501–520.
[45] P. Amestoy, I. Duff, J. LÉxcellent, J. Koster, A fully asynchronous multifrontal solver using distributed dynamic scheduling, SIAM J. Matrix Anal. Appl. 23 (2001) 15–41.
[46] C.S. Peskin, The immersed boundary method, Acta Numer. 11 (2002) 479–517.
[47] S. Gsell, U. D'Ortona, J. Favier, Explicit and viscosity-independent immersed-boundary scheme for the lattice Boltzmann method, Phys. Rev. E (2019) 033306.
[48] S. Gsell, J. Favier, Direct-forcing immersed-boundary method: a simple correction preventing boundary slip error, J. Comput. Phys. 435 (2021) 110265.
[49] V. Babu, S. Korpela, Numerical solutions of the incompressible, three-dimensional Navier-Stokes equations, Comput. Fluids 23 (1994) 675–691.
[50] U. Ghia, K. Ghia, C. Shin, Hig-re solutions for incompressible flow using the Navier-Stokes equations and a multigrid method, J. Comput. Phys. 48 (1982) 387–411.
[51] B. Souayeh, M. Alam, F. Hammami, N. Hdhiri, E. Yasin, Predicting the unsteady states of 2D and 3D lid-driven cavities induced by a centrally located circle and sphere, Fluid Dyn. Res. 52 (2020) 025507.
[52] J. Zhu, L.E. Holmedal, H. Wang, D. Myrhaug, Flow patterns in a steady lid-driven rectangular cavity with an embedded circular cylinder, Fluid Dyn. Res. 52 (2020) 065508.
[53] S.-G. Cai, A. Ouahsine, J. Favier, Y. Hoarau, H. Smaoui, Immersed boundary method for the simulation of lid-driven cavity flow with an embedded cylinder, in: VI International Conference on Computational Methods for Coupled Problems in Science and Engineering, CIMNE, 2015, pp. 1130–1137.
[54] S.-G. Cai, A. Ouahsine, J. Favier, Y. Hoarau, Moving immersed boundary method, Int. J. Numer. Methods Fluids 85 (2017) 288–323.
[55] C. Santarelli, T. Kempe, J. Fröhlich, Immersed boundary methods for heat transfer, Int. J. Numer. Methods Heat Fluid Flow 26 (2016) 504–514.
[56] K. Khanafer, S. Aithal, Laminar mixed convection flow and heat transfer characteristics in a lid driven cavity with a circular cylinder, Int. J. Heat Mass Transf. 66 (2013) 200–209.
[57] T. Huang, H. Zhao, H. Chen, Y. Yao, P. Yu, A hybrid cartesian-meshless method for the simulation of thermal flows with complex immersed objects, Phys. Fluids 34 (2022) 103318.
[58] Y. Wang, C. Shu, L. Yang, Boundary condition-enforced immersed boundary-lattice Boltzmann flux solver for thermal flows with Neumann boundary conditions, J. Comput. Phys. 306 (2016) 237–252.
[59] P. Leopardi, A partition of the unit sphere into regions of equal area and small diameter, Electron. Trans. Numer. Anal. 25 (2006) 309–327.
[60] D. Young, Y. Lin, C. Fan, C. Chiu, The method of fundamental solutions for solving incompressible Navier–Stokes problems, Eng. Anal. Bound. Elem. 33 (2009) 1031–1044.

[61] A. Povitsky, Three-dimensional flow in cavity at yaw, Nonlinear Anal., Theory Methods Appl. 63 (2005) e1573–e1584.
[62] Y. Feldman, Theoretical analysis of three-dimensional bifurcated flow inside a diagonally lid-driven cavity, Theor. Comput. Fluid Dyn. 29 (2015) 245–261.
[63] Y. Feldman, A.Y. Gelfgat, Oscillatory instability of a three-dimensional lid-driven flow in a cube, Phys. Fluids 22 (2010) 093602.
[64] A. Gelfgat, Linear instability of the lid-driven flow in a cubic cavity, Theor. Comput. Fluid Dyn. 33 (2019) 59–82.
[65] H.S. Yoon, D.H. Yu, M.Y. Ha, Y.G. Park, Three-dimensional natural convection in an enclosure with a sphere at different vertical locations, Int. J. Heat Mass Transf. 53 (2010) 3143–3155.
[66] J. Jeong, F. Hussain, On the identification of a vortex, J. Fluid Mech. 285 (1995) 69–94.
[67] Y.M. Seo, J.H. Doo, M.Y. Ha, Three-dimensional flow instability of natural convection induced by variation in radius of inner circular cylinder inside cubic enclosure, Int. J. Heat Mass Transf. 95 (2016) 566–578.
[68] N. Scurtu, B. Futterer, C. Egbers, Three-dimensional natural convection in spherical annuli, J. Phys. Conf. Ser. 137 (012017) (2008) 1–9.
[69] Y. Feldman, T. Colonius, On a transitional and turbulent natural convection in spherical shells, Int. J. Heat Mass Transf. 64 (2013) 514–525.
[70] V. Travnikov, K. Eckert, S. Odenbach, Linear stability analysis of the convective flow in a spherical gap with η = 0.714, Int. J. Heat Mass Transf. 80 (2015) 266–273.

Chapter 4

Implicit IBM with Vanka 'big-box' smoother

This chapter is based on: Goncharuk, K., Feldman, Y., & Oshri, O. (2025). *Implicit immersed boundary method integrated into a Vanka 'big box' smoother. Theoretical and Computational Fluid Dynamics.* https://doi.org/10.1007/s00162-025-00754-0.

The implicit Vanka–IBM is introduced to eliminate the decoupling error inherent to staged pressure–velocity and boundary-traction updates in semi-implicit schemes. Although computationally costlier than the SIMPLE-based IBM of Chapter 3, the present approach drives interfacial leakage to (practically) zero and stabilises added-mass coupling, enabling accurate near-boundary phenomena (e.g. vortex detachment from a supercritical NACA 0012).

Structure of the chapter.

1. **Introduction.** Motivation for an implicit interface treatment; contrast with the cheaper semi-implicit scheme (decoupling error vs. leakage/robustness).
2. **Theoretical background.**
   (a) **Governing equations.** Incompressible flow with immersed, moving boundaries (Lagrangian markers; regularised coupling).
   (b) **Numerical procedure.** Vanka "big-box'' blocks updating velocity, pressure, and immersed forces together; multigrid acceleration.
   (c) **Condition number and convergence.** Effects of implicit interface coupling on solver behaviour.
   (d) **Efficiency considerations.** Cost trade-offs relative to the semi-implicit scheme.

3. **Numerical results.** 2D/3D benchmarks, moving bodies, and vortex detachment from supercritical NACA 0012; leakage, accuracy, and stability.

4. **Conclusion.**

Theor. Comput. Fluid Dyn. (2025) 39:36
https://doi.org/10.1007/s00162-025-00754-0

ORIGINAL ARTICLE

Kirill Goncharuk · Mukesh Kumar · Oz Oshri · Yuri Feldman

Implicit immersed boundary method integrated into the Vanka 'big box' smoother.

Received: 23 February 2025 / Accepted: 18 August 2025

Abstract The current study introduces a novel fully coupled monolithic solver for the direct forcing immersed boundary method (IBM) in incompressible flows. The solver simultaneously integrates pressure, velocity, nonlinear convection terms, and Lagrangian forces into a unified framework, leveraging a modified big-box Vanka smoother extended with additional Lagrange multipliers arising from the IBM formulation. Central to the approach is the use of a Schur complement decomposition, which reduces the operator size by two-thirds while preserving both stability and accuracy. The solver's monolithic structure eliminates splitting errors and artificial pressure boundary conditions, common drawbacks of segregated methods. Additionally, the developed methodology enables high CFL numbers (up to 0.5), making it particularly effective for moving boundary simulations. Verification studies cover a broad set of benchmark problems, including both stationary and moving immersed bodies across a wide range of Reynolds numbers. These tests confirm that the solver achieves computational times comparable to existing semi-implicit methods while enhancing accuracy and stability. By addressing key challenges in high-fidelity incompressible flow simulations, the proposed method offers a robust and broadly applicable monolithic solver.

Keywords Immersed Boundary Method · Vanka Smoother · Fluid-Structure Interaction · Pressure-Velocity Coupling

Introduction

The immersed boundary method (IBM), introduced by Peskin [1], is a foundational computational tool for simulating fluid-structure interactions (FSI) in systems with complex geometrical interfaces. Its versatility and efficiency in handling boundary conditions on non-conforming meshes make it a widely used tool for applications encompassing biological fluid dynamics, particulate flows, and a wide spectrum of industrial applications including mixing processes, fluidized beds, membrane filtration systems, and wind turbine aerodynamics, to name but a few. For an in-depth review of IBM's formulations, implementations, and applications, refer to Verzicco et al. [2].

K. Goncharuk · M. Kumar · O. Oshri · Y. Feldman (✉)
Department of Mechanical Engineering, Ben-Gurion University of the Negev, David Ben Gurion Blvd, Beer-Sheva 8410501, Israel, Israel
E-mail: yurifeld@bgu.ac.il

K. Goncharuk
E-mail: kirillg@post.bgu.ac.il

M. Kumar
E-mail: mukesh@post.bgu.ac.il

O. Oshri
E-mail: oshrioz@bgu.ac.il

Published online: 08 September 2025

The immersed boundary method is not a self-contained solver; rather it operates in conjunction with an incompressible Navier–Stokes formulation, on which its accuracy and efficiency depend. In such formulations, pressure lacks an independent evolution equation and serves as a distributed Lagrange multiplier (DLM) to enforce the divergence-free constraint on the velocity field [3]. This gives rise to a saddle-point problem in which velocity and pressure are coupled through a differential constraint rather than through temporal dynamics. The resulting discrete system features a block structure with a zero diagonal in the pressure block, posing significant challenges for numerical solvers. To address this difficulty, one can consider decoupling strategies, such as the SIMPLE algorithm or projection-based methods. However, decoupling errors can lead to spurious pressure modes and mass conservation errors, especially at moderate-to-high Reynolds numbers.

Among IBM formulations, the direct forcing approach [4,5] has emerged as a computationally efficient method for enforcing no-slip boundary conditions. To implement this, Lagrangian forces are introduced to match the fluid velocity to that of the immersed surface, without assuming specific material properties. These Lagrangian forces serve as additional DLM, expanding the existing saddle-point structure. The resulting system simultaneously handles both the kinematic no-slip and the divergence-free constraints, which makes it considerably more challenging to solve.

Various strategies have been developed to solve the coupled saddle-point systems that arise in IBM formulations. Early methods used an explicit approach [6,7], where Lagrangian forces were computed from an intermediate velocity field that did not satisfy incompressibility. While simple, these methods required very small time steps to enforce the velocity constraint accurately. Semi-implicit formulations [8,9] improved stability by reformulating IBM into a projection-based saddle-point framework. However, they typically decoupled pressure and Lagrangian constraints from the velocity update. More recent methods based on the SIMPLE algorithm [10,11] improved coupling and efficiency but still involve operator splitting, which may reduce accuracy in highly unsteady or rapidly evolving flows.

Building on these developments, several recent studies have proposed fully monolithic approaches that couple all unknowns–velocity, pressure, and Lagrangian forces–within a single system [12–16]. Most of these methods, except for [15], solve the linear Stokes system using GMRES or direct solvers while treating the nonlinear convection terms explicitly. This strategy is adequate for low Reynolds number flows or smooth geometries but can compromise stability and accuracy in moderate to high Reynolds number regimes, particularly when dealing with complex or non-smooth geometries. Furthermore, the resulting linear systems are often large and ill-conditioned, requiring advanced and computationally demanding preconditioners to achieve convergence. For instance, [12,16] developed problem-specific preconditioners to manage these challenges. The method in [15] treats all nonlinear terms and constraints in a fully implicit manner, avoiding operator splitting. However, this comes with significant computational cost, making it practical primarily for applications such as slender-body dynamics where geometric stiffness dominates.

A key limitation of both explicit and semi-implicit IBM formulations is the decoupling of velocity from Lagrangian forces and pressure. This separation introduces consistency errors in the enforcement of kinematic and incompressibility constraints. This may result in fluid penetration, and spurious high-frequency oscillations of the Lagrangian forces. While acceptable in qualitative studies, such errors can undermine accuracy and stability in complex or unsteady simulations.

The purpose of the current study is twofold. First, we aim to develop an efficient solution strategy for the coupled saddle-point systems arising in the direct forcing IBM, by leveraging the proven effectiveness of the Vanka smoother for incompressible Navier–Stokes equations [17,18]. The Vanka smoother has demonstrated strong performance through its monolithic treatment of pressure–velocity coupling, thereby eliminating the need for artificial pressure boundary conditions. While Vanka-type smoothers have previously been explored in the context of implicit immersed boundary methods for the Stokes equations, for example as both solver and preconditioner in the continuous forcing formulation by [19], these approaches rely on force condensation and fully eliminate the Lagrangian variables from the system. In contrast, our contribution extends the Vanka framework to the direct forcing IBM by treating both Lagrangian forces and pressure as monolithic DLM. This fully coupled formulation enables direct enforcement of incompressibility and no-slip constraints at the solver level, without relying on elastic-body analogies or auxiliary constitutive laws.

Second, the monolithic solver developed in this study is well suited to serve as a computational framework for linear stability analysis of immersed boundary configurations. While time-stepping schemes are primarily used for transient simulations, they also provide a basis for computing steady states and analyzing their stability. In particular, they approximate the action of the Jacobian exponential, enabling matrix-free implementations of Newton–Krylov solvers and Arnoldi iterations [20]. Such methods are especially relevant for IBM, where linear stability studies remain limited to two-dimensional settings involving stationary [13,21,22], rotating

[23], or elastically mounted bodies [24–26]. This scarcity is largely due to the limitations of explicit and semi-implicit IBM formulations, which are generally incompatible with matrix-free iterative algorithms due to splitting errors and incomplete enforcement of velocity constraints. By directly coupling velocity, pressure, and Lagrangian forces within a unified solver, the present method overcomes these limitations and establishes a foundation for extending linear stability analysis to more complex immersed boundary problems in future studies.

Theoretical Background

Governing equations

The problem is governed by incompressible continuity and NS equations:

$$\begin{aligned} \nabla \cdot \mathbf{u} &= 0, \\ \frac{\partial \mathbf{u}}{\partial t} + (\mathbf{u} \cdot \nabla)\mathbf{u} &= -\nabla p + \frac{1}{Re}\nabla^2 \mathbf{u} + \mathbf{f}, \end{aligned} \tag{1}$$

where $\mathbf{u}$ is the velocity vector, p is the pressure field, $\mathbf{f}$ is the force density, and t corresponds to time. The equations were rendered dimensionless by utilizing L, U_0, L/U_0, ρU_0^2, and $\frac{\rho U_0^2}{L}$ to scale length, velocity, time, pressure, and force density, respectively, leading to a system governed by a single non-dimensional parameter, namely, the Reynolds number ($Re = \frac{LU_0}{\nu}$), where ν is the kinematic viscosity of the fluid.

According to the formalism of the IBM, the force density $\mathbf{f}$ entering the NS equations is regularized from the Lagrangian force density $\mathbf{F}$ determined around every point of the immersed body. This procedure, which constitutes the dynamic constraint, is implemented by introducing the regularization operator $R[\mathbf{F}]$. Closure of the overall system, as appears in Eq.(2), is achieved by introducing the kinematic constraint of no-slip, ensuring the same velocity values for the flow and for the surface of the immersed body,$\boldsymbol{U}_\Gamma$. This is accomplished by introducing an interpolation operator $I[\mathbf{u}]$ that interpolates the Eulerian velocities $\mathbf{u}$ on the surface of the immersed body. The two operators R and I are adjoint to each other and are implemented by using the discrete Dirac delta function. In the current study, we used the discrete Dirac delta functions developed in [27,28] for stationary immersed bodies, and in [29] for moving immersed bodies. The latter version of the discrete delta function aids in preventing spurious numerical oscillations of the solution at high CFL numbers.

$$\begin{aligned} \nabla \cdot \mathbf{u} &= 0, \\ \frac{\partial \mathbf{u}}{\partial t} + (\mathbf{u} \cdot \nabla)\mathbf{u} &= -\nabla p + \frac{1}{Re}\nabla^2 \mathbf{u} + R[\mathbf{F}], \\ I[\mathbf{u}] &= \boldsymbol{U}_\Gamma. \end{aligned} \tag{2}$$

The key feature of the developed method is based on recognizing that both pressure and force density fields constitute DLMs, contributing to the enforcement of incompressibility and no-slip kinematic constraints, respectively. Consequently, we treat both fields as a single DLM vector. To avoid working with stiff operators implicitly coupling all the flow and the DLM fields, we utilize the Vanka smoother approach [17], originally developed for pressure-velocity coupling via the symmetrical coupled Gauss-Seidel (SCGS) operator. The novelty of the developed method lies in proposing a modified SCGS operator encompassing an extended DLM, consisting of pressure and Lagrangian force density fields, that are fully coupled.

We start by focusing on a typical segment of a staggered Eulerian grid with a fragment of the immersed body's surface superimposed on it, as shown in Fig.1. Note that the fragment of the surface of the immersed body is determined by a single point where the unknown Lagrangian force densities F_x and F_y are introduced. Next, we express all the values of the unknown fields at the current iteration $k+1$ in terms of the sum of the values taken from the previous iteration k and the corresponding correction fields:

$$\mathbf{u}^{k+1} = \mathbf{u}^k + \mathbf{u}'; \quad p^{k+1} = p^k + p'; \quad \mathbf{F}^{k+1} = \mathbf{F}^k + \mathbf{F}'. \tag{3}$$

Plugging the above expressions back into Eqs. (2) leads to an extended formulation of the Vanka smoother:

$$-\left(\frac{u'_e - u'_w}{\Delta x} + \frac{v'_n - v'_s}{\Delta y}\right) = \underbrace{\left(\frac{u_e - u_w}{\Delta x} + \frac{v_n - v_s}{\Delta y}\right)^k}_{\text{Continuity equation residual}}; \tag{4}$$

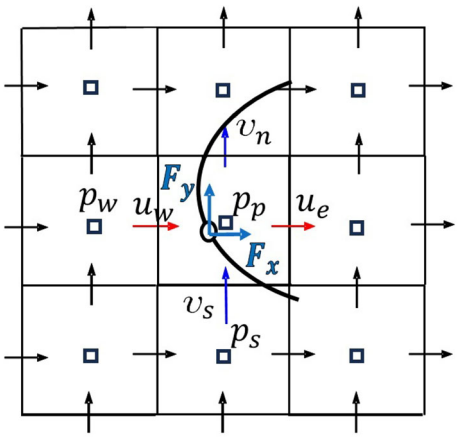

Fig. 1 A segment of a staggered Eulerian grid with a fragment of the immersed body's surface superimposed on it. The solid line represents the immersed body; symbols ∘ indicate Lagrangian points on the body with the corresponding body forces **F**. Symbols □ denote pressure field locations on the staggered grid, while → and ↑ represent horizontal and vertical velocity component locations, respectively

$$\left(\frac{3}{2}\Delta t + a_w \frac{1}{\mathrm{Re}}\right) u'_w + a_p p'_p - a_w p'_w + \sum_i R[F'_{x_i}]$$
$$= \underbrace{[-\partial_x p - \nabla\cdot(u\mathbf{u}) + \frac{1}{Re}\nabla^2 u - \frac{3}{2}\Delta t u_w]^k + (2u_w^n - \frac{1}{2}u_w^{n-1})\Delta t - \sum_i R[F^k_{x_i}]}_{\text{X-momentum equation residual}}; \tag{5}$$

$$\left(\frac{3}{2}\Delta t + a_s \frac{1}{\mathrm{Re}}\right) v'_s + a_p p'_p - a_s p'_s + \sum_i R[F'_{y_i}]$$
$$= \underbrace{[-\partial_y p - \nabla\cdot(v\mathbf{u}) + \frac{1}{Re}\nabla^2 v - \frac{3}{2}\Delta t v_s]^k + (2v_s^n - \frac{1}{2}v_s^{n-1})\Delta t - \sum_i R[F^k_{y_i}]}_{\text{Y-momentum equation residual}}; \tag{6}$$

$$\sum_i I[\mathbf{u}'_i] = \underbrace{\mathbf{U}^\Gamma - \sum_i I[\mathbf{u}^k_i]}_{\text{No-slip kinematic constraint residual}}, \tag{7}$$

where index i in the summation spans all the Lagrangian and Eulerian points for the regularization R and interpolation I operators, respectively. This provides an additional layer of coupling between the Lagrangian forces exerted by the body on the surrounding flow and the flow's velocity and pressure fields. Note that the above system of equations is not closed, as the momentum equations are formulated for u_w and v_s velocity components attached to the "west" and the "south" boundaries of a single finite volume (see Fig. 1), whereas the continuity equation includes the velocities attached to all the boundaries, i.e., "west", "east", "north" and "south". Closure is achieved by assembling the whole set of equations belonging to the entire computational domain in a 'big-box' manner, as proposed in [19,30]. Thereafter we exploit the special structure of the assembled operator to efficiently solve the system by employing the Schur complement approach and the direct open-source solver MUMPS [31,32], as detailed in the next section.

Numerical procedure

All the spatial terms in the governing equations were discretized using the standard finite volume method on a staggered grid [33], where the central difference was employed for approximating all the fluxes and shear stresses on the faces of the corresponding finite volumes. A second-order backward finite difference was utilized for the time derivative discretization.

To demonstrate the techniques that were further employed in the solution method that deals with the extended Vanka SCGS operator, we first use the original 'big-box' Vanka block operator as an example, without invoking the IBM formalism. We ensure that the currently built operator, given by $\begin{pmatrix} D & B^T \\ B & 0 \end{pmatrix}$, is symmetric by design. This symmetry is achieved by incorporating the discrete form of the continuity equation (matrix B) with a negative sign and by the diagonal structure of matrix D, with entries $a_{u,v}$ derived either from the conservation of linear momentum equations or from the boundary conditions. Overall, the system can be written as:

$$\begin{pmatrix} D & B^T \\ B & 0 \end{pmatrix} \begin{pmatrix} \mathbf{u}' \\ \mathbf{p}' \end{pmatrix} = \begin{pmatrix} \mathbf{r_u} \\ \mathbf{r}_p \end{pmatrix}, \tag{8}$$

where the residuals $\mathbf{r_u}$ and $\mathbf{r}_p$ correspond to the right hand side of the momentum and continuity equations, respectively. The above matrix can be decomposed using the Schur complement approach as follows:

$$(BD^{-1}B^T)\mathbf{p}' = BD^{-1}\mathbf{r}_u - \mathbf{r}_p, \tag{9}$$

$$\mathbf{u}' = D^{-1}\mathbf{r_u} - D^{-1}B^T\mathbf{p}'. \tag{10}$$

To solve the pressure correction equation (Eq.(9)), the matrix $(BD^{-1}B^T)$ is first constructed and subsequently factorized using LU decomposition. Given that D is a diagonal matrix, its inverse D^{-1} can be directly computed as a diagonal matrix with reciprocal values along its main diagonal. The matrix $(BD^{-1}B^T)$ is then efficiently assembled through the utilization of standard MKL [34] utilities for sparse matrix-vector multiplications. This approach offers two principal advantages over the original formulation in Eq. (8): a significant reduction in system size (to one-third of the original) and the guarantee of symmetry and positive definiteness. Furthermore, the latter enables the MUMPS solver to leverage efficient decomposition into the LDL^T form for symmetric positive definite matrices. On average, the algorithm converges within $O(10)$ iterations per time step, with convergence behavior influenced by the CFL number, providing a mechanism for effective control.

For cases where $(BD^{-1}B^T)$ does not incorporate IBM forces, the Conjugate Gradient (CG) method can be applied efficiently without preconditioning, yielding solutions to machine precision faster than direct solvers. This efficiency is attributed to the relatively low condition number inherent to the system. However, the inclusion of IBM forces induces a substantial increase in the condition number, thereby rendering the CG method less effective in the absence of appropriate preconditioning. In such instances, the direct solver is preferred due to its robustness and reduced sensitivity to the condition number, ensuring both stability and accuracy in the solution process.

Embedding of the immersed boundary capability

In line with the idea of combining pressure and force density fields into a unified DLM field, we next determine the extended M and M^T operators as $M = \begin{pmatrix} B \\ I \end{pmatrix}$ and $M^T = \begin{pmatrix} B^T & R \end{pmatrix}$. The corresponding right hand side operators are extended accordingly as $\mathbf{m}' = \begin{pmatrix} \mathbf{p}' \\ \mathbf{f}' \end{pmatrix}$ and $\mathbf{r}_m = \begin{pmatrix} \mathbf{r}_p \\ \mathbf{r_f} \end{pmatrix}$, where $\mathbf{r_f}$ is a residual corresponding to the kinematic constraint of no-slip on the surface of the immersed body. By following the above conventions, the system of Eqs.(8) is reformulated to address the immersed boundary capability as follows:

$$\begin{pmatrix} D & M^T \\ M & 0 \end{pmatrix} \begin{pmatrix} \mathbf{u}' \\ \mathbf{m}' \end{pmatrix} = \begin{pmatrix} \mathbf{r_u} \\ \mathbf{r_m} \end{pmatrix}. \tag{11}$$

Similarly to the configuration not invoking the immersed boundary capability, the above system is again decomposed by the Schur complement approach, resulting in:

$$(MD^{-1}M^T)\mathbf{m}' = MD^{-1}\mathbf{r_u} - \mathbf{r_m}. \tag{12}$$

$$\mathbf{u}' = D^{-1}(\mathbf{r_u} - B^T\mathbf{p}' - R\mathbf{f}'), \tag{13}$$

The operator $MD^{-1}M^T$ governing Eq. 12 is also symmetric and positive definite. Moreover, it can be built in a block matrix manner as:

$$(MD^{-1}M^T) = \begin{pmatrix} BD^{-1}B^T & BD^{-1}R \\ ID^{-1}B^T & ID^{-1}R \end{pmatrix}. \tag{14}$$

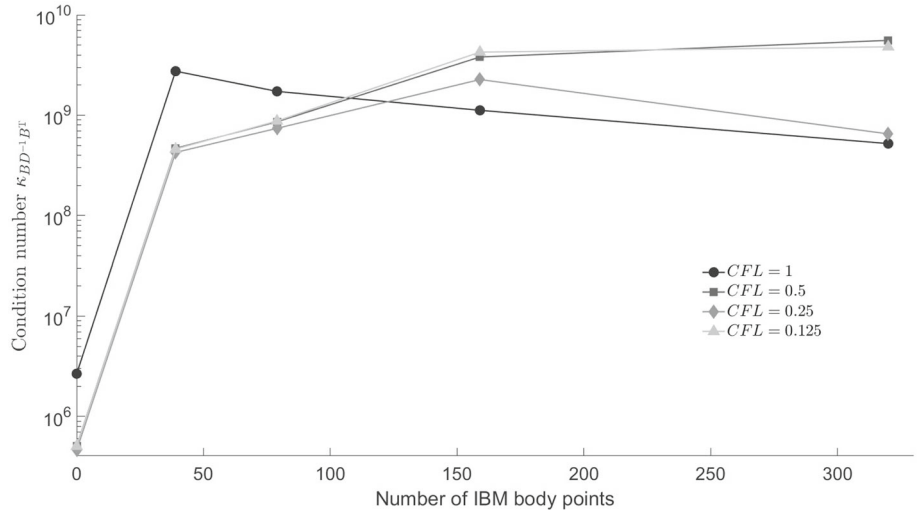

Fig. 2 Condition number $\kappa_{BD^{-1}B^{\mathrm{T}}}$ for lid-driven cavity problem simulated on 128^2 grid versus immersed-boundary point count for four CFL numbers. The points on the Y axis corresponds to the baseline case without an immersed boundary

In examining the above representation, it is clear that the biggest part is contributed by the original $(BD^{-1}B^T)$ block. As expected, the condition number of the extended formulation is significantly influenced by the operators I and R and can still be high. At the same time, the smoothing characteristics of the Vanka operator provide sustainable convergence, allowing for an accurate solution even for high values of the CFL number.

Condition number and convergence

We define the condition number of Schur complement as the 2-norm relation $\kappa_{BD^{-1}B^{\mathrm{T}}} = \|BD^{-1}B^{\mathrm{T}}\|_2 \, \|(BD^{-1}B^{\mathrm{T}})^{-1}\|_2$. For the Vanka 'big-box' solver, $\kappa_{BD^{-1}B^{\mathrm{T}}}$ increases by roughly three orders of magnitude once immersed-boundary (IB) forces are incorporated (Fig. 2).

Increasing the amount of IB points from 39 to 320 was implemented by varying the diameter of the cylinder placed in the center of cavity from $d = 0.1$ to $d = 0.8$. Domain discretized by 128^2 grid and $\Delta s \approx \Delta x$ is kept constant. The change in number of Lagrangian markers does *not* exacerbate the ill-conditioning: all curves align near 10^9–10^{10}, irrespective of the CFL number. Without IBM, the Schur complement $BD^{-1}B^T$ is sensitive to CFL, yet this dependence vanishes once the velocity–force interaction is added. The condition number is further influenced by the problem physics and mesh resolution. More intricate bodies, such as a NACA airfoil, yield higher condition numbers than simpler configurations (e.g. a tandem cylinder system), and $\kappa_{BD^{-1}B^{\mathrm{T}}}$ growth as the grid is refined. Consequently, Krylov-subspace solvers become impracticable for this solver with IBM unless proper preconditioner is employed.

Even though the condition number plateaus, solver performance still remains governed by the CFL number. Figures 3a and 3b reveal an almost linear growth in iteration count with CFL. Thus, increasing the CFL slows convergence even when the underlying linear system is no further ill-conditioned.

Efficiency considerations

A significant advantage of the $MD^{-1}M^T$ operator structure, determined by Eq. (14), becomes evident when applying it to the simulation of moving boundary problems. In this case, the $(BD^{-1}B^T)$ block does not include the moving boundary characteristics and should, therefore, be computed only once at the beginning of the simulation. Consequently, only the remaining much smaller blocks, incorporating regularization or interpolation operators, need to be recalculated in each time step. This significantly boosts the overall computational efficiency of the developed method.

Another important advantage of the developed approach is its natural suitability for domain decomposition. While the current analysis uses the 'big-box' Vanka approach across the entire computational domain, the formulation can readily integrate domain decomposition techniques similar to those explored in [30]. This decomposition reduces operator stiffness within each patch of the decomposed domain. However, since domain

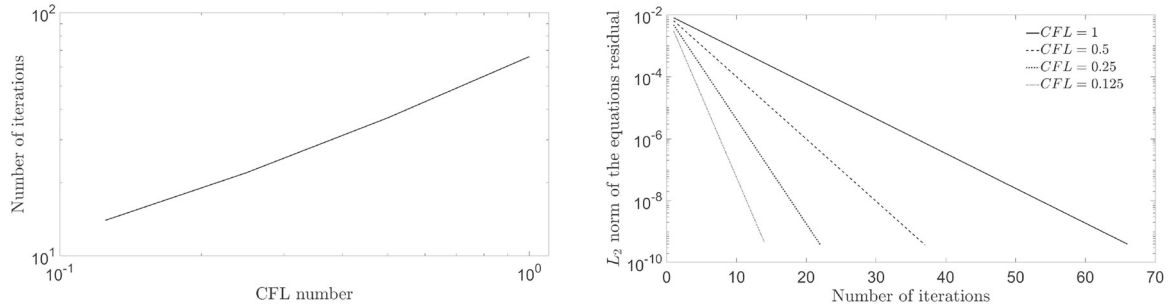

(a) Iterations required to reach $\|\mathbf{r}\|_2 < 10^{-9}$ as a function of CFL.

(b) L_2 residual norm versus iteration count for the four CFL numbers.

Fig. 3 Convergence behaviour of the Vanka big-box solver with an immersed boundary for lid-driven cavity problem simulated on 128^2 grid with a cylinder of $d = 0.5$ determined by 200 IB points. Smaller CFL numbers expedite convergence even though the condition number remains essentially unchanged (Fig. 2)

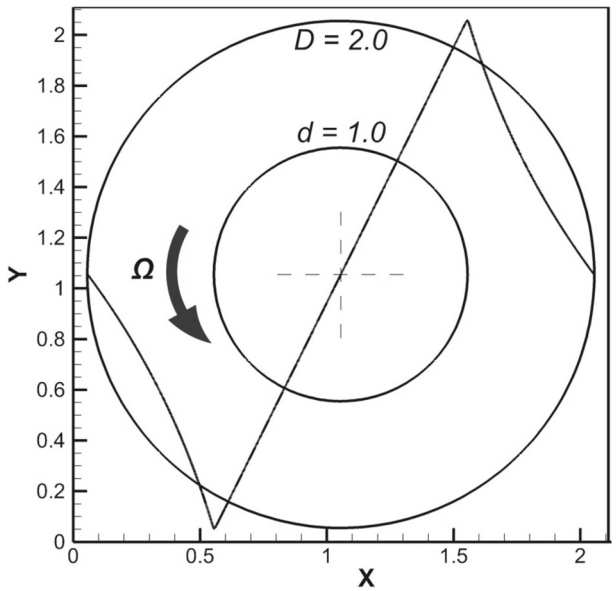

Fig. 4 Schematic of the computational setup and analytical solution for the u_θ velocity field. The setup consists of a rotating cylinder with diameter $d = 1.0$ placed inside a statiomary cylinder with diameter $D = 2.0$. Both cylinders placed within a periodic square domain of size $L = 2.11$. The inner cylinder rotates with an angular velocity $\Omega = 1 + \tanh((t - 0.2)/0.05)$, and the Reynolds number is set to $Re = 100$. The direction of rotation is indicated by the arrow. The black line corresponds to the analytical solution at steady state

decomposition typically increases the required iteration count, we opted for a single domain in these 2D configurations. Future research will explore domain decomposition for 3D flow simulations.

The convergence can be further accelerated using the multigrid method established in [17]. However, our numerical experiments showed minimal iteration reduction in 2D simulations. The current implementation achieves significant problem size reduction through the Schur complement approach with the 'big-box' Vanka solver without compromising solution convergence. Both domain decomposition and multigrid methods will be evaluated for future 3D configurations.

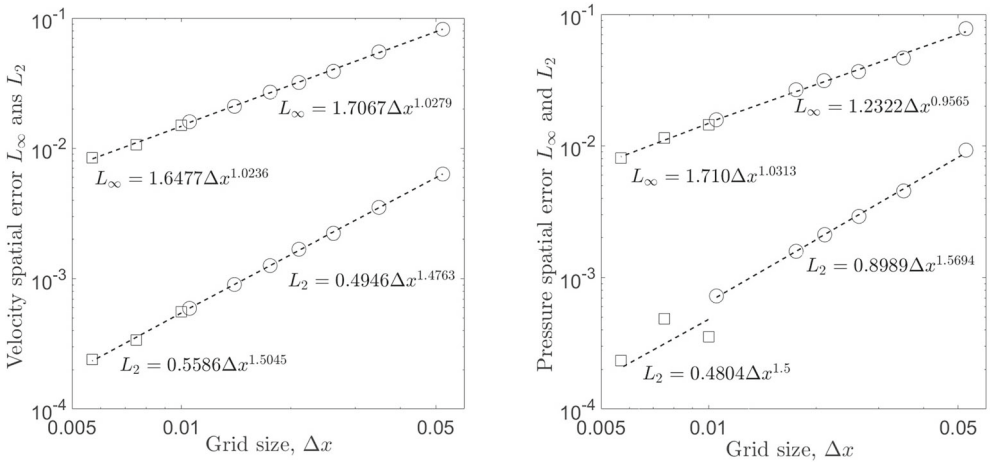

Fig. 5 Spatial error convergence for velocity and pressure in the rotating cylinder setup estimated in terms of L_∞ and L_2 norms of the errors. Squares and circles correspond to the currently obtained values and the corresponding data reported in [9], respectively. The dotted lines represent the corresponding least square power trends

Numerical results

Flow inside two concentric cylinders: spatial convergence and memory scaling

To investigate the efficiency of our method in terms of grid convergence and memory consumption, we conducted a comparison of the obtained results with those presented in [9] for the flow inside two concentric cylinders. This setup is most suitable as a test case for immersed boundary methods, as it has analytical solution to assess the spatial accuracy of numerical solvers.

The computational setup consists of two concentric cylinders: an inner rotating cylinder with prescribed angular velocity $\mathbf{\Omega}$ and a stationary outer cylinder (see Fig. 4). The Reynolds number was set to $Re = 100$, and the angular velocity of the inner cylinder was defined as $\mathbf{\Omega} = 1 + \tanh((t - 0.2)/0.05)$. The boundary conditions for the entire computational domain were set to be periodic, consistent with the configuration used in [9]. Spatial convergence was evaluated by comparing our results to an analytical solution for this setup in terms of L_1 and L_∞ norms of the difference between the numerical and the analytical solutions. For the sake of consistency in calculation of the pressure field, a Dirichlet point for pressure was placed precisely at (1.055, 1.055).

The difference norms plotted on a log-log scale (see Fig. 5) visualize the grid convergence rates, derived by fitting trendlines to the data points. The observed convergence rates matched the expected values reported in [9], verifying the accuracy of the currently developed method. For the L_∞ norm, the convergence rate was approximately 1.0 for both pressures and velocity fields, consistently with the reference results.

The present results can be meaningfully compared with those reported in [9] since periodic boundary conditions eliminate decoupling errors typical of semi-implicit IBM, enabling direct accuracy comparison with our fully coupled formulation. For non-periodic boundaries, our method should achieve superior accuracy by inherently avoiding these decoupling errors.

In addition to the spatial accuracy, we evaluate the memory consumption of the solver under varying grid resolutions. Despite the monolithic nature of the solver and the memory-intensive requirements typical of direct solvers using the MUMPS solver, we achieved reduced memory consumption due to the following factors:

- Only the BDB^T matrix requires LDL^T factorization, significantly reducing the matrix size.
- The BDB^T is symmetric positive definite matrix , enabling LDL^T decomposition without pivoting and requiring storage of only a single factorized L matrix and a main diagonal.

To optimize memory usage further, we examine the conjugate gradient (CG) method scaling. Using CG with the immersed boundary method requires symmetric preconditioning to enhance convergence, as previously discussed. The CG solver achieves approximately twofold reduction in memory consumption compared to MUMPS for the 2D case, while maintaining the same linear scaling. The results obtained for this benchmark confirm the first-order spatial accuracy of the L_∞ norm and demonstrate the linear scaling in memory con-

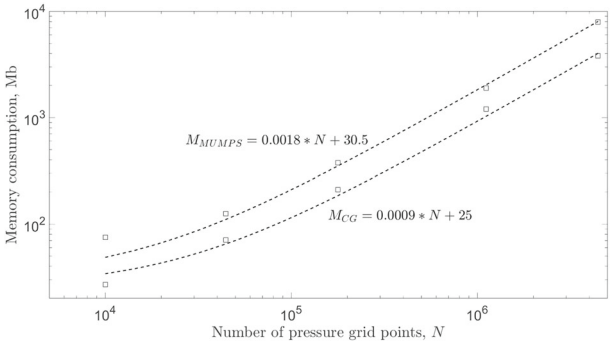

Fig. 6 Memory consumption as a function of grid resolution for the 2D simulation of flow between two concentric cylinders. Values are shown for both symmetric LDL^T factorization and conjugate gradient method solvers. The dotted lines represent the corresponding linear least square trends

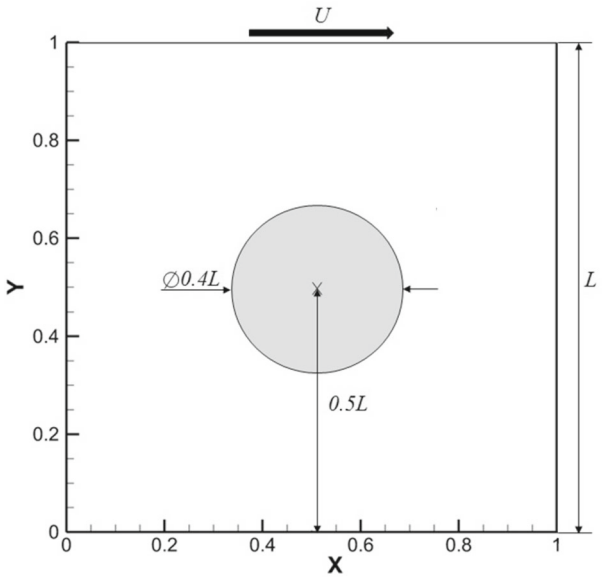

Fig. 7 Lid-driven cavity with a cylinder placed at the center: physical model

sumtion with the number of grid points in 2D simulations. Having verified the method's accuracy, we proceed to examine standard test cases.

Lid-driven cavity with a cylinder placed in a center

The configuration considered is the lid-driven cavity problem with a circular cylinder placed in the cavity center. The geometry consists of a square cavity of side L containing a cylinder of diameter $0.4L$ at its center. The top lid moves with constant velocity U in the x-direction, while all other boundaries remain stationary (see Figs. 6 and 7). No-slip boundary conditions were applied to all the cavity boundaries and to the cylinder surface. The steady-state criterion was established as $l_2 \leq 10^{-6}$, where l_2 is the second norm calculated for the relative deviation between two consecutive time steps for all the flow variables.

The results of the grid independence study performed for the above configuration are summarized in Table 1 in terms of the extreme values obtained for the x and y velocity components. The simulations were conducted for three different values of Re on three progressively refined grids, with grid resolution doubling each time. The relative deviations between the corresponding extreme values of all the velocity components obtained on the 256^2 and 512^2 grids did not exceed 0.5%, 1.6%, and 2.4% for $Re = 1000$, 5000, and 8000, respectively. Based on the above analysis, all further simulations of supercritical and subcritical flow regimes were conducted on a 512^2 grid.

Table 1 Results of a grid independence study obtained at three different Re values for the lid-driven cavity flow with a cylinder of diameter $D = 0.4$ placed at the cavity center

Grid	$Re = 1000$			$Re = 5000$			$Re = 8000$		
	$u_{x_{min}}$	$u_{y_{max}}$	$u_{y_{min}}$	$u_{x_{min}}$	$u_{y_{max}}$	$u_{y_{min}}$	$u_{x_{min}}$	$u_{y_{max}}$	$u_{y_{min}}$
128^2	−0.3371	0.3241	−0.4559	−0.4063	0.3924	−0.5148	−0.4027	0.3937	−0.5011
256^2	−0.3428	0.3291	−0.4634	−0.4289	0.4125	−0.5425	−0.4361	0.4242	−0.5438
512^2	−0.3445	0.3307	−0.4655	−0.4351	0.4181	−0.5509	−0.4462	0.4325	−0.5569

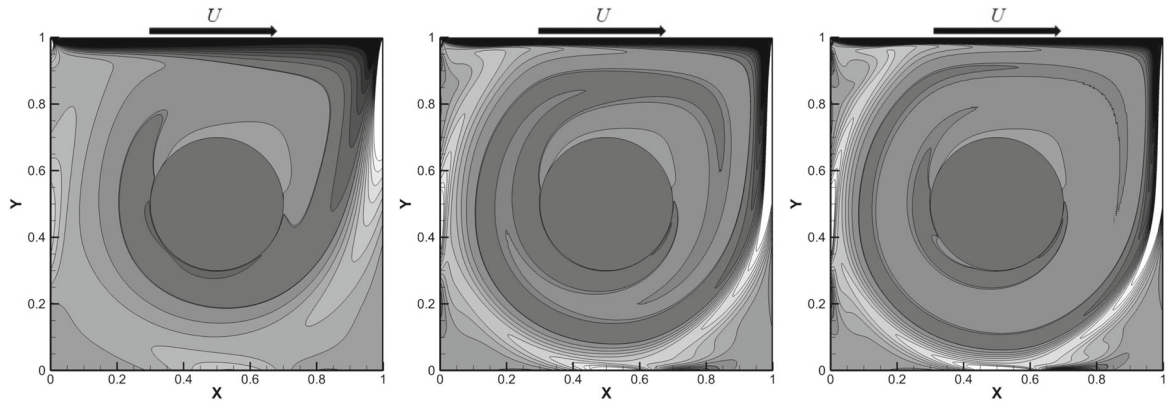

Fig. 8 Vorticity field inside the cavity with cylinder at $Re = 1000$ (left), $Re = 5000$ (center) and $Re = 8000$ (right). Contour levels were set from -12 to 12 in increments of 1.6 with an additional value of -2.35

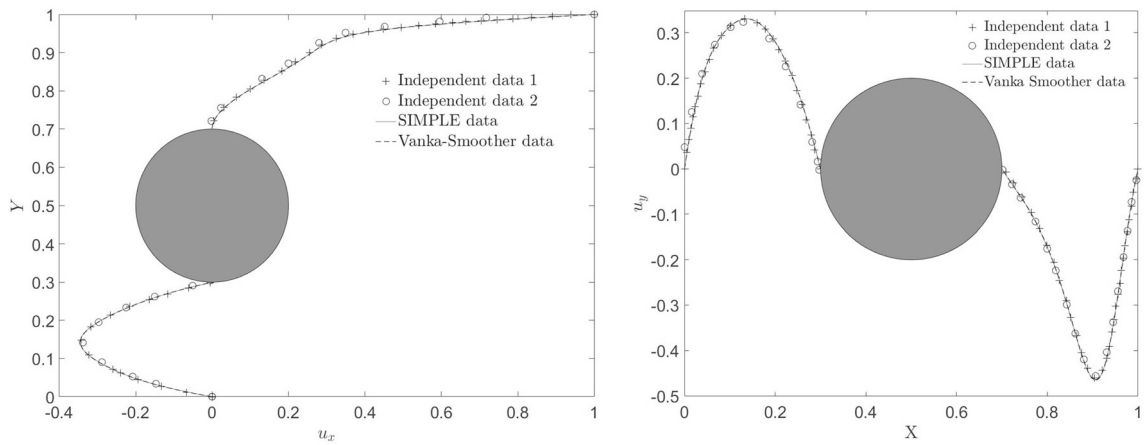

Fig. 9 Velocity components measured along the cavity center lines, $Re = 1000$: (a) v_x velocity component measured along the vertical center line; (b) v_y velocity component measured along the horizontal centre line. The solid line corresponds to the data obtained by SIMPLE algorithm[10], the dashed line represents currently obtained data, ∘ symbols correspond to the data reported in [35], and + symbols correspond to the data reported in [36]

To verify the obtained data, we compared vorticity fields calculated at $Re = 1000$, 5000, and 8000 with the corresponding results available in the literature. Our results presented in Fig. 8 are in good qualitative agreement with the corresponding data reported in [36] as well as with our previous study [10]. Additionally, we conducted a quantitative comparison of the u_x and u_y velocity components along the cavity's vertical and horizontal center lines at $Re = 1000$. The comparison was performed between our results and the values reported in [35,36]. Furthermore, we compared our results with those from our previous study that used the SIMPLE-based algorithm [10]. The comparison shown in Fig. 9 shows excellent agreement between our results and the data reported in all the previous studies.

We conclude this section by presenting results obtained for supercritical flow regimes at $Re = 8600$, 8700, 8800, and 8900. Table 2 summarises the amplitude values for the first three harmonics and the oscillation

Table 2 Oscillation frequencies f and amplitudes A at the control point $(0.9, 0.1)$ for slightly super-critical lid-driven-cavity flow. Present results are compared with the [10], for data that was available. A dash (—) indicates that no value was given in the earlier work

Re	Harmonic 1 ($n = 1$)			Harmonic 2 ($n = 2$)				Harmonic 3 ($n = 3$)	
	f	f Ref. [10]	A	ARef. [10]	f	f Ref. [10]	A	f	A
8900	0.500	–	$1.14 * 10^{-3}$	–	1.000	–	$7.84 * 10^{-5}$	1.500	$3.39 * 10^{-6}$
8800	0.500	0.489	$1.00 * 10^{-3}$	$6.96 * 10^{-4}$	1.000	0.978	$5.93 * 10^{-5}$	1.500	$2.89 * 10^{-6}$
8700	0.500	0.489	$8.40 * 10^{-4}$	$5.11 * 10^{-4}$	1.000	0.978	$3.78 * 10^{-5}$	1.500	$1.89 * 10^{-6}$
8600	0.500	0.491	$6.61 * 10^{-4}$	$6.23 * 10^{-5}$	1.000	0.982	$1.54 * 10^{-5}$	1.500	$1.24 * 10^{-6}$

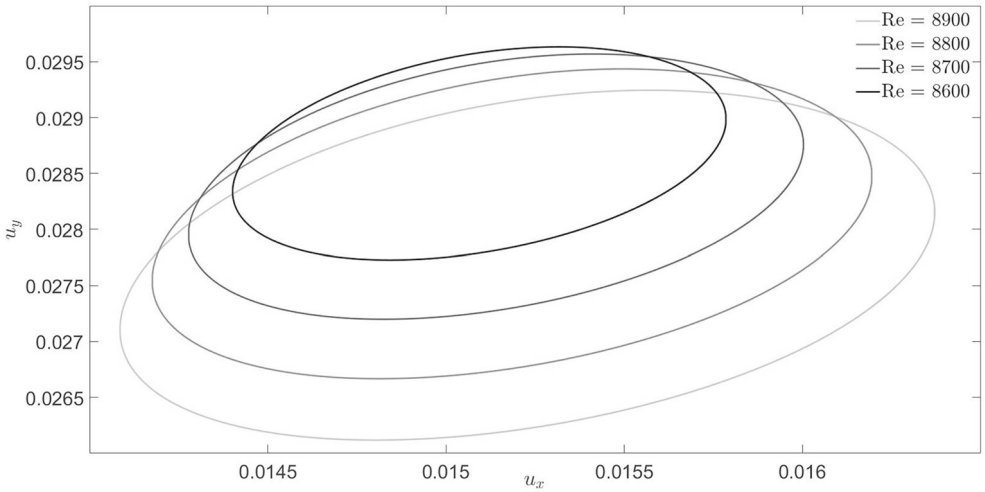

Fig. 10 Velocity trajectories measured at (0.9,0.1) in the supercritical mode for four different Re numbers: 8600, 8700, 8800 and 8900

frequencies f values obtained for different Re numbers. Remarkably, the frequency values of the main harmonic and its multipliers, typically showing up for non-linear dynamic systems, coincide with each other for the entire range of the Re values and are in agreement (not exceeding 2% frequency discrepancy) with the corresponding data previously reported by us in [10].

The accuracy of the obtained slightly supercritical results was further confirmed by examining the corresponding velocity trajectories at the point (0.9,0.1) (see Fig. 10). These trajectories establish clearly recognizable limit cycles, indicating that periodic stationary flow was reached for the entire range of Re values.

Three-dimensional lid-driven cavity with an embedded sphere

We next examine confined shear flow in a cubic lid–driven cavity of side L containing a sphere of diameter $D = 0.25L$ placed in the center of the cavity (Fig. 11). The top wall moves with a uniform velocity U in the x-direction, while the remaining walls and the sphere remain stationary. All quantities are scaled using the characteristic chamber length L and lid velocity U, yielding a characteristic time scale of L/U.

Immersed-boundary discretisation.

The spherical surface is represented by uniformly distributed Lagrangian markers generated with the non-iterative algorithm of Leopardi [37]. The marker spacing is chosen to be close to the local Eulerian grid spacing around the immersed surface to maximize interpolation accuracy.

Grid-independence study.

To establish a suitable mesh, simulations were carried out on N^3 Cartesian grids with $N = \{100, 150, 200\}$ at $Re = 1,\ 100,\ 400$. Figure 12 illustrates contours of the streamwise velocity u_x in the cross mid-plane obtained on the finest grid; the distributions remain symmetric with respect to the vertical centre-plane for all Reynolds numbers, and the boundary layer narrowing with Re matches the trends reported by [38].

Table 3 summarises the the grid independance study. The focus is on the extreme values of the centre-line velocities. For each Reynolds number we extract $u_x^{\max}(z),\ u_x^{\min}(z)$ along the vertical centre-line, and

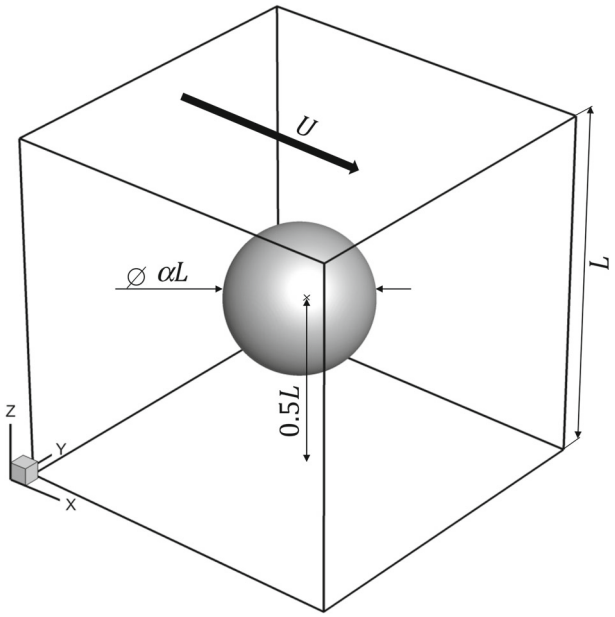

Fig. 11 Cubic lid-driven cavity with a sphere placed in the center of cavity: physical model

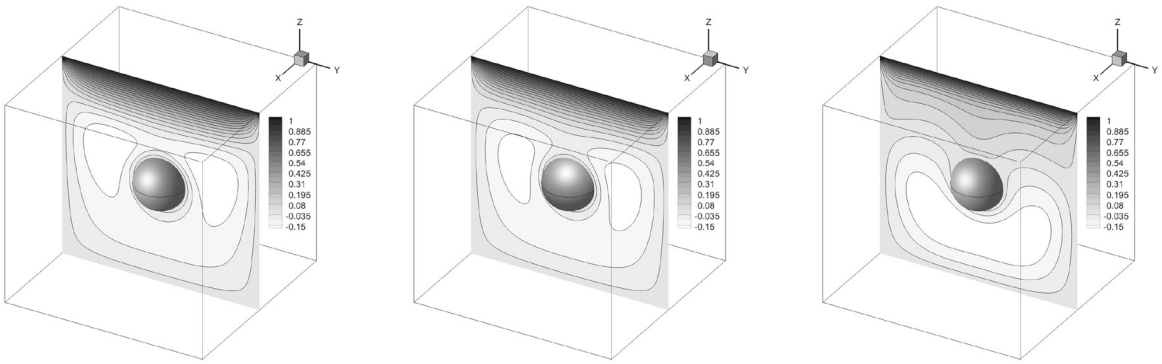

Fig. 12 3D lid driven cavity contours of the streamwise velocity u_x in the mid-plane for obtained for $Re = 1$ (left), $Re = 100$ (center) and $Re = 400$ (right)

$u_z^{\max}(x)$, $u_z^{\min}(x)$ along the horizontal centre-line, together with the coordinates at which the extrema occur. Table 3 lists these four quantities obtained on the grids 100^3, 150^3, and 200^3. Convergence is deemed satisfactory when the change between the two finest meshes falls below 1%.

Verification study.

Following the performed grid independence study, velocity profiles computed on the 200^3 mesh were compared with the data from [38] and with the numerical data from our previous research [10]. Table 4 reports the comparison at twelve test locations, while we define the relative error $\varepsilon_{\text{rel}} = |\phi_{\text{present}} - \phi_{\text{ref}}|/|\phi_{\text{ref}}|$. For the majority of points the error stays below 5%; the largest deviations (up to 10%) occur where the reference velocity is close to zero, consistent with earlier studies.

In addition to the velocity profiles, we report the drag (C_D), lift (C_L), and spanwise (C_S) force coefficients for the three Reynolds numbers considered. In our formulation, the immersed-boundary method computes the regularized force density $\mathbf{f}_k$ at each of the N_b Lagrangian markers. This force density is distributed within a narrow shell of one Eulerian cell width surrounding each Lagrangian point, as described by the integration procedure in Eqs. (16b) of the Appendix. The total hydrodynamic load on the sphere is then approximated by

Table 3 Grid-independence study: extreme centre-line velocities and the coordinates at which they occur

	100^3		150^3		200^3	
	z or x	u_x or u_z	z or x	u_x or u_z	z or x	u_x or u_z
$Re = 1$						
$u_x^{\max}$	1.0	1.0	1.0	1.0	1.0	1.0
$u_x^{\min}$	0.235	−0.1168	0.230	−0.1202	0.232	−0.1159
$u_z^{\max}$	0.195	0.1755	0.197	0.1751	0.197	0.1743
$u_z^{\min}$	0.805	−0.1759	0.803	−0.1793	0.803	−0.1748
$Re = 100$						
$u_x^{\max}$	1.0	1.0	1.0	1.0	1.0	1.0
$u_x^{\min}$	0.235	−0.1234	0.23	−0.1248	0.233	−0.1227
$u_z^{\max}$	0.195	0.1576	0.197	0.1588	0.198	0.1562
$u_z^{\min}$	0.815	−0.215	0.817	−0.219	0.818	−0.216
$Re = 400$						
$u_x^{\max}$	1.0	1.0	1.0	1.0	1.0	1.0
$u_x^{\min}$	0.225	−0.1915	0.23	−0.1958	0.228	−0.1904
$u_z^{\max}$	0.165	0.1880	0.17	0.1915	0.168	0.1866
$u_z^{\min}$	0.855	−0.322	0.857	−0.328	0.857	−0.320

Table 4 Centre-line streamwise velocity $u_x(z)$ at twelve locations for three Reynolds numbers. Present results are compared with[10,38]

	$Re = 1$			$Re = 100$			$Re = 400$		
z	[38]	[10]	Present	[38]	[10]	Present	[38]	[10]	Present
0.95	0.713	0.678	0.685	0.657	0.628	0.634	0.525	0.464	0.464
0.90	0.423	0.402	0.414	0.352	0.340	0.347	0.246	0.227	0.223
0.85	0.1932	0.1708	0.1956	0.1423	0.1467	0.1556	0.1665	0.1574	0.1491
0.80	0.0214	0.00838	0.0340	0.0257	0.0241	0.0356	0.1360	0.1254	0.1175
0.75	−0.0828	−0.0866	−0.0701	−0.0349	−0.0441	−0.0362	0.1079	0.0998	0.0926
0.70	−0.1317	−0.1292	−0.1134	−0.0726	−0.0760	−0.0679	0.0802	0.0704	0.0655
0.30	−0.1053	−0.1028	−0.0981	−0.1125	−0.1120	−0.1046	−0.1842	−0.1779	−0.1557
0.25	−0.1182	−0.1199	−0.1147	−0.1276	−0.1308	−0.1217	−0.218	−0.217	−0.1876
0.20	−0.1168	−0.1177	−0.1135	−0.1235	−0.1282	−0.1196	−0.214	−0.218	−0.1862
0.15	−0.1027	−0.1040	−0.1006	−0.1076	−0.1130	−0.1055	−0.1805	−0.1926	−0.1623
0.10	−0.0791	−0.0807	−0.0780	−0.0820	−0.0874	−0.0818	−0.1345	−0.1488	−0.1234
0.05	−0.0461	−0.0470	−0.0453	−0.0465	−0.0510	−0.0476	−0.0739	−0.086	−0.0713

summing the contributions over all markers:

$$\mathbf{F} \approx \sum_{k=1}^{N_b} \mathbf{f}_k \, \Delta V_k, \qquad \Delta V_k \approx (\Delta s)^3,$$

where Δs is the uniform marker spacing along the surface.

Using the sphere diameter $D = 0.25L$ scaled by the reference length L, the drag, lift and spanwise coefficients become

$$C_D = \frac{F_x}{\frac{1}{2}\rho U_\infty^2 D}, \quad C_L = \frac{F_y}{\frac{1}{2}\rho U_\infty^2 D}, \quad C_S = \frac{F_z}{\frac{1}{2}\rho U_\infty^2 D}.$$

With the present non-dimensionalisation $C_D = 8\,F_x$, $C_L = 8\,F_y$, $C_S = 8\,F_z$. The latter coefficient is 0 because of the symmetry of the flow thus effectively establishing an achieved numerical 0 for the current force calculations.

Flow around a stationary cylinder

The incident flow around a stationary circular cylinder is considered. The computational domain contains a cylinder of diameter $D = 1$ placed at the center of a square domain of dimensions $(60D, 60D)$. These dimensions of the computational domain (see Fig. 13) were chosen to ensure that the boundary conditions

Table 5 Drag (C_D), lift (C_L), and spanwise (C_S) coefficients for the embedded sphere at three Reynolds numbers

Coefficient	$Re = 1$	$Re = 100$	$Re = 400$
C_D	-7.11	$-6.48 \cdot 10^{-2}$	$-7.31 \cdot 10^{-3}$
C_L	$2.90 \cdot 10^{-2}$	$6.53 \cdot 10^{-2}$	$1.200 \cdot 10^{-2}$
C_S	$5.00 \cdot 10^{-6}$	$4.88 \cdot 10^{-6}$	$-2.01 \cdot 10^{-5}$

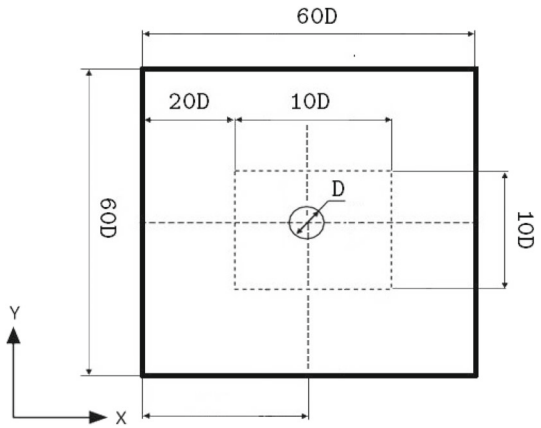

Fig. 13 Schematic representation of the geometrical model and characteristics of the computational domain for a single cylinder within the incident flow

did not influence the flow near the cylinder. To address the challenges posed by spatial discretization in a large domain, a non-uniform grid was used in both the x and y directions. The cylinder was discretized with an arc length step of $\Delta s \approx 0.015$, aligning with the smallest grid steps near the cylinder, uniformly set at $\Delta x_{min} = 0.015$ within a range of $\pm 5D$. Then, the size of the grid was gradually increased to a maximum value of $\Delta x_{min} = 0.3$ near the boundaries, employing a smooth sinusoidal transition to preserve the accuracy of the results. A uniform value of the velocity in the x direction $\mathbf{u} = (1, 0)$ was applied along the left, top, and bottom boundaries, while a convective boundary condition $\partial_t \mathbf{u} + \partial_x \mathbf{u} = 0$ was applied at the outlet (right boundary) to facilitate the undisturbed exit of the vorticity. A uniform value of $\mathbf{u} = (1, 0)$ was set as the initial condition throughout the computational domain.

The results obtained for the steady-state flow at $Re = 20$ and $Re = 40$ were verified against published drag and lift coefficients, as well as against the wake geometry illustrated in Fig. 14. The hydrodynamic forces on the cylinder are evaluated directly from the immersed-boundary forcing field $\mathbf{f}_k$ defined on the Lagrangian markers so that the non-dimensional coefficients read

$$C_d = \frac{F_x}{\frac{1}{2}\rho U_\infty^2 D}, \qquad C_l = \frac{F_y}{\frac{1}{2}\rho U_\infty^2 D},$$

with the cylinder diameter D as the reference length. Under the current scaling these reduce to $C_d = 2F_x$ and $C_l = 2F_y$.

All the compared results are summarised in Tables 5and 6. The present values agree closely with both numerical and experimental benchmarks [9,39–42]. Figure 15 shows the spanwise vorticity fields for $Re = 20$ and $Re = 40$; the computed structures reproduce the patterns reported in literature.

Following the verification of the sub-critical flow regimes, we extended our simulations to the value of $Re = 200$ to investigate the periodic vortex shedding phenomenon. The simulations started from a uniform initial flow, and the onset of vortex shedding was naturally triggered by the smallest numerical perturbations in the calculations. The numerical results replicate the periodic shedding of vortices, forming the typical von Kármán vortex street. The vorticity contours and shedding patterns are illustrated in Fig. 16. The resulting lift and drag coefficients are compared to the values reported in previous studies. In addition, we compare the currently obtained Strouhal number, which is defined as $St = \frac{f_s d}{u_\infty}$, where f_s denotes the shedding frequency with values of the literature[9,42–46]. As shown in Table 7, good agreement between our and the independent results was obtained for all the supercritical flow characteristics.

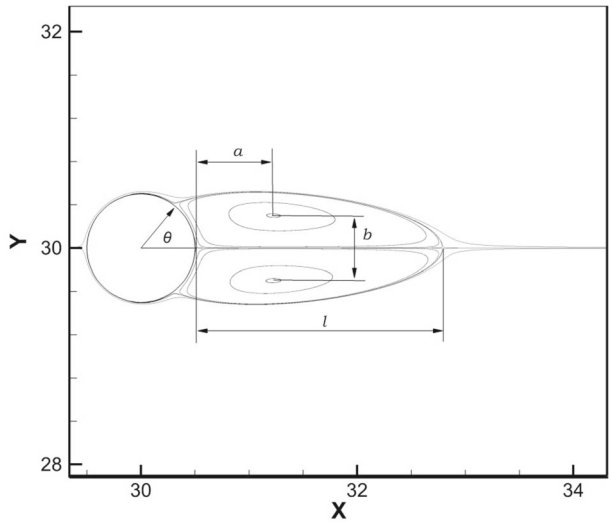

Fig. 14 Geometric characteristics of the flow wake developing behind the cylinder: θ – flow separation angle; l – length of the recirculating bubble; a – distance between the cylinder's trailing edge and the center of the recirculating bubble; b – distance between the opposite recirculating bubbles

Table 6 Comparison of the currently obtained results with the corresponding data available in the literature for the steady state flow at $Re = 20$ and $Re = 40$

Re	Study	l/d	a/d	b/d	θ	C_d
20	Coutanceau & Bouard [39]	0.93	0.33	0.46	45.0°	–
	Tritton [40]	–	–	–	–	2.09
	Dennis & Chang [41]	0.94	–	–	43.7°	2.05
	Linnick & Fasel [42]	0.93	0.36	0.43	43.5°	2.06
	Taira & Colonius (Case A)[9]	0.97	0.39	0.43	44.1°	2.07
	Taira & Colonius (Case B)[9]	0.94	0.37	0.43	43.3°	2.06
	Current study	0.943	0.366	0.431	42.6°	2.05
40	Coutanceau & Bouard [39]	2.13	0.76	0.59	53.8°	–
	Tritton [40]	–	–	–	–	1.59
	Dennis & Chang [41]	2.35	–	–	53.8°	1.52
	Linnick & Fasel [42]	2.28	0.72	0.60	53.6°	1.54
	Taira & Colonius (Case A)[9]	2.33	0.75	0.60	54.1°	1.55
	Taira & Colonius (Case B)[9]	2.30	0.73	0.60	53.7°	1.54
	Current study	2.29	0.724	0.599	53.8°	1.534

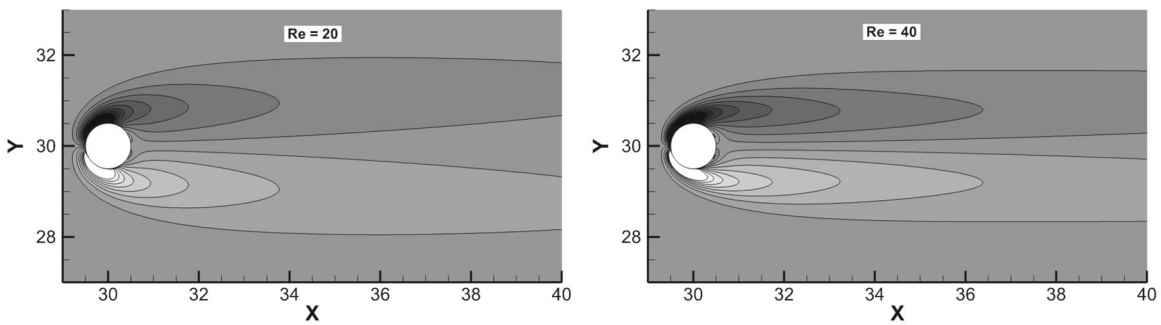

Fig. 15 Vorticity distribution obtained for $Re = 20$ (left) and $Re = 40$ (right). Contour levels are set from -3 to 3 in increments of 0.4

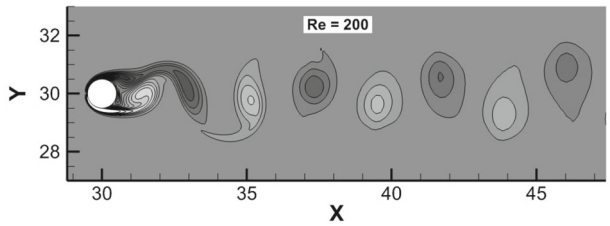

Fig. 16 Snapshot of the vorticity field around the cylinder obtained for $Re = 200$. Contour levels are set from -3 to 3 in increments of 0.4

Table 7 Comparison of the Strouhal number and the drag and lift coefficients for the incident flow over a cylinder from experimental and numerical studies at $Re = 200$

Study	St	C_d	C_l
Belov et al. [43]	0.193	1.19 ± 0.042	± 0.64
Liu et al. [44]	0.192	1.31 ± 0.049	± 0.69
Lai and Peskin [45]	0.190	–	–
Roshko [46]	0.19	–	–
Linnick and Fasel [42]	0.197	1.34 ± 0.044	± 0.69
Taira & Colonius (Case B)[9]	0.196	1.35 ± 0.048	± 0.68
Taira & Colonius (Case C)[9]	0.195	1.34 ± 0.047	± 0.68
Taira & Colonius (Case D)[9]	0.197	1.36 ± 0.043	± 0.69
Current study	0.1960	1.340 ± 0.0445	± 0.682

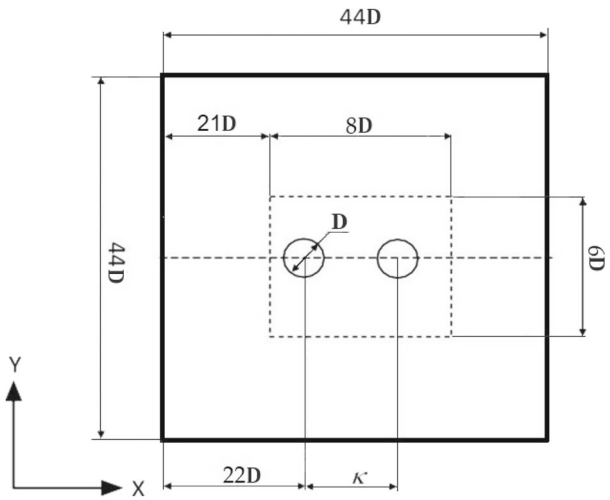

Fig. 17 Schematic representation of the geometrical model and discretization of the computational domain for the flow around a tandem of horizontally aligned cylinders

Flow around a tandem of two horizontally aligned cylinders

In this section, the verification of the currently developed computational methodology is extended by examining the fluid dynamics around a tandem of two horizontally aligned circular cylinders at $Re = 200$. This configuration serves as a benchmark to demonstrate the capabilities of capturing the effects of multiple stationary bodies on flow behavior. The computational domain, schematically shown in Fig. 17, is discretized by a 1075×1075 non-uniform mesh. A central region surrounding the cylinders, sized $8d \times 6d$, is refined with a 800×600 uniform mesh, where the grid steps are $\Delta x = \Delta y = 0.01$. Beyond this detailed area, the mesh size gradually expands to $\Delta x \approx \Delta y \approx 0.20$ at the domain boundaries. Different vortex shedding dynamics were assessed by setting the cylinders at varying center-to-center distances, $\kappa = L_x/d = [1.5, 2.3, 5]$. The boundary and initial conditions were chosen to be exactly the same as for the single cylinder configuration.

Each separation distance, κ, induces a distinct vortex shedding scenario:

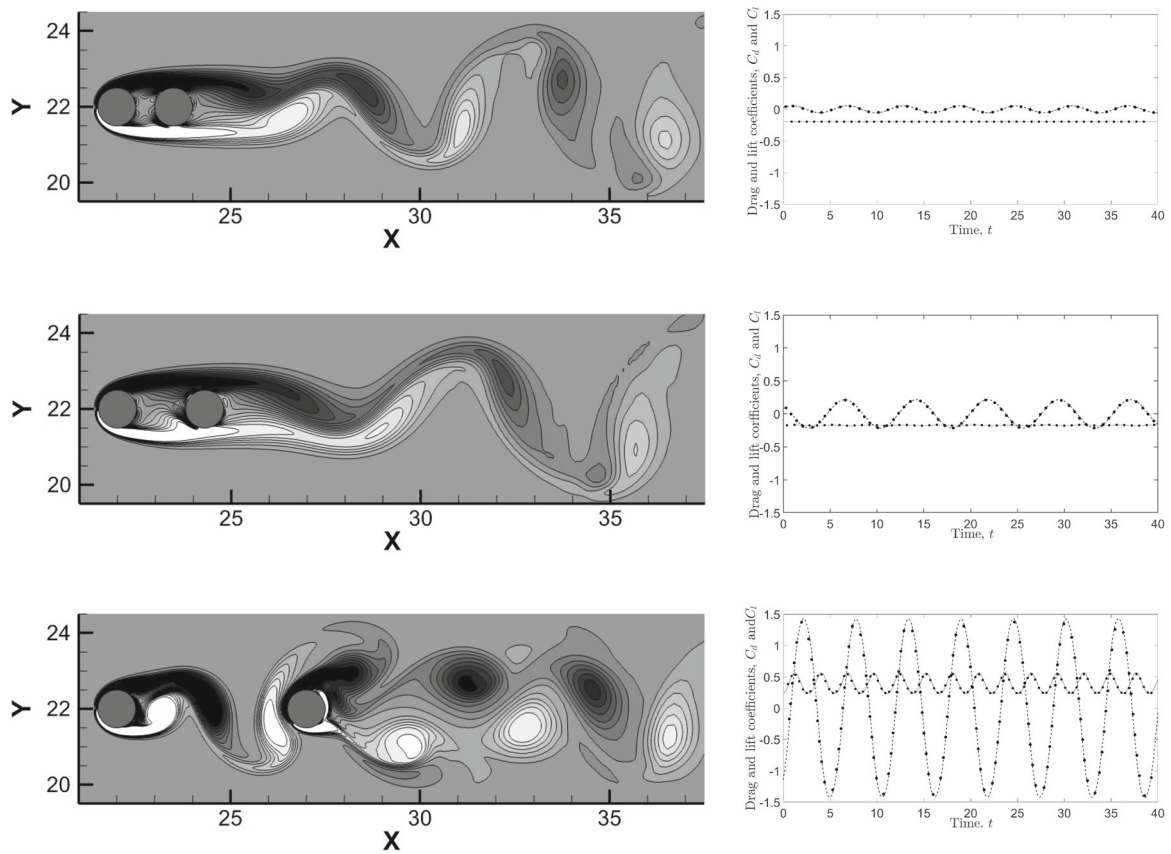

Fig. 18 The vorticity field contours on the left illustrate vortex shedding regimes around two cylinders in a horizontal tandem alignment for the values of $\kappa = 1.5, 2.3, 5.0$, in that specific order. Contour levels range from -2.2 to 2.2 in increments of 0.3. The graphs on the right depict the time evolution of the drag (gray solid line) and lift (black dashed line) coefficients, as calculated for the downstream cylinder. Black points are the reference data from [47]

Table 8 Comparison of the oscillating frequencies and average drag coefficients for different configurations at $Re = 200$

κ	St_L(Present/Ref[48]/Ref[47])	St_D(Present/Ref[48]/Ref[47])	$\overline{C_D}$(Present/Ref[48]/Ref[47])
1.5	0.333/0.338/0.332	0.167/0.169/0.166	−0.193/−0.196/−0.194
2.3	0.267/0.263/0.264	0.133/0.132/0.132	−0.174/−0.173/−0.172
5	0.357/0.360/0.355	0.178/0.181/0.178	0.387/0.423/0.401

- **SG (Symmetric in the Gap) for** $\kappa = 1.5$: Exhibits symmetric vortex shedding in the gap between the cylinders.
- **AG (Alternating in the Gap) for** $\kappa = 2.3$: Features alternating vortices with significant oscillations in lift and drag.
- **WG (Wake in the Gap) for** $\kappa = 5$: Mimics the behavior around a single cylinder with stable and well-defined vortex shedding downstream.

The vorticity contours and the vortex shedding patterns obtained for the three scenarios are illustrated in Fig.18. The resulting lift and drag coefficients calculated for the downstream cylinder were compared to the values reported in previous studies [47,48]. Furthermore, we compared with the same studies the Strouhal number values, defined as $St_L = \frac{f_{CL}d}{u_\infty}$ and $St_D = \frac{f_{CD}d}{u_\infty}$, where f_{CL} and f_{CD} denote the shedding frequencies of lift and drag oscillations, respectively. The time-averaged drag coefficient of the downstream cylinder, $\overline{C_D}$, was also compared. A summary of all the results is presented in Table 8.

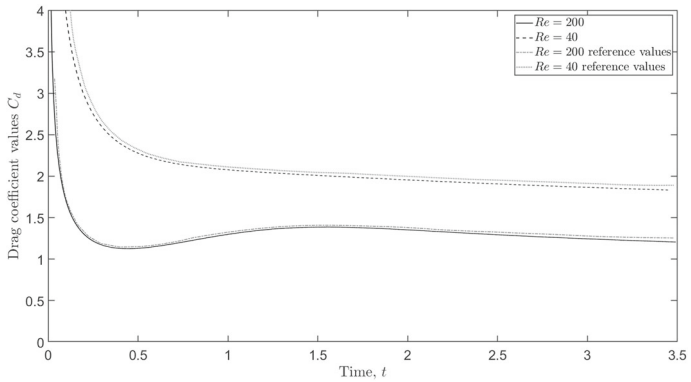

Fig. 19 Time evolution of the cylinder drag coefficient calculated for $Re = 200$ and $Re = 40$. Reference values are obtained by digital photogrammetry from [9]

Spontaneous start

We next verify the developed method for the simulation of moving boundary configurations. Specifically, a spontaneous start of a circular cylinder was simulated. Initially at rest, a cylinder of diameter $D = 1$ was impulsively set to move to the left with a constant velocity $u_0 = -1$. The simulations were performed at $Re = 40$ and 200. A square computational domain with dimensions $[0, 30D] \times [0, 30D]$ was chosen. The cylinder was placed at the center of the domain to diminish the influence of no-slip boundary conditions for all the velocity components.

We employed a non-uniform grid, maintaining a finer resolution near the cylinder ($\Delta x_{\min} = 1/256$) to capture the flow dynamics accurately. A constant time step $\Delta t = 5 \times 10^{-4}$ was used, setting the upper bound value of 0.128 for the CFL number to ensure numerical stability throughout the simulation. The simulations spanned a range of $0 \le t \le 3.5$. In this specific case, an integrated version of the discrete Dirac delta function from [29] was utilized to avoid fully spurious oscillations (see Appendix A for details on the interpolation and regularization operators).

The cylinder started to move spontaneously within a quiescent fluid, generating complex flow patterns, including wake formation with consequent vortex shedding behind it. Instantaneous vorticity fields at times $t = 1, 2.5$, and 3.5 are shown in Fig. 20, demonstrating the time evolution of the flow. The obtained contours agree well with the data reported in [9].

In Fig. 19, we plotted the time evolution of the drag coefficients for $Re = 40$ and 200. Initially, the force implied for a spontaneous start was, as expected, singular [49], and the solution scheme successfully captured this behavior. The resulting drag coefficients were slightly lower than those provided by [9], which appears to be a consequence of the higher grid resolution and lower CFL numbers employed in the current study. Concluding this benchmark, the results demonstrate the capability of the computational model to accurately replicate the spontaneous start scenario, verifying the adequate accuracy of the developed method in simulating flow developing around a moving boundary.

Flow around an airfoil at supercritical angle of attack

The flow around a NACA0012 airfoil at $Re = 1000$ at the supercritical angle of attack of 34 degrees was considered. The current set-up was similar to that used for the simulation of a tandem of two cylinders in incident flow: the computational domain is discretized by a 1075×1075 non-uniform grid. A central region surrounding the airfoil, of dimensions $6L \times 8L$, is refined with an 600×600 uniform mesh, with grid steps equal to $\Delta x = \Delta y = 0.01$. Beyond this refined domain, the mesh size gradually expands, reaching $\Delta x \approx \Delta y \approx 0.20$ at the domain boundaries. All the length dimensions are scaled by a chord length $L = 1$, as illustrated in Figure 21. Additionally, the NACA profile is carefully built to preserve an almost constant arc-length spacing close to that of the minimum grid size.

For the 34-degree angle of attack, we compared our results with both experimental and numerical [50–53] data in terms of streamline snapshots captured at different times. The currently obtained results shown in Fig.

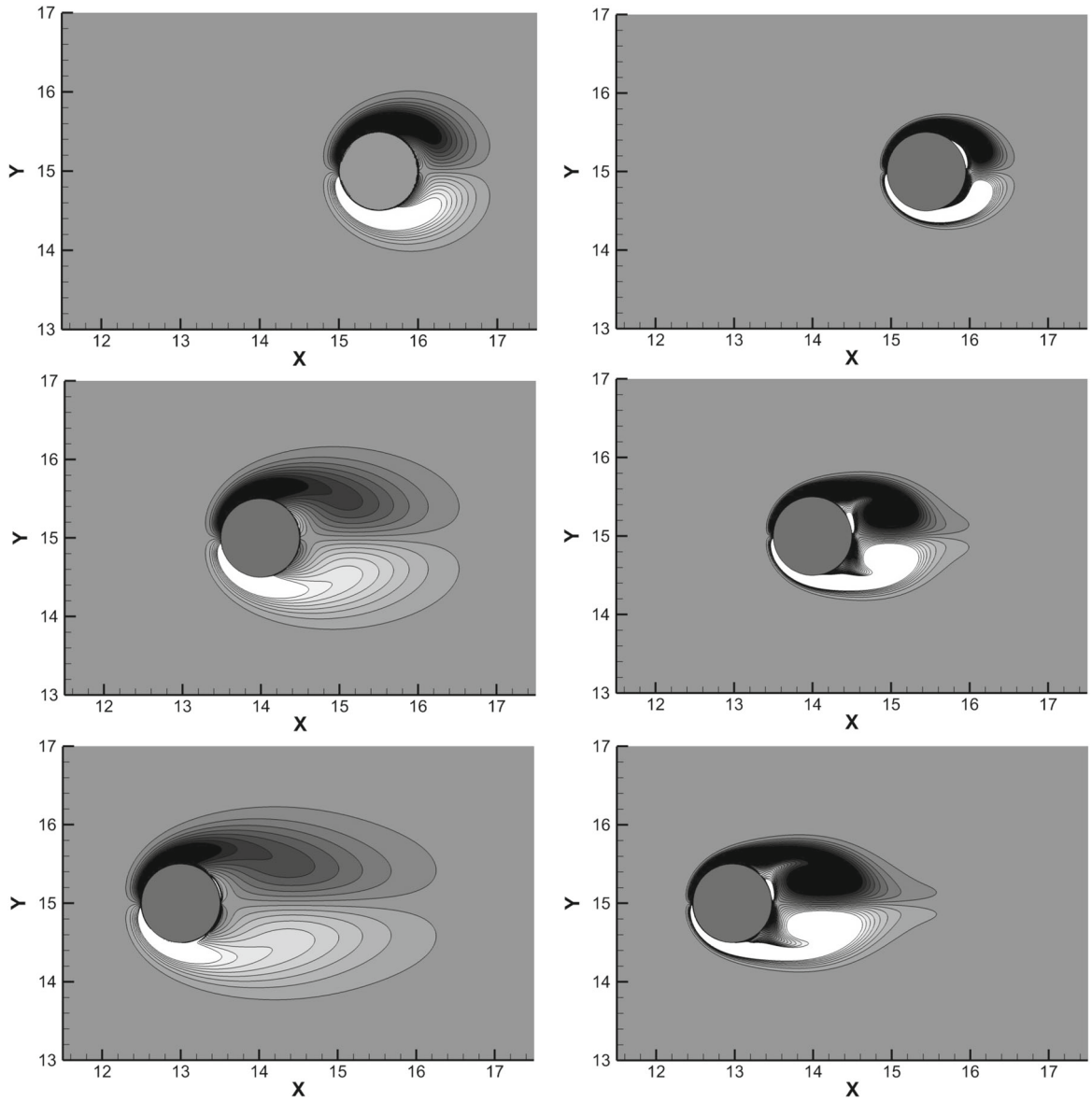

Fig. 20 Instantaneous vorticity fields around a moving circular cylinder at $Re = 40$ (left) and $Re = 200$ (right) shown at non-dimensional times of 1, 2.5, and 3.5 (from top to bottom). Contour levels ranging from -3 to 3 in increments of 0.4 were chosen

22 for times $t = 1.6$ (left) and $t = 3.2$ (right) exhibit satisfactory agreement with the corresponding numerical and experimental independent data.

Table 9 summarises the comparison by listing the geometric centres of vortices $A - D$ at both time instants, together with the reference coordinates reported by [53]. The discrepancies are minor, indicating that the present solver captures the primary vortex dynamics and vortex formation with an accuracy comparable to simulations carried out on body-fitted grids and experiments.

Conclusion

The current study introduces a novel methodology for the simulation of incompressible flows around immersed bodies. The key idea lies in establishing a modified Vanka smoother that implicitly incorporates the direct forcing IBM formalism. The developed solver leverages the Schur complement decomposition of the extended

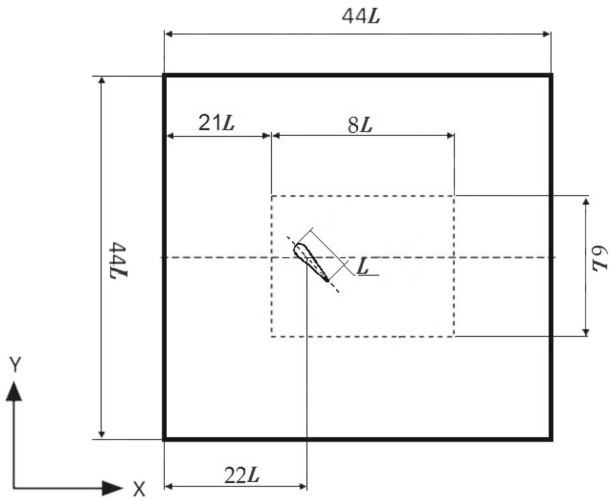

Fig. 21 Computational domain and grid setup for NACA0012 at the angle of attack $\alpha = 34°$

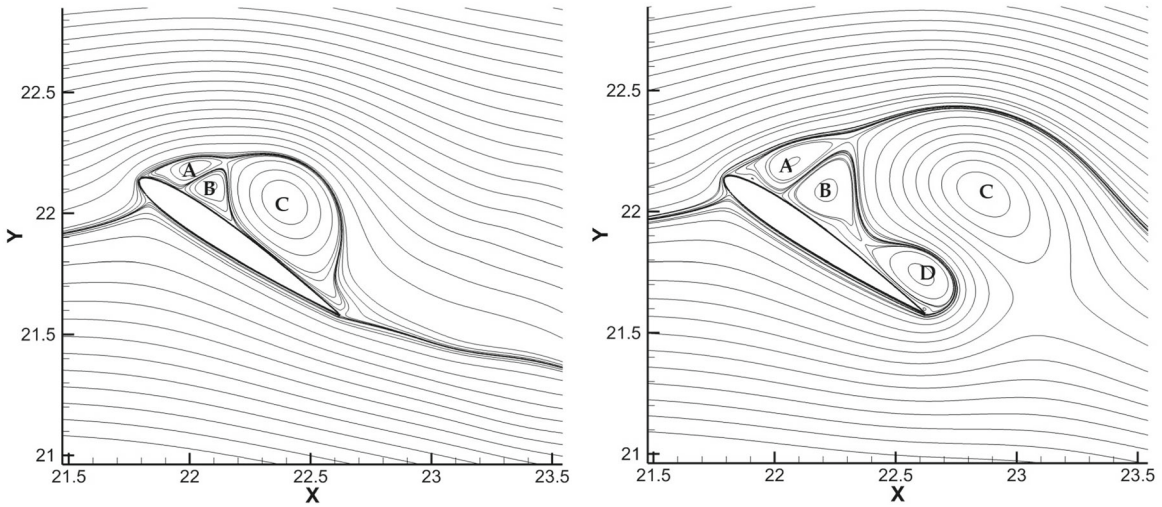

Fig. 22 Streamlines at $t = 1.6$ and $t = 3.2$ for an angle of attack $\alpha = 34°$. A, B, C and D mark the centres of the corresponding vortices

Table 9 Geometric-centre coordinates (x, y) of the dominant vortices at two instants, compared with the measurements of [53]

Vortex	$t = 1.6$		$t = 3.2$	
	Present	Ref. [53]	Present	Ref. [53]
A	(−0.092, 0.166)	(−0.110, 0.162)	(−0.056, 0.217)	(−0.040, 0.219)
B	(0.013, 0.144)	(−0.021, 0.126)	(0.132, 0.192)	(0.133, 0.169)
C	(0.296, 0.262)	(0.220, 0.268)	(0.665, 0.545)	(0.608, 0.464)
D	–	–	(0.655, 0.113)	(0.720, 0.064)

Vanka-type operator, exploiting its symmetrical structure and fully diagonal part of the matrix attributed to velocity corrections to optimize computational performance. This decomposition efficiently reduces the operator size to approximately one-third of its original size without compromising numerical stability or accuracy. The method's accuracy stems from its fully coupled treatment of all terms, including pressure-velocity coupling, non-linear convection terms and Lagrangian forces, thereby eliminating splitting errors inherent in segregated approaches such as fractional step, projection, or SIMPLE methods. Furthermore, this monolithic approach avoids the need to explicitly prescribe pressure boundary conditions, which is an aspect that can pose challenges in segregated methods, particularly in Dirichlet condition cases [3].

Extensive verification studies were conducted across a range of canonical flows, including flow between two concentric rotating cylinders; 2D and 3D lid-driven cavity flows with an immersed cylinder and sphere placed at the cavity center, respectively; flow around single and tandem stationary cylinders; flow developing following the spontaneous start of a cylinder; and flow past a NACA0012 airfoil. Throughout these tests, the method exhibited good agreement with both numerical and experimental data across the entire range of Reynolds numbers and geometric configurations examined. The solver consistently achieved solution times comparable to semi-implicit approaches while offering improved accuracy and stability at CFL numbers up to 0.5. This capability of handling relatively high CFL numbers is particularly advantageous for simulating flows with moving boundaries, where precise resolution of fluid-structure interaction is crucial.

Future work will focus on extending the methodology to three-dimensional configurations through domain decomposition techniques. This extension will leverage parallel computing architectures to handle the increased computational demands of 3D simulations while maintaining the method's favorable stability characteristics. Beyond direct time integration, the developed solver serves as a foundation for linear stability analysis by functioning as a time-stepper that approximates the Jacobian's exponential, enabling matrix-free implementations of Newton-Krylov methods and Arnoldi iterations. This approach overcomes limitations of existing IBM implementations, where neither explicit nor semi-implicit formulations can provide the robust and rapid convergence required for stability analysis. The extension to fully three-dimensional flows will significantly broaden the scope of fluid-structure interaction problems amenable to systematic stability investigation.

Acknowledgements This research was partially supported by the Israel Science Foundation (grant no. 950/22) and by the Israel Ministry of Energy and Infrastructure (grant No. 315-222-11-049).

Funding Open access funding provided by Ben-Gurion University.

Declarations

Author Contribution K.G. : analysis and related examples, programming, validation, writing. M.K.: analysis, programming, validation. O.O.: supervision, validation, writing. Y.F.: conceptaluaziation, supervision, software, validation, writing.

Data Availability No datasets were generated or analysed during the current study.

Competing interests The authors declare no competing interests.

A Interpolation and Regularization Operators

The immersed boundary method (IBM) relies on two key operators to couple Lagrangian dynamics with the Eulerian flow field: the interpolation operator **I** and the regularization operator **R**. In the classical IBM formulation [1], the surface of the immersed body is represented by a series of Lagrangian markers that typically do not coincide with the underlying Eulerian grid, where the Navier–Stokes equations are solved. Consequently, **I** interpolates Eulerian fields (e.g., velocity) onto the Lagrangian points, while **R** smears Lagrangian quantities back to the Eulerian grid.

These operators are constructed using discrete approximations of the Dirac delta function, which serve a dual role: (1) they provide information transfer between non-conforming grids, and (2) they regularize sharp or even singular source terms, such as the force required to enforce no-slip boundary conditions, thereby ensuring stability and numerical consistency. Throughout this study, we use the three-point discrete delta function developed by Roma et al. [28], which has compact support and satisfies key conservation and smoothness

properties on staggered, uniformly spaced grids:

$$\delta(r) = \begin{cases} \frac{1}{6\Delta r}\left[5 - 3\frac{|r|}{\Delta r} - \sqrt{-3\left(1 - \frac{|r|}{\Delta r}\right)^2 + 1}\right] & \text{for } 0.5\Delta r \le |r| \le 1.5\Delta r, \\ \frac{1}{3\Delta r}\left[1 + \sqrt{-3\left(\frac{|r|}{\Delta r}\right)^2 + 1}\right] & \text{for } |r| \le 0.5\Delta r, \\ 0 & \text{otherwise}, \end{cases} \tag{15}$$

This kernel provides a favorable balance between computational locality and accuracy but assumes evenly spaced grids and marker distributions. Deviation from this assumption may lead to increased stiffness or degraded interpolation accuracy.

The formal definitions of the regularization and interpolation operators are given by:

$$\boldsymbol{R}(\boldsymbol{F}^k) = \int_S (\boldsymbol{F}^k(\boldsymbol{X}^k)) \cdot \delta(\boldsymbol{x}_i - \boldsymbol{X}^k), dV_S^k, \tag{16a}$$

$$\boldsymbol{I}\left(\boldsymbol{u}(\boldsymbol{x}_i)\right) = \int_\Omega \left(\boldsymbol{u}(\boldsymbol{x}_i)\right) \cdot \delta(\boldsymbol{X}^k - \boldsymbol{x}i), dV_{\Omega_i}, \tag{16b}$$

where dV_S^k and dV_{Ω_i} denote the control volumes around the k^{th} Lagrangian marker and the i^{th} Eulerian cell, respectively.

In some cases, particularly for moving bodies, delta functions can introduce nonphysical oscillations in the computed forces. These oscillations appear over time with small amplitudes that depend on the coupling strategy and discretization scheme. To suppress spurious force oscillations, we replace the Roma et al. delta function [28] with the integrated smoothed delta function [29] in this specific case. This alternative kernel improves the stability of the interpolation and regularization steps by more smoothly distributing the discontinuous forcing introduced at early times, when the velocity mismatch between the fluid and structure is initially large.

References

1. Peskin, C.S.: Flow patterns around heart valves: A numerical method. J. Comput. Phys. **10**(2), 252–271 (1972). https://doi.org/10.1016/0021-9991(72)90065-4
2. Verzicco, R.: Immersed boundary methods: Historical perspective and future outlook. Annu. Rev. Fluid Mech. **55**, 129–155 (2023)
3. Gresho, P.M., Sani, R.L.: On pressure boundary conditions for the incompressible Navier-Stokes equations†. Int. J. Numer. Meth. Fluids **7**(10), 1111–1145 (1987). https://doi.org/10.1002/fld.1650071008. (**First published: October 1987; Based on an invited lecture; 441 citations (as of original note)**)
4. Mohd-Yusof, J.: Combined immersed-boundary/b-spline methods for simulations of flow in complex geometries. Center for Turbulence Research, Annual Research Briefs, 317–327 (1997)
5. Fadlun, E.A., Verzicco, R., Orlandi, P., Mohd-Yusof, J.: Combined immersed-boundary finite-difference methods for three-dimensional complex flow simulations. J. Comput. Phys. **161**(1), 35–60 (2000)
6. Uhlmann, M.: An immersed boundary method with direct forcing for the simulation of particulate flows. J. Comput. Phys. **209**, 448–476 (2005)
7. Le, D.V., Khoo, B.C., Lim, K.M.: An implicit-forcing immersed boundary method for simulating viscous flows in irregular domains. Comput. Methods Appl. Mech. Eng. **197**, 2119–2130 (2008)
8. Glowinski, R., Pan, T.W., Périaux, J.: Distributed Lagrange multiplier methods for incompressible viscous flow around moving rigid bodies. Comput. Methods Appl. Mech. Eng. **151**, 181–194 (1998)
9. Taira, K., Colonius, T.: The immersed boundary method: a projection approach. J. Comput. Phys. **225**, 3121–3133 (2007)
10. Goncharuk, K., Oshri, O., Feldman, Y.: The immersed boundary method: A simple approach. J. Comput. Phys. **487**, 112148 (2023)
11. Yovel, R., Treister, E., Feldman, Y.: The immersed boundary method: an accelerated simple approach for moving bodies. arXiv (2025). https://doi.org/10.48550/arXiv.2501.15314, arXiv:2501.15314 [physics.flu-dyn]
12. Kallemov, B., Bhalla, A., Griffith, B., Donev, A.: An immersed boundary method for rigid bodies. Commun. Appl. Math. Comput. Sci. **11**, 79–141 (2016)
13. Feldman, Y., Gulberg, Y.: An extension of the immersed boundary method based on the distributed lagrange multiplier approach. J. Comput. Phys. **322**, 248–266 (2016)
14. Gulberg, Y., Feldman, Y.: Flow control through the use of heterogeneous porous media: "smart" passive thermo-insulating materials. Int. J. Therm. Sci. **110**, 369–382 (2016). https://doi.org/10.1016/j.ijthermalsci.2016.07.008
15. Goza, A., Colonius, T.: A strongly-coupled immersed-boundary formulation for thin elastic structures. J. Comput. Phys. **336**, 401–411 (2017)
16. Stein, D., Guy, R., Thomases, B.: Immersed boundary smooth extension (ibse): a high-order method for solving incompressible flows in arbitrary smooth domains. J. Comput. Phys. **335**, 155–178 (2017)
17. Vanka, S.: Block-implicit multigrid solution of navier–stokes equations in primitive variables. J. Comput. Phys. **65**, 138–158 (1986)

18. Vanka, S.: A calculation procedure for three-dimensional steady recirculating flows using multigrid methods. Comp. Meth. Appl. Mech. Eng. **55**, 321–338 (1986)
19. Guy, R., Philip, B.: A multigrid method for a model of the implicit immersed boundary equations. Commun. Comput. Phys **12**, 378–400 (2012)
20. Tuckerman, L.S., Barkley, D.: Bifurcation analysis for timesteppers. Numerical Methods for Bifurcation Problems and Large-Scale Dynamical Systems **119**, 453–466 (2000). https://doi.org/10.1007/978-1-4612-1282-1_20
21. Feldman, Y.: Oscillatory instability of 2d natural convection flow in a square enclosure with a tandem of vertically aligned cylinders. Fluid Dyn. Res. **50**, 051410 (2018)
22. Giannetti, F., Luchini, P.: Structural sensitivity of the first instability of the cylinder wake. J. Fluid Mech. **581**, 167–197 (2007)
23. Tchoufag, J., Fabre, D., Magnaudet, J.: Global linear stability analysis of the wake and path of buoyancy-driven disks and thin cylinders. J. Fluid Mech. **740**, 278–311 (2014)
24. Tirri, A., Nitti, A., Sierra-Ausin, J., Giannetti, F., Tullio, M.D.: Linear stability analysis of fluid-structure interaction problems with an immersed boundary method. J. Fluids Struct. **117**, 103830 (2023)
25. Banks, J.W., Henshaw, W.D., Schwendeman, D.W., Tang, Q.: A stable partitioned fsi algorithm for rigid bodies and incompressible flow in three dimensions. J. Comput. Phys. **373**, 445–492 (2018)
26. Frederic, A., Jean-Christophe, R., Xavier, G.: A domain decomposition matrix-free method for global linear stability. Computers & Fluids **66**, 63–84 (2012)
27. Peskin, C.: The immersed boundary method. Acta Numerica, 479–517 (2002)
28. Roma, A., Peskin, C., Berger, M.: An adaptive version of the immersed boundary method. J. Comput. Phys. **153**, 509–537 (1999)
29. Yang, X., Zhang, X., Li, Z., He, G.-W.: A smoothing technique for discrete delta functions with application to immersed boundary method in moving boundary simulations. J. Comput. Phys. **228**(20), 7821–7836 (2009). https://doi.org/10.1016/j.jcp.2009.07.023
30. Guy, R., Philip, B., Griffith, B.: Geometric multigrid for an implicit-time immersed boundary method. Advances Comput. Math. **41**, 635–662 (2015)
31. Amestoy, P.R., Duff, I.S., Koster, J., L'Excellent, J.-Y.: A fully asynchronous multifrontal solver using distributed dynamic scheduling. SIAM J. Matrix Anal. Appl. **23**(1), 15–41 (2001)
32. Amestoy, P.R., Guermouche, A., L'Excellent, J.-Y., Pralet, S.: Hybrid scheduling for the parallel solution of linear systems. Parallel Comput. **32**(2), 136–156 (2006)
33. Patankar, S.: Numerical Heat Transfer and Fluid Flow. CRC press, (2018)
34. Intel Corporation: Intel Math Kernel Library, Version 2024.0. (2024). Available from https://software.intel.com/content/www/us/en/develop/tools/oneapi/components/onemkl.html
35. Zhu, J., Holmedal, L.E., Wang, H., Myrhaug, D.: Flow patterns in a steady lid-driven rectangular cavity with an embedded circular cylinder. Fluid Dyn. Res. **52**(6), 065508 (2020)
36. Cai, S.-G., Ouahsine, A., Favier, J., Hoarau, Y.: Moving immersed boundary method. Int. J. Numer. Meth. Fluids **85**(5), 288–323 (2017)
37. Leopardi, P.: A partition of the unit sphere into regions of equal area and small diameter. Electron. Trans. Numer. Anal. **25**, 309–327 (2006)
38. Young, D.L., Lin, Y.C., Fan, C.M., Chiu, C.L.: The method of fundamental solutions for solving incompressible navier–stokes problems. Eng. Anal. Boundary Elem. **33**, 1031–1044 (2009)
39. Coutanceau, M., Bouard, R.: Experimental determination of the main features of the viscous flow in the wake of a circular cylinder in uniform translation. part 1. steady flow. J. Fluid Mech. **79**(2), 231–256 (1977)
40. Tritton, D.J.: Experiments on the flow past a circular cylinder at low reynolds number. J. Fluid Mech. **6**, 547–567 (1959)
41. Dennis, S.C.R., Chang, G.: Numerical solutions for steady flow past a circular cylinder at reynolds number up to 100. J. Fluid Mech. **42**(3), 471–489 (1970)
42. Linnick, M.N., Fasel, H.F.: A high-order immersed interface method for simulating unsteady incompressible flows on irregular domains. J. Comput. Phys. **204**(1), 157–192 (2005). https://doi.org/10.1016/j.jcp.2004.09.017
43. Belov, A., Martinelli, L., Jameson, A.: A New Implicit Algorithm with Multigrid for Unsteady Incompressible Flow Calculations. In: 33rd Aerospace Sciences Meeting and Exhibit, Reno, NV (1995)
44. Liu, C., Zheng, X., Sung, C.H.: Preconditioned multigrid methods for unsteady incompressible flows. J. Comput. Phys. **139**, 35–57 (1998)
45. Lai, M.-C., Peskin, C.S.: An immersed boundary method with formal second-order accuracy and reduced numerical viscosity. J. Comput. Phys. **160**(2), 705–719 (2000). https://doi.org/10.1006/jcph.2000.6483
46. Roshko, A.: Report 1191: On the development of turbulent wakes from vortex streets. Technical report, NACA (1954)
47. Carmo, B.S., Meneghini, J.R., Sherwin, S.J.: Possible states in the flow around two circular cylinders in tandem with separations in the vicinity of the drag inversion spacing. Phys. Fluids **22**(5), 054101 (2010). https://doi.org/10.1063/1.3420111
48. Feldman, Y., Gulberg, Y.: An extension of the immersed boundary method based on the distributed lagrange multiplier approach. J. Comput. Phys. **322**, 248–266 (2016). https://doi.org/10.1016/j.jcp.2016.06.039
49. Bar-Lev, M., Yang, H.T.: Initial flow field over an impulsively started circular cylinder. J. Fluid Mech. **72**(4), 625–647 (1997). https://doi.org/10.1017/S0022112077001617
50. George, A., Huang, L.C., Tang, W.-P., Wu, Y.D.: Numerical simulation of unsteady incompressible flow (re $\leq$ 9500) on the curvilinear half-staggered mesh. SIAM J. Sci. Comput. **21**(6), 2331–2351 (2000)
51. George, A., Tang, W.-P., Wu, Y.D.: Multilevel one-way dissection factorization. SIAM J. Matrix Anal. Appl. **22**(3), 752–771 (2001). https://doi.org/10.1137/S0895479898332564
52. Bouchon, F., Dubois, T., James, N.: A second-order cut-cell method for the numerical simulation of 2d flows past obstacles. Computers & Fluids **65**, 80–91 (2012)

53. Daube, O., Loc, T.P., Monnet, P., Coutanceau, M.: Ecoulement instationnaire décollé d'un fluide incompressible autour d'un profil: une comparaison théorie-expérience. In: AGARD CP 386, Paper 3 (1985)

Chapter 5

Summary

This thesis investigates dynamic instabilities of thin elastic sheets interacting with surrounding fluids, with a view to unifying simplified analytical understanding and practical computation for realistic, strongly coupled configurations. Two complementary gaps motivate the work. *Analytical.* While experiments and static theories are abundant, a quantitative, dynamical account of how a freely evolving thin sheet drives a pressure difference and a net flux in a confined fluid remains incomplete. We therefore pose a canonical problem: a post-buckled sheet, prepared in its second mode and released in an inviscid fluid, and derive relations that connect its time-dependent kinematics to the induced pressure difference and to the transport it generates. *Numerical.* Available solvers either achieve speed via segregated coupling at the cost of residual decoupling and potential leakage, or guarantee robustness via fully coupled Newton–Krylov frameworks at a cost that hinders broad parameter exploration. What is needed for slender-body, two-way-coupled FSI is a practical, implicit/semi-implicit, direct-forcing IBM that enforces near-impenetrability up to the discretisation error and yet remains light enough for ensembles.

The analytical approach establishes a canonical flutter problem in a confined chamber and develops a small-slope, asymptotically controlled framework that yields predictive, testable relations. Starting from a post-buckled base shape prepared in the second bending mode, we derive explicit scaling laws linking the evolving sheet kinematics to the induced pressure difference and to the net transport generated by the motion. Within this framework, growth rates near the prepared state, the exchange between sheet elastic energy and fluid inertia, and the time to the first pressure maximum admit closed-form descriptions that depend on the structure–fluid mass ratio λ. Crucially, the analysis exposes a smooth transition between solid-dominated and fluid-dominated response as λ crosses order one, with clear consequences for amplitudes, characteristic time scales, and transport efficiency. These relations are then

confronted with full, unsimplified computations, where we verify the predicted scalings, the measured times to peak, and the evolution of the pressure difference up to (and including) the first peak.The comparisons with the numerical results are presented in Chapter 2, while the numerical methodology used for these comparisons is detailed in Appendix A.For completeness, the canonical setting is also extended conceptually to an open domain [88], where the same methodology indicates which scalings persist once the geometric confinement is relaxed.

To compute faithfully beyond the limits of analytical approximations, we build two complementary solvers and specify their roles. The SIMPLE-based immersed boundary method on a staggered grid provides very fast data processing and broad applicability for canonical testing and parametric scanning; it is the right instrument whenever interface decoupling errors remain subdominant. For the practically important regime of fast motion, tight clearances, and strong coupling, like the canonical problem case presented in analytical part, we introduce a monolithic, fully implicit variant. By treating pressure and the Lagrangian force density as a single distributed multiplier within a big-box Vanka smoother, and by solving the associated symmetric block system via a Schur complement reduction to a positive-definite symmetric operator, the method advances stably at higher CFL numbers and maintains near-impenetrability without any need for pressure boundary conditions. Although costlier per step than the SIMPLE baseline, it remains sufficiently lean for systematic studies and is verified on a broad benchmark set (including concentric-cylinder rotation, a cavity with an internal cylinder, spontaneous start, two-cylinder wakes, and a supercritical-angle NACA0012 case), establishing accuracy precisely where near-boundary physics matters most.

Analytical and numerical parts are linked by the fact that the analysis provides explicit, checkable targets, and the computations are built to test and extend them in the full viscous problem. Chapter 2 isolates the inertial–elastic mechanism in its cleanest form and delivers explicit predictions for quantities that are measurable and computable in any setting: the sheet mode amplitude and phase, the chamber pressure difference, and the net transport. Chapters 3–4 then provide a route to compute the same observables once the idealisations of Chapter 2 are relaxed, in particular when viscosity, finite-slope geometry, near-wall effects, and strong two-way coupling become non-negligible. In this view, the numerical strand is not a separate topic but the means to carry the Chapter 2 scalings into progressively more realistic regimes, and to identify where and how they break. This is also the natural meeting point for future coupled-sheet simulations: the Chapter 2 relations supply sharp normalisations and diagnostic targets, while the full simulations quantify

viscous corrections and enable extensions to parameter ensembles and, ultimately, three-dimensional sheet models.

Together, these approaches provide a coherent picture of flutter-induced transport in confinement. The analytical model, by isolating the essential balances, delivers sharp scalings and quantitative targets; the computations, by resolving viscosity, interface enforcement, and strong coupling, both validate those predictions and extend them into practically relevant regimes where asymptotics alone would be inconclusive. In practice, this yields a clear operating principle: employ the simple, controlled analytical picture to understand thresholds, time scales, and parametric trends; deploy the implicit monolithic method whenever transport is governed by near-interface physics, rapid motion, or complex geometry. In this way, we extend the understanding of dynamic transitions in flutter-induced flow and provide a set of tools for questions the analytical approach cannot address on its own — for example, dissipation pathways and energy loss, which are inaccessible in the idealised model but can be quantified numerically.

Future work will extend the analytical framework beyond confined configurations to open-domain problems and other related flow–sheet interaction scenarios, in order to clarify the general physical mechanisms governing fluid–structure energy transfer in thin-sheet dynamics, including the effect of vorticity in open-domain configurations. In parallel, the numerical framework will be advanced towards a fully monolithic formulation in which the thin-sheet equations are incorporated directly into the Vanka solver, providing a more consistent and computationally efficient approach for strongly coupled fluid–structure interaction.

To sum up, the thesis closes the analytical gap by providing a canonical, solvable dynamical formulation for flutter-induced transport, and bridges the numerical gap by providing a practical implicit immersed-boundary framework that enforces near-impenetrability while remaining efficient enough for broad exploration. Simple where it can be, implicit where it must be, the approach makes the dynamics of thin-sheet instabilities both intelligible and computable across the regimes of interest in confined FSI.

Appendix A

Numerical validation of flutter-induced flow

This appendix summarises the two numerical routes used to confront the asymptotic predictions in Chapter 2 (flutter-induced flow in a closed chamber): (i) fully nonlinear viscous computations of the coupled problem up to the first pressure maximum, and (ii) linear stability analysis about the prepared post-buckled state.

All equations are written in the dimensionless variables used throughout the thesis. In particular, the sheet (Kirchhoff rod) equations are normalised so that no dimensional parameters appear explicitly. The fluid equations contain only Re and λ, with $1/\lambda$ placed in front of the pressure gradient.

A.1 Fully nonlinear viscous computations

Coupled governing equations

The inextensible sheet is modelled as a planar Kirchhoff rod parameterised by the dimensionless arclength $s \in [0,1]$ with centreline $\mathbf{x}(s,t) = (x(s,t), y(s,t))$ and tangent angle $\theta(s,t)$. The unit tangent is $\widehat{\mathbf{t}} = (\cos\theta, \sin\theta)$ and the curvature is $\kappa = \partial_s\theta$. The internal force resultant is $\mathbf{F}(s,t) = (F_x, F_y)$.

The unsimplified inextensibility constraints read

$$\partial_s x = \cos\theta, \qquad \partial_s y = \sin\theta. \tag{A.1}$$

The (dimensionless) force balance for the centreline is

$$\partial_{tt}\mathbf{x} = \partial_s\mathbf{F} + \mathbf{F}_{hd}(s,t), \tag{A.2}$$

where $\mathbf{F}_{hd}(s,t)$ denotes the hydrodynamic force per unit length exerted by the fluid

on the sheet.

The moment balance (Kirchhoff rod) is written in the standard form

$$\partial_s \kappa + \mathbf{F} \times \widehat{\mathbf{t}} = 0, \tag{A.3}$$

The fluid is governed by the incompressible Navier–Stokes equations in the chamber,

$$\partial_t \mathbf{u} + (\mathbf{u} \cdot \nabla)\mathbf{u} = -\lambda \nabla p + \frac{1}{Re}\nabla^2 \mathbf{u} - \lambda \mathbf{f}_{hd}(\mathbf{x}, t), \qquad \nabla \cdot \mathbf{u} = 0. \tag{A.4}$$

The coupling uses the same physical interaction in the two subproblems. Specifically, $\mathbf{f}_{hd}$ is the Eulerian representation of $\mathbf{F}_{hd}$, and the sign in (A.4) ensures action–reaction consistency.

The kinematic coupling is imposed as a no-slip constraint on the sheet,

$$\mathbf{u}\big(\mathbf{x}(s,t), t\big) = \partial_t \mathbf{x}(s,t). \tag{A.5}$$

Boundary conditions and prepared state

The sheet ends are pinned with fixed positions, and the end curvature is set to zero:

$$\mathbf{x}(0,t) = \mathbf{x}_L, \qquad \mathbf{x}(1,t) = \mathbf{x}_R, \tag{A.6}$$

$$\kappa(0,t) = 0, \qquad \kappa(1,t) = 0. \tag{A.7}$$

These six scalar constraints close the inextensible sheet system. The initial condition corresponds to the prepared post-buckled configuration (second bending mode) used in the analysis, with the corresponding fluid initial state.

Sheet discretisation in space

The sheet is discretised at $N+1$ Lagrangian points $s_j = j\Delta s$, $j = 0, \ldots, N$, with $\Delta s = 1/N$. Unknowns $\{x_j, y_j, \dot{x}_j, \dot{y}_j, \theta_j, F_{x,j}, F_{y,j}\}$ are stored at the points. All governing equations are written between points (midpoint form), leaving exactly the six boundary conditions (A.6)–(A.7) to be prescribed.

A representative second-order discretisation of the geometric constraints is

$$\frac{x_{j+1} - x_j}{\Delta s} = \cos\theta_{j+1/2}, \qquad \frac{y_{j+1} - y_j}{\Delta s} = \sin\theta_{j+1/2}, \qquad j = 0, \ldots, N-1, \tag{A.8}$$

with a midpoint angle $\theta_{j+1/2}$ defined consistently with the chosen scheme. Curvature at midpoints is

$$\kappa_{j+1/2} = \frac{\theta_{j+1} - \theta_j}{\Delta s}, \qquad j = 0, \ldots, N-1. \tag{A.9}$$

The discrete moment balance is enforced in the form

$$\frac{\kappa_{j+1/2} - \kappa_{j-1/2}}{\Delta s} + \left(\mathbf{F}_j \times \widehat{\mathbf{t}}_j\right) = 0, \qquad j = 1, \dots, N-1, \tag{A.10}$$

where $\widehat{\mathbf{t}}_j = (\cos\theta_j, \sin\theta_j)$. With the curvature boundary conditions $\kappa_{1/2} = 0$ and $\kappa_{N-1/2} = 0$, (A.10) is equivalently written as the recurrence

$$\kappa_{j+1/2} = \kappa_{j-1/2} - \Delta s \left(\mathbf{F}_j \times \widehat{\mathbf{t}}_j\right), \qquad j = 1, \dots, N-1. \tag{A.11}$$

Force balance is enforced on inter-point control volumes:

$$\ddot{\mathbf{x}}_{j+1/2} = \frac{\mathbf{F}_{j+1} - \mathbf{F}_j}{\Delta s} + \mathbf{F}_{hd,j+1/2}, \qquad j = 0, \dots, N-1, \tag{A.12}$$

where $\mathbf{F}_{hd,j+1/2}$ is the discrete hydrodynamic force per unit length, consistent with the fluid–structure coupling.

Monolithic solve at each time step

At each time step a fully coupled nonlinear system is solved,

$$\mathbf{R}(\mathbf{q}^{n+1}) = \mathbf{0}, \qquad \mathbf{q} = \left[\mathbf{u}^{n+1}, p^{n+1}, \mathbf{x}^{n+1}, \theta^{n+1}, \mathbf{F}^{n+1}, \mathbf{F}_{hd}^{n+1}\right]. \tag{A.13}$$

The coupling force $\mathbf{F}_{hd}$ appears in both subproblems via (A.2) and (A.4) with opposite sign (action–reaction), and the kinematic constraint (A.5) is enforced within the same coupled system.

The nonlinear system (A.13) is solved by a monolithic Newton method:

$$\mathbf{J}(\mathbf{q}^{(k)})\, \delta\mathbf{q}^{(k)} = -\mathbf{R}(\mathbf{q}^{(k)}), \qquad \mathbf{q}^{(k+1)} = \mathbf{q}^{(k)} + \delta\mathbf{q}^{(k)}. \tag{A.14}$$

The resulting time histories (sheet kinematics, chamber pressure difference, and the time to the first pressure maximum) are used for the quantitative theory–numerics comparisons reported in Chapter 2.

A.2 Linear stability analysis

Perturbation ansatz and discretisation spaces

Let $(\mathbf{u}_0, p_0, \mathbf{x}_0, \theta_0)$ denote the prepared base state. Perturbations are sought in the modal form

$$\mathbf{u} = \mathbf{u}_0 + \varepsilon\hat{\mathbf{u}}\, e^{\sigma t}, \quad p = p_0 + \varepsilon\hat{p}\, e^{\sigma t}, \quad \mathbf{x} = \mathbf{x}_0 + \varepsilon\hat{\mathbf{x}}\, e^{\sigma t}, \quad \theta = \theta_0 + \varepsilon\hat{\theta}\, e^{\sigma t}. \tag{A.15}$$

The fluid perturbations $(\hat{\mathbf{u}}, \hat{p})$ are discretised using Taylor–Hood Q_2/Q_1 elements, namely biquadratic interpolation for the velocity field and bilinear interpolation for the pressure field on quadrilateral elements [89–91]. This choice satisfies the discrete Ladyzhenskaya–Babuška–Brezzi (LBB), or inf–sup, stability condition for incompressible mixed finite element formulations, which ensures a proper compatibility between the discrete velocity and pressure spaces [90–92]. As a result, the discretisation avoids the spurious pressure modes and related non-physical oscillations that can occur for unstable velocity–pressure pairs [90, 91]. The sheet perturbations are discretised by quadratic three-node (P_2) elements along the arclength.

Weak form and the traction coupling term

In the linearised fluid equations, the coupling to the sheet is not introduced as an ad hoc volumetric forcing. Instead, it arises automatically as an interface traction contribution after weakening and integrating by parts.

Define the (dimensionless) perturbation Cauchy stress consistent with (A.4):

$$\hat{\boldsymbol{\sigma}} = -\lambda \hat{p}\,\mathbf{I} + \frac{1}{Re}\big(\nabla\hat{\mathbf{u}} + (\nabla\hat{\mathbf{u}})^T\big). \tag{A.16}$$

Let $\Gamma_0 = \mathbf{x}_0([0,1])$ denote the sheet curve in the base configuration, with unit normal $\mathbf{n}_0$. In the weak fluid problem, the stress divergence produces the interface term

$$\int_{\Gamma_0} \big(\hat{\boldsymbol{\sigma}}\,\mathbf{n}_0\big) \cdot \hat{\mathbf{v}}\,\mathrm{d}\Gamma, \tag{A.17}$$

where $\hat{\mathbf{v}}$ is the velocity test function.

We denote the interface traction by

$$\hat{\mathbf{F}}_{hd} \equiv \hat{\boldsymbol{\sigma}}\,\mathbf{n}_0 \quad \text{on } \Gamma_0. \tag{A.18}$$

This traction is the quantity used to couple to the linearised Kirchhoff rod problem. It is the same physical interaction as in the nonlinear computations, now appearing naturally within the weak formulation.

The linearised kinematic coupling on the base interface is

$$\hat{\mathbf{u}}\big|_{\Gamma_0} = \sigma\,\hat{\mathbf{x}}. \tag{A.19}$$

Coupled eigenproblem and solution method

The linearised Kirchhoff rod equations provide a sheet block schematically of the form

$$\sigma^2\hat{\mathbf{x}} = \partial_s\hat{\mathbf{F}} + \hat{\mathbf{F}}_{hd}, \tag{A.20}$$

together with the linearised inextensibility constraints and the linearised moment balance obtained from (A.3). Here $\hat{\mathbf{F}}_{hd}$ is precisely the traction (A.18) acting on the sheet.

After finite element assembly (including the interface constraints), the coupled problem takes the form of a generalised eigenvalue problem

$$\mathbf{A}\mathbf{z} = \sigma\,\mathbf{B}\mathbf{z}, \qquad \mathbf{z} = \left[\hat{\mathbf{u}}_h, \hat{p}_h, \hat{\mathbf{x}}_h, \hat{\mathbf{F}}_{hd,h}\right]^T, \tag{A.21}$$

where $\hat{\mathbf{F}}_{hd,h}$ represents the discrete interface traction degrees of freedom (the stress term arising from the weak form). The eigenpairs $(\sigma, \mathbf{z})$ are computed by an inverse iteration (shifted inverse power) method. For a prescribed shift σ_0, the iteration reads

$$(\mathbf{A} - \sigma_0\mathbf{B})\,\mathbf{y}_{k+1} = \mathbf{B}\mathbf{z}_k, \qquad \mathbf{z}_{k+1} = \frac{\mathbf{y}_{k+1}}{\|\mathbf{y}_{k+1}\|}, \tag{A.22}$$

with an eigenvalue update obtained from a Rayleigh quotient,

$$\sigma_{k+1} = \frac{\mathbf{z}_{k+1}^T\mathbf{A}\mathbf{z}_{k+1}}{\mathbf{z}_{k+1}^T\mathbf{B}\mathbf{z}_{k+1}}. \tag{A.23}$$

The computed growth rates and eigenmodes are then compared against the analytical predictions in the parameter regime where the asymptotic framework is expected to apply.

Appendix B

Notation map

This appendix summarises the principal notation reused across the thesis. Additional symbols introduced only for local derivations are defined in the relevant chapter or section.

Symbol	Meaning	Used in
Sheet variables and properties		
$\mathbf{x}$	Position vector	Chs. 2–4
x, y, z	Cartesian coordinates	Chs. 2–4
s	Arclength coordinate along the sheet	Ch. 2
L	Sheet length	Ch. 2
L_x, L_y	Chamber dimensions	Ch. 2
h	Sheet thickness	Ch. 2
θ	Angle of the sheet tangent with the horizontal axis	Ch. 2
κ	Sheet curvature	Ch. 2
Δ	End-shortening / confinement parameter	Ch. 2
ρ_{sh}	Sheet density	Ch. 2
F_x, F_y	Components of the internal sheet force resultant	Ch. 2
B	Bending modulus	Ch. 2
E	Young's modulus; where stated explicitly, energy	Chs. 2–4
$t_\star$	Characteristic time scale	Ch. 2
Fluid variables and properties		
$\mathbf{u}$	Velocity vector	Chs. 2–4
u, v, w	Velocity components	Chs. 2–4
p	Pressure	Chs. 2–4
ρ_ℓ	Fluid density	Ch. 2
ϕ_i	Velocity potential in i(u for the upper and d for the lower chamber)	Ch. 2
λ	Structure–fluid mass ratio parameter	Ch. 2
σ	Linear growth rate	Ch. 2
ω	Angular frequency	Ch. 2

Symbol	Meaning	Used in
Modal and variational quantities		
A_n	Amplitudes of the sheet modes in $y = \sum_n A_n \sin(\pi n x)$	Ch. 2
a_m	Amplitudes in the modal expansion of the fluid potential	Ch. 2
$\mathcal{L}$	Lagrangian of the coupled sheet–fluid system	Ch. 2
Numerical formulation		
Re	Reynolds number	Chs. 3–4
$\mathbf{F}$	Lagrangian force density in the immersed-boundary formulation	Chs. 3–4
I	Interpolation operator from Eulerian to Lagrangian grid	Chs. 3–4
R	Regularisation operator from Lagrangian to Eulerian grid	Chs. 3–4

Bibliography

[1] Praveena Nair Sivasankaran, Thomas Arthur Ward, Erfan Salami, Rubentheren Viyapuri, Christopher J. Fearday, and Mohd Rafie Johan. An experimental study of elastic properties of dragonfly-like flapping wings for use in biomimetic micro air vehicles (bmavs). *Chinese Journal of Aeronautics*, 30(2):726–737, 2017. ISSN 1000-9361. doi: https://doi.org/10.1016/j.cja.2017.02.011. URL `https://www.sciencedirect.com/science/article/pii/S1000936117300316`.

[2] C. C. Hopkins, S. J. Haward, and A. Q. Shen. Purely elastic fluid–structure interactions in microfluidics: Implications for mucociliary flows. *Small*, 16: 1903872, 2020.

[3] Alison Wright. Pushed to the limit. *Nature Physics*, 3(1):19–19, 2007.

[4] E. Cerda and L. Mahadevan. Geometry and physics of wrinkling. *Phys. Rev. Lett.*, 90:074302, Feb 2003. doi: 10.1103/PhysRevLett.90.074302. URL `https://link.aps.org/doi/10.1103/PhysRevLett.90.074302`.

[5] Médéric Argentina and L. Mahadevan. Fluid-flow-induced flutter of a flag. *Proceedings of the National Academy of Sciences*, 102(6):1829–1834, 2005. doi: 10.1073/pnas.0408383102.

[6] Hassen M.Ouakada and Mohammad I.Younisbc. On using the dynamic snap-through motion of mems initially curved microbeams for filtering applications. *Journal of Sound and Vibration*, 333:555–568, 2014.

[7] Sergei E. Medvedev and Yuri Yu. Podladchikov. New extended thin-sheet approximation for geodynamic applications—I. Model formulation. *Geophysical Journal International*, 136(3):567–585, 03 1999.

[8] A. E. Pusok and Boris J. P. Kaus. Development of topography in 3-d continental-collision models. *Geochemistry, Geophysics, Geosystems*, 16(5): 1378–1400, 2015.

[9] J.B. Naliboff, C. Lithgow-Bertelloni, L.J. Ruff, and N. de Koker. The effects of lithospheric thickness and density structure on earth's stress field. *Geophysical Journal International*, 188(1):1–17, 01 2012.

[10] Mobin Marvi and Majid Ghadiri. A mathematical model for vibration behavior analysis of dna and using a resonant frequency of dna for genome engineering. *Scientific Reports*, 10, 02 2020.

[11] Jiyu Sun and Bharat Bhushan. The structure and mechanical properties of dragonfly wings and their role on flyability. *Comptes Rendus Mécanique*, 340 (1):3–17, 2012.

[12] Zachary Manchester and Abraham Loeb. Stability of a light sail riding on a laser beam. *The Astrophysical Journal Letters*, 837(2):L20, mar 2017.

[13] Douglas P. Holmes. Elasticity and stability of shape-shifting structures. *Current Opinion in Colloid and Interface Science*, 40:118–137, 2019. ISSN 1359-0294. doi: https://doi.org/10.1016/j.cocis.2019.02.008. Particle Systems.

[14] S.P. Timoshenko and J.N. Goodier. *Theory of Elasticity*. McGraw-Hill Book Company, 1964.

[15] S.P. Timoshenko and J. M. Gere. *Theory of elastic stabiility*. McGraw-Hill Book Company, 1961.

[16] S. Timoshenko and S. Woinowsky-Krieger. *Theory of Plates and Shells, 2nd edn. McGraw-Hill, New York*. McGraw-Hill Book Company, 1987 edition, 1959.

[17] Alan R. Champneys, Timothy J. Dodwell, Rainer M. J. Groh, Giles W. Hunt, Robin M. Neville, Alberto Pirrera, Amir H. Sakhaei, Mark Schenk, and M. Ahmer Wadee. Happy catastrophe: Recent progress in analysis and exploitation of elastic instability. *Frontiers in Applied Mathematics and Statistics*, 5, 2019.

[18] J.M. T. Thompson. Catastrophe theory in mechanics: Progress or digression. *Journal of Structural Mechanics*, 10(2):167–175, 1982.

[19] Luka Pocivavsek, Robert Dellsy, Andrew Kern, Sebastián Johnson, Binhua Lin, Ka Yee C Lee, and Enrique Cerda. Stress and fold localization in thin elastic membranes. *Science*, 320(5878):912–916, 2008.

[20] Oz Oshri, Fabian Brau, and Haim Diamant. Wrinkles and folds in a fluid-supported sheet of finite size. *Physical Review E*, 91(5):052408, 2015.

[21] Haim Diamant and Thomas A. Witten. Compression induced folding of a sheet: An integrable system. *Phys. Rev. Lett.*, 107:164302, Oct 2011. doi: 10.1103/PhysRevLett.107.164302. URL https://link.aps.org/doi/10.1103/PhysRevLett.107.164302.

[22] Oz Oshri and Haim Diamant. Pattern transitions in a compressible floating elastic sheet. *Physical Chemistry Chemical Physics*, 19(35):23817–23824, 2017. doi: 10.1039/C7CP03239K. URL https://doi.org/10.1039/C7CP03239K.

[23] Fabian Brau, Hugues Vandeparre, Abbas Sabbah, Christophe Poulard, Arezki Boudaoud, and Pascal Damman. Multiple-length-scale elastic instability mimics parametric resonance of nonlinear oscillators. *Nature Physics*, 7(1):56–60, 2011.

[24] K. Matan, R.B. Williams, T.A. Witten, and S.R. Nagel. Crumpling a thin sheet. *Physical Review Letters*, 88(7):076101, 2002. doi: 10.1103/PhysRevLett.88.076101. URL https://doi.org/10.1103/PhysRevLett.88.076101.

[25] M. Ben Amar and Y. Pomeau. Crumpled paper. *Proc. R. Soc. Lond. A*, 129:729–755, 1996.

[26] T.A. Witten. Stress focusing in elastic sheets. *Reviews of Modern Physics*, 79(2):643–675, 2007. doi: 10.1103/RevModPhys.79.643. URL https://doi.org/10.1103/RevModPhys.79.643.

[27] Jiangshui Huang, Megan Juszkiewicz, Wim H De Jeu, Enrique Cerda, Todd Emrick, Narayanan Menon, and Thomas P Russell. Capillary wrinkling of floating thin polymer films. *Science*, 317(5838):650–653, 2007.

[28] Hunter King, R Schroll, Benny Davidovitch, and Narayanan Menon. A sheet on a drop reveals wrinkling and crumpling as distinct symmetry-breaking instabilities. *submitted for publication at PNAS*, 2012.

[29] Benny Davidovitch, Robert D Schroll, Dominic Vella, Mokhtar Adda-Bedia, and Enrique A Cerda. Prototypical model for tensional wrinkling in thin sheets. *Proceedings of the National Academy of Sciences*, 108(45):18227–18232, 2011.

[30] Charlotte Py, Paul Reverdy, Lionel Doppler, José Bico, Benoît Roman, and Charles N. Baroud. Capillary origami: Spontaneous wrapping of a droplet with an elastic sheet. *Phys. Rev. Lett.*, 98:156103, Apr 2007.

[31] José Bico, Étienne Reyssat, and Benoît Roman. Elastocapillarity: When surface tension deforms elastic solids. *Annual Review of Fluid Mechanics*, 50(1): 629–659, 2018. doi: 10.1146/annurev-fluid-122316-050130.

[32] José Bico, Benoît Roman, Loïc Moulin, and Arezki Boudaoud. Elastocapillary coalescence in wet hair. *Nature*, 432(7018):690–690, Dec 2004. ISSN 1476-4687. doi: 10.1038/432690a.

[33] Y. Forterre, J. M. Skotheim, J. Dumais, and L. Mahadevan. How the venus flytrap snaps. *Nature*, 433:421–425, 2005.

[34] Michael Gomez, Derek E. Moulton, and Dominic Vella. Passive control of viscous flow via elastic snap-through. *Phys. Rev. Lett.*, 119:144502, Oct 2017. doi: 10.1103/PhysRevLett.119.144502.

[35] P.G. Ledda and co-authors. Fluid-induced snap-through instability of spherical shells. *arXiv e-prints*, 2025. URL `https://arxiv.org/abs/2506.12247`. Low-Reynolds-number flow; critical Cauchy number at onset.

[36] M.A. Pi, Y.-L.and Bradford. Nonlinear dynamic buckling of pinned–fixed shallow arches under a sudden central concentrated load. *Nonlinear Dyn*, 73:1289–1306, 2013.

[37] Basile Radisson and Eva Kanso. Dynamic behavior of elastic strips near shape transitions. *Physical Review E*, 108:024201, 2023. doi: 10.1103/PhysRevE.108.024201.

[38] Michael Gomez, Derek E. Moulton, and Dominic Vella. Dynamics of viscoelastic snap-through. *Journal of the Mechanics and Physics of Solids*, 124:781–813, 2019.

[39] A. Abbasi, T.G. Sano, D. Yan, and P.M. Reis. Snap buckling of bistable beams under combined mechanical and magnetic loading. *Philosophical Transactions of the Royal Society A*, 381(2244):20220029, 2023. doi: 10.1098/rsta.2022.0029. URL `https://doi.org/10.1098/rsta.2022.0029`.

[40] Ousmane Kodio, Alain Goriely, and Dominic Vella. Dynamic buckling of an inextensible elastic ring: Linear and nonlinear analyses. *PHYSICAL REVIEW E*, 101:053002, 2020.

[41] Doireann O'Kiely, Finn Box, Ousmane Kodio, Jonathan Whiteley, and Dominic Vella. Impact on floating thin elastic sheets: A mathematical model. *Physical Review Fluids*, 5(1):014003, 2020.

[42] Xianheng Guan, Anantha P Sarma, Eashwaren Kakarla Hamesh, Junyu Yang, Nhung Nguyen, Enrique Cerda, Luka Pocivavsek, and Sachin S Velankar. Compression-induced buckling of thin films bonded to viscous substrates: Uniform wrinkles vs localized ridges. *International Journal of Solids and Structures*, 254:111843, 2022.

[43] Xianheng Guan, Nhung Nguyen, Luka Pocivavsek, Enrique Cerda, and Sachin S. Velankar. Flat, wrinkled, or ridged: Relaxation of an elastic film on a viscous substrate undergoing continuous compression. *International Journal of Solids and Structures*, 275:112242, 2023. ISSN 0020-7683. doi: https://doi.org/10.1016/j.ijsolstr.2023.112242.

[44] A. Fargette, S. Neukirch, and A. Antkowiak. Elastocapillary snapping: Capillarity induces snap-through instabilities in small elastic beams. *Phys. Rev. Lett.*, 112:137802, 2014.

[45] Evgeniy Boyko, Howard A. Stone, and Ivan C. Christov. Flow rate–pressure drop relation for deformable channels via fluidic and elastic reciprocal theorems. *Physical Review Fluids*, 7:L092201, 2022. doi: 10.1103/PhysRevFluids.7.L092201.

[46] Ofek Peretz, Anand K. Mishra, Robert F. Shepherd, and Amir D. Gat. Underactuated fluidic control of a continuous multistable membrane. *Proceedings of the National Academy of Sciences*, 117(10):5217–5221, 2020. doi: 10.1073/pnas.1919738117.

[47] Hyeonseong Kim, Mohsen Lahooti, Junsoo Kim, and Daegyoum Kim. Flow-induced periodic snap-through dynamics of elastic beams. *Journal of Fluid Mechanics*, 913:A52, 2021. doi: 10.1017/jfm.2021.57.

[48] Oz Oshri, Kirill Goncharuk, and Yuri Feldman. Snap-induced flow in a closed channel. *Journal of Fluid Mechanics*, 986:A12, 2024. doi: 10.1017/jfm.2024.312.

[49] Michael Bonthron and Eleonora Tubaldi. Flow-induced snap through of bistable arches with generalized boundary conditions. *Journal of Applied Mechanics*, 92 (10):101009, 06 2025. ISSN 0021-8936. doi: 10.1115/1.4068862. URL `https://doi.org/10.1115/1.4068862`.

[50] Benjamin S. H. Connel and Dick K. P. Yue. Flapping dynamics of a flag in a uniform stream. *Journal of Fluid Mechanics*, 581:33–67, 2007. doi: 10.1017/S0022112007005307.

[51] Mohammad Tavallaeinejad, Michael P. Païdoussis, Mathias Legrand, and Mojtaba Kheiri. Instability and the post-critical behaviour of two-dimensional inverted flags in axial flow. *Journal of Fluid Mechanics*, 889:A16, 2020. doi: 10.1017/jfm.2020.111.

[52] Michael P. Païdoussis. The dynamics of cantilevered structures subject to axial flow. *Journal of Fluids and Structures*, 125:104075, 2024. doi: 10.1016/j.jfluidstructs.2024.104075.

[53] Cecilia Huertas-Cerdeira, Andres Goza, John E. Sader, Tim Colonius, and Morteza Gharib. Dynamics of an inverted cantilever plate at moderate angle of attack. *Journal of Fluid Mechanics*, 909:A20, 2021. doi: 10.1017/jfm.2020.922.

[54] Michael Gomez, Derek E. Moulton, and Dominic Vella. Critical slowing down in purely elastic 'snap-through' instabilities. *Nature Physics*, 13(2):142–145, Feb 2017. ISSN 1745-2481. doi: 10.1038/nphys3915.

[55] Luoding Zhu and Charles S. Peskin. Simulation of a flapping flexible filament in a flowing soap film by the immersed boundary method. *Journal of Computational Physics*, 179(2):452–468, 2002. ISSN 0021-9991. doi: https://doi.org/10.1006/jcph.2002.7066. URL `https://www.sciencedirect.com/science/article/pii/S002199910297066X`.

[56] Ronghui Zhang, Feng You, Zhihan Lv, Zhaocheng He, Haiwei Wang, and Ling Huang. Development and characterization a single-active-chamber piezoelectric membrane pump with multiple passive check valves. *Sensors*, 16(12), 2016. ISSN 1424-8220. doi: 10.3390/s16122108. URL `https://www.mdpi.com/1424-8220/16/12/2108`.

[57] Oz Oshri. Volume-constrained deformation of a thin sheet as a route to harvest elastic energy. *Phys. Rev. E*, 103:033001, Mar 2021. doi: 10.1103/PhysRevE.103.033001.

[58] Ganlin Lyu, Chao Chen, Xi Du, Mohammed S. Mughal, and Spencer J. Sherwin. Open-source framework for transonic boundary layer natural transition analysis over complex geometries. In *AIAA SCITECH 2022 Forum*, number AIAA 2022-4032, San Diego, CA, 2022. Session: Boundary Layer Transition II.

[59] Jacques Y. Xing, Chris D. Cantwell, and David Moxey. Enhancing the spectral/hp element framework for parallel-in-time simulations. *Computer Physics Communications*, 2025. in press.

[60] Oriol Colomés, Francesc Verdugo, and Ido Akkerman. A monolithic finite element formulation for the hydroelastic analysis of very large floating structures. *International Journal for Numerical Methods in Engineering*, 124(3):714–751, 2023.

[61] Kaloyan S. Kirilov, Jingtian Zhou, Joaquim Peiró, Mashy Green, David Moxey, Lourenço Beirão da Veiga, Alessandro Russo, and Franco Dassi. Mesh generation of curvilinear polygons for the high-order virtual element method (vem). *Computer-Aided Design*, Sep 2025.

[62] Jean Donea and Antonio Huerta. Arbitrary lagrangian–eulerian methods. In Erwin Stein, René de Borst, and Thomas J. R. Hughes, editors, *Encyclopedia of Computational Mechanics*. John Wiley & Sons, Ltd, Chichester, 2004. ISBN 0-470-84699-2. doi: 10.1002/0470091355.ecm009.

[63] V. Gravemeiera, S.M. Civanerb, and W.A. Wall. A partitioned-monolithic finite element method for thermo-fluid–structure interaction. *Comp. Meth. Applied Mechan. Engin.*, 401:115596, 2022.

[64] C. S. Peskin. Flow patterns around heart valves: a numerical method. *Journal of Computational Physics*, 10:252–271, 1972.

[65] Charles S. Peskin. The immersed boundary method. *Acta Numerica*, 11:479–517, 2002.

[66] Y. Tseng and J. Ferziger. A ghost-cell immersed boundary method for flow in complex geometry. *J. Comput. Phys.*, 192:593–623, 2003.

[67] Hans Johansen and Phillip Colella. A cartesian grid embedded boundary method for Poisson's equation on irregular domains. *Journal of Computational Physics*, 147(1):60–85, 1998. doi: 10.1006/jcph.1998.6075.

[68] Alex Main and Guglielmo Scovazzi. The shifted boundary method (sbm) for embedded boundary problems in computational mechanics. part i: Poisson and stokes problems. *Journal of Computational Physics*, 372:972–995, 2018. doi: 10.1016/j.jcp.2018.06.030.

[69] Alex Main and Guglielmo Scovazzi. The shifted boundary method (sbm) for embedded boundary problems in computational mechanics. part ii: Elliptic and stokes problems with discontinuous coefficients and stiff source terms. *Journal of Computational Physics*, 372:996–1026, 2018. doi: 10.1016/j.jcp.2018.06.028.

[70] Erik Burman, Peter Hansbo, Mats G. Larson, and Anders Massing. CutFEM: Discretizing geometry and partial differential equations. *International Journal for Numerical Methods in Engineering*, 104(7):472–501, 2015. doi: 10.1002/nme.4823.

[71] A. Roma, C. S. Peskin, and M. J. Berger. An adaptive version of the immersed boundary method. *Journal of Computational Physics*, 153:509–534, 1999.

[72] Ming-Chih Lai and Charles S. Peskin. An immersed boundary method with formal second-order accuracy and reduced numerical viscosity. *Journal of Computational Physics*, 160(2):705–719, 2000. doi: 10.1006/jcph.2000.6483.

[73] J. Mohd-Yusof. Combined immersed-boundary/b-spline methods for simulations of flow in complex geometries. *Center for Turbulence Research, Annual Research Briefs*, pages 317–327, 1997.

[74] E. A. Faldun, R. Verzicco, P. Orlandi, and J. Mohd-Yusof. Combined immersed-boundary finite-difference methods for three-dimensional complex flow simulations. *Journal of Computational Physics*, 161:35–60, 2000.

[75] Markus Uhlmann. An immersed boundary method with direct forcing for the simulation of particulate flows. *Journal of Computational Physics*, 209 (2):448–476, 2005. ISSN 0021-9991. doi: https://doi.org/10.1016/j.jcp.2005.03.017. URL `https://www.sciencedirect.com/science/article/pii/S0021999105001385`.

[76] Wouter-Paul Breugem. A second-order accurate immersed boundary method for fully resolved simulations of particle-laden flows. *Journal of Computational Physics*, 231(13):4469–4498, 2012. doi: 10.1016/j.jcp.2012.02.026.

[77] Tobias Kempe and Jochen Fröhlich. An improved immersed boundary method with direct forcing for the simulation of particle laden flows. *Journal of Computational Physics*, 231(9):3663–3684, 2012. doi: 10.1016/j.jcp.2012.01.021.

[78] K. Taira and T. Colonius. The immersed boundary method: A projection approach. *Journal of Computational Physics*, 225:3121–3133, 2007.

[79] D V Le, B C Khoo, and K M Lim. An implicit-forcing immersed boundary method for simulating viscous flows in irregular domains. *Computer Methods in Applied Mechanics and Engineering*, 197:2119–2130, 2008.

[80] Duc-Vinh Le, John White, Jaime Peraire, Kian Ming Lim, and Boo Cheong Khoo. An implicit immersed boundary method for three-dimensional fluid–membrane interactions. *Journal of Computational Physics*, 228:8427–8445, 2009. doi: 10.1016/j.jcp.2009.08.018.

[81] . Feldman and Y. Gulbeg. An extension of the immersed boundary method based on the distributed lagrange multiplier approach. *J. Comput. Phys.*, 322: 248–266, 2016.

[82] Y. Feldman. Oscillatory instability of 2d natural convection flow in a square enclosure with a tandem of vertically aligned cylinders. *Fluid Dyn. Res.*, 50: 051410, 2018.

[83] R. Sela, E. Zemach, and Y. Feldman. A semi-implicit direct forcing immersed boundary method for periodically moving immersed bodies: A schur complement approach. *Comput. Methods Appl. Mech. Engrg.*, 373:113498, 2021.

[84] W. Kim and H. Choi. Immersed boundary methods for fluid-structure interaction: A review. *Int.J. Heat Fluid Flow*, 75:301–3–09, 2019.

[85] Yongsam Kim and Charles S. Peskin. Penalty immersed boundary method for an elastic boundary with mass. *Physics of Fluids*, 19(5):053103, 05 2007. ISSN 1070-6631. doi: 10.1063/1.2734674. URL `https://doi.org/10.1063/1.2734674`.

[86] A. Goza and T. Colonius. A strongly-coupled immersed-boundary formulation for thin elastic structures. *J. Comput. Phys.*, 336:401–411, 2017.

[87] Nirmal J. Nair and Andres Goza. A strongly coupled immersed boundary method for fluid-structure interaction that mimics the efficiency of stationary body methods. *Journal of Computational Physics*, 454:110897, 2022. ISSN 0021-9991. doi: https://doi.org/10.1016/j.jcp.2021.110897. URL `https://www.sciencedirect.com/science/article/pii/S0021999121007920`.

[88] Kirill Goncharuk, Saichand Chowkampally, Yuri Feldman, and Oz Oshri. Unsteady relaxation of a thin sheet in a quiescent fluid. Preprint, August 2025.

[89] C. Taylor and P. Hood. A numerical solution of the navier–stokes equations using the finite element technique. *Computers & Fluids*, 1(1):73–100, 1973. doi: 10.1016/0045-7930(73)90027-3.

[90] Daniele Boffi, Franco Brezzi, and Michel Fortin. *Mixed Finite Element Methods and Applications*, volume 44 of *Springer Series in Computational Mathematics*. Springer, 2013. doi: 10.1007/978-3-642-36519-5.

[91] Volker John. *Finite Element Methods for Incompressible Flow Problems*, volume 51 of *Springer Series in Computational Mathematics*. Springer, 2016. doi: 10.1007/978-3-319-45750-5.

[92] J. N. Reddy, N. K. Anand, and P. Roy. *Finite Element and Finite Volume Methods for Heat Transfer and Fluid Dynamics*. Cambridge University Press, 2024.

ובכך מבטל את פירוק־הצימוד בממשק עד לדיוק מכונה. אף שהוא איטי מן הסכמה החצי־אימפליציטית, הפותר נותר נגיש עם צריכת זיכרון מסדר N ועלות חישובית מסדר $N^{4/3}$ על רשתות קרטזיות. השיטה איתנה בצימוד חזק בין זורם למבנה, בתנועה מהירה, במרווחים קטנים ובהעתקות גלובליות גדולות, והיא כלי הבחירה לאי־יציבויות מצומדות חזק.

תקציר

האינטראקציה בין יריעות אלסטיות דקות לבין זורמים נפוצה בטבע ובטכנולוגיה, מן כנפי חרקים באוויר ועד שסתומים גמישים במכשירים מיקרופלואידיים. בהשראת מערכות אלו, עבודת דוקטורט זו מעמיקה את ההבנה של הצימוד בין יריעה לזורם באמצעות ניתוח האיזון הבסיסי בין אינרציה, אלסטיות והתנגדות זורם, ובאמצעות פיתוח שיטות נומריות המסוגלות ללכוד צימוד דו־כיווני מהיר של מבנה וזורם.

העבודה מבוססת על שלושה מאמרים. המאמר הראשון, שפורסם ב-Journal of Fluid Mechanics, מציב מסגרת אנליטית להובלה הנוצרת מפרפור בתצורה חדשה. אנו בוחנים את תחילת התנועה של הזורם בתוך חלל סגור, תוצאה של דפורמציות דינמיות של יריעה אלסטית. היריעה דחוסה בין דפנות הצד ומחלקת את החלל לשני תאים, שכל אחד מהם מכיל בתחילה זורם בלתי־צמיג במנוחה. כאשר מתאפשר חילוף זורם בין התאים, היריעה נעשית בלתי יציבה ומשרה זרימה. נבנית מסגרת אנליטית המתארת את הצימוד הדו־כיווני בין היריעה לבין הזורם, ואנו מנתחים את הדינמיקה בשלבי ההתחלה והביניים. קצבי הגדילה ותדירויות התנודה של האופן השני והאופן הראשון מתקבלים אנליטית בתחום המשרעת הקטנה. בשלבים מאוחרים יותר נבחן המעבר מן האופן השני הבלתי יציב אל האופן הראשון היציב. עבור גאומטריית תא נתונה נמצא כי אנרגיית האלסטיות ההתחלתית של היריעה מומרת בעיקר לאנרגיה ההידרודינמית של הזורם כאשר היריעה קלה יחסית לזורם, ומומרת בעיקר לאנרגיה הקינטית של היריעה כאשר היא כבדה יחסית.

המאמר השני, שפורסם ב-Journal of Computational Physics, מציג שיטה חצי־אימפליציטית מסוג direct-forcing immersed-boundary המשולבת בסכימת SIMPLE. ליבת SIMPLE נשמרת: צעד ניבוי מהירות מתקדם באמצעות הלחץ מן הצעד הקודם, ומשוואת תיקון־לחץ אוכפת אי־דחיסות תוך הכרה בתפקידו של הלחץ ככופל לגראנז׳ של משוואות Navier–Stokes הבלתי דחיסות. החידוש הוא שילוב אילוץ הגבול השקוע בתוך אותו תיקון עצמו: כוח הגבול מטופל ככופל לגראנז׳ המכתיב את מהירות הגוף השקוע ונפתר יחד עם הלחץ בצעד תיקון יחיד ומצומד. כך נאכפים בו־זמנית אי־דחיסות ואי־החלקה בשלב התיקון, בעוד צעד הניבוי נותר ללא שינוי. מתקבל פותר מהיר מאוד שבו שייר פירוק־הצימוד בממשק זעיר, המתאים למחקרי פרמטרים רחבים ולחישובי FSI בקני מידה גדולים.

המאמר השלישי, שפורסם ב-Theoretical and Computational Fluid Dynamics, מפתח פותר immersed-boundary אימפליציטי מלא המבוסס על big-box Vanka smoother. הפתרון מתבצע בכל צעד זמן למערכת מצומדת אחת של משוואות Navier–Stokes יחד עם אילוץ הגבול השקוע,

אי יציבות דינמית של יריעות דקות בתוך הזורם

עבודה זו מוגשת כחלק מהדרישות
לקבלת התואר "דוקטור לפילוסופיה"

מאת

קיריל גונצ'רוק

הוגשה לסנאט אוניברסיטת בן-גוריון בנגב

_____ אישור המנחים

אוקטובר 2025

באר שבע

אי יציבות דינמית של יריעות דקות בתוך הזורם

עבודה זו מוגשת כחלק מהדרישות
לקבלת התואר "דוקטור לפילוסופיה"

מאת

קיריל גונצ'רוק

הוגשה לסנאט אוניברסיטת בן-גוריון בנגב

אוקטובר 2025

באר שבע